

M0010779TP

6080234 0

A Source-Extraction Based Coupling Method for Computational Aeroacoustics

Zongkang Wang

A thesis submitted in partial fulfilment of the requirements
for the Degree of Doctor of Philosophy



University of Greenwich
London, U.K.

January 2004

Abstract

This thesis involves the computation of aerodynamically generated sound using a source-extraction based coupling approach.

In the present coupling method, the unsteady aerodynamic calculation and the calculation of sound propagation are separated artificially. A set of acoustic perturbation equations is derived by decomposing all flow variables into their dominant part and their fluctuating part, and neglecting some small-magnitude terms, and further simplified into a set of isentropic perturbation equations. Accompanying the derivation of the acoustic perturbation equations, a new extracting formulation for the acoustic source terms contained in the unsteady flow field is proposed. The acoustic source terms required in solving the acoustic perturbation equations are computed numerically from the time-dependent solutions of the unsteady flow field.

In the simulation of the unsteady flow, the unsteady Reynolds-Averaged-Navier-Stokes equations (RANS) based cell-centred finite volume method is mainly used. A large eddy simulation (LES) technique is also employed in the investigation of one application case. A powerful and efficient high order dispersion-relation-preserving (DRP) finite difference scheme with fully staggered-grid variable arrangements is implemented in the solution of the acoustic perturbation equations. The performance of a set of radiation boundary conditions is examined for various background flows. A suitable and efficient coupling procedure, in conjunction with the source-extraction formulation, is designed between the cell-centred finite volume based CFD solver and the fully-staggered finite difference based acoustic solver.

A range of acoustic model problems are investigated with the purpose of assessing the feasibility and accuracy of the source-extraction formulation associated with the coupling procedure. These model problems include wave propagation, reflection, interaction, and scattering, of acoustic pulse with/without background mean flow. The accuracy of computational results from these model problems is very encouraging when reasonable

computational mesh sizes and time steps are used in both the CFD solver and the acoustic solver.

Several applications of the source-extraction based coupling method to some more complex cases have also been examined. These cases are: 1) generation and propagation of sound by a series of vortices impinging on a finite thin flat plate; 2) generation and propagation of sound from a subsonic flow past a finite thin flat plate with a small angle of attack; 3) generation and near field radiation of aerodynamic sound from an low speed, laminar flow over a two-dimensional automobile door cavity; 4) flow-induced noise from an open cavity turbulent flow. These application calculations have demonstrated preliminarily the capability and potential of the new source extraction formulation for solving more realistic aeroacoustic problems.

Acknowledgement

The author wishes to express his gratitude to the University of Greenwich which sponsored this study.

I would like to thank my supervisors Dr. Choi-Hong Lai, Professor Koulis Pericleous and Dr. Georgi Djambazov for their concern and guidance at the various stages of the research process. I also appreciate Dr. Nick Croft for his helpful advice in the application of the in-house CFD code for this research.

And last but not least, I would like to thank my parents and my elder brother for their constant understanding, care and support.

Zongkang Wang

List of Figures

1.1. Schematic of a possible domain decomposition of computational domain	16
2.1. Decomposition of $q(x_i, t)$ into $\bar{q}(x_i, t)$ and $q'(x_i, t)$	49
3.1. A typical control volume for a 2-D Cartesian mesh.....	63
3.2. Two adjacent control volumes and the interface in a 2-D Cartesian mesh	66
3.3. Schematic for the QUICK interpolation formula in x direction	73
3.4. The flowchart of the SIMPLE algorithm.....	84
3.5. The flowchart of the SIMPLE algorithm for transient flow calculation	85
4.1. $\bar{\alpha}\Delta x$ versus $\alpha\Delta x$ for the optimized 4th-order DRP difference scheme	95
4.2. Comparison of the optimized 4th-order DRP scheme with several standard central finite difference schemes.....	96
4.3. Comparison of group velocity of the DRP scheme with the 6th-order standard central difference scheme	97
4.4. Locations of variables for a fully staggered mesh scheme for a 2-D case	104
4.5. Solution of the parametric equation for the staggered scheme coefficient a_1	107
4.6. Comparison of the non-staggered optimized 4th-order DRP scheme with the staggered optimized 4th-order DRP scheme	108
4.7. Parametric solutions for the temporal integration coefficient b_0	109
4.8. Effect of the point number per wavelength on numerical accuracy	115
4.9. Effect of the size of time step on computational results	115
4.10. Comparison of computed solution with exact solution at two propagating locations	117
4.11. Sketch of computational domain for the 2-D initial pulse propagation problem with a uniform mean flow	117
4.12. Computed pressure contours of the 2-D wave propagation in a uniform mean flow with at 4 time instants	118
4.13. Sketch of computational domain for the initial 2-D pulse propagation in a non-uniform mean flow.....	119

4.14. Computed pressure contours of the 2-D wave propagation in a non-uniform mean flow at 4 time instants.....	120
4.15. Sketch of computational domain for the initial 2-D pulse propagation in a shear mean flow	121
4.16. Computed pressure contours of the 2-D wave propagation in a shear mean flow at 4 time instants.....	122
4.17. Sketch of computational domain for the initial 2-D pulse propagation in an incidence mean flow	122
4.18. Computed pressure contours of the initial 2-D pulse propagation in an incidence mean flow at 4 time instants	123
5.1. Sketch of integral approximation for the evaluation of the source term	127
5.2. Schematic of a CFD simulation domain and an acoustic computation domain as well as their representative meshes	129
5.3. Schematic of the mapping of CFD data onto the CAA mesh (k : CFD cell number, i, j : CAA cell number; N : number of CFD cells in each of the CAA cell).....	130
5.4. Staggered storage locations for the acoustic source terms and the mean flow variables.....	130
5.5. Flow chart for the coupling procedure of a CFD solver and an acoustic solver	132
5.6. Pressure distribution along x-axis at 40th, 140th, 240th, 340th, 440th, 540th acoustic time steps with the first-order interpolation.....	135
5.7. Pressure distribution along x-axis at 40th, 140th, 240th, 340th, 440th and 540th acoustic time steps with the second-order interpolation.....	135
5.8. Pressure distribution along $y = 0.03125\text{m}$ at 50th, 100th, 150th, 200th and 250th acoustic time steps for the acoustic pulse without mean flow	137
5.9. Pressure distribution along $y = 7.46875\text{m}$ at 75th, 150th, 225th and 300th time steps for the acoustic pulse with a mean flow	138
5.10. Instantaneous computed corrected pressure contours at 4 acoustic time instants for the acoustic pulse with mean flow	139
5.11. Pressure distribution along $y = 0.03125\text{m}$ at 50th, 100th, and 150th acoustic time steps for two simultaneous pulses without mean flow	141
5.12. Instantaneous corrected pressure contours at four acoustic time steps for two simultaneous pulses without mean flow	142
5.13. Pressure distribution along $y = 0.03125\text{m}$ at 75th, 150th, 225th, 300th acoustic time steps for the reflection of the acoustic pulse by the infinite flat plate.....	144
5.14. Comparison of the CFD pressure and the acoustic perturbation pressure along $y = 0.03125\text{m}$ at 75th, 150th, 225th, 300th acoustic time steps	144

5.15. Pressure distribution along $x = 0.5\text{m}$ at 4 acoustic time steps for the reflection of the acoustic pulse by the infinite flat plate.....	145
5.16. Instantaneous corrected pressure contours at four acoustic time steps for the reflection of the acoustic pulse by the infinite flat plate.....	146
5.17. Pressure distribution along $y = 8.275\text{m}$ at four acoustic time steps for the pulse scattering by the square object.....	148
5.18. Pressure distribution along $y = 7.525\text{m}$ at four acoustic time steps for the pulse scattering by the square object.....	149
5.19. Pressure distribution along $x = 8.225\text{m}$ at four acoustic time steps for the pulse scattering by the square object.....	150
5.20. Pressure distribution along $x = 10.525\text{m}$ at four acoustic time steps for the pulse scattering by the square object.....	151
5.21. Instantaneous corrected pressure contours at four acoustic time steps for the pulse square object.....	152
5.22. Time history of the corrected pressure and the reference solution at 3 points for the pulse scattering by the square object.....	153
6.1. Sketch of vortices impinging on a thin flat plate and CFD boundary conditions	156
6.2. Computational domain and boundary conditions for the acoustic calculation.....	157
6.3. Perturbation velocity vectors in the unsteady flow field at 4 different CFD time steps	158
6.4. Contours of the acoustic source term, \bar{R}_c , in Eq.(2.90) at the 200th and the 250th acoustic time step	159
6.5. Contours of the acoustic source term, $\bar{R}_{m,x}$, in Eq.(2.90) at the 200th and the 250th acoustic time step	160
6.6. Contours of the acoustic source term, $\bar{R}_{m,y}$, in Eq.(2.90) at the 200th and the 250th acoustic time step	161
6.7. Perturbation pressure in the specified cells above and below the flat plate	162
6.8. Instantaneous corrected pressure contours at 4 acoustic time step for the vortices impinging on the thin flat plate	163
6.9. Instantaneous acoustic perturbation pressure contours at 4 acoustic time steps for the vortices impinging on the thin flat plate	164
6.10. Perturbation velocity vectors in the unsteady flow field at 4 different CFD time steps	166
6.11. Instantaneous acoustic perturbation pressure contours at 4 acoustic time steps	167
6.12. Schematic of the car door cavity and the computational domain sizes	168
6.13. Computational grid around the cavity mouth and the cavity	169

6.14. The computed boundary layer velocity profile in the vicinity of the trailing edge of the cavity lip	170
6.15. Time history of pressure and normal component of velocity at the corner right before the rear cavity edge.....	171
6.16. Time history of pressure at 3 selected points	172
6.17. Instantaneous vorticity contours at 4 time instants.....	173, 174
6.18. Instantaneous pressure contours at 4 time instants.....	175, 176
6.19 Instantaneous velocity vectors of the unsteady flow field at 0.00242s	177
6.20. Mean pressure coefficients on the floor of the cavity	177
6.21. Sketch of the cavity configuration and the selected points for FFT	178
6.22. Power spectrums of the time of the pressure at 4 selected points.....	179
6.23 Power spectrums of the pressure and the normal velocity at point 5	180
6.24. Computational mesh for acoustic calculation.....	182
6.25. Instantaneous acoustic perturbation pressure contours at 4 time instants	183, 184
6.26. Instantaneous contours of the acoustic source term in Eq.(2.90) at the 240 th acoustic time step.....	185
6.27. Sketch of the 3 selected points and their coordinates.....	186
6.28. Schematic of the 2-D open cavity flowfield and the computational domain sizes.....	188
6.29. Computational mesh for the CFD simulation of the open cavity flow.....	189
6.30. Time history of pressure from $k - \varepsilon$ modelling, a) near the corner of the leading edge; b) near the middle on the floor; c) near the corner of the trailing edge.....	190
6.31. Instantaneous vorticity contours from $k - \varepsilon$ modelling at 5 different CFD time instants	191
6.32. Time history of pressure from LES, a) near the corner of the leading edge; b) near the middle on the floor; c) near the corner of the trailing edge	194
6.33. Instantaneous vorticity contours from LES for the cavity flowfield at 5 different CFD time instants	195
6.34. Instantaneous pressure contours and velocity vectors from LES for the cavity flowfield at time instant of 0.0042s. a) pressure contours; b) velocity vectors	196
6.35. Power spectrums of the pressure and normal velocity near the corner of the trailing edge.....	197
6.36. Instantaneous perturbation pressure contours in the near acoustic field at 2 acoustic time instants.....	199

List of Tables

1.1. Length and time scales involved in aeroacoustic calculation for turbulent flows	15
3.1. Meaning of various terms in the general equation	62
6.1. Meaning of various terms in the general equation	187
6.2. Comparison of computational spectral frequencies with the predicted from the modified Rossiter formula (6.5)	198

Contents

Acknowledgements

List of Figures

List of Tables

1. Introduction	1
1.1. Acoustics and Aeroacoustics	1
1.2. Computational Aeroacoustics (CAA)	4
1.3. A brief comparison of CAA and CFD	6
1.4. Solution strategies in CAA	9
1.4.1. Direct computation of sound	10
1.4.2. Coupling computation of sound	15
1.5. Objectives.....	21
1.6. Thesis layout	21
2. Acoustic Equations and Acoustic Sources	23
2.1. Lighthill's acoustic analogy theory.....	24
2.2. Some modifications and extensions of the Lighthill acoustic analogy	27
2.2.1. Powell's equation and Howe's equation.....	28
2.2.2. The Ffowcs Williams-Hawkings equation	30
2.2.3. Phillip's equation and Lilley's equation	31
2.3. Some treatments of acoustic sources associated with other acoustic propagation equations	33
2.3.1. Hardin and Pope's formulation and the treatment of source terms	34
2.3.2. Morris et al's nonlinear perturbation equations and the treatment of source terms	37
2.3.3. Bailly et al's momentum source terms for the linearized Euler equations.....	40
2.3.4. Billson et al's source terms for the linearized Euler equations.....	42
2.3.5. Ewert et al's acoustic perturbation equations and source terms	43
2.3.6. Golanski et al's source terms for the linearized Euler equations.....	45
2.4. A new acoustic source terms extraction formulation for the linearized Euler equations	47

3. Simulation of Unsteady Flow Field.....	59
3.1. Governing equations of fluid motion	60
3.2. Discretization of the general equation.....	62
3.2.1. Transient term	64
3.2.2. Source term	64
3.2.3. Diffusive term	65
3.2.4. Convective term.....	67
3.3. Interpolation schemes	68
3.4. Rhie-Chow interpolation method	74
3.5. Momentum pressure coupling---SIMPLE algorithm	76
3.6. Solution of algebraic equation.....	80
3.7. Implementation of boundary conditions	81
3.8. Determination of time step	82
3.9. Solution procedure of unsteady flow simulation	83
4. Numerical Solution of Acoustic Equations	86
4.1. Numerical schemes for acoustic wave calculation	87
4.2. DRP scheme.....	90
4.2.1. Spatial discretization.....	91
4.2.2. Optimized multi-level time discretization.....	98
4.2.3. Artificial selected damping.....	100
4.2.4. Solid wall boundary treatment	101
4.3. Staggered DRP-type scheme	102
4.3.1. Arrangement of variables on a fully staggered mesh	103
4.3.2. Staggered spatial discretization.....	104
4.3.3. Time integration of the staggered-type scheme	108
4.3.4. Solid wall boundary conditions.....	110
4.3.5. Radiation boundary conditions.....	111
4.4. Validation examples	113
5. The Coupling Procedure and Model Problem Investigations	125
5.1. The source-extraction based coupling procedure	125
5.2. Investigations of acoustic model problems.....	133
5.2.1. A 1-D pulse problem without mean flow	134
5.2.2. A 2-D pulse problem with/without mean flow	136
5.2.3. Interaction of two 2-D pulses in a static medium	139
5.2.4. Reflection of a 2-D pulse from an infinite plate	143
5.2.5. Scattering of a 2-D pulse by a square object.....	147

6. Preliminary Application Investigations	154
6.1. Acoustic field of vortices impinging on a thin flat plate	155
6.2. Sound generation due to a subsonic flow past a thin flat plate.....	165
6.3. Flow-induced cavity noise.....	167
6.4. A open cavity flow-induced noise using LES for the unsteady flow	187
7. Summary and Future Work	200
7.1. Summary	200
7.2. Suggestions for future work	202
Bibliography	205

Chapter 1

Introduction

1.1 Acoustics and Aeroacoustics

Sound is, just like light, one of the natural phenomena that are earliest known to human beings. In the real world, there exist various sounds. Sound is everywhere in our life. Sound may be good or bad. In most ordinary people's mind, harmonic and melodious music is a kind of good sound while roaring from engines/motors in transportation systems is just a kind of bad sound. We normally refer to such bad sound as noise.

Acoustics was originally, as one of the oldest branches in physics, related to the study of small pressure waves in a medium which can be detected by human ear. In other words, acoustics was mainly concerned with audible "sounds" (the typical range of frequency in which our ear can detect is : $20 \text{ Hz} \leq f \leq 20 \text{ kHz}$). In modern denomination, the scope of acoustics has been extended to higher and lower frequencies: ultrasound and infrasound. Structural vibrations are often included in acoustics. In addition to frequency, the study of sound is conventionally divided, according to the propagation medium, into aeroacoustics, solid acoustics and underwater acoustics. In this thesis, the original definition and the propagation of sound in fluids, particularly air, is considered.

Aerodynamic sound is an inevitable product of unsteady flow, and mainly the result of the unsteady flow fluctuation as well as its interactions with structures immersed in the flow. Once aerodynamic sound is generated it propagates/radiates outwards in the surrounding medium. Hence aeroacoustics may be defined as the study of how sound is generated in air flow, and how it propagates/radiates in the non-uniformly moving medium.

The goals of aeroacoustics are to understand the physics of aerodynamic sound generation, to develop effective and accurate prediction and analysis methods, and ultimately, to reduce the noise level which emitted from jet engine or any other units with highly unsteady flows. Naturally, aeroacoustics forms the basis of applications that relate to our daily life, such as hall acoustics, environmental acoustics, speech acoustics, physiological acoustics, and so on. Besides, aeroacoustics is important in many other fields, like automotive and energy industry.

Undoubtedly, the pioneering and distinguished textbook “Theory of Sound” by Rayleigh [1877] remains as the true basis of acoustics. Many fundamental ideas have been expressed in the book, and new facets of the celebrated scientific work have been giving great impulse to further research. However, aeroacoustics had long been a part of *aerodynamics* and had not become an independent field of research.

Aeroacoustic studies have being motivated by a variety of practical engineering needs from aviation and other sectors. The reduction of aerodynamic noise needs always to develop revolutionary concepts in the theory of aeroacoustics as well as accurate prediction techniques. After World War II, new challenges made the research of aeroacoustics enter the first golden age of aeroacoustics, which focused on the problems of jet noise and jet engine noise, and lasted from the late 1940s until the mid 1970s.

In 1952 Sir James Lighthill first proposed the famous theory of Lighthill’s acoustic analogy for sound generation by turbulence [Lighthill, 1952; 1954] in response to the demand of finding ways to reduce the noise produced by jet engines. The important work of Lighthill is now widely considered as the birth of aeroacoustics as an independent field of research. Since the pioneering work of Lighthill, much work later in aeroacoustics has been based on the well-known Lighthill’s acoustic analogy with certain modifications, simplifications, and adaptations to the particular flow conditions.

A recent survey from aircraft industry expects a growth of passenger kilometres of 100% or more in the next 15 years. In order to satisfy the resulting demand for larger and/or faster airplanes, more recently, several alternative air vehicles have been proposed for civilian transportation. These include the supersonic civilian airplanes, large civil transports propelled by modern profans, and others. The introduction of these alternatives, or other advanced aviation technology concepts and innovations, potentially increase aircraft noise. The noise of future supersonic civilian airplanes (supersonic jet noise and sonic boom), the

noise of future subsonic propulsion systems (e.g., large high bypass-ratio ducted fans with short inlet ducts), the noise of open rotors (e.g., helicopter rotors in descent), and the airframe noise of large airplanes are a few examples from aviation applications.

Regulatory agencies have begun to impose stricter noise regulations. Aeroacoustics researchers and engineers are now faced with the task of reducing the noise levels, not only of existing classes of aircrafts, but also of new, possibly even noisier ones. On the other hand, aeroacoustics has been listed by NASA as one of ten critical disciplines of science and engineering that will lead to gain scientific understanding in order to pioneer new and revolutionary concepts in aeronautics and to improve the theoretical, experimental, and computational tools for the design and analysis of advanced aerospace systems [Hessenius, 1993].

It is well-known to all that the reduction of the aerodynamic noise is very important for civil aeroplanes. The flow-induced noise is also one of the principal concerns military aircrafts. For high-speed fighter aircrafts, the vibration of structural loads, which partly results from the flow-induced aeroacoustic environment, on the vehicle and on weapons that may be in the vicinity of the aircraft, should be taken into account. The several dB reduction of sound pressure level could gain an obvious increase of the fatigue life of a particular vehicle.

In order to be able to compete with air traffic on short distance, high speed trains have to become faster. Hence, the need to reduce the aerodynamic noise is true for future high speed trains since the generated noise by unsteady pressure fluctuations on train body surface increases approximately in proportion to the sixth power of the travelling speed [Ogawa & Kamioka, 1999]. In addition, small-size cooling fans for computers or electronic systems, as well as air-conditioning devices, are more and more present in everyday life. Human beings need and call for silence, not only during the fly-over of an aircraft, but when experiencing the flow of a hair-dryer too.

Facing the stricter regulations and new practical problems encountered in the use of new technology, presently, aeroacoustics can be viewed as flourishing. As stated by Sir James Lighthill [Lighthill, 1993], the research of aeroacoustics has recently entered its second 'golden age'.

1.2 Computational Aeroacoustics

There are three distinct streams in the study of aeroacoustics: analytical methods, experimental methods and numerical methods.

Before the development of large memory and high-speed computers, the study of aeroacoustic problems was mainly based on the first two methods mentioned above, or empirical approaches combined with both theoretical methods and experimental methods. With rapid advancement in computational power and significant strides in numerical algorithm development, many problems in scientific and engineering fields have been studied using the computer as a tool. Consequently, many new branches of research have been generated, such as, computational mathematics, computational physics, computational chemistry, and so on. Similarly, the dramatically increasing in numerical investigations for aeroacoustic problems led to a new research field---Computational Aeroacoustics (CAA). Although aeroacoustics is not a new discipline, CAA is a relatively new research field in aeroacoustics. CAA is a broad field that encompasses research in the use of numerical simulations to better understand aerodynamic noise, and increasingly playing an important role in acoustic prediction and analysis of noise problems. According to a definition at the ICASE/NASA LaRc workshop in 1993 [Hardin, 1993], CAA is a relatively new research field of aeroacoustics, deals with the *direct calculation* of acoustic field generated by flow and of the interaction of acoustic field with flow. The phrase *direct calculation* means that the methodology proceeds directly from the fundamental physical principles that govern the time-dependent motion of the compressible flows.

The fact that the physics behind the unsteadiness that generates aerodynamic sound is very complicated inevitably leads to many challenges for CAA. Fluctuations tend to grow in shear layers and vortical structures. Resolving these fluctuations in shear layers and vortical structures can be difficult. Trying to capture the fluctuations in them is even more challenging. Separated regions, instabilities, and large and small scale turbulence structures can all contribute to the sound field. Furthermore, energy that is radiated as noise is typically only a small fraction of the total energy near the acoustic source. This is part of the scale disparity between acoustic and hydrodynamic fluctuations. The human ear is able to distinguish between signals with vastly varying amplitudes, so it is typical to use a logarithmic scale to describe them. The sound pressure level (SPL) is given by

$SPL = 20 \log(p'_{rms} / p_{ref})$ with units of decibels (dB). The reference pressure $p_{ref} = 20 \times 10^{-6}$ Pa is the threshold of human hearing in air at 1kHz for a typical human ear, and *rms* means the root mean square of the acoustic pressure perturbations. The ratio of pressure amplitudes between a quiet conversation, 60dB, and a rock 'n' roll concert, 120dB, is 1000. In addition, atmospheric pressure is 3500 times greater than the pressure amplitude of a 120dB signal. At 120dB, one starts feeling discomfort and experiences a ringing in the ears. Although this level is very loud to humans, it is so small that a typical computational fluid dynamics (CFD) simulation very easily loses the sound waves among the large hydrodynamic fluctuations. Simultaneously resolving the hydrodynamic fluctuations and the wide range of acoustic signals is very difficult.

Acousticians also have to deal with very disparate length and time scales. Most people can hear fairly well between frequencies of 100Hz and 10kHz. This corresponds to wavelengths of 0.034m and 3.4m, respectively. The requirement of enough mesh points in the domain to resolve the very short wavelength while having a domain large enough to encompass the long wavelength results in enormous computational mesh point number. One is also faced with the challenge of trying to propagate the signal to observers located at great distances from the sources. A similar scale problem occurs temporally. The wavelength λ of an acoustic wave is related to the temporal period T by $\lambda = cT$, where c is the speed of sound. The periods for 100Hz and 10kHz are 0.01s and 0.0001s, respectively. Hence, one needs many time steps for the short period, and long running time to get a significant sample of the long period. This problem is usually exacerbated by initial transients in numerical solutions which must decay sufficiently before one can start sampling the acoustics. Even when using sampling techniques developed for experimental work, it is difficult to run codes long enough to get statistically significant samples of pseudo-random phenomena. Furthermore, the disparity between different acoustic waves is only part of the problem. One also has to compare the acoustic scales with those of other fluid phenomena and the geometry. All these indicate that sound generated by aerodynamic flows are of multi-scale.

From the perspective of physics, two fundamental problems in CAA can be classified as follows:

- to model numerically sound generation (acoustic sources) as accurate as possible in the unsteady flows;
- to compute accurately the propagation/radiation of the resulting acoustic waves.

Broad goals of CAA are to enable aeroacoustic predictions in a variety of engineering flows, and to advance our understanding of the sound generation process in general. Flexibility with geometrical shapes and generality with physical boundary conditions is a major strength of computational approach in dealing with aeroacoustic problems. Also, as discussed in a review by Lele [1997], computational approaches to engineering problems should be supplemented, when possible, with other tools such as model and full scale testing, asymptotic analysis, etc. to gain the greatest insight into the problem at hand.

1.3 A brief comparison of CAA and CFD

In general, the study of aeroacoustics is concerned with noise produced by aerodynamic sources, including turbulence and moving aerodynamic surfaces. The process of generation and propagation of aerodynamic sound cannot be separated from the development process of unsteady flow field. Physically, both the flow field and the accompanying acoustic field are described by the same governing equations. In other words, the generation and propagation of aerodynamic sound are both governed by the Navier-Stokes equations. As we all know, computational fluid dynamics (CFD) is the analysis of systems involving fluid flow, heat transfer and associated phenomena by means of computer-based simulation according to a hierarchical mathematical model of Navier-Stokes equations. CFD has made impressive progress during the last two decades, especially in aerodynamic computations. In the hands of competent engineers, CFD has become not only an indispensable method for aircraft load predictions but also a reliable design tool.

CAA is rapidly emerging as an essential element in the study of aeroacoustics. Currently, much effort has been made in developing numerical schemes and methods in CAA. A natural question to ask is “why not use existing conventional CFD methods to solve aeroacoustic problems?” No attempt is made here to give a complete comparison between the computational aerodynamics with the standard CFD methodology and the computational aeroacoustics. Comparisons are only given in the following selective aspects.

Although both the flow field and the resulting acoustic field are governed by the same equations of motion of fluids----unsteady compressible Navier-Stokes equations, one must recognize that the nature and objectives of aeroacoustic problems are distinctly different from those commonly encountered in aerodynamics. Aerodynamic problems are often the time independent ones, whereas aeroacoustic problems are, by definition, time dependent [Tam, 1995]. When CFD methods were developed for aerodynamic computations, the numerical algorithms were generally devised for the steady solutions of flows. The main objective of computational aerodynamics is to obtain aerodynamic loads acting on various components of a vehicle, whereas one of the main objectives in CAA is to calculate wave propagation and far-field acoustic characteristics (e.g., SPL, directivity, etc.) which is of little significance in typical aerodynamic computations. Further, the characteristics of the unsteady flow field and that of the acoustic field are also significantly different. Sound waves are simply propagating pressure perturbations superimposed onto the mean flow field. Generally speaking, acoustic perturbations are several orders of magnitude smaller than the mean quantities of flow. Typical acoustic fluctuation has energy level of 8-10 orders of magnitude smaller than that of the hydrodynamic fluctuation in the flow field which contains the generation of the aerodynamic sound. On the other hand, the wavelength of acoustic waves is many times larger than the characteristic hydrodynamic length scales in the unsteady flow field. Therefore, the frequencies of acoustic waves are generally very high.

Another important issue which also reflects significantly different requirements for both computational aerodynamics and CAA is numerical dissipation and dispersion of a numerical scheme. The word 'dissipation' refers to the gradual decrease in the amplitude of the resulting acoustic waves as they propagate through a medium on the used computational grid. The word 'dispersion' refers to the propagation of the different wave components in the acoustic field at spurious, grid-dependent speed. Unfortunately, most conventional CFD schemes are with apparent numerical dissipation and dispersion. In fact, the numerical dissipation and dispersion as well as spurious, high-frequency reflection at computational boundaries present probably the biggest barriers to numerical solution of aeroacoustic problems where solutions are required at a great distance from the sound sources and a long running time. Though the same numerical concerns tend to occur in the calculations by means of CFD codes designed to capture the aerodynamic loading on a body, for the most

part they do not cause difficulty in obtaining appropriate solutions in the purely aerodynamic case since flow properties are required accurately only on the body itself. Numerical dissipation, which rapidly contaminates calculated aeroacoustic waveforms, is considered to be beneficial in solutions to aerodynamic problems since it increases the stability of the solution. Dispersion is rarely noted in conventional aerodynamic computations using standard CFD codes, again since there is no requirement that the solution be accurate throughout the computational domain. It may be expected that the use of the conventional CFD methods for aeroacoustic calculations cannot obtain good results. This may be easily shown through a simple numerical experiment in which one-dimensional propagation of sound waves generated by a piston at one end that starts oscillating at time zero was computed by a CFD solver (upwind fully implicit scheme) using the Reynolds-averaged-Navier-Stokes equations [Djambazov et al., 1998a]. The CFD solutions agree only well in a very narrow region next to the source end. The acoustic pressure decay quickly. Refining of the mesh does not change the result at all.

From a computational viewpoint, the implementation of the numerical solutions for both the aerodynamic flow field and the resulting sound field has significant differences. For example, in order to accurately resolve the structure of the flow field in which some regions involving strong gradients in flow variables, stretched meshes are generally employed in an aerodynamic computation using a CFD method. However, the regular Cartesian mesh is more desirably adopted even for bodies with curved surfaces exist in the flow (of course, this will also give rise to some difficulties in the treatment of the solid boundary).

Generally, it is somewhat difficult to propagate an acoustic wave faithfully on a stretched mesh. This is partly because strong stretching in the computational mesh will inevitably introduce artificial inhomogeneities. On the other hand, non-uniform mesh will strongly affect the dissipative and dispersive features of a numerical scheme (especially finite difference based schemes). Vichnevetsky [1987] showed that if a wave is propagating into a stretched mesh, the wave can actually appear to change frequency and be reflected such that it starts propagating back in the other direction! Similarly, the unstructured meshes will create irregular numerical interface all over the physical space. In time-dependent aeroacoustic problems, they will affect the propagation of the acoustic waves and

cause some non-physical acoustic phenomena, such as non-physical sound scattering, reflecting, and so on.

One can also note that the order of a numerical scheme implemented in the aerodynamic calculations using conventional CFD methods is usually lower than third order whereas the use of high-order (refer here to the exceed third-order) numerical schemes is common in computational aeroacoustics due to the small amplitude of acoustic wave propagation and multiple- frequency waveforms. This does not mean that one may not use high-order numerical schemes in aerodynamic computations. While high order numerical schemes can generally obtain more accurate results for aerodynamic problems compared to the common numerical schemes, they will inevitably increase the span of the computational stencil, which increases the computational cost. For many aerodynamic problems, the use of the common numerical schemes (less than the third order) may achieve a reasonable accuracy of a numerical solution. However, this is not true for most aeroacoustic problems. Further, it must be pointed out that a high order scheme is not necessarily dispersion-preserving.

Because of the reasons above, there are still some computational issues that are relevant and unique to aeroacoustics. Among the treatment of boundary conditions by which allowing anechoic passage of out-going acoustic waves, maintaining a silent passage/outflow of vertical flow disturbances which may be nonlinear is most critical. Crighton [1993], Tam [1995] and Lele [1997] had given a good discussion on these aspects. As pointed out by Tam [1995], the development of CAA requires independent thinking.

1.4 Solution strategies in CAA

Like computational fluid dynamics (CFD), CAA encompasses a wide variety of physical systems, physical models, numerical algorithms, and solution philosophies. By solution philosophies here they mean the combination of physical models and approximations which are used to solve an aeroacoustic problem----invariably there are many possible algorithms for any particular problem, and subtle tradeoffs are to be made in choosing one. From a computational point of view, two solution strategies can be classified currently, i.e., the direct sound computation and coupling computation of sound.

1.4.1 Direct computation of sound

One of the prediction strategies in CAA is the direct sound computation. The unsteady flow and the sound generated by the unsteady flow can be computed together using the unsteady compressible Navier-Stokes equations, i.e. the unsteady flow and its sound are regarded as correlated parts of the same flow field. These first-principle based computations of sound generation provide physical insight into the sound generation mechanisms and its interaction with the flow. Such calculations are also invaluable in developing other prediction methods, such as coupling methods (hybrid methods). Since such direct computations of aerodynamic sound generation allow a very detailed look at practically any flow quantity of interest, the mechanism of sound generation can be explored at a fundamental level. As these are better understood, perhaps one can look for new paradigms for the control of the noise

The direct sound computation can be accomplished using various levels of approximation, yielding more or less detailed descriptions of the acoustic field. One level of the direct sound computation is to utilize direct numerical simulation (DNS) to solve the unsteady, compressible Navier-Stokes equations on a computational domain (domain of interest). From the computational perspective, such computation is the most accurate and also the most straightforward numerical method. In the direct sound computations based on DNS, the governing equations (compressible or incompressible Navier-Stokes equations) are discretized directly, and solved numerically. If the mesh is fine enough to resolve the smallest scales of motion, one can obtain an accurate time-dependent solution of the governing equations completely free of modelling assumptions, in which the only errors are those introduced by the numerical discretization. DNS makes it possible to compute and visualize any quantity of interest, including those that are difficult or impossible to measure experimentally, and to study the relationships between flow variables and acoustic variables. In the past decade, endeavours in the use of DNS in CAA have met with some success, and has yielded important insights into aeroacoustic physics (e.g., Colonus et al., [1993]; [1997]; [1999]; Freund et al., [1997]; [1998]; [2000]; Gloerfelt et al., [2001]; Mitchell et al., [1995]; [1996]; Avital et al., [1999a]; Al-Qadi & Scott, [1998]; Inoue et al., [2001]).

Although DNS is useful and attractive tool for the study of aeroacoustics, it has many limitations. First, the use of highly accurate, high-order schemes is desirable to limit dispersion and dissipation errors, these schemes (spectral methods, for example) tend to have little flexibility in handling complex geometries and general boundary conditions. Second, in order to properly resolve all scales of an unsteady flow in DNS calculation one has to discretize the equations on extremely fine grids. The size of the smallest scales decreases with increasing Reynolds numbers, the dimensionless parameter that measures the relative importance of convective and diffusive effects. At present, typical estimates are that, to resolve all the scales of motion for a three-dimensional DNS, one requires a number of grid points proportional to the $9/4$ power of the Reynolds number and the cost of the computation scales like the third power of the Reynolds number [Piomelli et al., 1997]. Since the sound source depends on time correlations, in principle the entire flow history must be stored; this would impose prohibitive storage requirements even to compute the sound radiated by a model flow like isotropic turbulence. In addition, a huge computational domain has to be chosen in order to simulate the propagation of acoustic waves. It is well-known that most technically relevant flows in aeroacoustics are characterized by relatively high Reynolds numbers (i.e., characterized by $Re = O(10^6 - 10^9)$), it can easily be shown that it will be impossible to apply DNS for practical flow and aeroacoustic problems in the foreseeable future. To fulfil these two conditions at the same time will be a challenge for some generations of researchers to come. Furthermore, numerical calculations that include both the unsteady flow field and the acoustic field will introduce additional numerical issues. For these reasons, the calculations of an acoustic field based on DNS have largely been limited to simple geometries at low Reynolds number.

The lower level of the direct sound computation strategy is to use directly Large Eddy Simulation (LES). LES is similar to DNS in that it provides a time dependent solution of Navier-Stokes equations. Unlike DNS where all scales in the unsteady flow must be calculated, LES computes accurately only the dynamics of the large scales (i.e., the energy-containing eddies), which are known to contribute most to the sound generation in many problems, by using the filtered equations while the scales of the order of the grid spacing or less are modelled in some appropriate fashion, usually in a dynamic procedure. This method is based on the consideration that, while the large eddies are flow-dependent, the small

scales tend to be more universal, as well as isotropic. Furthermore, small scales react more rapidly to perturbations, and recover equilibrium quickly. Thus, the modelling of the subgrid scales is significantly simpler than that of the large scales, and can be more accurate. For this reason, LES is not restricted to low Reynolds number, which makes the use of LES very attractive, especially at Reynolds numbers of engineering interest. Because the effect of small (subgrid) scale eddies on the large (resolved) scale motion is modelled in LES, the computational cost is drastically reduced compared with direct numerical simulation (DNS). In recent years, some acoustic calculations from LES have been reported (e.g., Bogey et al., [2000a]; Bogey & Bailly, [2002, 2003]; Choi et al., [1999]; Avital et al., [1999b]; [2001]; Constantinescu & Lele, [2001]; Piomelli et al., [1997]; Zhao et al., [2000a]; Uzun et al., [2002]; Lupoglazoff et al., [2002]; Gloerfelt et al., [2002]; Katoh, [1992]; Lui & Lele, [2002]). In some numerical studies on jet noise based on LES, Reynolds numbers of one or two orders of magnitude higher than those being used in the investigations based on DNS are seen. Most features of the flow field and the acoustic field were in good agreement with computational results from DNS or experimental data. These investigations reveal that LES methods are capable of simulating flows at higher Reynolds numbers and capturing the main physics of flows. Since sound generation is an unsteady process, LES will probably be the most powerful computational tool to be used in aeroacoustic research in the foreseeable future since it is a better way to obtain time-accurate solutions.

Although the LES results in the literature are encouraging and show the potential promise of LES application to aeroacoustic prediction, it should be pointed out that LES has its own weaknesses. One of the weaknesses, which might affect the application of LES to sound computations, is the effect of the small scales on the acoustic sources. For example, none of the LES studies on jet noise done so far has predicted the high-frequency noise associated with the unresolved scales. This implies acoustic power may have been underestimated if the contribution of these unresolved scales is simply neglected. Although the contribution of the small scales to the momentum transport is usually small, their contribution to the sound generation may be significant. However, the problem of evaluating the sound generation of the unresolved, subgrid-scale motions may be alleviated or overcome by developing *new* subgrid-scale models. Piomelli et al [1997], Rubinstein and Zhou [1999], Seror et al. [1999], Zhao et al. [2000b], Bodony and Lele [2002], Bogey and

Bailly [2003] did some initial work on the investigation of the contribution of small-scale to the noise spectrum. More research on the development of subgrid-scale models is need.

It has also been noted that the highest Reynolds number achieved in the LES simulations, which is much higher than that attained by current DNS calculations, so far is still below those practical Reynolds number of interest ($Re = O(10^6 - 10^9)$). Simulations of aeroacoustic problems at higher Reynolds number (for example, jet noise) would be very useful in analyzing the broadband noise spectrum at such high Reynolds numbers. The recent jet noise computations of Bogey and Bailly [2002; 2003] are perhaps the most successful LES calculations done for *reasonably* high Reynolds number jets at the time of this writing. Similar with DNS, this is mainly a resolution problem. In LES the contribution of the large-scale structures is computed exactly. The similarity of the small scales, which only transmit energy to smaller scales (energy cascade), and the fact that the dissipation is set by the large scales are exploited by subgrid-scale models, of which the main purpose is to reproduce the energy transfer accurately, at least in a statistical sense. When the filter cutoff is in the inertial region of the spectrum, therefore, the resolution required by LES is nearly independent of the Reynolds number. However, the cost of LES calculation depends on the Reynolds number if a solid surface is present, since the length scale of the energy-carrying large structures is Reynolds number dependent near the wall [Meneveau & Katz, 2000]. In addition, the motion of the large scales must be computed accurately in time and space, fine grids (or high-order schemes) and small time-steps are required. Chapman [1979] estimated that the resolution requirements for the application of LES to a turbulent boundary layer of flat plate, in which the resolution required to resolve the outer layer of the growing boundary layer is proportional to $Re^{0.4}$, while for the sublayer (which, in aeronautical applications, only accounts for approximately 1% of the boundary layer thickness) the number of points need an increase at least like $Re^{1.8}$. Furthermore, since the turbulent motions are intrinsically three-dimensional, even flows that are two-dimensional or one-dimensional in the mean must be computed using a three-dimensional approach. Finally, for both the flow field and the resulting acoustic field, the equations of motion must be integrated over long time. Thus, while LES gives some relative improvements over DNS on the computational cost, its application to engineering flows remains expensive. Until recently, the direct sound calculation using LES is still used in academic environments and

research laboratories to study the mechanism of sound generation. In the author's opinion, with the development of subgrid scale models for wall layer modelling and the decreasing cost of computational power, the application of LES to direct sound computation in computational aeroacoustics is bound to become more and more affordable.

Apart from the direct computation of aerodynamic sound based on DNS and LES, several direct computations of sound from the unsteady solution of Reynolds-averaged-Navier-Stokes equations (RANS) were presented by some researchers. Shieh and Morris [Shieh & Morris, 1999; 2000] studied two-dimensional and three-dimensional acoustics of cavity flows with the use of unsteady RANS simulations. In their computations, the one-equation Spalart-Allmaras turbulence model [Spalart & Allmaras, 1992] and the Detached Eddy Simulation (DES) have been implemented to account for the turbulent flow field. Loh and Wang [2000] applied a new space time conservation element and solution element method (CE/SE for short) to compute the typical vortex-induced, self-excited oscillation gap noise problem and the subsonic cavity noise problem. Ashcroft et al. [2000a; 2000b] investigated numerically noise problem of an automobile door cavity using a multi-block, compressible, finite-volume, unsteady RANS solver with a Wilcox $k - \omega$ turbulence model [Wilcox, 1988]. Zhang et al. [1995] analysed far-field noise radiation from an unsteady supersonic cavity flow using RANS in conjunction with $k - \omega$ turbulence model. Although these computations have shown, to some extent, success, it should be noted that direct simulations of acoustic field based on RANS with algebraic Baldwin-Lomax turbulence model [Baldwin & Lomax, 1978] and $k - \varepsilon$ turbulence model [Jones & Launder, 1973] cannot usually obtain reasonable acoustic results due to their excessive turbulent dissipation (e.g., Baysal et al., [1992]; Shih et al., [1994]). Sinha and Arunajatesan [2000] criticized the use of RANS in flows that involve strong coupling with acoustics.

According to the discussion above, direct sound computation based on DNS for high/moderate-Reynolds number flows of practical interest is limited by tremendous resolution requirements that are far beyond the reach of the capability of even the fastest supercomputers available. On the other hand, direct sound computation based on LES for aeroacoustic problems is not inexpensive, and has some particular issues that need to be tackled. Under the circumstances, researchers in computational aeroacoustics field have to

seek for more practical solution strategy. The development of coupling methods for aeroacoustic problems has been an active area of research in computational aeroacoustics.

1.4.2 Coupling computation of sound

The major basis for the use of coupling methods comes from a theoretical analysis and the observation of characteristics of the flow field and the resulting acoustic field.

Most aeroacoustic problems of technological importance involve unsteady viscous flows (either laminar or turbulent). In many cases (such as jet noise or airframe noise) if there were no viscous effects of flows or instabilities, there would be no sound generation. However, an enormous range of length scales and time scales are involved in simulating unsteady viscous flows, especially turbulent flows, for aeroacoustic purposes. The following Table given by Morfey [2000] shows an estimation of these scales. In the table, $Re = u_e l_e / \nu$ is the Reynolds number and $Ma = u_e / c$ is the Mach number, where u_e and l_e denote velocity and length scales for the energy-containing eddies in the flow. The corresponding eddy time scale is $t_e = l_e / u_e$, while the smallest time and length scales in the flow (i.e., those at which dissipation takes place) are determined by the kinematic viscosity, ν , and the energy dissipation rate per mass, ε . The latter is assumed to scale as $\varepsilon \sim u_e^3 / l_e$.

Table 1.1. Length and time scales involved in aeroacoustic calculation for turbulent flows

Type of scale	Kolmogorov scale (smallest relevant scale)	Acoustic scale (largest scale)
Length	$\eta = \left(\frac{\nu^3}{\varepsilon} \right)^{0.25} \sim l_e Re^{-0.75}$	$l_e Ma^{-1}$
Time	$\tau = \left(\frac{\nu}{\varepsilon} \right)^{0.5} \sim t_e Re^{-0.5}$	t_e

Due to the distinct characteristics in both the unsteady flow field and the accompanying acoustic field, domain decomposition technique is generally adopted and is

also a natural consideration in computational aeroacoustics. Domain decomposition is a generic technique for solving large mathematical and computational problems by obtaining partial solutions of the different sub-problems that build up the original problem. The term ‘domain’ is most often used in a general sense and can refer to geometrical, physical, or any other type of subdivision. The coupling of viscous and inviscid calculations in some aerodynamic problems is an example of the application of domain decomposition in computational aerodynamics. In CAA, the implementation of concept of domain decomposition is that computational domain of interest is often divided into two parts considering different characteristics in both flow field and acoustic field. One is the ‘near field’ where main acoustic sources are contained. Other one is the ‘far field’ in which concerns are the propagation/radiation of the resulting acoustic waves. Figure 1.1 gives a schematic representation of a possible domain decomposition of the computational domain in computational aeroacoustics for jet noise problems and airframe noise problems of a multi-element airfoil system.

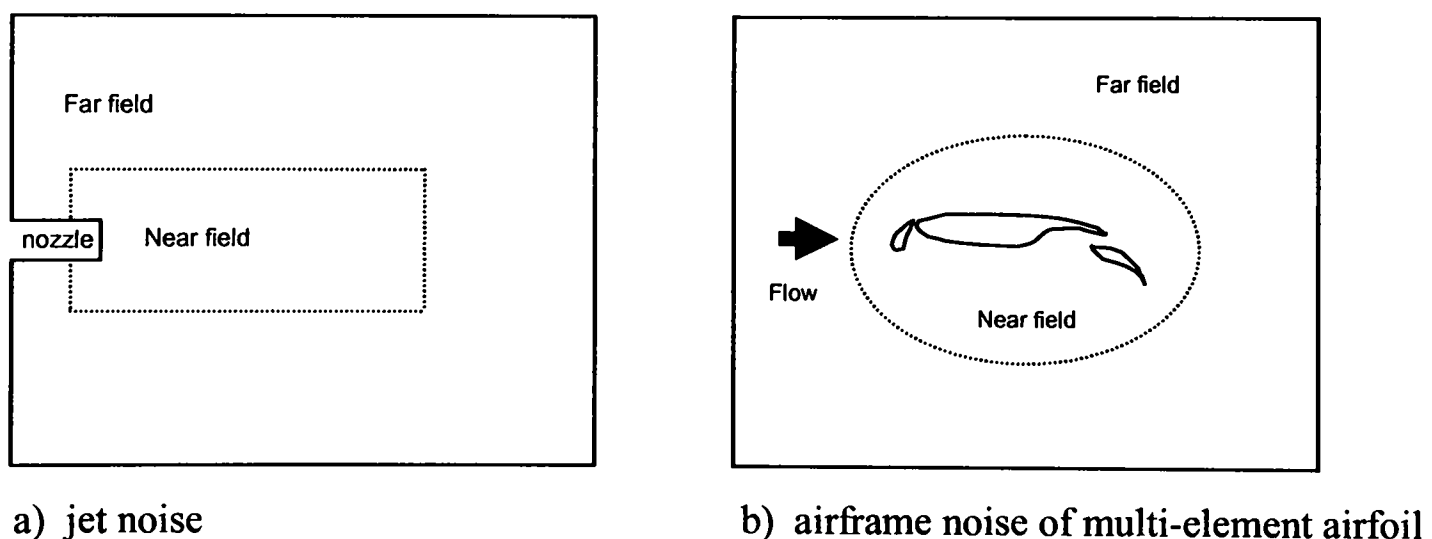


Fig. 1.1. Schematic of a possible domain decomposition of computational domain.

The flow field and the acoustic field are different and, at the same time, closely related each other. The acoustic sources are the result of the highly unsteady fluid motion in the near field or the interactions between the unsteady flow and bodies immersed in the flow. It could be said that calculating both acoustic waves and the small scale unsteady flow field is a harder problem than simply capturing the structure of the unsteady flow field itself. This suggests that the development of coupling methods is important in the

short/medium term. For coupling methods in CAA, the source region (the near-field of the unsteady flow) where detailed flow structures need to be resolved may be simulated by a CFD technique (DNS, LES or RANS). The acoustic field is then calculated via an acoustic analogy or by solving a set of acoustic perturbation equations. The most important advantage in such a fluid-acoustic coupled procedures is the aerodynamic calculation and the calculation of sound propagation/radiation are separated so that the most appropriate approach may be employed at each step. In such coupling calculations, the coupling is implemented through various types of the acoustic sources which may come from aeroacoustic theories, semi-empirical relations, experimental measurements, and direct numerical extraction from the unsteady solution in the flow field. The key to accurate prediction of aerodynamic sound depends greatly on the accurate description or simulation of the unsteady flow field, which is an essential requirement for all coupling methods. Undoubtedly, the use of coupling methods allows widely available general purpose CFD methods to be used as the first element of a coupled fluid-acoustic simulation, i.e. the unsteady calculation in the near field (or sound source field from an aeroacoustic point of view).

There are two types of coupling methods under the frame framework of the fluid-acoustic coupling. The first is to solve the full unsteady incompressible or compressible flow equations for the near-field of the unsteady flow (i.e. sound source region without any or with less extensive simplification), then make use of the calculated sources for the solution of the acoustic field through an acoustic integral approach. DNS, LES and unsteady RANS simulations as well as other appropriate methods can be used in the first step of the coupling. As discussed above, the use of DNS and LES in the whole computational domain of interest in solving aeroacoustic problems is still subject to certain limitations with the current computational resource. However, the flow phenomena involving the generation of acoustic sources are often located in a small near-field region, for example, for trailing-edge acoustics in the vicinity of the trailing edge or the acoustic physics in the vicinity of leading-edge of a slat. Thus, the computations of nonlinear unsteady flow fields in a limited region of the whole computational domain of interest using DNS or LES is feasible with the current computational power. For the solution of acoustic field, various versions of acoustic analogies can be applicable, such as Lighthill's wave equation [Lighthill, 1952; 1954], the Ffowcs Williams-Hawkings (FW-H) equation [Ffowcs Williams & Hawkings, 1969], and

Lilley's equations [Lilley, 1974]. An acoustic analogy is a rearrangement of the governing equations of fluid motion such that the left-hand side consists of a wave operator in an undisturbed medium and the right-hand side is comprised of acoustic source terms. The solution of the equation can be written as the convolution of the source terms with the Green function for the wave operator. Hence, with the strengths of the source terms obtained in the regions where they are significant, one can determine the acoustic signal at any point in the flow, including locations at long distances from the sources. The acoustic analogy is the most developed method and widely used in the aircraft industry. Another alternative is the Kirchhoff's surface method [Kirchhoff, 1883]. Although Kirchhoff-surface technique has been known for more than 100 years, it is only recently applied in CAA (e.g., Farassa & Myers, [1988]; [1995]; Lyrintzis & Mankbadi, [1988]; Pilon & Lyrintzis, [1998]; Difrancesantonio, [1997]; Brentner & Farassat, [1998]). In Kirchhoff-surface method, the acoustic sources are determined correspondingly from the unsteady solutions in the acoustic source field. In addition, the boundary element method (BEM) is also a choice for the prediction of far-field sound [Manoha et al., 1999]. The numerical simulation techniques (DNS, LES and RANS-based methods) can in principle be combined with each acoustic solver mentioned above. Hence a variety of different combinations is possible.

Coupling methods in which a numerical method (DNS, LES, or RANS) coupled with an acoustic analogy method or Kirchhoff-surface method have been used by many researchers, and achieved to some extent success in some aeroacoustic predictions. No attempt is made to give an overview due to the rapidly growing published literature. For such coupling methods, the most important advantage is that the calculation of acoustic field is economical computationally since certain integral formulation is used. However, the main drawback is that the details of the acoustic field cannot be obtained. In addition, an appropriate choice of the integral surface location, which may affect significantly the acoustic results, is not always handled easily.

In the past decade, the second type of coupling methods has already received much attention from CAA community. In the second type of coupling methods, the first step in the coupling is similar to the first step of the coupling procedure described above. The unsteady aerodynamic near-field, which contains the sound sources, is simulated by using DNS, LES and RANS-based methods. The difference between the two types of coupling methods lies in that for the second type of coupling methods the calculation of the acoustic

field is performed by solving a set of acoustic perturbation equations (APE) associated with source terms through certain numerical methods rather than an integral formula. Although the source terms are also extracted directly from the computed unsteady solution of the flow field, the extracting formulations for the acoustic source terms are developed corresponding to the set of acoustic equations. The extraction of the acoustic source terms is crucial in implementing the second type of coupling methods.

In general, a set of APE with source terms are derived from the Navier-Stokes equations through a decomposition of variable into base (non-acoustic) component and perturbation (acoustic) component and some simplified procedures. The acoustic perturbation equations govern the propagation of acoustic propagation/radiation. They are, in essence, the advanced versions of the classical Possion-type wave equation. However, the derivation of a set of APE remains more the form of the Navier-Stokes equations while acoustic analogies always result in *one* wave-operator-type acoustic equation for certain variables (e.g., acoustic pressure or density) with higher order partial derivatives than those in the original fluid flow governing equations.

One of the first attempts following the second type of coupling methods was made by Hardin and Pope [1994]. In their numerical procedure, the formulation for nearly incompressible flow is at leading-order strictly incompressible one. The pressure variations (required to maintain a strict divergence-free velocity field) in the incompressible flow are linked to an isentropic density perturbation. This nearly incompressible flow description is subtracted from the exact nonlinear compressible flow equations, and the resulting set of perturbation equations is viewed as a set of governing equations appropriate for the acoustic field and is discretized on an acoustic mesh which is chosen with a suitably large mesh spacing so that only the expected large-scale acoustic field is represented. Such a coupling procedure allows the implementation of the most efficient method on the most appropriate grid in each coupling step. The work of Hardin and Pope has made an important impact on the research of the second type of coupling methods. Hardin and Pope [1995] demonstrated its validity of their coupling procedure by conducting a simulation of acoustic field radiated from the laminar flow over a two-dimensional cavity. Lee and Koo [1995] investigated the sound generation due to an inviscid rotating vortex pair using Hardin and Pope's coupling method and obtained good prediction in comparison with an asymptotic solution. Recently, Shen and Sørensen [1999a] modified the aeroacoustic model in Hardin and Pope's non-

linear two-step procedure. The new formulation was applied to laminar flows around a circular cylinder [Shen & Sørensen, 1999b]. More recently, Shen and Sørensen [2001] further developed their formulation to deal with turbulent flows by using an eddy-viscous-based turbulence model, and calculated acoustic noise generated by the flow past a NACA0015 airfoil at an incidence of 20 degree. Miyake et al [Miyake et al., 2001] adopted the numerical coupling procedure proposed by Hardin and Pope to calculate the acoustic field from near-wall turbulent flow at low Mach number. However, the simulation of the acoustic source field in their coupling calculation is based on DNS. Viswanatham and Sankar [1995] employed a set of linearized Euler equations (LEE) with acoustic source terms which from the solution of RANS in the near field to predict noise radiated from axisymmetric supersonic jets. Morris et al [Morris et al., 1997] developed also a two-step coupling method in which a set of non-linear disturbance equations with source terms are derived. With the coupling between a RANS code and solving the non-linear disturbance equations with source terms, the acoustic field of some supersonic axisymmetric jets flow was investigated. Bailly and Daniel [1999] employed a treatment of acoustic source based on a stochastic approach in which RANS equations with a k- ϵ turbulence model were solved when LEE was used to calculate the subsonic jet noise. Actually, a turbulent velocity field from the knowledge of the local mean flow was used as a source term. Later, the source model with LEE was applied to compute sound field generated by two co-rotating vortices in a sheared mean flow through a coupling procedure in which the unsteady flow field are evaluated using a LES technique, see [Bailly et al., 2000]. Ewert et al [2000; 2001] proposed recently a set of acoustic perturbation equations for calculation of the propagation of the acoustic waves. At the same time, they also proposed a modelling way for acoustic sources when implementing the coupling procedure, and applied it to the calculation of the sound field generated by the low Mach number laminar flow over a circular cylinder and to predict trailing edge noise based on an LES of the compressible flow field and the acoustic perturbation equations. Compared to the first type of coupling method associated with acoustic analogies, the second type of coupling method not only obtains the acoustic sources strength directly from the unsteady flow but properly accounts for the refraction and scattering effects of non-uniform flow on the sound propagation as well. The detailed formulation description of some of the second type of coupling methods mentioned above and treatment for acoustic source terms will be discussed in following chapter.

1.5 Objectives of the Present Study

In the previous sections, a brief comparison between CAA and conventional CFD is made. Some difficulties and challenges faced in the development of CAA are pointed out. Current computational strategies used in CAA are discussed. The importance of adopting coupling methods for practical aeroacoustic prediction is particularly emphasized through the analysis of the characteristics in both the unsteady flow field and the acoustic field. The research in this thesis involves particularly the second type of coupling method. The main objectives of this research can be outlined as follows:

- to exploit a general numerical extracting formulation for the acoustic sources contained in the unsteady flow field, particularly under the framework of the second type of coupling methods, for the calculation of the resulting acoustic field by solving a set of acoustic perturbation equations.
- to investigate a high-order, optimized, staggered finite difference numerical method for the solution of the set of acoustic equations, including the use of a proper numerical boundary conditions.
- to build a suitable and efficient coupling procedure, in conjunction with the proposed source-extraction formulation, between a finite-volume based CFD solver and the finite-difference based acoustic solver.
- to apply the source-extraction formulation and the coupling procedure to some model acoustic problems and some more general problems with practical engineering background for test purposes.
- to achieve better understanding of the mechanism of aerodynamic sound generation in various complex flows.

1.5 Thesis Layout

This thesis consists of seven chapters. In Chapter 2 a brief overview of acoustic equation(s) and the treatment of acoustic sources under the coupling method framework are given. Lighthill's acoustic analogy theory is briefly introduced. Some extensions of the Lighthill acoustic analogy are also mentioned. Some weaknesses of the acoustic analogies are

discussed. A few representative extracting formulations for acoustic source terms provided by some other researchers in the implementation of the second type of coupling methods are emphatically discussed. A set of acoustic perturbation equations (APE) is derived, following the decomposition of variable, from the time-dependent, compressible Navier-Stokes equations. Accompanying the derivation of acoustic equations, a new extracting formulation of acoustic source terms is developed at the end of this chapter. The set of acoustic perturbation equations is further simplified into another form which directly involves the acoustic perturbation pressure following the isentropic relation of pressure and density.

Chapter 3 gives a description of the implementation of a RANS-based cell-centred finite volume method used to simulate the unsteady near-field flow.

In Chapter 4, numerical solution methods of acoustic perturbation equations are discussed. The dispersion-relation-preserving (DRP) high-order optimised finite difference scheme is first introduced. Then a staggered-type extension of the DRP scheme is described. A set of radiating boundary conditions are tested for various background flows. Code validation for the acoustic solver is presented.

In Chapter 5 a coupling procedure and data mapping between the finite-volume-discretization-based CFD solver and the finite-difference-discretization-based acoustic solver is built up and described. Some acoustic model problems are investigated based on the described coupling procedure associated with our new source-extraction formulation. Computational results from the coupling procedure are compared with exact solutions or reference solutions.

Chapter 6 presents some preliminary application of the new source-extraction formulation associated with the coupling procedure to some more complex cases. An attempt is also made in the end of this chapter to perform the coupling procedure through using a Large-Eddy Simulation technique in the unsteady computation in the near-field for the extraction of sources terms.

A summary and some suggestions of future work of this research are made in Chapter 7.

Chapter 2

Acoustic Equations and Acoustic Sources

In the first chapter the author has discussed the solution strategies adopted currently in sound prediction in aeroacoustics by means of numerical calculations. A key step in a coupling procedure is to identify and evaluate the acoustic sources. It will play a crucial role in calculating the propagation of the resulting acoustic waves and the analysis of the acoustic fields, such as, sound pressure level (SPL) and directivity of the acoustic field. In the past half century, much effort has been made to develop theories to describe the generation of aerodynamic sound and to model numerically the acoustic sources in coupling methods. At the same time, various forms of acoustic equations that describe approximately the propagation of acoustic waves are also derived by many researchers.

In this chapter, for the purposes of better understanding the research in this thesis, some important works on describing acoustic equation(s) and the modelling of acoustic sources will be introduced. Generally speaking, two kinds of acoustic sources can be identified in aeroacoustics. One arises from external excitation (for example, a vibrating solid surface). This kind of acoustic sources are relatively easy to be described and modelled. The other concerns sound sources generated by the flow itself (for example, vortex structures associated with shear layers or their interactions with solid obstacles). The complexity of unsteady flow field under various flow conditions (especially when turbulence is involved) results naturally in difficulties in describing the generation of aerodynamic sound and identifying the acoustic sources.

In the past fifty years, Lighthill's acoustic analogy and its some variants have been the dominant theory of aeroacoustics. Hence, a few selected important works following Lighthill's acoustic analogy theory are first outlined. Subsequently, a few recent ways of

modelling acoustic sources associated with the second coupling methods classified in the introduction chapter are briefly described. The concrete solution of the described acoustic equation/equations is not discussed. As an attempt in this research field, a new extracting formulation for acoustic source terms, in conjunction with a set of acoustic perturbation equations (a particular form of the linearized Euler equations), is derived and described in detail.

At the very beginning, it should be made clear that the research work in this thesis is not to develop a rigorous *theory* of the generation of aerodynamic sound in unsteady flows. In some sense, the source extraction exploited in this thesis is only a ‘numerical’ technique for modelling acoustic sources when the linearized Euler equations are employed to calculate the propagation of acoustic waves.

2.1 Lighthill’s acoustic analogy theory

Lighthill’s acoustic analogy is to be introduced first. The primary work of Lighthill [1952; 1954], performed in the fifties to tackle the problem of jet noise, is the most important advance in acoustics since the work of Rayleigh [1877] in the investigation of aerodynamics sound.

The basic idea of Lighthill’s acoustic analogy is the real problem of aerodynamic sound radiated in a highly disturbed flow may be replaced by the problem of the classical acoustic radiation *in a medium at rest* with equivalent acoustic sources. The difficulty of deriving exact equations is then avoided and replaced by the question of defining equivalent sources, which is essentially a task of aerodynamic nature. In fact, Lighthill’s acoustic analogy is the recasting of the exact equations of fluid motion (Navier-Stokes equations and continuity equation) in the form of an inhomogeneous wave equation suitable to be applied in the far field (and ignoring here nonlinear waveform distortion) where pressure (or density) perturbations propagate through still fluid at the ambient sound speed. If external mass injection and external forces, i.e. external sources, are not considered, the famous Lighthill equation can be written, with compact tensor notation (repeated indices presume the summation convention), as

$$\frac{\partial^2 \rho'}{\partial t^2} - c_0^2 \frac{\partial^2 \rho'}{\partial x_i^2} = \frac{\partial^2 T_{ij}}{\partial x_i \partial x_j} \quad (2.1)$$

where ρ' is density perturbation (defined as the deviation from the quiescent reference density), c_0 denotes the speed of sound in the ambient medium, T_{ij} represents the Lighthill stress tensor and is defined as

$$T_{ij} = \rho v_i v_j - \tau_{ij} + (p' - c_0^2 \rho') \delta_{ij} \quad (2.2)$$

where ρ stands for the quiescent reference density, p' is pressure perturbation, δ_{ij} is the Kronecker symbol ($\delta_{ij} = 1$ if $i = j$ and $\delta_{ij} = 0$ otherwise), τ_{ij} denotes viscous the stress tensor and is defined as

$$\tau_{ij} = 2\mu D_{ij} - \frac{2}{3}\mu \delta_{ij} D_{kk} \quad (2.3)$$

where D_{ij} is the rate of strain (deformation) tensor and is defined as

$$D_{ij} = \frac{1}{2} \left(\frac{\partial v_i}{\partial x_j} + \frac{\partial v_j}{\partial x_i} \right) \quad (2.4)$$

Eq.(2.1) is an inhomogeneous wave equation. The right-hand side of Eq.(2.1) is referred to as the acoustic sources which can be regarded as known.

Note that perturbations (ρ' , p') are defined as the deviations between the total flow variables (ρ , p) and the quiescent reference state (ρ_0 , p_0) during the derivation of Eq.(2.1), i.e.,

$$p' = p - p_0 \quad (2.5)$$

$$\rho' = \rho - \rho_0 \quad (2.6)$$

Eq.(2.1) is the original form given by Lighthill [1952]. Following the similar derivation above, later one gave an acoustic analogy equation, in which the pressure perturbation is used instead of the density perturbation,

$$\frac{\partial^2 p'}{\partial t^2} - c_0^2 \frac{\partial^2 p'}{\partial x_i^2} = \frac{\partial^2}{\partial x_i \partial x_j} (\rho v_i v_j - \tau_{ij}) - \frac{\partial^2}{\partial t^2} \left(\rho' - \frac{p'}{c_0^2} \right) \quad (2.7)$$

The Lighthill analogy described above is the first and the most influential attempt to create a *general* theoretical description for sound generation by turbulent flows. As no approximation has been made in the derivation of the Lighthill analogy equation for the ρ' and p' , it is exact. From the expression of the Lighthill stress tensor, T_{ij} , three basic aeroacoustic processes which contribution to the sources of sound:

- The non-linear convective forces described by the Reynolds stress tensor $\rho v_i v_j$,
- The viscous forces τ_{ij} ,
- The deviation from a uniform sound velocity c_0 or the deviation from an isentropic behaviour ($p' - c_0^2 \rho'$).

From Eq.(2.7), the sound produced by the source term $-\partial(\rho' - p'/c_0^2)/\partial t^2$ is also called *entropy sound*, see Pierce [1981]. The source term $\partial^2 T_{ij}/\partial x_i \partial x_j$ is normally usually referred to as the '*quadrupole sound source*' in literature.

The only assumption in the Lighthill acoustic analogy is that the resulting sound waves propagate in a homogeneous medium at rest. However, Lighthill's equation is in principle not easier to be solved than the original flow equations. When considered as independent an equation it contains less information than the original set of equations. The analogies are only convenient when one introduces approximations to determine the flow in the source region. A common assumption is that the source region is limited in space and that the flow in the source region is not sensitive to the acoustical boundary conditions in the quiescent fluid. This is often a reasonable approximation in *free space* when the

quiescent fluid is unbounded. In other words, one can neglect the feedback from the acoustic field to the flow in the source region. Obviously, this assumption is not valid for some cases, for example, duct-fan noise problems.

Another approximation is to neglect the wave propagation time across the source region. This is reasonable when the source region has a characteristic length which is much smaller than the acoustic wave length. That is to say that the source is *compact*. Similarly, this is not true for some aeroacoustic problems, for example, high-speed jet noise.

From Eq.(2.1) and Eq.(2.7), one can note that different choice of the variable in the wave equation leads to different noise source terms. The following section describes some modifications and extensions of the Lighthill acoustic analogy, one may further find that different propagation equation of acoustic waves will also lead to very different acoustic source terms.

In addition, it should be pointed out that the source terms in Lighthill's equation contain actually both acoustic sources and convection and refraction effects in the inhomogeneous acoustic domain. The convection effects included in the source terms will result in an unnecessary larger computational domain of acoustic calculation. For example, considering the trailing edge noise problem (i.e., the noise generated by the turbulent flow in the vicinity of a sharp trailing edge of an airfoil), in order to non-uniform convection effects, the source of Lighthill's equation has to be determined not only in the region closed to the trailing edge but also in the remaining inhomogeneous acoustic domain that can be considerably large even for small Mach number flows [Crighton, 1993]. Grogger et al [2001] showed that the convection effects due to the irrotational flow field around a Zhukhovski airfoil (12% thickness) are not sufficiently described by assuming a simple constant convection speed.

2.2 Some modifications and extensions of the Lighthill acoustic analogy

Lighthill's acoustic analogy has been influencing the study of aeroacoustics since it was published in the early 1950s. It can be said that much effort is made to modify, simplify, and adapt it to the particular flow conditions. In this section a few important modifications and alternative formulations of the Lighthill acoustic analogy theory are briefly described.

The main objective is to manifest the diversity of the description of acoustic sources in various processes of sound generation. This will help us to understand the descriptions of other acoustic equations and acoustic sources in the second half of this chapter.

2.2.1 Powell's equation and Howe's equation

Under the framework of acoustic analogy, many researchers try to modify and extend Lighthill's formulation, including the treatment of acoustic sources. One of important attempts is to identify the source of flow-noise in terms of the vorticity because the vorticity is a very convenient quantity to describe a low Mach number flow. This is in part reminiscent of the classical decomposition of perturbations as a superposition (in the linear regime) of acoustic, vortical and entropy modes. In the non-linear regime a second order development shows that vortex-vortex interactions generate the aerodynamic sound [Chu & Kovasznay, 1958]. Another advantage of using vorticity as the source of sound is that it is often much more concentrated than velocity. The first source formulation, associated with a simple wave equation in terms of the vorticity, was given by Powell [1964].

For subsonic low Mach number, an isentropic non-conductive frictionless fluid, Powell's simple wave equation with source term can be written as:

$$\frac{1}{c_0^2} \frac{\partial^2 p'}{\partial t^2} - \nabla^2 p' = \rho_0 \nabla \cdot (\boldsymbol{\omega} \times \mathbf{v}) \quad (2.8)$$

where $\boldsymbol{\omega}$ is vorticity, and defined as follows

$$\boldsymbol{\omega} = \nabla \times \mathbf{v} \quad (2.9)$$

Although the left-hand side of Eq.(2.8) is still a simple wave operator, the variable characterizing to sound is still pressure. The source term in the right-hand side of equation is quite different from that in Lighthill's equation. It can be seen that Powell's formulation explicitly stresses the fact the vorticity $\boldsymbol{\omega}$ is responsible for the generation of aerodynamic sound.

Howe [1975] further extended Powell's work. At low Mach number the inhomogeneous wave equation can be written as:

$$\frac{1}{c_0^2} \frac{D_0^2 B'}{Dt^2} - \nabla^2 B' = \nabla \cdot (\boldsymbol{\omega} \times \mathbf{v}) \quad (2.10)$$

where $B' = B - B_0$ and $D_0/Dt = \partial/\partial t + \mathbf{v}_0 \cdot \nabla$. For the reference flow \mathbf{v}_0 , we choose a potential flow with stagnation enthalpy B_0 . The total enthalpy B is

$$B = e + \frac{p}{\rho} + \frac{1}{2} |\mathbf{v}|^2 \quad (2.11)$$

where e is the specific energy of the fluid.

Once again, one can note that the variable characterizing sound and the wave operator are different from those in Lighthill's equation, and also different from that in Powell's equation. Howe's formulation is a more general form of Powell's formulation. In other words, Powell's formulation is an approximate of the Howe's formulation. Powell's formulation was originally derived for free space conditions. If we neglect some terms, Powell's formulation can be derived from Eq.(2.10). Howe's analyses [Howe, 1975; 1984] demonstrates that Eq.(2.10) is also valid for subsonic isentropic internal flows if convective effects in the wave propagation are neglected. This is an important modification of Lighthill's equation. From Eq.(2.8) and Eq.(2.10), it appears that the source term is a '*dipole-like sound source*'. This is completely different from Lighthill's '*quadrupole sound source*'. The Powell-Howe formulation is particularly powerful when a simplified vortex model is available for the flow considered. Examples of such flows are discussed by Howe [1975; 1996], Disselhorst and Van Wijngaarden [1980], and Peters and Hirschberg [1993]. In Powell's formulation one also neglects the compressibility of the flow in the source region.

2.2.2 The Ffowcs Williams-Hawkings equation

Most practical problems of sound generation by flow involve moving boundaries, moving sources interacting with those boundaries, or turbulence in shear layers separating a quiescent medium from a high-speed flow. To apply Lighthill's equation in these circumstances, a *control surface*, S , are introduced. These may coincide with the surface of a moving solid or mark a convenient interface between fluid regions of widely differing mean properties. A solution is then sought by imposing boundary conditions on S , either by first performing subsidiary calculations to determine the pressure or velocity on S , or when S coincides with the surface of a solid, by application of suitable impedance conditions.

Let $f(\vec{x}, t)$ be an indicator function that vanishes on the control surface S and satisfies $f(\vec{x}, t) > 0$ in the fluid outside S , and $f(\vec{x}, t) < 0$ within S . The Heavyside function $H(f)$ is defined as follows

$$H(f) = \begin{cases} 1 & \text{if } f > 0 \\ 0 & \text{if } f < 0 \end{cases} \quad (2.12)$$

Further assume S to move with a velocity $\vec{U}(\vec{x}, t)$. Using the same procedure as the Lighthill analogy, the Ffowcs Williams-Hawkings equation can be read as follows [Ffowcs Williams & Hawkings, 1969]:

$$\frac{\partial^2(\rho' H(f))}{\partial t^2} - c_0^2 \frac{\partial^2(\rho' H(f))}{\partial x_i^2} = Q_a \quad (2.13)$$

where ρ' is the same definition as in Eq.(2.6), and

$$Q_a = \frac{\partial^2(T_{ij} H(f))}{\partial x_i \partial x_j} + \frac{\partial(Q_m)}{\partial t} - \frac{\partial(F_i)}{\partial x_i} \quad (2.14)$$

where as before in the analogy of Lighthill, $T_{ij} = \rho v_i v_j - \tau_{ij} + (p' - c_0 \rho') \delta_{ij}$ and

$$Q_m = \left[\rho(v_j - U_j) + \rho_0 U_j \right] \frac{\partial H(f)}{\partial x_j} \quad (2.15)$$

$$F_i = \left[\rho v_i (v_j - U_j) + p' \delta_{ij} - \tau_{ij} \right] \frac{\partial H(f)}{\partial x_j} \quad (2.16)$$

Compared with the Lighthill equation (Eq.(2.1)), the variable in the simple wave operator and the form of the acoustic sources are changed. From Eq.(2.14), it is clear that the surface source term Q_m and the surface force F_i occur in the acoustic source terms. Upon till now, the Ffowcs Williams-Hawkings equation is the most general form of the original Lighthill analogy theory. In unbounded space it is easy to recover the Lighthill equation from Eq.(2.13). Because of considering the moving surfaces, the Ffowcs Williams-Hawkings equation is widely employed to investigate the noise from a helicopter's rotating blades.

2.2.3 Phillip's equation and Lilley's equation

In the Lighthill acoustic analogy the flow-noise problem is reduced to the propagation/radiation of a prescribed distribution of *equivalent sources* in a homogeneous medium at rest. In many cases, the refraction of sound from mean flow is of importance. For instance, in the case of noise radiation from turbulent jets, the sound waves generated by the fine scale turbulence have to traverse the shear layer of the mean flow before reaching an observer outside. The velocity and density gradients of the jet mean flow cause significant refraction of the radiated sound. As the initial formulation (Eq.(2.1)) is an exact combination of the fluid motion equations, the source contains, *in principle*, all the propagation effects of the flow (refraction, convection, scattering). But with the usual approximation of T_{ij} by $\rho_0 v_i v_j$, where \bar{v} is the 'non-acoustic' part of the velocity, these effects are completely lost. Even if they were kept in the source terms, the modelling of propagation effects mixed with sources would be very difficult due to the different orders of magnitude and different scales. Some researchers have tried to separate analytically the propagation effects from what they thought were truly source terms through modifying the simple wave propagation operator in the left side of Eq.(2.1).

The basic idea is to construct an equation resulting from the equations of mass and momentum (similarly to Lighthill's acoustic analogy), and to include the acoustic mean flow interaction in the left-hand side of the equation. Phillip's equation [Phillips, 1960] was the first such attempt. For a perfect gas at ambient temperature, and neglecting entropy contribution, Phillips's equation read

$$\frac{D^2(\ln p')}{Dt^2} - c_0^2 \frac{\partial^2(\ln p')}{\partial x_i^2} = \gamma \frac{\partial v_i}{\partial x_j} \frac{\partial v_j}{\partial x_i} + \frac{D}{Dt} \left(\frac{1}{c_v} \frac{DS}{Dt} \right) - \frac{\partial}{\partial x_i} \left(\frac{\gamma}{\rho'} \frac{\partial \tau_{ij}}{\partial x_j} \right) \quad (2.17)$$

where γ is the specific heat ratio, S the entropy, c_v is the specific heat at constant volume, and $D/Dt = \partial/\partial t + \vec{v} \cdot \nabla$. Note that the dependent variable is natural logarithm of perturbation p' instead of p' . The essential modification with respect to Lighthill's equation is that the time derivative $\partial/\partial t$ is replaced by the material derivative D/Dt . Phillips claimed that the left-hand side of Eq.(2.17) represented the propagation of sound in a moving medium and the right-hand side gave the sources. In fact, Phillips' equation accounted for only part of the acoustic-flow interactions.

In order to obtain an equation in which all the propagation effects are accounted for in the left-hand side of an equation, Lilley [1974] derived his famous equation by taking the material derivative of Phillips' equation. Lilley's equation may be written in the following form [Goldstein, 1976]:

$$\frac{D}{Dt} \left(\frac{D^2 \Pi}{Dt^2} - c_0^2 \frac{\partial^2 \Pi}{\partial x_i^2} \right) + 2c_0^2 \frac{\partial v_i}{\partial x_j} \frac{\partial^2 \Pi}{\partial x_i \partial x_j} = -2 \frac{\partial v_i}{\partial x_j} \frac{\partial v_j}{\partial x_i} \frac{\partial v_k}{\partial x_k} + \Phi \quad (2.18)$$

where $\Pi = \ln(p'/p_0)/\gamma$,

$$\Phi = 2 \frac{\partial v_i}{\partial x_k} \frac{\partial}{\partial x_i} \left(\frac{1}{\rho'} \frac{\partial \tau_{kj}}{\partial x_j} \right) - \frac{D}{Dt} \left(\frac{\partial}{\partial x_k} \left(\frac{1}{\rho'} \frac{\partial \tau_{kj}}{\partial x_k} \right) \right) + \frac{D^2}{Dt^2} \left(\frac{1}{c_p} \frac{DS}{Dt} \right) \quad (2.19)$$

and c_p is the specific heat at constant pressure.

Lilley's equation contains better wave propagation physics. Compared with the source terms in Lighthill's equation, Lilley's source terms is more accurate representation of *pure* sources because some wave propagation terms are moved back the left-hand side of the acoustic equation. It should be noted that velocity involved in the left-hand side of Phillips' or Lilley's equation is not just mean velocity but the total velocity. The perturbation velocities are generally small compared to the mean velocity. Hence, it is reasonable to linearize the left-hand side of Eq.(2.18). For the unidirectional mean flow case, the source term can also be simplified and various approximations have been developed, see Goldstein [1976]. Again, the variable characterizing sound and the source terms in Lilley's equation are different from those mentioned above. In addition, Lilley's equation is a third-order equation.

2.3 Some treatments of acoustic sources associated with other forms of acoustic propagation equations

In Section 2.1 and Section 2.2, Lighthill's equation for the propagation of acoustic waves and several important modifications and extensions have been briefly described. However, it must be particularly pointed out that their developments and derivations are all done under the framework of Lighthill's acoustic analogy. Two apparent important features can be seen. One important feature is that the choice of the variable to characterize sound significantly affects the form of acoustic source terms. Different selection of the variable leads to very different acoustic source terms. The other important feature is that the form of acoustic source terms also depends on the equation which describes sound propagation. Since the acoustic source terms contain unknown variables (velocity, pressure, and density), using an unsteady flow solver for the unsteady flow field which contains aerodynamic sources combined with an acoustic analogy for the far field acoustic calculations is quite common in aeroacoustics. From the perspective of accounting for the convection effects on acoustic waves from the flow, Lilley's equation is better choice. Unfortunately, as pointed out by Ribner [1981], Lilley's equation includes the prediction of hydrodynamic instabilities and thus, solutions can become unstable at critical mean flow profiles. Furthermore, Lilley's equation is a third order equation whose use is limited due to some difficulties in solution.

Under the framework of coupling methodology, the linearized Euler equations (LEE) or other acoustic perturbation equations (APE) with acoustic source terms have become a new research direction in CAA field in the last decade or so. The LEE or other APE contains the effects of convection, refraction and scattering from mean flow on the propagation of the resulting acoustic waves. Furthermore, the LEE or other APE also valid in various non-uniform flow conditions. In the implementation of a coupling method, the acoustic source terms associated with the acoustic equations of the acoustic waves need to be extracted from a CFD simulation which can be a DNS, a LES or an unsteady RANS-based solver. A crucial point of a coupling method is the determination of the acoustic source terms. Currently, in the coupling methods associated with a set of acoustic perturbation equations with acoustic source terms, the efficient and accurate evaluation of near-field sound sources still remains an *open* and *challenging* problem.

However, as far as acoustic equations and acoustic source terms are concerned, a point must be clarified: if one puts all wave propagation terms on the left-hand side of Navier-Stokes (i.e., the full Euler equations) to account for mean flow convection and refraction as well as non-linear steepening effects, at the same time, leaves all viscous terms in the right-hand side of Navier-Stokes equations, the acoustic source terms become only viscous terms from the perspective of acoustic analogy. This is definitely erroneous. It could be said that the derivation of acoustic equations used in the second type of coupling methods doesn't follow the idea of acoustic analogy. Before describing a new extracting formulation for acoustic source terms made in this thesis, some ways of modelling numerically acoustic source terms in acoustic perturbation equations with the second type of coupling methods are overviewed below. In order to avoid any confusion and errors, the formulations are written as close as possible to the original form as in the cited references.

2.3.1 Hardin and Pope's formulation and the treatment of source terms

One of the first attempts in deriving acoustic equations with source terms from flow governing equations without following the framework of Lighthill's acoustic analogy was made by Hardin and Pope [1994].

According to Hardin and Pope [1994], a hydrodynamic density correction ρ_1 to the ambient density ρ_0 is introduced as $\rho_1(x_i, t) = (P(x_i, t) - \bar{P}(x_i, t)) / c^2$, where c is the ambient speed of sound, P is the incompressible pressure, and \bar{P} is the time-averaged incompressible pressure distribution.

Suppose that flow variables are decomposed as follows

$$u_i = U_i + u'_i \quad (2.20)$$

$$p = P + p' \quad (2.21)$$

$$\rho = \rho_0 + \rho_1 + \rho' \quad (2.22)$$

where u'_i and p' are the fluctuation of the velocity components and pressure about their incompressible counterparts and ρ' is the fluctuation of the density about the corrected incompressible density $\rho_0 + \rho_1$. Furthermore, it is assumed that $p' = p'(\rho) = p(\rho, s) - P(\rho_0, s)$, where s denotes the entropy.

Inserting Eq.(2.20)~Eq.(2.22) into the compressible Navier-Stokes and neglecting the effect of viscosity on the fluctuation, a set of nonlinear equations for the fluctuation is obtained as

$$\frac{\partial \rho'}{\partial t} + \frac{\partial f_i}{\partial x_i} = - \left(\frac{\partial \rho_1}{\partial t} + U_i \frac{\partial \rho_1}{\partial x_i} \right) \quad (2.23)$$

$$\frac{\partial f_i}{\partial t} + \frac{\partial}{\partial x_j} [f_i (U_j + u'_j) + (\rho_0 + \rho_1) U_i u'_j + p' \delta_{ij}] = - \left[\frac{\partial}{\partial t} (\rho_1 U_i) - U_j \frac{\partial}{\partial x_j} (\rho_1 U_i) \right] \quad (2.24)$$

$$\frac{\partial p'}{\partial t} + c^2 \frac{\partial \rho'}{\partial t} = c^2 \frac{\partial \rho_1}{\partial t} \quad (2.25)$$

where $f_i = (\rho_0 + \rho_1) u'_i + \rho' (U_i + u'_i)$ and $c^2 = \gamma p / \rho = \gamma (P + p') / (\rho_0 + \rho_1 + \rho')$, γ is the ratio of specific heats.

These equations constitute a closed set of the acoustic perturbation variables ρ' , p' , and u'_i with the source terms on the right-hand side given by the incompressible solution. If

the incompressible flow were uniform, these equations reduce to the Euler equations. Note that the fluctuations about the incompressible flow are assumed isentropic whereas the background incompressible flow is viscous and dissipative. Eq.(2.23)~Eq.(2.25) have been solved for various cases [Hardin & Pope, 1994; 1995; Lee & Koo, 1995; Ekaterinaris, 1997; Tsujimoto et al., 1998; Miyake et al., 2001].

Hardin and Pope's formulation was later modified by Shen and Sørensen [1999a; 1999b]. Eq.(2.22) was replaced by $\rho = \rho_0 + \rho'$, where ρ' is the fluctuating density about ρ_0 . Similarly, substituting the newly decomposed variables into the Navier-Stokes equations and neglecting the viscous terms, Shen and Sørensen obtained the formulation

$$\frac{\partial \rho'}{\partial t} + \frac{\partial f_i}{\partial x_i} = 0 \quad (2.26)$$

$$\frac{\partial f_i}{\partial t} + \frac{\partial}{\partial x_j} [f_i (U_j + u'_j) + \rho_0 U_i u'_j + p' \delta_{ij}] = 0 \quad (2.27)$$

$$\frac{\partial p'}{\partial t} + c^2 \frac{\partial \rho'}{\partial t} = - \frac{\partial P}{\partial t} \quad (2.28)$$

where $f_i = \rho u'_i + \rho' U_i$. Note that the only acoustic source coming from the incompressible solution is the instantaneous pressure, and hence the acoustic calculation may be started at any time during the incompressible computation.

Recently Shen and Sørensen [2001] extended their formulation to handle incompressible turbulent flows when the Reynolds-averaged Navier-Stokes (RANS) equations are used with a turbulence model for the unsteady flow field. The formulation can be written as follows

$$\frac{\partial \rho'}{\partial t} + \frac{\partial f_i}{\partial x_i} = 0 \quad (2.29)$$

$$\frac{\partial f_i}{\partial t} + \frac{\partial}{\partial x_j} \left[f_i (\bar{U}_j + u'_j) + \rho_0 \bar{U}_i u'_j + (p' + \frac{2}{3} \rho' k) \delta_{ij} \right] = \frac{\partial}{\partial x_j} \left[\rho' \mu \left(\frac{\partial \bar{U}_i}{\partial x_j} + \frac{\partial \bar{U}_j}{\partial x_i} \right) \right] \quad (2.30)$$

$$\frac{\partial p'}{\partial t} + c^2 \frac{\partial \rho'}{\partial t} = -\frac{\partial \bar{P}}{\partial t} \quad (2.31)$$

where now the overbar stands for the averaged quantities in the RANS, $f_i = \rho u'_i + \rho' \bar{U}_i$, $c^2 = \gamma(\bar{P} + p')/(\rho_0 + \rho')$, μ is turbulence viscosity, and k is the turbulent kinetic energy. As compared to the laminar acoustic formulation, some extra terms relating to turbulence appear in the acoustic velocity equations. These terms are considered as additional acoustic source terms associated with the Reynolds stresses of the turbulent flow.

2.3.2 Morris et al's nonlinear equations and the treatment of source terms

From a conventional Reynolds decomposition of the full, time-dependent Navier-Stokes equations, Morris et al. [1997] proposed a set of non-linear disturbance equations with source terms. To derive the nonlinear disturbance equations, the flow vector q is split into its mean value \bar{q} and a perturbation q'

$$q = \bar{q} + q' \quad (2.32)$$

where $\bar{q} = \lim_{T \rightarrow \infty} \frac{1}{T} \int_{t_0}^{t_0+T} q(t) dt$ and the flow is assumed to be statistically stationary.

Substituting Eq.(2.32) into the full, time-dependent Navier-Stokes equations results in a set of perturbation equations. By definition, the mean flow is independent of time and only time derivative appearing in the equation set is that of the perturbation flow variables. The terms involving the perturbation quantities are retained on the left-hand side and the terms involving purely mean flow quantities are treated as source terms (on the right-hand side). The perturbation terms also contain nonlinear perturbation quantities. The viscous perturbation terms are neglected, as it is argued, following Hardin and Pope [1994], that the time-average properties are the result of dissipative mechanics, whereas the large-scale fluctuations are essentially inviscid in nature. After rearranging the mean flow and

perturbation terms as well as neglecting the viscous perturbation terms, the nonlinear disturbance equations in Cartesian form for two-dimensional case can be written as

$$\frac{\partial q'}{\partial t} + \frac{\partial F'}{\partial x} + \frac{\partial G'}{\partial y} + \frac{\partial F'_n}{\partial x} + \frac{\partial G'_n}{\partial y} = Q \quad (2.33)$$

where

$$q' = \begin{Bmatrix} \rho' \\ \bar{\rho}u' + \rho'\bar{u} + \rho'u' \\ \bar{\rho}v' + \rho'\bar{v} + \rho'v' \\ e' \end{Bmatrix} \quad (2.34)$$

$$F' = \begin{Bmatrix} \bar{\rho}u' + \rho'\bar{u} \\ \rho'\bar{u}^2 + 2\bar{\rho}u'u' + p' \\ \bar{\rho}u'v' + \bar{\rho}v'u' + \rho'u\bar{v} \\ u'(\bar{e} + \bar{p}) + \bar{u}(e' + p') \end{Bmatrix} \quad (2.35)$$

$$G' = \begin{Bmatrix} \bar{\rho}v' + \rho'\bar{v} \\ \bar{\rho}v'u' + \bar{\rho}u'v' + \rho'u\bar{v} \\ \rho'\bar{v}^2 + 2\bar{\rho}v'v' + p' \\ v'(\bar{e} + \bar{p}) + \bar{v}(e' + p') \end{Bmatrix} \quad (2.36)$$

and

$$F'_n = \begin{Bmatrix} \rho'u' \\ 2\rho'u'\bar{u} + \bar{\rho}u'^2 + \rho'u'^2 \\ \bar{\rho}u'v' + \rho'v'\bar{u} + \rho'u'\bar{v} + \rho'u'v' \\ u'(e' + p') \end{Bmatrix} \quad (2.37)$$

$$G'_n = \begin{Bmatrix} \rho'v' \\ \bar{\rho}u'v' + \rho'v'\bar{u} + \rho'u'\bar{v} + \rho'u'v' \\ 2\rho'v'\bar{u} + \bar{\rho}v'^2 + \rho'v'^2 \\ v'(e' + p') \end{Bmatrix} \quad (2.38)$$

The linear convective fluxes involving the perturbation quantities are F' , and G' , whereas F'_n , and G'_n are the nonlinear perturbation terms in the two coordinate directions. The mean flow source term Q in equation (2.33) may be written as

$$Q = -\left(\frac{\partial \bar{F}}{\partial x} + \frac{\partial \bar{G}}{\partial y}\right) + \frac{\partial \bar{R}}{\partial x} + \frac{\partial \bar{S}}{\partial y} \quad (2.39)$$

where the mean convective fluxes are given by

$$\bar{F} = \begin{Bmatrix} \bar{\rho u} \\ \bar{\rho u}^2 + \bar{p} \\ \bar{\rho u v} \\ \bar{u}(\bar{p} + \bar{e}) \end{Bmatrix} \quad (2.40)$$

$$\bar{G} = \begin{Bmatrix} \bar{\rho v} \\ \bar{\rho u v} \\ \bar{\rho v}^2 + \bar{p} \\ \bar{v}(\bar{p} + \bar{e}) \end{Bmatrix} \quad (2.41)$$

The mean viscous stresses \bar{R} and \bar{S} can be obtained by simply replacing the instantaneous quantities (u, v, T) in the definition of R and S by their corresponding mean value $(\bar{u}, \bar{v}, \bar{T})$. Here ρ', p', u', v' , and e' are perturbation density, pressure, velocity components, and total energy per unit volume of fluid, respectively, while their corresponding mean quantities are $\bar{\rho}, \bar{p}, \bar{u}, \bar{v}$, and \bar{e} . After the conservative perturbation variable q' is obtained from the solution of Eq.(2.33), the velocity perturbations u' and v' may be obtained from q' and the mean flow values using Eq.(2.34), while the fluctuating pressure p' may be obtained from

$$e' = \frac{p'}{(\gamma - 1)} + (\bar{\rho} + \rho')(u'\bar{u} + v'\bar{v}) + \frac{1}{2}(\bar{\rho} + \rho')(u'^2 + v'^2) + \frac{1}{2}\rho'(\bar{u}^2 + \bar{v}^2) \quad (2.42)$$

Note that source term Q is essentially the sum of the divergence of mean convective fluxes and the mean viscous stresses. Morris et al. [1997] pointed out that if Eq.(2.33) is time averaged, it becomes the RANS equations. The left-hand side would yield the Reynolds stress terms. The term Q could be replaced by the Reynolds stress terms from the

RANS equations and for a laminar flow $Q = 0$. In fact, when the nonlinear disturbance equations were applied to the calculation of supersonic axisymmetric jet noise by Morris et al. [1997], the mean flow source terms are neglected.

2.3.3 Bailly et al's momentum source terms for the linearized Euler equations

The linearized Euler equations (LEE) support acoustic, entropy, and vorticity waves [Tam, 1995]. Since LEE account for refraction and convection effects in flow, they are widely employed in a coupling method for the calculation of the propagation of acoustic wave. Generally speaking, source terms are often associated with certain form of LEE. Currently, there are some different formulations of source terms which combined with LEE.

Considering small perturbations around time averaged mean flow quantities, the perturbations are governed by LEE, written in a two-dimensional conservative form [Bailly et al., 2000], as

$$\frac{\partial U}{\partial t} + \frac{\partial E}{\partial x} + \frac{\partial F}{\partial y} + H = S \quad (2.43)$$

where

$$U = \begin{Bmatrix} \rho' \\ \bar{\rho}u' \\ \bar{\rho}v' \\ p' \end{Bmatrix} \quad (2.44)$$

$$E = \begin{Bmatrix} \rho'\bar{u} + \rho u' \\ \bar{u}\bar{\rho}u' + p' \\ \bar{u}\bar{\rho}v' \\ \bar{u}p' + \gamma\bar{p}u' \end{Bmatrix} \quad (2.45)$$

$$F = \begin{Bmatrix} \rho'\bar{v} + \bar{\rho}v' \\ \bar{v}\bar{\rho}u' \\ \bar{v}\bar{\rho}v' + p' \\ \bar{v}p' + \gamma\bar{p}v' \end{Bmatrix} \quad (2.46)$$

$$H = \begin{Bmatrix} 0 \\ (\bar{\rho}u' + \rho'u)\frac{\partial \bar{u}}{\partial x} + (\bar{\rho}v' + \rho'v)\frac{\partial \bar{u}}{\partial y} \\ (\bar{\rho}u' + \rho'u)\frac{\partial \bar{v}}{\partial x} + (\bar{\rho}v' + \rho'v)\frac{\partial \bar{v}}{\partial y} \\ (\gamma - 1)p'\nabla \cdot \bar{\mathbf{v}} - (\gamma - 1)\mathbf{v}' \cdot \nabla \bar{p} \end{Bmatrix} \quad (2.47)$$

The term H is zero for a uniform mean flow. It contains part of the refraction effects. S is a possible aerodynamic source term. Assuming isentropic flows, noise generation is provided by source terms in the momentum equations of LEE. Bailly et al [2000] gave the formulation of sound sources, which can be written as

$$S = \begin{Bmatrix} 0 \\ S_1 - \bar{S}_1 \\ S_2 - \bar{S}_2 \\ 0 \end{Bmatrix} \quad (2.48)$$

where

$$S_i = -\frac{\partial \rho v'_i v'_j}{\partial x_j}, \quad \bar{S}_j = -\overline{\frac{\partial \rho v'_i v'_j}{\partial x_j}} \quad (2.49)$$

This expression of source terms S_i in Eq.(2.43) is found by using an analogy with Lilley's equation. The source terms S_i are nonlinear in velocity fluctuations, and their mean values \bar{S}_i are subtracted. Data provided by incompressible or compressible simulations can be used to estimate S_i . In compressible case, however, the acoustic field is included in the source terms, through density and fluctuating velocity, but this acoustic component is very small compared to aerodynamic fluctuations. The cross terms involving acoustic and aerodynamic perturbations are associated to sound scattering by turbulence, which is generally small. According to Bailly et al [2002], using the mean density value instead of the instantaneous one does not affect the computation because the terms $\rho'v'_i v'_j$ involving three fluctuating quantities are negligible. It should be pointed out that the source terms (Eq.(2.48)) cannot be used in the case of a non-isothermal flow.

The source terms combined with LEE have been used to simulate sound field generated by two co-rotative vortices in a medium at rest, sound field generated by two co-rotative vortices in a sheared mean flow, and sound field generated by a mixing layer [Bailly et al., 2000; Bogey et al., 2002].

2.3.4 Billson et al's source terms for the linearized Euler equations

Recently, Billson et al [2002] derived a formulation of source terms in the linearized Euler equations in conservative form. Their derivation starts with the Euler equations, and rewrites the Euler equations in a way that the left-hand side of the equations are the linearized Euler equations. The remaining nonlinear terms in the derivation are put in the right-hand side to form the source terms. The linearized Euler equations with approximate source terms are given as follows

$$\frac{\partial \rho'}{\partial t} + \frac{\partial(\rho v_j)'}{\partial x_j} = 0 \quad (2.50)$$

$$\frac{\partial(\rho v_i)'}{\partial t} + \frac{\partial[\tilde{v}_j(\rho v_i)' + \tilde{v}_i(\rho v_j)' - \rho \tilde{v}_i \tilde{v}_j + p' \delta_{ij}]}{\partial x_j} = - \frac{\partial[\rho(v_i' v_j' - \tilde{v}_i \tilde{v}_j)]}{\partial x_j} \quad (2.51)$$

$$\frac{\partial(\rho e_0)'}{\partial t} + \frac{\partial[\tilde{h}_0(\rho v_j)' + \tilde{v}_j(\rho h_0) - \rho \tilde{h}_0 \tilde{v}_j]}{\partial x_j} = - \frac{\partial([v_i \rho(v_i' v_j' - \tilde{v}_i \tilde{v}_j)])}{\partial x_j} \quad (2.52)$$

where ρe_0 is total energy per unit volume, ρh_0 the total enthalpy per unit volume. The average of a variable, for example, \tilde{v}_i , is a Favre time average defined by $\tilde{v}_i = \rho v_i / \rho$.

Comparing Bailly et al's formulation (i.e., Eq.(2.43)~Eq.(2.49)) with Billson et al's linearized Euler equations with source terms, Bailly uses $(\rho', \rho u', \rho v', p')$ as solution variables, whereas Billson use conservative variables, $(\rho', (\rho u)', (\rho v)', (\rho e)')$, as solution variables. Furthermore, in this formulation the source terms are involved not only in the momentum equations but also in the energy equation. In Bailly's et al's formulation of source terms (i.e. Eq.(2.48)), source terms are involved only in the momentum equations.

Sound field by a forced two-dimensional mixing layer is calculated using Eq.(2.50)~Eq.(2.52). The computational sound field shows a good agreement with the sound field of direct numerical simulation.

2.3.5 Ewert et al's acoustic perturbation equations and source terms

Recently, Ewert et al proposed a set of acoustic perturbation equations (APE) to compute acoustic sound fields with a coupling method based on a large eddy simulation (LES) of the compressible or the incompressible flow problem [Ewert et al., 2001; 2002; 2003].

The APE for wave propagation is derived by means of a flow decomposition of a flow quantity into acoustic and non-acoustic quantities, based on a filtering of the nonlinear and viscous terms of the Navier-Stokes equations, respectively, in Fourier/Laplace space [Ewert et al., 2000; 2001; 2002; 2003]. The APE system for the perturbation variables (p' , \mathbf{v}^a) may be written as follows [2003]

$$\frac{\partial p'}{\partial t} + \bar{c}^2 \nabla \cdot (\bar{\rho} \mathbf{v}^a + \frac{p'}{\bar{c}^2} \bar{\mathbf{v}}) = \bar{c}^2 q_c \quad (2.53)$$

$$\frac{\partial \mathbf{v}^a}{\partial t} + \nabla \cdot (\bar{\mathbf{v}} \cdot \mathbf{v}^a) + \nabla \cdot \left(\frac{p'}{\bar{\rho}} \right) = \mathbf{q}_m \quad (2.54)$$

where \mathbf{v}^a is the acoustic velocity perturbation, which is the irrotational part of the complete perturbation velocity $\mathbf{v}' = \mathbf{v}^a + \mathbf{v}^v$, and \mathbf{v}^v is the solenoidal vertical velocity perturbation.

The left-hand side of this system describes wave propagation in a non-uniform mean flow field $\bar{\mathbf{v}}$. The computation of the propagation of the acoustic waves, including the convective effects, in a time averaged steady flow field allows to restrict the unsteady flow simulation just to the immediate vicinity of a source region under consideration, while the mean flow field can be computed using RANS-based or other methods.

Explicit formulation for the source terms, q_c and \mathbf{q}_m , on the right-hand side of the APE (Eq.(2.53) and Eq.(2.54)) are obtained from a source filtering [Ewert et al., 2003]. The source terms, q_c and \mathbf{q}_m , can be written as

$$q_c = -\nabla\bar{\rho} \cdot \mathbf{v}^v - \nabla \cdot [(\rho' \mathbf{v}') - \overline{(\rho' \mathbf{v}')}] + \frac{\bar{\rho}}{c_p} \frac{D\bar{s}'}{Dt} \quad (2.55)$$

$$\begin{aligned} \mathbf{q}_m = & -\frac{\partial \mathbf{v}^v}{\partial t} - \nabla \cdot (\bar{\mathbf{v}} \mathbf{v}^v) - [(\boldsymbol{\omega} \times \mathbf{v}) - \overline{(\boldsymbol{\omega} \times \mathbf{v})}] - \nabla \frac{(\mathbf{v}')^2}{2} \\ & + \left[\left(\frac{\nabla \cdot \underline{\tau}}{\rho} \right) - \overline{\left(\frac{\nabla \cdot \underline{\tau}}{\rho} \right)} \right] + T' \nabla \bar{s} - \nabla \bar{T} s' \end{aligned} \quad (2.56)$$

where $\bar{D}/Dt = \partial/\partial t + \bar{\mathbf{v}} \cdot \nabla$, $\underline{\tau}$ is the stress tensor, c_p is the specific heat at constant pressure, s is entropy, the vorticity $\boldsymbol{\omega}$ is defined as $\boldsymbol{\omega} = \nabla \times \mathbf{v}$, T represents temperature, and the overbar denotes time averaging.

Non-linear entropy fluctuation in Eq.(2.55) and Eq.(2.56) is not considered. Note that since \mathbf{v}^a on the left-hand side of Eq.(2.54) is irrotational, i.e., it can be expressed through the gradient of a velocity potential, the curl of the whole left-hand side vanishes, and to do so for all the right-hand side terms, i.e., the terms of Eq.(2.56) are irrotational. Furthermore, the sources also contain linear terms.

The solenoidal perturbations follow directly from an incompressible flow simulation, which might be sufficient for low Mach number problems to describe the remaining source terms involving the complete perturbation velocities properly too. In order to obtain the solenoidal velocity components from the perturbation velocities of a compressible flow simulation, Biot Savart's law has to be used, for instance, by solving one Poisson equation in two-dimensional case.

The source term formulation (Eq.(2.55) and Eq.(2.56)) involves the substantial time derivative of the solenoidal perturbation velocity. Hence, neglecting the nonlinear and viscous terms it yields a zero source for passively convecting vorticity in a uniform mean flow, which is acoustically silent, such that no vortex dynamics has to be simulated as part of the acoustic calculation. This feature of the source term formulation might make it worthwhile to solve the Poisson equation.

Ewert et al has shown [2003] and proved computationally [2001] that the physical growing instability excited by the source terms in global unstable mean flows is prevented due to the properties of the APE system.

2.3.6 Golanski et al's source terms for the linearized Euler equations

More recently, Golanski et al [2003] proposed a treatment of acoustic source terms for LEE coupled with a set of equations of the low Mach number approximation (LMNA) which are deduced from the compressible Navier-Stokes equations for a perfect gas.

The LEE with their acoustic source terms for a small perturbation $q' = (\rho', v'_i, p')$ over a *steady* mean flow $\bar{q} = (\bar{\rho}, \bar{v}_j, \bar{p})$ are written in Cartesian coordinates [Golanski et al., 2003]

$$\frac{\partial \rho'}{\partial t} + \frac{\partial}{\partial x_j} (\bar{\rho} v'_j + \rho' \bar{v}_j) = S_\rho \quad (2.57)$$

$$\frac{\partial}{\partial t} (\bar{\rho} v'_i) + (\bar{\rho} v'_j + \rho' \bar{v}_j) \frac{\partial \bar{v}_i}{\partial x_j} + \frac{\partial}{\partial x_j} (\bar{\rho} \bar{v}_j v'_i) + \frac{\partial p'}{\partial x_i} = S_{v_i} \quad (2.58)$$

$$\frac{\partial p'}{\partial t} + \frac{\partial}{\partial x_j} (p' \bar{v}_j + \bar{p} v'_j) + (\gamma - 1) p' \frac{\partial \bar{v}_j}{\partial x_j} - (\gamma - 1) \bar{v}_j \frac{\partial \bar{p}}{\partial x_j} = S_p \quad (2.59)$$

where S_ρ , S_{v_i} , S_p are respectively the source terms corresponding to the mass, momentum and energy conservation.

Through an analysis of the two systems of equations (the system of equations of LMNA and the system of LEE) and some assumptions, a specific formulation of the acoustic source terms for the LEE coupled with the LMNA are given as follows

$$\left\{ \begin{array}{l} S_\rho = 0 \\ S_{v_i} = - \left[\frac{\partial (\rho^{(0)} v_i^{(0)})}{\partial t} + \frac{\partial (\rho^{(0)} v_i^{(0)} v_j^{(0)})}{\partial x_j} \right] \\ S_p = 0 \end{array} \right. \quad (2.60)$$

According to Golanski et al, the source terms and the mean flow are obtained from a set of equations of the LMNA. The system of equations of the LMNA is deduced from the compressible Navier-Stokes equations for a perfect gas by expanding all the variables of

flow in power series in $\varepsilon = \gamma M^2$. These expansions are expressed as follows [Golanski et al., 2003]

$$\rho = \rho^{(0)} + \varepsilon \rho^{(1)} + \dots \quad (2.61)$$

$$v_i = v_i^{(0)} + \varepsilon v_i^{(1)} + \dots \quad (2.62)$$

$$T = T^{(0)} + \varepsilon T^{(1)} + \dots \quad (2.63)$$

$$p = \frac{p^{(0)}}{\varepsilon} + p^{(1)} + \dots \quad (2.64)$$

The system of equations of the LMNA for the hydrodynamic problem are presented as follows in the lowest order in ε

$$\frac{\partial \rho^{(0)}}{\partial t} + \frac{\partial \rho^{(0)} v_i^{(0)}}{\partial x_i} = 0 \quad (2.65)$$

$$\frac{\partial \rho^{(0)} v_i^{(0)}}{\partial t} + \frac{\partial \rho^{(0)} v_i^{(0)} v_j^{(0)}}{\partial x_j} = -\frac{\partial p^{(1)}}{\partial x_i} + \frac{\partial \tau_{ij}^{(0)}}{\partial x_j} \quad (2.66)$$

$$\rho^{(0)} \frac{\partial v_j^{(0)}}{\partial x_j} = \frac{1}{\text{RePr} T^{(0)}} \frac{\partial^2 T^{(0)}}{\partial x_j^2} \quad (2.67)$$

$$p^{(0)} = \rho^{(0)} T^{(0)} \quad (2.68)$$

where τ_{ij} is the viscous stress tensor, Re denotes the Reynolds number, and Pr represents the Prandtl number. Note that all variables have been non-dimensional variables using L_{ref} , U_{ref} , ρ_{ref} , T_{ref} , and $t_{ref} = L_{ref}/U_{ref}$ as reference length, velocity, density, temperature and time.

Golanski et al. [2003] pointed out that Eq.(2.65)~Eq.(2.68) are only valid for a vanishing Mach number. However, there is no restriction about the density variations in space and time. Rigorously, the Mach number does not appear in a CFD simulation based on LMNA. An appropriate rescaling of the results of such a simulation allows doing predictions corresponding to flow evolving at different Mach numbers. However, the

formulation of source terms and the system of equations of the LMNA is more suitable to low Mach number flows.

From the expression (2.60), the term $\partial(\rho^{(0)}v_i^{(0)}v_j^{(0)})/\partial x_j$ corresponds to the fluctuations of velocity in the flow. It contains the shear noise and the self noise. This is similar to the one mentioned above by Bailly et al [Bailly_4], and is sufficient for isothermal flow. The term $\partial(\rho^{(0)}v_i^{(0)})/\partial t$ is required in a non-isothermal case. It corresponds to the temporal fluctuations of momentum in the flow, in the case where the density distribution is not homogeneous. This supplementary acoustic source is a part of the so-called entropy noise deduced from Lighthill's acoustic analogy. According Golanski et al [2003], the source term (2.60) is coherent with Hardin and Pope's source term and Bailly et al's source term.

2.4 A new acoustic source terms extraction formulation for the linearized Euler equations

In Section 2.3, under the framework of the second type of coupling methods, some representative acoustic equations describing wave propagation and their accompanying acoustic source terms are briefly overviewed. Basically, the derivation of these acoustic equations and the formulation of the acoustic source terms come from the governing equations of fluid motion, and make use of decomposition of variables as well as more or less approximations. These acoustic source terms need to be extracted from the hydrodynamic solutions of the flow field. The calculation of acoustic propagation will be based on the extracted acoustic source terms. Each of the treatments of the acoustic source terms has seen to some extent success in some examined cases when a two-step coupling procedure is implemented. Since some assumptions are made in the derivation of the source terms, the use of each formulation of source terms inevitably has some limitations, such as low-speed flows, isothermal flow, etc. In addition, one can also note that different acoustic equations have generally different formulation of acoustic source terms. Even if the acoustic equations are the LEE, different source terms can also occur due to different approximate treatment in the process of derivation. The phenomenon is similar with that of the acoustic equation and acoustic source terms derived from the acoustic analogy. In this thesis we do

not intend to make a comparison between those treatments of acoustic source terms. As mentioned in Section 2.3, the treatment of acoustic source terms with the second type of coupling methods is still *open*, and receiving more attention from CAA community than before. It is not the intention of the new extracting formulation for acoustic source terms proposed in this section to supplant other existing ways of numerically modelling acoustic source terms. Rather, we wish to furnish the “toolbox” of the extracting sound sources for with a new extracting formulation that has its own some features and advantages.

The new extracting formulation of acoustic source terms associated with a set of acoustic equations will be described in detail in this section. This attempt mainly follows an initial idea in [Djambazov, 1998b; Djambazov et al., 2000a].

The derivation of acoustic equations and their accompanying acoustic source terms starts with the governing equations of fluid motion. The time-dependent, compressible Navier-Stokes equations and continuity equation in a Cartesian coordinate system may be written as

$$\frac{\partial \rho}{\partial t} + \rho \frac{\partial v_j}{\partial x_j} + v_j \frac{\partial \rho}{\partial x_j} = 0 \quad (2.69)$$

$$\rho \frac{\partial v_i}{\partial t} + \rho v_j \frac{\partial v_i}{\partial x_j} = -\frac{\partial p}{\partial x_i} + \frac{\partial}{\partial x_j} \left[\mu \left(\frac{\partial v_i}{\partial x_j} + \frac{\partial v_j}{\partial x_i} \right) - \frac{2}{3} \mu \delta_{ij} \frac{\partial v_k}{\partial x_k} \right] \quad (2.70)$$

Similarly, following decomposition of variable, the flow variables are decomposed into a *dominant* component and a *perturbation* component as follows

$$q(x_i, t) = \bar{q}(x_i, t) + q'(x_i, t) \quad (2.71)$$

where q presents ρ , p , or v_i , and \bar{q} denotes the dominant component, and q' is perturbation component. This variable decomposition allows separate treatment of the large-scale mean flow motion and small acoustic perturbation superimposed upon it [Hardin, 1993].

In this study only two-scale decomposition of q , based on the order of magnitude of the variable, is considered. It needs to be pointed out that the dominant part, \bar{q} , of the

variable decomposition does not necessarily refer to the “ensemble-averaged” component. If Eq.(2.70) is of time averaged, it becomes the RANS equations. When the RANS equations are adopted to simulate the unsteady flow field, \bar{q} may be regarded as the “ensemble-averaged” quantities. When LES technique is used to compute the unsteady flow field, \bar{q} implies the spatial LES filtered quantities. \bar{q} as appeared in the decomposition is the *unsteady* solution of the flow field obtained by a CFD solver for solving Eq.(2.69) and Eq.(2.70). In other words, \bar{q} is not assumed to be statistically stationary but may be allowed to change with respect to time. However, the variation of \bar{q} is slow compared to q' . A schematic representation of the two-scale decomposition of flow variable is shown in Figure 2.1.

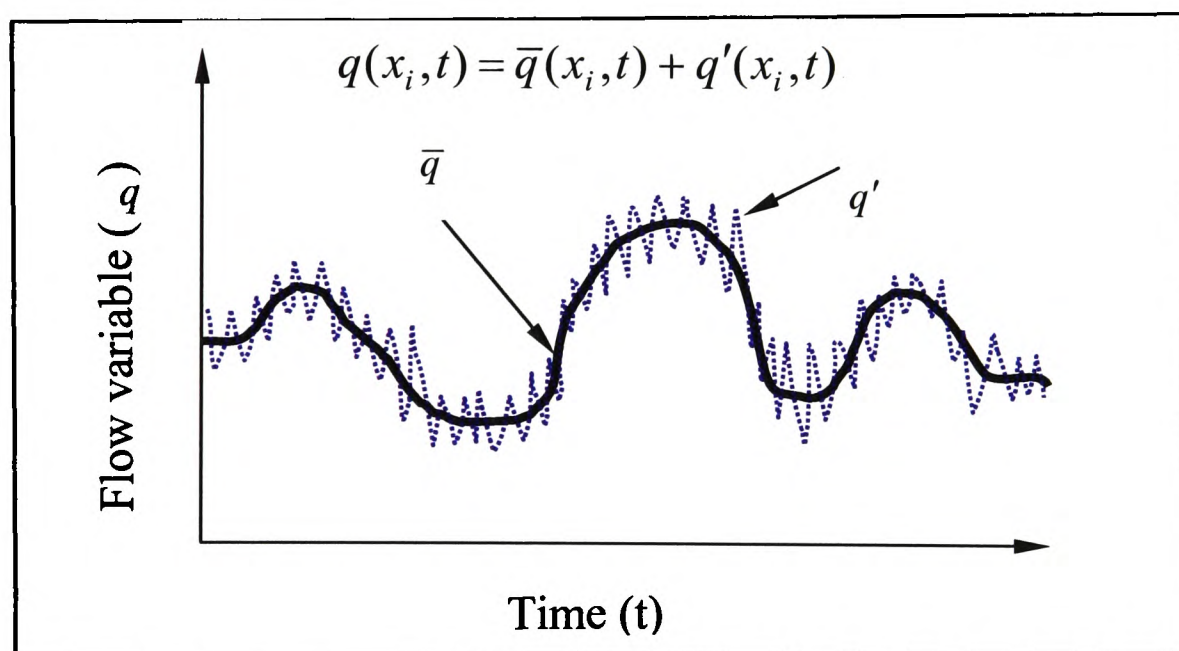


Fig. 2.1. Decomposition of $q(x_i, t)$ into $\bar{q}(x_i, t)$ and $q'(x_i, t)$.

The perturbation should be viewed as the sum of an acoustic fluctuation and an unsteady flow-field fluctuation (e.g., turbulent fluctuation). Since unsteady flow-field fluctuations/turbulent fluctuations are dissipative, the far-field should only consist of acoustic perturbation. On the other hand, acoustic fluctuations can be neglected in the near flow field when compared to the unsteady flow-field fluctuations/turbulent fluctuations. In fact, it might be difficult to distinguish both the unsteady flow-field fluctuations and the acoustic perturbations in the near-field of the unsteady flow.

A defect correction concept described in [Böhmer & Stetter, 1984] is borrowed to build a mathematical framework of the following derivation. The concept of defect correction has been used in various contexts and ways. A typical example of defect correction is the computation of a refined approximate solution \bar{x} of the nonlinear equation $f(x) = 0$. Since \bar{x} is an approximate solution, the defect may be computed as $-f(\bar{x})$. Most defect correction is used in conjunction with discretization methods and two-level multigrid methods [Böhmer & Stetter, 1984]. In this research, the author would like to concentrate on using the defect correction concept from the physical perspective rather than purely mathematical one.

Mathematically, the mean flow quantities can be viewed as the approximate solutions for the governing equations of fluid motion. From an order of magnitude viewpoint, the perturbations can be regarded as the correction to be added to the approximate flow solutions for the decomposition of variable in Eq.(2.71).

The decomposed variables are substituted into Eq.(2.69) and Eq.(2.71), the governing equations may then be expanded and rearranged. It should be pointed out that the particular expansion and rearrangement will lead to somewhat different forms of the acoustic perturbation equations.

For the sake of simplicity and clarity, we derive the mathematical formulation with the aid of operators. Let $L\{q\}$ be a non-linear operator depending on the flow variables, Eq.(2.69) and Eq.(2.70) may be represented by $\partial q/\partial t + L\{q\}q = 0$. Substituting the decomposed variables into the nonlinear equation $\partial q/\partial t + L\{q\}q = 0$ leads to the following:

$$\frac{\partial(\bar{q} + q')}{\partial t} + L\{\bar{q} + q'\}(\bar{q} + q') = 0 \quad (2.72)$$

where $L\{q\}(q)$ is an nonlinear operator depending on variable q . Expanding equation (2.72), one may arrange the resulting equations as follows

$$\frac{\partial(\bar{q} + q')}{\partial t} + L\{\bar{q} + q'\}(\bar{q} + q') = \frac{\partial\bar{q}}{\partial t} + L\{\bar{q}\}\bar{q} + \frac{\partial q'}{\partial t} + E\{\bar{q}\}q' + K[\partial_t, \bar{q}, q'] \quad (2.73)$$

where $E\{\bar{q}\}$ is operator depending on \bar{q} , and $K[\partial_i, \bar{q}, q']$ is a functional depending on the knowledge of both \bar{q} and q' as well as their derivatives. As pointed out above, \bar{q} may be considered as an approximate solution to Eq.(2.72) after the decomposition of variable. In order to obtain the time-dependent approximation solution of Eq.(2.72), one may solve *numerically an approximate model* of Eq.(2.72), which is represented as $\partial\bar{q}/\partial t + \Psi\{\bar{q}\}\bar{q} = 0$, using a CFD code or a suitable CFD package. For example, if Reynolds' averaging (i.e., the long-time average of a quantity) is applied to the equations of motion (Eq.(2.70)), $\partial\bar{q}/\partial t + \Psi\{\bar{q}\}\bar{q} = 0$ is RANS equations. If a spatial filtering is implemented to the governing equations (Eq.(2.69) and Eq.(2.70)) in entire domain, $\partial\bar{q}/\partial t + \Psi\{\bar{q}\}\bar{q} = 0$ stands for the filtered equations to be solved in LES. \bar{q} represents the solutions of the RANS or LES, respectively. After obtaining the approximation solutions, following the defect correction concept the residue of Eq.(2.72) with respect to the approximation solution can be expressed as:

$$\bar{R} = \frac{\partial(\bar{q} + q')}{\partial t} + L\{\bar{q} + q'\}(\bar{q} + q') - \left[\frac{\partial\bar{q}}{\partial t} + L\{\bar{q}\}\bar{q} \right] = - \left[\frac{\partial\bar{q}}{\partial t} + L\{\bar{q}\}\bar{q} \right] \quad (2.74)$$

Substitution of Eq.(2.74) into Eq.(2.73) results in below expression

$$\frac{\partial q'}{\partial t} + E\{\bar{q}\}q' + K[\partial_i, \bar{q}, q'] = \bar{R} \quad (2.75)$$

The implementation of the above procedures for compressible, time-dependent Navier-Stokes equations, i.e., Eq.(2.69) and Eq.(2.70), the terms in Eq.(2.75) can correspondingly be written as follows,

$$q' = \begin{bmatrix} \rho' \\ v'_i \end{bmatrix} \quad (2.76)$$

$$E\{\bar{q}\}q' = \left[\begin{array}{c} \bar{v}_j \frac{\partial \rho'}{\partial x_j} + \bar{\rho} \frac{\partial v'_j}{\partial x_j} \\ \bar{v}_j \frac{\partial v'_i}{\partial x_j} + \frac{1}{\bar{\rho}} \frac{\partial p'}{\partial x_i} - \frac{1}{\bar{\rho}} \left[\mu \left(\frac{\partial v'_i}{\partial x_j} + \frac{\partial v'_j}{\partial x_i} \right) - \frac{2}{3} \mu \delta_{ij} \frac{\partial v'_k}{\partial x_k} \right] \end{array} \right] \quad (2.77)$$

$$K[\partial_t, \bar{q}, q'] = \left[\begin{array}{c} v'_j \frac{\partial (\bar{\rho} + \rho')}{\partial x_j} + \rho' \frac{\partial (\bar{v}_j + v'_j)}{\partial x_j} \\ \frac{\rho'}{\bar{\rho}} \frac{\partial (\bar{v}_i + v'_i)}{\partial t} + \left(v'_j + \frac{\rho'}{\rho} (\bar{v}_j + v'_j) \right) \frac{\partial (\bar{v}_i + v'_i)}{\partial x_j} \end{array} \right] \quad (2.78)$$

$$\bar{R} = \left[\begin{array}{c} - \left(\frac{\partial \bar{\rho}}{\partial t} + \bar{v}_j \frac{\partial \bar{\rho}}{\partial x_j} + \bar{\rho} \frac{\partial \bar{v}_j}{\partial x_j} \right) \\ - \left(\frac{\partial \bar{v}_i}{\partial t} + \bar{v}_j \frac{\partial \bar{v}_i}{\partial x_j} + \frac{1}{\bar{\rho}} \frac{\partial \bar{p}}{\partial x_i} - \frac{1}{\bar{\rho}} \frac{\partial}{\partial x_j} \left[\mu \left(\frac{\partial \bar{v}_i}{\partial x_j} + \frac{\partial \bar{v}_j}{\partial x_i} \right) - \frac{2}{3} \mu \delta_{ij} \frac{\partial \bar{v}_k}{\partial x_k} \right] \right) \end{array} \right] \quad (2.79)$$

From expression (2.77), one can see that $E\{\bar{q}\}q'$ contains only derivatives of perturbation quantities, and the obtained approximate flow quantities as their coefficients. The term on the right-hand side of Eq.(2.75) (i.e., \bar{R}) contains only the overbared quantities in the decomposition of flow variables. Hence, \bar{R} may be numerically evaluated after the approximate solutions are obtained using numerical techniques.

$K[\partial_t, \bar{q}, q']$ contains simultaneously both the obtained approximate flow solutions and the perturbation quantities. Furthermore, one may also note that $K[\partial_t, \bar{q}, q']$ contains the nonlinear term of the Eq.(2.72). Physically, $K[\partial_t, \bar{q}, q']$ encapsulates certain effects of feedback of the resulting acoustic field on the flow field from. If a problem was completely linear, and at the same time one considers the fact that the acoustic perturbation may be several orders of magnitude smaller than the overbared flow quantities (especially outside the near-field), the influence of the term $K[\partial_t, \bar{q}, q']$ could be considered to be neglected as a means of obtaining approximately a set of acoustic perturbation equations. Neglecting of $K[\partial_t, \bar{q}, q']$ means nonlinear acoustic propagation and the effect of the acoustic field on the unsteady flow field due to non-linear mode interaction are not considered. However, in some cases, for example, sonic boom production and acoustic resonance, the problems are

far from linear in nature. That is to say, the solution of aeroacoustic problems may involve nonlinear interactions between the aerodynamic field and the acoustic field. Under these circumstances, $K[\partial_t, \bar{q}, q']$ should not be omitted. For many aeroacoustic problems, though they are *physically* nonlinear, previous studies based on instability wave models have shown that acoustic mechanism are weakly nonlinear in nature [Tam & Burton, 1984; Tam & Morris, 1985]. The omission of $K[\partial_t, \bar{q}, q']$ will not significantly affect the propagation/radiation of the aerodynamic sound in many cases.

In addition, it should be noted that $K[\partial_t, \bar{q}, q']$ contains still the shear refraction term (i.e., $v'_j \partial \bar{v}_i / \partial x_j$) which may affect the short wave components. Strictly, after $K[\partial_t, \bar{q}, q']$ is dropped, the resulting acoustic equations describe principally the propagation of the long wavelength's acoustic waves. Due to mathematically and physically complex features of $K[\partial_t, \bar{q}, q']$, further study and investigation on issues of neglecting $K[\partial_t, \bar{q}, q']$ and its effects on the propagation of acoustic waves and the generation of the aerodynamic sound will be needed.

In the present work, $K[\partial_t, \bar{q}, q']$ is removed. A set of acoustic perturbation equations is obtained approximately from Eq.(2.75) as follows,

$$\frac{\partial q'}{\partial t} + E\{\bar{q}\}q' \approx \bar{R} \quad (2.80)$$

In computational aeroacoustics, the expression of acoustic sources is not unique but strongly depends on the equations which describe the sound propagation/radiation. This has been pointed out in previous sections where various acoustic analogies and in many coupling methods are discussed. The right-hand side of Eq.(2.80), known as the *residue* due to the un-resolved quantities at each or certain selected time step in the discretized numerical computation of the unsteady flow, may be viewed as the acoustic sources. It is no doubt that sound sources exist physically as certain flow properties encapsulated in the '*residue*' and could be extracted via suitable techniques. With this assumption, the 'acoustic sources' of the acoustic perturbation equations (Eq.(2.80)) may be obtained by computing the *residue* expressed in Eq.(2.79) using an appropriate high order approximation. However, it should be stated that the right-hand side of Eq.(2.80) is by no means a *theoretically*

rigorous representation of the acoustic sources in the unsteady flow. In addition, the expression (i.e., Eq.(2.79)) is valid only for the acoustic perturbation equations (i.e. Eq.(2.80)). It can not be borrowed simply to be applied to other acoustic perturbation equations.

On the other hand, the viscous terms on the left-hand side of Eq.(2.80) may be neglected. As pointed out by Hardin and Pope [1994; 1995], Tam and Dong [1993] and Morris et al. [1997], the time-average properties are the result of dissipative mechanics, whereas the large-scale fluctuations are essentially inviscid in nature. Therefore, the effect of viscosity on the propagation of acoustic waves, if any, is negligibly small within a considerably long distance. Once the viscous perturbation terms are neglected, then the left-hand side of the acoustic perturbation equations (Eq.(2.80)) turns into a succinct form of convenient use for practical acoustic calculations. In fact, it may be viewed as a particular form of the linearized Euler equations with source terms. The acoustic perturbation equations account for convection, refraction and scattering effects of the unsteady flow on the propagation/radiation of the acoustic waves. As a result, the set of acoustic equations may generally provide a good prediction to acoustic field for many aeroacoustic problems.

Lighthill [1952; 1962] once pointed out that for free subsonic flows at sufficiently high Reynolds number, viscous noise can be neglected with respect to shear noise. In other words, the viscous term on the right-hand side of Eq.(2.80) may also be removed. However, it is still not very clear whether unsteady viscous dissipation contributes significantly to the generation of the aerodynamic sound in other flow conditions. Generally speaking, it is a safe way that the viscous term involving the unsteady flow quantities on the right-hand side of Eq.(2.80) would need to be retained. In many aeroacoustic problems, the viscous terms in expression (2.79) can definitely be omitted. However, it must be careful when neglecting the viscous term in the source terms. In this thesis, calculations of the source terms in some cases (e.g., the case of flow-induced car-door cavity noise) have considered the viscous terms in the acoustic source terms.

It is the source terms in which only the obtained flow quantities in the computed unsteady flow field are contained that provides an *connection* between the near field unsteady flow and the acoustic wave propagation, and *bridge* a CFD solver and an acoustic solver. As a result, the source terms also form the basis of the source extraction based coupling method in this thesis. This is *similar* to other coupling methods used currently in

CAA. The main advantages of the present extracting formulation for acoustic source terms are:

- There is no Mach number limit. This new extracting formulation, therefore, can be applied to both compressible and incompressible flows;
- There is no requirement in taking account of acoustic source characteristics (dipole, quadrupole or other mixed type). It automatically extracts various types of aerodynamic sound sources contained in the unsteady flows;
- It is convenient for the implementation of a coupling procedure because the source terms are formulated in the primitive variables of fluid motion equations.

This new formulation is general and particularly suitable for the computation of acoustic field where aerodynamic sound is generated by both compact and distributed sound sources. One source term, which comes naturally from the derivation, occurs in the first equation in the set of Eq.(2.79). One may note that source term associated with the continuity equation is often taken to be zero in most formulations of acoustic source terms described in the previous section. From the formulation of acoustic source terms (2.79), the source term is zero when only the flow is strictly incompressible (without density perturbations) and the uniform velocity.

The disadvantage existing in this new formulation of acoustic source terms is that the source terms in the present formulation might be not necessarily ‘*pure*’ sound sources. Some pseudo-acoustic sources due to numerical errors are probably extracted to enter the solution of acoustic perturbation equations. Due to generality of the present formulation, the source terms in the present formulation are somewhat uneasy to interpret from a traditional acoustic source-type perspective.

Since the derivation of the acoustic equations and their source terms does not currently involve the energy equation of fluid motion, this is sufficient to many aeroacoustic problems of practical interest in which acoustic heat sources are not involved. If an aeroacoustic problem is significantly related to extremely large change in temperature or entropy fluctuation, for instance, supersonic *hot* jet noise, a corresponding energy perturbation equation and its accompanying source term is required.

In this thesis, the set of acoustic perturbation equations (i.e., Eq.(4.80)) may further be changed into another form which directly involves the acoustic perturbation pressure through using an approximate relation between the perturbation pressure and perturbation density.

According to the fundamental law of thermodynamics, an additional state equation is introduced as closure condition for the governing equations of fluid flow. The state equation is specified as $p = p(\rho, s)$. A Taylor expansion for the pressure $p = p(\rho, s)$, as a function of the density and the entropy, gives

$$\begin{aligned} p(\rho, s) &= p(\bar{\rho}, \bar{s}) + \left(\frac{\partial p}{\partial \rho} \right)_{\bar{s}} (\rho - \bar{\rho}) + \left(\frac{\partial p}{\partial s} \right)_{\bar{\rho}} (s - \bar{s}) + \dots \\ &\approx \bar{p} + c^2 (\rho - \bar{\rho}) + \frac{\bar{p}}{c_v} (s - \bar{s}) \end{aligned} \quad (2.81)$$

Fluctuations of pressure, density and entropy are connected approximately by the relation $p' = c^2 \rho' + (\bar{p}/c_v)s'$. Thus, if the fluctuation of the entropy is neglected, the acoustic pressure perturbation and the density perturbation in the process of acoustic wave propagation approximately complies with the following relation

$$\frac{\partial p'}{\partial \rho'} \approx \frac{p'}{\rho'} \approx c^2 \quad (2.82)$$

For cold flows the assumption of no fluctuation of the entropy is not necessary. The above relation (i.e., Eq.(2.84)) also holds for a perfect gas flow because entropy is only convected without production. Utilizing Eq.(2.84), the perturbation density in Eq.(2.80) can be excluded, and the following equation is derived

$$\frac{\partial p'}{\partial t} + \bar{v}_j \frac{\partial p'}{\partial x_j} + \bar{\rho} c^2 \frac{\partial v'_j}{\partial x_j} = -c^2 \left(\frac{\partial \bar{\rho}}{\partial t} + \bar{v}_j \frac{\partial \bar{\rho}}{\partial x_j} + \bar{\rho} \frac{\partial \bar{v}_j}{\partial x_j} \right) \quad (2.83)$$

In aerodynamics, especially for external aerodynamic problems, the generation of heat from the change of state of air flow is negligible, and may be neglected *approximately*. In other words, the process of air flow may be considered *approximately* as isentropic processes for most external aerodynamic problems. For such a process forces due to friction (gas viscosity) do not work on the aerodynamic devices, that is, entropy remains constant during the change of state of air [Granger, 1985]. Hence, adopting isentropic process for the unsteady flow field does not affect the sound generation. For some aerodynamic problems in which *hot* flows are involved, for example, internal flows of engine and some combustion processes, the isentropic process breaks down. However, such hot flows are not the cases considered in this thesis.

For the isentropic flow of a perfect gas, a simple pressure-density relation may be obtained, i.e.,

$$p = \bar{p} + p' = K(\bar{\rho} + \rho')^\gamma = K\rho^\gamma \quad (2.84)$$

where $K = \text{const.}$, and γ is the ratio of specific heats ($\gamma = 1.4$ in air). According to the definition of the speed of sound represented by c , the following relation is hold approximately:

$$\frac{\partial \bar{p}}{\partial \bar{\rho}} \approx \frac{\partial p}{\partial \rho} = \frac{\partial(\bar{p} + p')}{\partial(\bar{\rho} + \rho')} = c^2 = \gamma \frac{p}{\rho} = \gamma \frac{\bar{p} + p'}{\bar{\rho} + \rho'} \approx \gamma \frac{\bar{p}}{\bar{\rho}} \quad (2.85)$$

By using the above relation, the Eq.(2.83) may be cast into the following form

$$\frac{\partial p'}{\partial t} + \bar{v}_j \frac{\partial p'}{\partial x_j} + \bar{\rho} c^2 \frac{\partial v'_j}{\partial x_j} = - \left(\frac{\partial \bar{p}}{\partial t} + \bar{v}_j \frac{\partial \bar{p}}{\partial x_j} + \bar{\rho} c^2 \frac{\partial \bar{v}_j}{\partial x_j} \right) \quad (2.86)$$

It should also be mentioned that using \bar{p} instead of $\bar{\rho}$ makes the computational procedure numerically more stable when the in-house CFD code described in the following Chapter is used.

For the sake of simplicity, the prime denoting the perturbation variables are removed, the set of acoustic perturbation equations (a particular form of the linearized Euler equations) with new acoustic terms may be rewritten as follows

$$\frac{\partial p}{\partial t} + \bar{v}_j \frac{\partial p}{\partial x_j} + \bar{\rho} c^2 \frac{\partial v_j}{\partial x_j} = \bar{R}_c \quad (2.87)$$

$$\frac{\partial v_i}{\partial t} + \bar{v}_j \frac{\partial v_i}{\partial x_j} + \frac{1}{\bar{\rho}} \frac{\partial p}{\partial x_i} = \bar{R}_{m,i} \quad (2.88)$$

$$\begin{bmatrix} \bar{R}_c \\ \bar{R}_{m,i} \end{bmatrix} = \begin{bmatrix} -c^2 \left(\frac{\partial \bar{\rho}}{\partial t} + \bar{v}_j \frac{\partial \bar{\rho}}{\partial x_j} + \bar{\rho} \frac{\partial \bar{v}_j}{\partial x_j} \right) \\ - \left(\frac{\partial \bar{v}_i}{\partial t} + \bar{v}_j \frac{\partial \bar{v}_i}{\partial x_j} + \frac{1}{\bar{\rho}} \frac{\partial \bar{p}}{\partial x_i} - \frac{1}{\bar{\rho}} \frac{\partial}{\partial x_j} \left[\mu \left(\frac{\partial \bar{v}_i}{\partial x_j} + \frac{\partial \bar{v}_j}{\partial x_i} \right) - \frac{2}{3} \mu \delta_{ij} \frac{\partial \bar{v}_k}{\partial x_k} \right] \right) \end{bmatrix} \quad (2.89)$$

or, for isentropic flow of a perfect gas

$$\begin{bmatrix} \bar{R}_c \\ \bar{R}_{m,i} \end{bmatrix} = \begin{bmatrix} - \left(\frac{\partial \bar{p}}{\partial t} + \bar{v}_j \frac{\partial \bar{p}}{\partial x_j} + \bar{\rho} c^2 \frac{\partial \bar{v}_j}{\partial x_j} \right) \\ - \left(\frac{\partial \bar{v}_i}{\partial t} + \bar{v}_j \frac{\partial \bar{v}_i}{\partial x_j} + \frac{1}{\bar{\rho}} \frac{\partial \bar{p}}{\partial x_i} - \frac{1}{\bar{\rho}} \frac{\partial}{\partial x_j} \left[\mu \left(\frac{\partial \bar{v}_i}{\partial x_j} + \frac{\partial \bar{v}_j}{\partial x_i} \right) - \frac{2}{3} \mu \delta_{ij} \frac{\partial \bar{v}_k}{\partial x_k} \right] \right) \end{bmatrix} \quad (2.90)$$

It should be noted that in the viscous terms in above sources the effective viscosity (i.e., the sum of laminar viscosity and the turbulent viscosity) should be used when turbulent flows are considered so that turbulent diffusion of momentum is included.

Eq.(2.87)-Eq.(2.88) will be employed to calculate the propagation of the acoustic waves in the resulting acoustic field. The solution of the above system of acoustic equations will be discussed in detail in Chapter 4.

Chapter 3

Simulation of Unsteady Flow Field

As pointed out in Chapter 1, the thesis involves the computation of aerodynamically generated sound using a source-extraction based coupling method. The solution procedure of the coupling method is actually a *two-step* procedure. In such a coupling method, the unsteady flow field in which acoustic sources are contained and the resulting acoustic field are separated *artificially* so that the most appropriate method can be employed at each step. The unsteady flow field is, as the first step, simulated by using an appropriate numerical method. The simulation of the sound source contained in the unsteady flow field is a main issue of CFD.

The simulation and calculation of the unsteady flows under various flow conditions have made great progress in the past over decades. A wide variety of numerical methods with physically different approximations in the computation of unsteady flows has been developed. They include direct numerical simulation (DNS) techniques, large eddy simulation (LES) methods, and Reynolds-averaged Navier-Stokes equations (RANS) based methods.

As discussed previously, the extremely high computational cost of the use of the DNS techniques make them unpractical to be applied to engineering flows, i.e., at high Reynolds number and in complex geometries, in the near future. Currently, RANS-based numerical methods are, in conjunction with a wide variety of turbulence models, most widely used in solving practical flow problems of engineering interests. LES is a technique intermediate between the DNS and the RANS simulations. Although the implementation of LES is at a fraction of the cost of DNS, the application of LES to the complex unsteady flow at high Reynolds number is still computationally expensive under current computational resource

available. In author's opinion, LES technique is the most powerful and attractive numerical method for computations of unsteady flows.

In this thesis, the simulation and computation of the unsteady flow for extracting aerodynamically-generated sound sources mainly employ unsteady RANS-based method. In an application case in Chapter 6, the use of a LES technique in the simulation of the unsteady flow field is also attempted.

An in-house CFD code (PHYSICA) [Croft et al., 1995], which is based on incompressible/compressible RANS on structured/unstructured meshes by a cell-centred finite volume discretization, is employed. The objectives of this chapter are to give a description of the unsteady RANS-based finite volume method and relevant numerical issues that are involved in the present work, such as the discretization of governing equations, Rhie-Chow interpolation procedure, the SIMPLE algorithm the treatment of boundary conditions.

3.1 Governing equations of fluid motion

The governing equations of fluid flow represent mathematical statements of the conservation laws of physics, i.e., mass conservation, momentum conservation and energy conservation. For Newtonian fluids, the continuity equation, momentum equations and the energy equation can be written as follows

$$\frac{\partial \rho}{\partial t} + \frac{\partial(\rho v_i)}{\partial x_i} = 0 \quad (3.1)$$

$$\frac{\partial(\rho v_j)}{\partial t} + \frac{\partial(\rho v_i v_j)}{\partial x_i} = \frac{\partial}{\partial x_i} \left(\mu \frac{\partial v_j}{\partial x_i} \right) - \frac{\partial p}{\partial x_j} + B_j + V_j \quad (3.2)$$

$$\frac{\partial(\rho h)}{\partial t} + \frac{\partial(\rho v_i h)}{\partial x_i} = \frac{\partial}{\partial x_i} \left(\frac{k}{c_p} \frac{\partial h}{\partial x_i} \right) + S_h \quad (3.3)$$

where ρ is the density, v_i velocity component in i th direction, p pressure, μ viscosity, B_j the body force per unit volume, V_j consists of viscous terms other than those expressed by the first term the j direction, h the enthalpy, k the thermal conductivity, c_p the constant

pressure specific heat, and S_h represents the volumetric rate of internal heat generation. In this thesis, $k - \varepsilon$ two-equation turbulence model, one of the most widely used turbulence models in the simulation of turbulent flow, is involved. The two equations may read:

$$\frac{\partial(\rho k)}{\partial t} + \frac{\partial(\rho v_i k)}{\partial x_i} = \frac{\partial}{\partial x_i} \left(\frac{\mu_t}{\sigma_k} \frac{\partial k}{\partial x_i} \right) + G - \rho \varepsilon \quad (3.4)$$

$$\frac{\partial(\rho \varepsilon)}{\partial t} + \frac{\partial(\rho v_i \varepsilon)}{\partial x_i} = \frac{\partial}{\partial x_i} \left(\frac{\mu_t}{\sigma_\varepsilon} \frac{\partial \varepsilon}{\partial x_i} \right) + (c_1 G - c_2 \rho \varepsilon) \frac{\varepsilon}{k} \quad (3.5)$$

where k is the kinetic energy of turbulence, ε the turbulence dissipation rate, μ_t the turbulence viscosity, G the rate of generation of turbulence, and σ_k , σ_ε , c_1 and c_2 are empirical constants.

Close inspection of the above conservation equations (Eq.(3.1)~Eq.(3.5)) reveals the significant similarity in their forms. It is useful to write the conservation equations in a general form. The discretization and analysis can then be carried out in a general manner; when necessary, terms peculiar to an equation can be handled separately. If a general variable ϕ (scalar quantity) is introduced, the general equation can be written as:

$$\frac{\partial(\rho \phi)}{\partial t} + \frac{\partial(\rho v_i \phi)}{\partial x_i} = \frac{\partial}{\partial x_i} \left(\Gamma_\phi \frac{\partial \phi}{\partial x_i} \right) + S_\phi \quad (3.6)$$

where S_ϕ is the source or sink of the quantity ϕ and Γ_ϕ is the diffusion coefficient for the quantity ϕ . For describing conveniently the implementation of finite volume method used in this thesis, Eq.(3.6) can be re-written in the following coordinate-free vector form

$$\frac{\partial(\rho \phi)}{\partial t} + \text{div}(\rho \mathbf{v} \phi) = \text{div}(\Gamma_\phi \text{grad} \phi) + S_\phi \quad (3.7)$$

where \mathbf{v} represents velocity vector. Table 3.1 summarizes the meaning of various terms (ϕ , Γ_ϕ and S_ϕ) appearing in the general equation. One may easily recover each of the

governing equations according to Table 3.1. The four terms in the general differential equation (Eq.(3.7)) are, from left to right, the *transient* term, the *convective* term, the *diffusive* term, and the *source* terms. Eq.(3.7) is the so-called transport equation for property ϕ , and used as the starting point for computational procedures in the finite volume method.

Table 3.1. Meaning of various terms in the general equation

	ϕ	Γ_ϕ	S_ϕ
Mass	1	0	0
Momentum	v_j	μ	$-\partial p/\partial x_j + B_j + V_j$
Energy	h	k/c_p	S_h
Turbulence Kinetic Energy	k	μ_t/σ_k	$G - \rho\varepsilon$
Turbulence Dissipation Rate	ε	μ_t/σ_ε	$(c_1G - c_2\rho\varepsilon)\varepsilon/k$

3.2 Discretization of the general equation

In this section, we shall consider only the general conservation equation for a quantity ϕ and assume that the velocity field, pressure field and all fluid properties are known. Under certain assumptions the described discretization method can also be applied to the momentum conservation equations.

The finite volume method uses the integral form of the conservation equation as the starting point. Finite volume discretization of the general conservation equation may have different ways, for instance, cell-vertex finite volume discretization, cell-centred finite volume discretization, etc.. In the present work, the finite volume discretization is based on cell-centred formulation. In this method the solution domain is subdivided into a finite number of contiguous and non-overlapping volumes (i.e., computational mesh), and the conservation equations are applied to each control volume. At the centre of each these control volumes a single node is positioned. The value of ϕ is sought at centres of all control volumes on the computational mesh.

Since only 2-D Cartesian meshes are used in the computations in this thesis, the following description are all based on Cartesian coordinate system. A typical two dimensional Cartesian control volume is show in Figure 3.1. The surface of control volume can be subdivided into four plane faces, denoted by lower case letters corresponding to their direction (e , w , n , and s) with respect to the central node (P). Four neighbouring centres of control volumes are represented by E , W , N , and S , respectively.

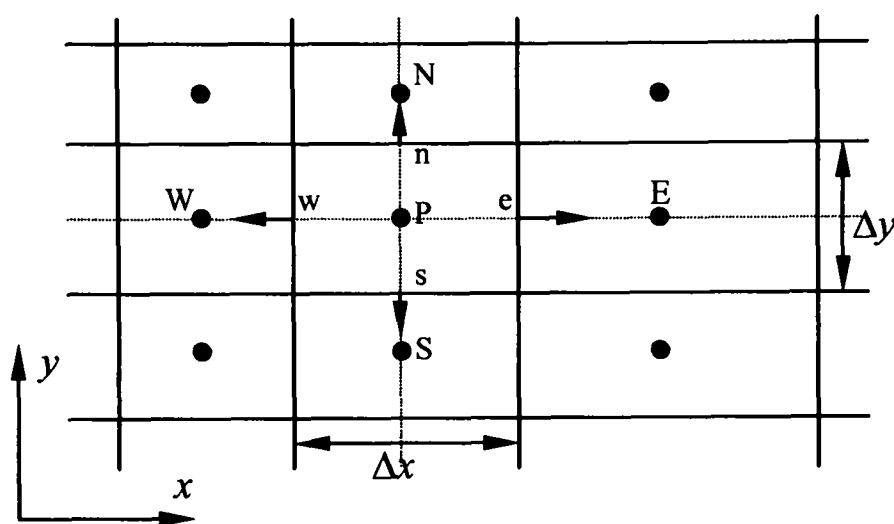


Fig. 3.1. A typical control volume for a 2-D Cartesian mesh

If computational mesh is stationary, the volume of each control volume does not change with time. Thus, the order of the integrals in space and time can be reversed. Integrating the general conservation equation, Eq.(3.7), over each control volume as well as over time gives

$$\int_{t-\Delta t}^t \frac{\partial}{\partial t} \left(\int_V (\rho\phi) dV \right) dt + \int_{t-\Delta t}^t \int_V \text{div}(\rho\mathbf{v}\phi) dV dt = \int_{t-\Delta t}^t \int_V \text{div}(\Gamma_\phi \text{grad}(\phi)) dV dt + \int_{t-\Delta t}^t \int_V S_\phi dV dt \quad (3.8)$$

The volume integrals in the second term on the left-hand side, the convective term, and in the first term on the right-hand side, the diffusive term, may be re-written as integrals over the entire bounding surface of the control volume by using *Gauss' divergence theorem*. Eq.(3.8) is converted into the following form

$$\int_{t-\Delta t}^t \frac{\partial}{\partial t} \left(\int_V (\rho\phi) dV \right) dt + \int_{t-\Delta t}^t \int_S (\rho \mathbf{v}\phi) \cdot \mathbf{n} dS dt = \int_{t-\Delta t}^t \int_S (\Gamma_\phi \mathbf{grad}(\phi)) \cdot \mathbf{n} dS dt + \int_{t-\Delta t}^t \int_V S_\phi dV dt \quad (3.9)$$

Where S represents the entire bounding surface of the control volume, and \mathbf{n} is the unit outward normal to the surface.

In the following sections the discretization techniques applied to each of the terms in the integral conservation equation (Eq.(3.8)) are described in turn.

3.2.1 Transient term

Using the superscript 0 to indicate values at the previous time step and the subscript P to represent value at the centre of the control volume, the discretization of the transient term, Eq.(3.9), can be approximated by

$$\int_{t-\Delta t}^t \frac{\partial}{\partial t} \left(\int_V (\rho\phi) dV \right) dt = \frac{(\rho_P \phi_P - \rho_P^0 \phi_P^0) V_P}{\Delta t} \quad (3.10)$$

where V_P is the volume of the control volume. For two dimensional cases, the calculations of the volume can be done using simple formula in Cartesian meshes.

For every other term in Eq.(3.8) fully implicit assumptions are used. This implies that the time integration of the remaining terms leads to a multiplying factor of Δt . In the following sections, describing the discretization of the remaining terms, the integration over time will be ignored.

3.2.2 Source term

The source term can be expressed in a linearized form [Patankar, 1980]

$$S_\phi = S_C - S_P \phi \quad (3.11)$$

where S_C and S_P can be functions of any stored value including ϕ . To maintain diagonal dominance of the resulting equation the value of S_P must not be negative. The equations used to evaluate the values of S_C and S_P can significantly affect both the rate of convergence and stability of the solution procedure. For speed as large a portion of the source as possible should be placed in the linear part (i.e., $S_P\phi$). This speed will be compromised if the size of S_C is also increased. Stability will be affected if changes in any aspect of the solution results in large changes in the values of S_C and S_P . When the linearized source term is integrated over the control volume all terms are evaluated at the centre of the control volume to give a contribution

$$V_P(S_C - S_P\phi_P) \quad (3.12)$$

3.2.3 Diffusive term

The net diffusive flux through the entire bounding surface of each control volume is the sum of integrals over each surface of the control volume, i.e.,

$$\int_S (\Gamma_\phi \text{grad}(\phi)) \cdot \mathbf{n} dS = \sum_f \int_{S_f} (\Gamma_\phi \text{grad}(\phi)) \cdot \mathbf{n} dS \quad (3.13)$$

where f denotes the number of surfaces of the control volume, S_f is the area of the surface at the surface f . The gradient of ϕ at the surface can be expressed either in terms of the derivatives with respect to Cartesian coordinates or local orthogonal coordinate (n, t) , for example, in two dimensional case

$$\text{grad} \phi = \frac{\partial \phi}{\partial x} \mathbf{i} + \frac{\partial \phi}{\partial y} \mathbf{j} = \frac{\partial \phi}{\partial n} \mathbf{n} + \frac{\partial \phi}{\partial t} \mathbf{t} \quad (3.14)$$

where n and t represent the coordinate directions normal and tangential to the surface, respectively. With the expression (3.14) equation (3.13) is turn into

$$\int_S (\Gamma_\phi \text{grad}(\phi)) \cdot \mathbf{n} dS = \sum_f \int_{S_f} \Gamma_\phi \frac{\partial \phi}{\partial n} dS \quad (3.15)$$

Let A denote the adjacent control volume of control volume P and f be one surface of the two control volume, see Figure 3.2.

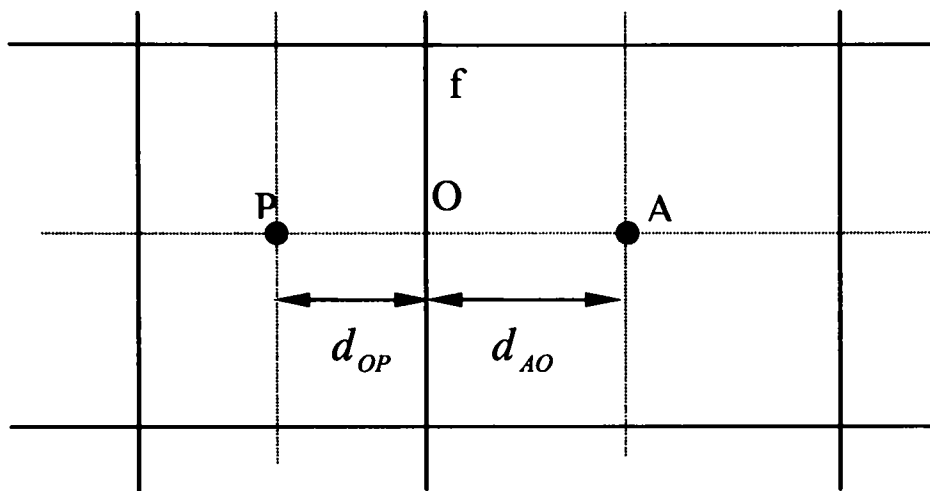


Fig.3.2. Two adjacent control volumes and the interface in a 2-D Cartesian mesh

There are many ways to approximate the derivative normal to the surface. If the distance between the considered node P and its neighbouring node A is represented as d_{AP} then the normal derivative in Eq.(3.15) is approximately equal to $\partial\phi/\partial n = (\phi_A - \phi_P)/d_{AP}$. The approximation is similar to the central difference way. On the Cartesian mesh, the normal derivative is of second-order accuracy. Substituting the above normal derivative into Eq.(3.15), leads to the discretization of the diffusion term

$$\int_S (\Gamma_\phi \text{grad}(\phi)) \cdot \mathbf{n} dS = \sum_f \int_{S_f} \Gamma_\phi \frac{\partial \phi}{\partial n} dS = \sum_f (\Gamma_\phi)_f S_f \left(\frac{\phi_A - \phi_P}{d_{AP}} \right) \quad (3.16)$$

In the discretization of the diffusion term, i.e., Eq.(3.16), the value of Γ_ϕ on the surface need to be approximated. A common approximation to the value is to use linear interpolation between the two nearest nodes (the used notation refers to Fig. 3.2)

$$\begin{aligned}
 (\Gamma_\phi)_f &= \alpha_f (\Gamma_\phi)_P + (1 - \alpha_f) (\Gamma_\phi)_A \\
 \alpha_f &= \frac{d_{AO}}{d_{AO} + d_{OP}}
 \end{aligned}
 \tag{3.17}$$

where the linear interpolation factor, d_{AO} and d_{OP} are the distances between the point O and two centres of the adjacent control volumes. Expression (3.17) is second order accurate if the mesh is Cartesian one. This way suffers from the drawback that if $(\Gamma_\phi)_A$ is equal to zero it is to be expected that there would be no flux of ϕ at the interface of the control volumes containing P and A when Eq.(3.17) approximates a value for Γ_ϕ between the nodes as $\alpha_f (\Gamma_\phi)_P$ which will not normally be the expected zero. Similarly, if $(\Gamma_\phi)_A$ is relatively much less than $(\Gamma_\phi)_P$, there would be relatively little resistance to the flux of ϕ between P and the interface compared to that between A and the surface. In this case it would be expected that $(\Gamma_\phi)_f$ would depend on $(\Gamma_\phi)_A$ and inversely on α_f whereas Eq.(3.17) would lead to $(\Gamma_\phi)_f = \alpha_f (\Gamma_\phi)_P$. In this thesis, a harmonic mean way is used as follows

$$(\Gamma_\phi)_f = \frac{(\Gamma_\phi)_A (\Gamma_\phi)_P}{\alpha_f (\Gamma_\phi)_P + (1 - \alpha_f) (\Gamma_\phi)_A}
 \tag{3.18}$$

This formula gives a better approximation of the value $(\Gamma_\phi)_f$. If either $(\Gamma_\phi)_A$ or $(\Gamma_\phi)_P$ is zero, $(\Gamma_\phi)_f = 0.0$. If $(\Gamma_\phi)_P \gg (\Gamma_\phi)_A$, then $(\Gamma_\phi)_f \approx (\Gamma_\phi)_A / \alpha_f$ as required.

3.2.4 Convective term

In discretizing the convective term, \mathbf{v} may represent the relative velocity of the fluid. In the present work, computational mesh is a stationary one on which the relative velocity is equal to the fluid velocity. When using a moving mesh this relative velocity is equal to the fluid velocity minus the moving velocity of the mesh.

Similarly, the net convective flux through the entire bounding surface of each control volume is the sum of integrals over each surface of the control volume, i.e.,

$$\int_s (\rho \mathbf{v} \phi) \cdot \mathbf{n} dS = \sum_f \int_{s_f} (\rho \mathbf{v} \phi) \cdot \mathbf{n} dS = \sum_f \rho_f (\mathbf{v} \cdot \mathbf{n})_f \phi_f S_f \quad (3.19)$$

In the discretization of the convection term, Eq.(3.19), the value of ρ_f is calculated using a upwind interpolation, i.e., taken the value in the upwind control volume.

$$\rho_f = \begin{cases} \rho_P & \text{if } (\mathbf{v} \cdot \mathbf{n})_f > 0.0 \\ \rho_A & \text{if } (\mathbf{v} \cdot \mathbf{n})_f < 0.0 \end{cases} \quad (3.20)$$

Note that this upwind interpolation is a first order approximation. The approximation of the surface value of the scalar variable (ϕ_f) is very important for obtain good solutions. One straightforward approximation for the value at surface is linear interpolation, i.e.

$$\phi_f = \alpha_f \phi_P + (1 - \alpha_f) \phi_A \quad (3.21)$$

However, this choice may give rise to the oscillation of the solutions even solution divergence. This problem and some different interpolation schemes will be discussed in more detail in the following section.

The remaining is how to calculate $(\mathbf{v} \cdot \mathbf{n})_f$ at each surface of the control volume. Again, it is also a very important issue for cell-centred finite volume methods. Rhie and Chow [1983] developed a momentum interpolation method, which has been widely used because of the simplicity of its algorithm, especially when the numerical mesh is non-orthogonal. The Rhie-Chow interpolation method will be described in Section 3.4.

3.3 Interpolation schemes

If interpolation formula (3.21) is used for the discretization of the convective term, when only the convective and diffusive terms are considered, the discretization of the general equation becomes

$$\sum_f A_f \left\{ \rho_f (\mathbf{v} \cdot \mathbf{n})_f [\alpha_f \phi_P + (1 - \alpha_f) \phi_A] \right\} + (\Gamma_\phi)_f \left(\frac{\phi_P - \phi_A}{d_{AP}} \right) = 0 \quad (3.22)$$

The quantities F_f and D_f are now introduced: $F_f = A_f \rho_f (\mathbf{v} \cdot \mathbf{n})_f$ and $D_f = A_f (\Gamma_\phi)_f / d_{AP}$. F_f is the strength of the convection of ϕ and D_f is the diffusion conductance. The Peclet number, Pe_f , can be defined as $Pe_f = F_f / D_f = \rho_f (\mathbf{v} \cdot \mathbf{n})_f / (\Gamma_\phi)_f$. Eq.(3.22) can now be expanded, and rewritten as follows

$$a_P \phi_P = \sum_{nb} a_{nb} \phi_{nb} \quad (3.23)$$

where the summation is over all neighbouring control volumes. The equations for the coefficients in Eq.(3.23) are

$$a_{nb} = D_f - (1 - \alpha_f) F_f$$

$$a_P = \sum_f (D_f + \alpha_f F_f) = \sum_{nb} a_{nb} + \sum_f F_f \quad (3.24)$$

The discretization techniques can be applied to the steady continuity equation $div(\rho \mathbf{v}) = 0$. This is a special case of the general conservation equation (Eq.(3.7)) with $\phi = 1$ and $\Gamma_\phi = 0.0$. Substitution of these values of Γ_ϕ and ϕ into the steady continuity equation gives $\sum_f F_f = 0$. Thus there is $a_P = \sum_{nb} a_{nb}$.

In the above section, we mentioned the use of the linear interpolation (3.21) for ϕ_f may give rise to oscillation of solutions, even divergence of solutions because the resulting coefficients can not be guaranteed to be positive. One way to avoid the problem of negative coefficients is to use upwind interpolation scheme which has been used in the treatment of face value of density. Similarly, ϕ_f is approximated as

$$\phi_f = \begin{cases} \phi_P & \text{if } (\mathbf{v} \cdot \mathbf{n})_f > 0.0 \\ \phi_A & \text{if } (\mathbf{v} \cdot \mathbf{n})_f < 0.0 \end{cases} \quad (3.25)$$

In this case the coefficients in expression (3.24) are

$$a_P = \sum_f \left[D_f + \max(F_f, 0.0) \right] = \sum_{nb} a_{nb} + \sum_f F_f \quad (3.26)$$

This is only approximation that satisfies the boundedness criteria unconditionally, i.e. it will yield non-oscillatory solutions. However, it is first order accurate and numerically diffusive, as had been pointed out by Raithby [1976].

In order to remain the positive coefficients and decrease the numerical diffusion, some other interpolation ways are also developed, such as, Spalding's hybrid interpolation scheme [Spalding, 1972], Patankar's power law interpolation scheme [Patankar, 1980], etc. In the steady calculations of the present work, the hybrid interpolation scheme is implemented. In hybrid interpolation scheme, the following approximations are used.

$$\begin{aligned} \frac{a_{nb}}{D_f} &= -Pe_f, & \text{if } Pe_f < -2 \\ \frac{a_{nb}}{D_f} &= 1.0 - 0.5Pe_f, & \text{if } |Pe_f| < 2 \\ \frac{a_{nb}}{D_f} &= 0.0, & \text{if } Pe_f > 2 \end{aligned} \quad (3.27)$$

This means that the coefficients in Eq.(3.23) become

$$\begin{aligned} a_{nb} &= \max(-F_f, D_f - \frac{F_f}{2}, 0.0) \\ a_P &= \sum_{nb} a_{nb} + \sum_f F_f \end{aligned} \quad (3.28)$$

It should be noted that when the Peclet number is in the range -2 to 2 then the hybrid scheme reduces to a central interpolation scheme and outside this range it uses a modification of the upwind interpolation scheme where the diffusion has been set to zero.

On combining the discretized terms described in previous sections, the discretized form of the general conservation equation is obtained.

$$\frac{(\rho_P \phi_P - \rho_P^0 \phi_P^0) V_P}{\Delta t} + \sum_f \left\{ D_f A(|Pe_f|) + \max(-F_f, 0.0) (\phi_P - \phi_A) + F_f \phi_P \right\} = (S_C - S_P \phi_P) V_P \quad (3.29)$$

where $A(|Pe_f|)$ is the function for a chosen interpolation scheme. For the hybrid interpolation scheme

$$A(|Pe_f|) = \max(0.0, 1.0 - 0.5|Pe_f|) \quad (3.30)$$

The continuity equation $\partial \rho / \partial t + \text{div}(\rho \mathbf{v}) = 0$ can similarly be discretized to give

$$\frac{(\rho_P - \rho_P^0) V_P}{\Delta t} + \sum_f F_f = 0 \quad (3.31)$$

Multiplying Eq.(3.31) by ϕ_P and substituting into Eq.(3.30) gives an equation of the form

$$a_P \phi_P = \sum_{nb} a_{nb} \phi_{nb} + b_P \quad (3.32)$$

where the summation is over all control volumes which share a surface with control volume P . The coefficients in Eq.(3.32) are calculated from the following expressions

$$\begin{aligned} a_{nb} &= D_f A(|Pe_f|) + \max(-F_f, 0.0) \\ b_P &= S_C V_P + \frac{\rho_P^0 \phi_P^0}{\Delta t} V_P \\ a_P &= \sum_{nb} a_{nb} + \frac{\rho_P^0}{\Delta t} V_P + S_P V_P \end{aligned} \quad (3.33)$$

Equation (3.32) is the final form of the discretized equation which can now be solved, after decisions are made as to how to handle surfaces coinciding with the boundaries of the solution domain, to give the values of ϕ at all the control volume centres.

However, the described interpolation schemes above are first order or second order accurate. When very large variable gradients occur in the unsteady flow field, these order interpolation schemes will inevitably overestimate the diffusion and underestimate the gradients. In the computations in this thesis, a high order interpolation scheme is employed for the calculation of the face value. The high order interpolation scheme was proposed by Leonard [1979] and gave it the name QUICK (Quadratic Upwind Interpolation for Convective Kinematics). The QUICK scheme has been found to offer solutions with high accuracy and have good stability in computations.

In first order interpolation schemes the value of a surface value are all approximated through the contribution of two adjacent control volumes. In QUICK scheme, the contribution of three control volumes will be considered. For the simplicity, the QUICK interpolation formula is demonstrated on 1-D Cartesian mesh.

According to Hayase et al [1992], after considering the nature of convection, the formula for the QUICK scheme for a face of control volume f , see Figure 3.3 can be expressed as

$$\phi_f = \begin{cases} \phi_P + (C_W^+ \phi_W + C_P^+ \phi_P + C_E^+ \phi_E) & \text{if } u_f \geq 0.0 \\ \phi_E + (C_{EE}^- \phi_{EE} + C_E^- \phi_E + C_P^- \phi_P) & \text{if } u_f < 0.0 \end{cases} \quad (3.34)$$

where

$$\begin{aligned} C_W^+ &= -\frac{\Delta x_P \Delta x_E}{(\Delta x_W + \Delta x_P)(\Delta x_W + 2\Delta x_P + \Delta x_E)}, & C_P^- &= \frac{(-\Delta x_W - \Delta x_P + \Delta x_E)\Delta x_P}{(\Delta x_W + \Delta x_P)(\Delta x_P + \Delta x_E)} \\ C_P^- &= \frac{(2\Delta x_E + \Delta x_{EE})\Delta x_E}{(\Delta x_P + 2\Delta x_E + \Delta x_{EE})(\Delta x_P + \Delta x_E)}, & C_E^+ &= \frac{(\Delta x_W + 2\Delta x_P)\Delta x_P}{(\Delta x_W + 2\Delta x_P + \Delta x_E)(\Delta x_P + \Delta x_E)} \\ C_E^- &= \frac{(\Delta x_P - \Delta x_E - \Delta x_{EE})\Delta x_E}{(\Delta x_P + \Delta x_E)(\Delta x_E + \Delta x_{EE})}, & C_{EE}^- &= -\frac{\Delta x_P \Delta x_E}{(\Delta x_E + \Delta x_{EE})(\Delta x_P + 2\Delta x_E + \Delta x_{EE})} \end{aligned}$$

The dimensions of control volume, Δx_W , Δx_P , Δx_E , and Δx_{EE} are shown in Figure 3.3. Similar formula can be written for the other surfaces.

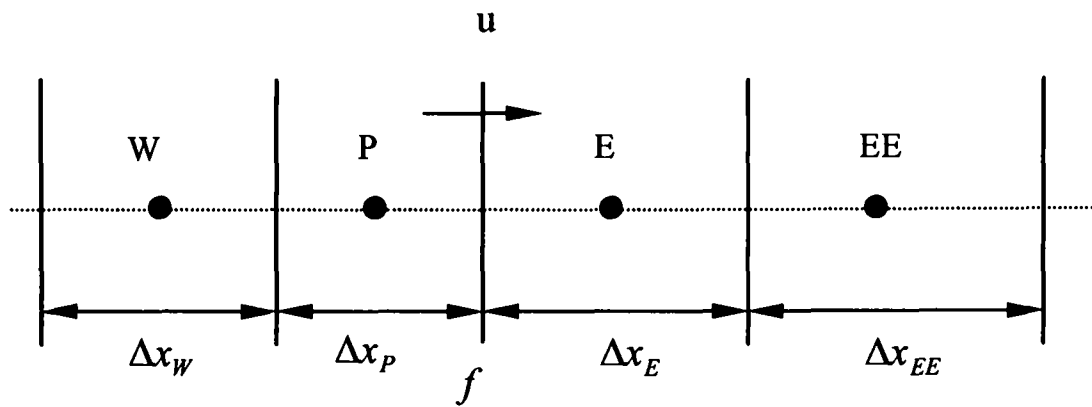


Fig. 3.3. Schematic for the QUICK interpolation formula in x direction

It is noted that on the right-hand side of Eq.(3.34), the first term is the first order upwind scheme. The first term is used to form the discretized equation coefficients and the term in parentheses is incorporated in the source term. By using this technique, the coefficient matrix of the resulting discretized equations is always diagonally dominant. This interpolation formula has a *third* order accuracy on both *uniform* and *non-uniform* Cartesian meshes. On a uniform Cartesian mesh expression (3.34) becomes

$$\phi_f = \begin{cases} 0.75\phi_P + 0.375\phi_E - 0.125\phi_W & \text{if } u_f \geq 0.0 \\ 0.75\phi_E + 0.375\phi_P - 0.125\phi_{EE} & \text{if } u_f < 0.0 \end{cases} \quad (3.35)$$

When the above QUICK interpolation scheme is used for the surface value ϕ_f in the discretization of the convective term, the first coefficient in Eq. (3.33) is calculated via the following formula in the present work so that diagonal dominance of the system matrix is guaranteed.

$$a_{nb} = D_f + 0.625 \max(-F_f, 0.0) \quad (3.36)$$

The negative of this value is placed in the off diagonal position corresponding to the adjacent control volume. There is also a source term of the form for $u_f \geq 0.0$

$$\begin{aligned} & -0.125 \max(F_f, 0.0)(\phi_P - \phi_W) - 0.125 \max(-F_f, 0.0)(\phi_W - \phi_E) \\ & - 0.375 \max(F_f, 0.0)(\phi_E - \phi_P) \end{aligned} \quad (3.37)$$

Similar expression may easily be given for $u_f < 0.0$. For the unsteady calculations in the present work, the above QUICK formulation is employed.

3.4 Rhie-Chow interpolation method

The discretization of the general conservation equation described above is based on cell-centred finite volume method, i.e., discretized on a collocated mesh arrangement. All vector variables and scalar variables are stored at the same location---the centres of control volumes. The use of collocated meshes greatly reduces the required storage memory and shortens the computational time in three-dimensional calculations, especially for unstructured/curvilinear body-fitted meshes. However, the discretization based on a collocated mesh is prone to produce the *checkerboard effect* of variable. One can note that there is a pressure gradient term. In their discretizations, checkerboard pressure probably occurs when a linear interpolation scheme is used for the face values of pressure. Similarly, when steady incompressible continuity equation is considered, a checkerboard velocity is also caused probably. One way to avoid the problem is to implement the discretizations of the governing equations on a staggered mesh on which vector components and scalar variables are stored at different locations. Using staggered meshes typically results in stable and robust solutions. For general non-orthogonal meshes, however, the implementation of staggered mesh arrangements tends to become rather complex, and even impossible. Rhie and Chow [1983] proposed a momentum interpolation method to eliminate the checkerboard pressure and to calculate the face mass fluxes of control volumes in the continuity equation.

Let us consider the momentum equation in the x -direction

$$\frac{\partial(\rho u)}{\partial t} + \text{div}(\rho \mathbf{v}u) = -\frac{\partial p}{\partial x} + \text{div}(\mu \text{grad}(\rho)) + S \quad (3.38)$$

Using the techniques described in the previous sections, over the control volume about a node P , the discretized equation (3.38) can be written in the form

$$a_P u_P + (\nabla_x p)_P = (\sum a_{nb} u_{nb})_P + S_P \quad (3.39)$$

where $\nabla_x p$ is the discretized contribution from the pressure gradient term. Similarly for the adjacent node A

$$a_A u_A + (\nabla_x p)_A = (\sum a_{nb} u_{nb})_A + S_A \quad (3.40)$$

From the conservation principle of the control volume formulation the u velocity at a point on the face between the nodes must also have a discretized momentum equation of the form

$$a_f u_f + (\nabla_x p)_f = (\sum a_{nb} u_{nb})_f + S_f \quad (3.41)$$

The key point of the Rhie-Chow momentum interpolation method is to use Eq.(3.39) and Eq.(3.40) to approximate a solution of equation (3.41). It is assumed that the right-hand side of Eq.(3.41) may be approximated by using a weighted linear interpolation of the corresponding terms in Eq.(3.39) and Eq.(3.40). Thus

$$a_f u_f + (\nabla_x p)_f = \overline{(\sum a_{nb} u_{nb})_f + S_f} = \overline{a_f u_f} + \overline{(\nabla_x p)_f} \quad (3.42)$$

where the overline in the above equation indicates a weighted linear interpolation of the variable. Assuming that $a_f \approx \overline{a_f}$ then

$$u_f = \overline{u_f} + \overline{d_f} (\overline{(\nabla_x p)_f} - \nabla_x p_f) \quad (3.43)$$

where if α is the weighting factor used

$$\begin{aligned}
 \overline{u_f} &= \alpha u_p + (1 - \alpha) u_A \\
 \overline{\nabla_x p_f} &= \alpha \nabla_x p_p + (1 - \alpha) \nabla_x p_A \\
 \nabla_x p_f &= A_f n_x (p_A - p_p) \\
 a_f &= \alpha a_p + (1 - \alpha) a_A \\
 \overline{d_f} &= a_f^{-1}
 \end{aligned} \tag{3.44}$$

All that is now required to complete the Rhie-Chow interpolation method is to select the weighting factor α . The obvious choice is that α should be equal to the distance of the node in control volume A to the face divided by the distance from the same node to the node in element P . In computations in this thesis, the weighting factor α is set to 0.5.

3.5 Momentum-pressure coupling---SIMPLE algorithm

In the collocated mesh approach, the resulting discretized system of equations for a control volume has no direct coupling between the pressure and velocities in the control volume. As a result, if the pressure is not correct, the velocities consequently will not satisfy the continuity equation. In the present work, the SIMPLE (Semi-Implicit Method for Pressure-Linked Equations) algorithm [Patankar & Spalding, 1972] is taken to perform a solution procedure. The algorithm is essentially a guess-and-correct procedure for the calculation of pressure.

The discretized form of the continuity equation can be written as

$$\frac{(\rho_p - \rho_p^0) V_p}{\Delta t} + \sum_f A_f \rho_f (\mathbf{v} \cdot \mathbf{n}) = 0 \tag{3.45}$$

where the superscript 0 represents the previous time step value. Rhie-Chow interpolation gives the equation for a face velocity component as

$$u_f = \overline{u_f} + \frac{1}{a_p} (\overline{\nabla_x p_f} - \nabla_x p_f) \tag{3.46}$$

where the overbar indicates linear interpolation of the relevant quantity between the element centre values in the control volumes either side of face f . In Eq.(3.46) the $\nabla_x p_f$ term is approximated by $A_f n_x (p_A - p_P)$ where the subscripts P and A denote the current and adjacent control volumes respectively. At any solution stage, assumed p^* and u^* are estimated pressure and u-velocity component values at the centre of control volume, the face value of the u component of velocity is given by

$$u_f^* = \overline{u_f^*} + \frac{1}{a_p} (\overline{\nabla_x p_f^*} - \nabla_x p_f^*) \quad (3.47)$$

The objective is to improve the guessed pressure p^* so that the starred velocity components get gradually closer to satisfying the continuity equation. We define the correction p' as the difference between the correct pressure and the guessed pressure, so that

$$p = p^* + p' \quad (3.48)$$

Similarly we define velocity correction u' , v' and w' to relate the correct velocities u , v and w to the guessed velocities u^* , v^* and w^*

$$u = u^* + u', \quad v = v^* + v', \quad w = w^* + w' \quad (3.49)$$

If Eq.(3.47) is subtracted from Eq.(3.46) then we can obtain the following velocity correction formula

$$u_f' = \overline{u_f'} + \frac{1}{a_p} (\overline{\nabla_x p_f'}) - \nabla_x p_f' \quad (3.50)$$

The use of all terms in Eq.(3.50) would produce an equation in which the pressure correction in a control volume is directly dependent on corrections in both neighbouring control volumes and control volumes adjacent to these neighbours. This would lead to the

need to solve a linear matrix with a much larger number of non zero elements per row than any of the matrices constructed in the solution of the other solved variables. In order to simplify the resulting pressure correction equation, the first two terms in Eq.(3.50) are dropped. Hence

$$u'_f = -\frac{1}{a_p}(\nabla_x p'_f) = \frac{1}{a_p} A_f n_x (p'_P - p'_A) \quad (3.51)$$

Finally substituting Eq(3.49), using Eq.(3.51) for the correction term, into the discretized continuity equation (3.45) gives

$$\sum_f \rho_f A_f^2 \frac{n_i^2}{a_i} (p'_P - p'_A)_f = \frac{(\rho_P^0 - \rho_P) V_P}{\Delta t} - \sum_f A_f \rho_f (\mathbf{v}^* \cdot \mathbf{n})_f \quad (3.52)$$

where the subscript i in the first term indicates a summation over the three coordinate directions. The above equation can be written in the form

$$a_p p'_P + \sum_{nb} a_{nb} p'_{nb} = b_p \quad (3.53)$$

where the summation in Eq.(3.53) is over all control volumes sharing a face with control volume P and

$$\begin{aligned} a_{nb} &= -\rho_f A_f^2 \sum_{i=1}^3 \frac{n_i^2}{a_i} \\ a_p &= -\sum_{nb} a_{nb} \\ b_p &= \frac{(\rho_P^0 - \rho_P) V_P}{\Delta t} - \sum_f A_f \rho_f (\mathbf{v}^* \cdot \mathbf{n})_f \end{aligned} \quad (3.54)$$

These equations for the coefficients lead to a set of linear equations with weak diagonal dominance, the diagonal being at least as large as the sum of absolute values the off diagonal elements. Boundary conditions, or a fixed reference pressure point, will guarantee

diagonal dominance on some rows. Consequently, the matrix equation can be solved using the same iterative techniques which are employed to obtain the solution for any solved scalar variables.

Eq.(3.53) represents the discretized continuity equation as an *equation for pressure correction* p' . The source term b_p in the equation is the continuity imbalance arising from the incorrect velocity field \mathbf{v}^* . By solving Eq.(3.53), the pressure correction field is known, the correct pressure field p' can be obtained at all points. Once the pressure correction field is known, the correct pressure field may be obtained using formula (3.48).

The pressure correction equation is susceptible to divergence unless some *under-relaxation* is used during the iterative process and new, improved, pressure p^{new} are obtained with

$$p^{new} = p^* + \beta p' \quad (3.55)$$

where β is the pressure under-relaxation factor. In computations in this thesis, the value of β is set to 0.6.

Note that the velocity correction, Eq.(3.51), need to be applied to the centre value of the control volume rather than those face values. If the discretized form of the momentum equation is considered

$$a_p u_p = \sum_{nb} a_{nb} u_{nb} + b - \nabla_x p_p \quad (3.56)$$

then at any stage given a guessed pressure field p^* an estimated velocity field \mathbf{v}^* can be calculated.

$$a_p u_p^* = \sum_{nb} a_{nb} u_{nb}^* + b - \nabla_x p_p^* \quad (3.57)$$

subtracting Eq.(3.57) from (3.56) and using Eq.(3.48) and Eq.(3.49) an equation is obtained expressing the velocity correction in the control volume as a function of neighbouring

velocity corrections and the integrated gradient of the pressure correction in the control volume

$$a_p u'_p = \sum_{nb} a_{nb} u'_{nb} - \nabla_x p'_p \quad (3.58)$$

After the summation term is dropped, the following simplified velocity correction is obtained.

$$u'_p = -\frac{1}{a_p} \nabla_x p'_p = -\frac{1}{a_p} \sum_f A_f n_x p'_f \quad (3.59)$$

The omission of terms in the derivation of Eq.(3.59) does not affect the final solution because the pressure correction and velocity corrections will all be zero in a converged solution giving $p^* = p$ and $\mathbf{v}^* = \mathbf{v}$. Expanding the right-hand side gives the following equation for the velocity correction in terms of pressure corrections in the control volume and all its neighbours.

$$u'_p = -\frac{1}{a_p} \sum_{nb} n_x A_f (\alpha_f p'_p + (1 - \alpha_f)) p'_{nb} \quad (3.60)$$

where α_f is the under-relaxation factor.

3.6 Solution of algebraic equation

The linear algebraic equation is obtained from the discretization of general equation. Due to large number of unknown variables on the mesh of the entire computational domain, iteration methods are widely employed to solve the linear algebraic equation (i.e., Eq.(3.32)). To avoid any divergence it is desirable to control the magnitude of the dependent variable change in the iteration process. Generally, the use of underrelaxation

greatly helps to avoid divergence in the iterative solution. Relaxation iterative form of Eq.(3.32) can be expressed as follows:

$$\phi_p^{i+1} = (1 - \alpha)\phi_p^i + \alpha\left(\frac{\sum a_{nb}\phi_p^i + b_p}{a_p}\right) \quad (3.61)$$

where ϕ_p^i denotes the value of ϕ_p at the i th iteration, ϕ_p^{i+1} is the value at the $(i+1)$ th iteration, α represents an underrelaxation factor (i.e., $0 < \alpha < 1$). When two successive iteration values satisfy certain criteria specified by us in advance (e.g., $|\phi_p^{i+1} - \phi_p^i| \leq \varepsilon$, ε is certain criteria), it implies that a converged solution has reached. Any relaxation iteration method must produce the final converged solution.

There are no general rules for choosing the best value of α . The optimum value depends on many factors, such as the nature of the problem, the mesh spacing, and the iterative procedure used. Usually a suitable value of the relaxation factor can be some exploratory computations for a given problem. In the used CFD solver in this thesis, many fully iterative linear solvers, such as the Gauss-Seidel (GS), Successive Relaxation (SR), and Jacobi Preconditioned Conjugate Gradient (JPCG) method, can be employed.

3.7 Implementation of boundary conditions

All CFD problems are defined in terms of initial and boundary conditions. These boundaries include boundaries of computational domain because computational domain is finite size and some solid boundaries when there are bodies in the flow. It is important to correctly specify boundary conditions in numerical calculations. The present section describes the implementation and treatment of the most common boundary conditions which occur in computations in this thesis.

At an inflow boundary, all quantities except for pressure have to be specified. Since the velocity and other variables are given as free stream values, all the convective fluxes can be calculated. The diffusive fluxes are usually not known, but they can be approximated using known boundary values of the variables and one-sided interpolation approximations for the gradients.

At the outflow we usually know little about the flow. Usually one extrapolates along mesh lines from the interior to the boundary. Zero gradient approximation along mesh lines is used. For the convective flux this means that a first order upwind approximation is used, i.e., mass flux evaluated using velocity components at centre of control volume. Pressure is specified. Also, pressure is specified at the upper domain boundary.

At the solid wall boundaries, since there is no flow through the wall, convective fluxes of all quantities are zero. For viscous flow cases, no-slip condition is used. The pressure on the wall is evaluated via extrapolated approximation from the interior centres of control volumes. Diffusive fluxes require some attention. For other scalar quantities, they may be zero, they may be specified, or the value of the scalar may be prescribed

The conditions at a symmetry boundary are: (i) no flow across the boundary and (ii) no scalar flux across the boundary. In the implementation, normal velocities are set to zero at a symmetry boundary and the values of all other properties just outside the computational domain are equated to their values at the nearest node just inside the domain.

3.8 Determination of time step

Since SIMPLE algorithm is a semi-implicit, iterative scheme, time step in the steady and unsteady calculations is limited by numerical stability. For steady calculations, time restriction can be alleviated, to some extent, by using the maximum allowable *local* time step in each control volume because only the final steady solution is of interest. The unsteady solution need, however, to be time-accurate. The same time step should be set up in the whole computational domain. In computations of this thesis, a time step is first determined approximately for each control volume through the following formula

$$\Delta t_P = \frac{V_P}{\max_{f \in P} (\mathbf{v}_f \cdot \mathbf{S}_f + c \cdot |\mathbf{S}_f|)} \quad (3.62)$$

where Δt_P is time step for the control volume P , \mathbf{v}_f represents velocity vector at the surface f , V_P is the volume of the control volume, c denotes speed of sound, and \mathbf{S}_f is the surface area vector at surface f . The minimum value of all time steps of control

volumes is then multiplied by a *CFL* (Courant-Friedrich-Lewy) number for unsteady calculations.

$$\Delta t_{CFD} = CFL \cdot \min_{P \in \Omega}(\Delta t_P) \quad (3.63)$$

where Ω stands for the whole computational domain. The *CFL* number is adjustable, and is set to 0.8 in computations of this thesis.

3.9 Solution procedure of unsteady flow simulation

Algorithm and relevant issues described in the previous sections will be used to unsteady flow calculation in a chosen near field. The determination of the computational domain of the unsteady flow near field is problem dependent. *Ideally*, the unsteady flow near field should contain *all possible* acoustic sources, meanwhile, should be kept as small as possible in order to reduce the computational time and memory. In unsteady flow calculations with the implicit formulation, the iterative procedures for employing SIMPLE are applied at each time level until convergence is achieved. Figure 3.4 and Figure 3.5 show the SIMPLE algorithm structure and solution procedure of unsteady flow calculation.

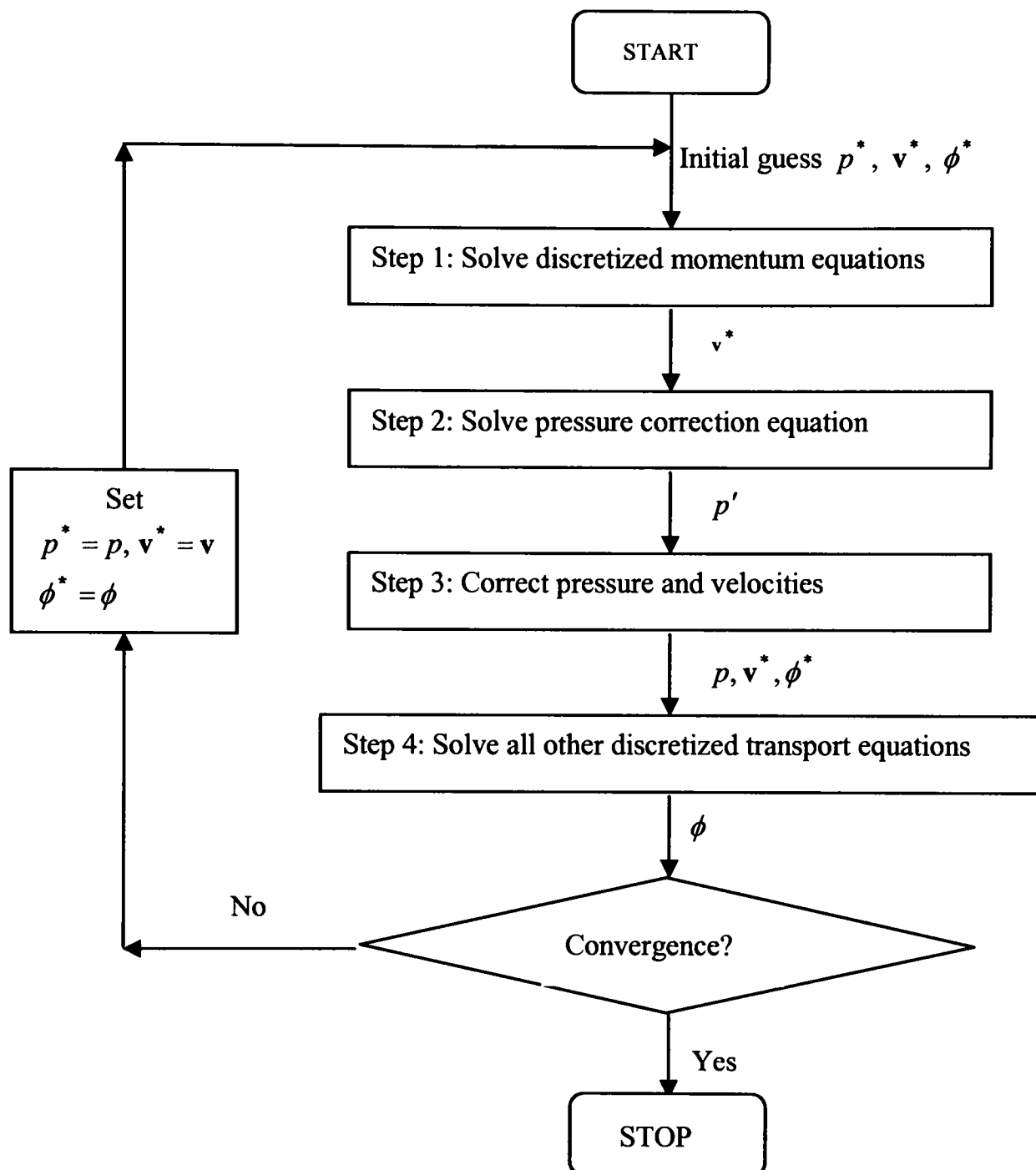


Fig. 3.4. The flowchart of the SIMPLE algorithm

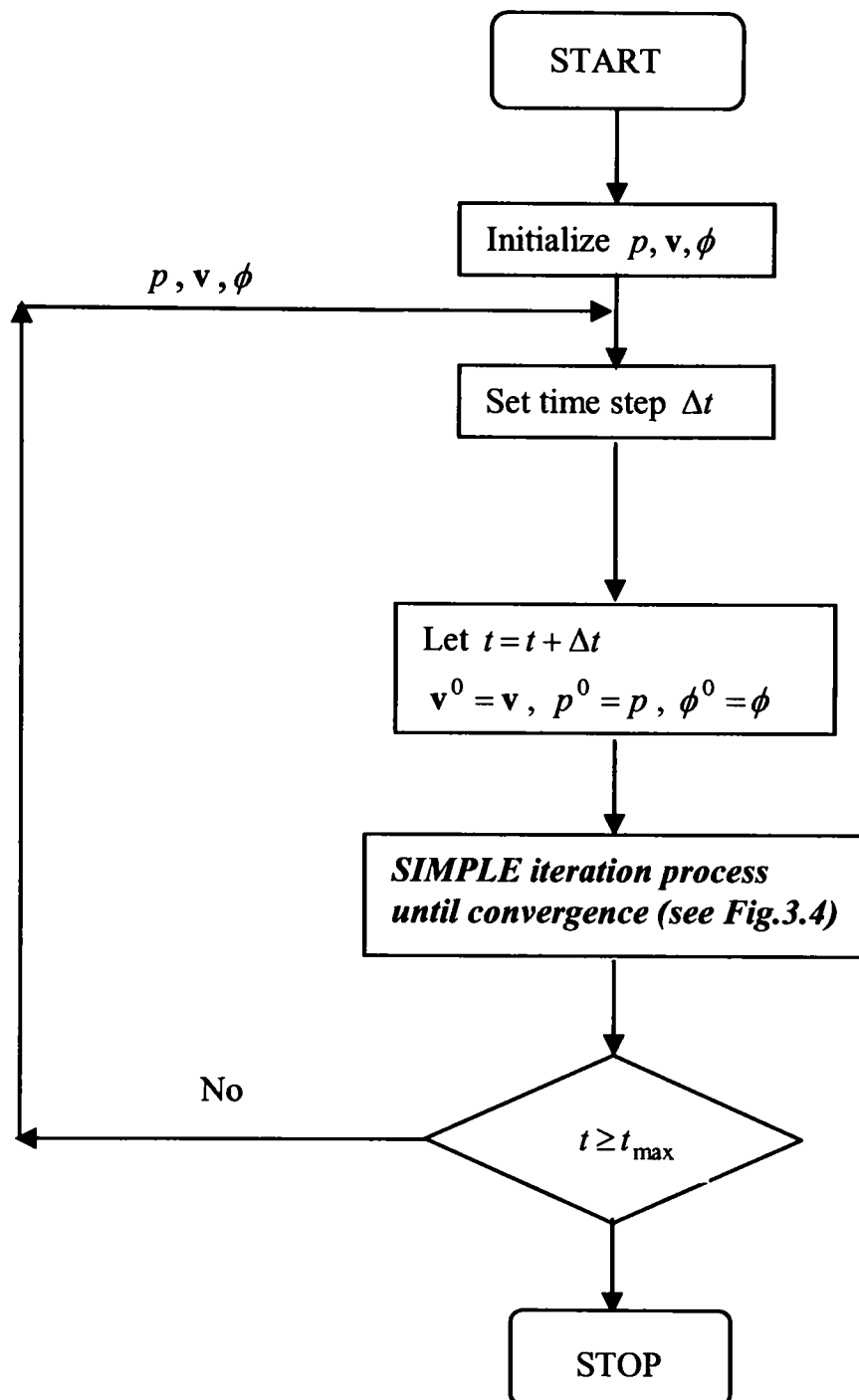


Fig. 3.5. The flowchart of the SIMPLE algorithm for transient flow calculation

Chapter 4

Numerical Solution of Acoustic Equations

The generation of aerodynamic sounds and the propagation of sounds are two main issues in computational aeroacoustics (CAA). In a coupling method, the generation of aerodynamic sound and the propagation of the resulting sound are calculated separately. In the second step of the two-step coupling procedure, a set of acoustic perturbation equations with extracted sources from the solutions of the unsteady flow field need to be solved to obtain the propagation/radiation of the resulting aerodynamically sound.

As discussed in Chapter 1, the large disparity of the temporal and spatial scales leads to different characteristics and features between the unsteady flow field and the accompanying sound field. Moreover, since the nature and objectives of aeroacoustic problems are distinctly different from common aerodynamic problems and other fluid flow problems, standard CFD techniques do not perform well when applied to wave propagation problems. Currently, the calculation of the propagation of acoustic waves generated from the unsteady flows, after long time and large distance with minimized dissipative errors and dispersive errors, faces *still* some challenges. Like numerical methods used in CFD, a variety of numerical methods have been developing for the calculation of propagating waves in CAA field. In this thesis, an optimized, staggered-type dispersion-relation-preserving (DRP) high-order finite difference method is used to solve the acoustic equations.

The aim of this chapter is to discuss how to accurately calculate acoustic perturbations through the set of acoustic perturbation equations (i.e., Eq.(2.87)~Eq.(2.88)) by using DRP finite difference schemes. Meanwhile, some relevant numerical issues encountered with the use of the numerical schemes are discussed.

4.1 Numerical schemes for acoustic wave calculation

The governing equations of fluid flow motion and the acoustic equations of acoustic wave propagation are, in essence, nonlinear partial differential equations. Generally speaking, closed form solutions of such nonlinear partial differential equations are difficult to be obtained due to their nonlinearity and unsteadiness. Numerical methods have to be developed for solving these differential equations. One of the most widely used numerical methods is finite difference method. The accuracy and efficiency of a numerical method greatly depends on the numerical scheme used to discretize the partial differential equations. Numerical discretization of a partial differential equation is to approximate the partial derivatives of spatial and temporal derivative on a computational mesh. Finite difference schemes are usually derived using Taylor series such that they yield truncation errors of a given order. By order it means that the errors will be of the same magnitude as the spatial or temporal step rose to the order power. The use of a Taylor series is equivalent to fitting the data with a polynomial of varying degree, and differentiating the polynomial to obtain an approximation of the derivative. The term stencil is commonly used to refer to the points that are used in the fitting. As more points are included in the stencil, the degree of the polynomial increases and the approximation becomes better. A wider computational stencil therefore permits higher order accuracy by introducing more unknowns into the approximation expression.

It is known that the majority of conventional CFD schemes available currently fall into low order category. Low order scheme here refers to truncation errors of derivatives are of no greater than *second* order. For numerical methods with low order scheme are relatively easy to be developed and coded. Since stencil size is small in low order schemes, the treatment of boundary conditions is also relatively easy. Unfortunately, as pointed out previously, for wave propagation over longer distances, the grid resolution requirements of *second-order* schemes can become *excessive* (even if they were without other numerical errors), leading to impractical CPU and memory requirements. This is one of the main reasons why the majority of conventional CFD schemes are not adequately accurate for calculating the propagation of acoustic waves.

Sound waves are propagating perturbations which are superimposed onto the unsteady background flow field. Their amplitudes are often *several* orders of magnitude *smaller* than

the mean quantities, and the frequencies are much *higher* than those considered in a typical unsteady flow field generating the sound. Furthermore, acoustic waves propagate outward at a particular propagating speed in the fluid medium, and the loss of the amplitude and the change of the propagating speed of the waveform are *not obvious* within a longer travelling distance. High-fidelity is paramount for the investigations of acoustic problems. Considering the features of the acoustic waves and avoiding excessively fine meshes for many practical problems, in order to adequately capture the behaviour of the desired portion of the waveform, high order schemes have to be often employed in the solution of the acoustic equations. Consequently, some high order differencing schemes have been developed for the calculation of wave propagation (e.g., Cohen & Joly, [1990]; Kim et al., [1997]; Zingg et al., [1998]; Goodrich, [1997]). Most of these schemes require filtering of the high frequency components which cannot be resolved adequately. Generalization of matching Taylor series for difference schemes is provided by Pade for so-called compact finite difference schemes [Thomas, 1995]. Compared to other numerical methods (e.g., finite volume method), high order schemes in finite difference method are relatively easy to be realized due to the approximation of the partial differential derivatives on Cartesian meshes. Naturally, a price must be paid for the use of high order difference schemes. The increased stencil size can render the boundary conditions inconvenience to enforce. Either biased (one sided) stencils must be used or more information from outside the domain prescribed. When complex geometrical configurations are involved, the treatment of wall boundary conditions becomes even more difficult. At the same time, computational cost also increases.

It is well-known that any numerical schemes are subject to numerical errors which arise from both the spatial and temporal discretization. These numerical errors include dissipative error (amplitude error) and dispersive error (phase error). Numerical dissipation errors in numerical calculations may be eliminated via employing symmetry-type difference schemes. A high order symmetrical scheme can greatly decrease the loss of the amplitude of the acoustic waves over longer distance. Since acoustic waves generated by the unsteady flow do not propagate at the convection velocity of the unsteady flow, keeping correct wave speed is crucial for the propagation of the acoustic waves. However, a consistent, stable, and convergent high order scheme is not necessarily dispersion-relation preserving and thus does not necessarily guarantee a good quality numerical wave solution for an acoustic

problems. Hence, numerical schemes with low dissipation and dispersion are desirable. Furthermore, it can be advantageous to modify the coefficients of a potentially higher order scheme, thereby lowering the order of accuracy, to produce reduced errors over a range of wavenumbers with the same computation effort. Such schemes are termed usually as *optimized* schemes. In an optimized finite difference scheme, the error behaviour over a range of special wavenumbers is optimized according to some criterion, usually based on Fourier analysis. This approach contrasts with conventional Taylor series truncation methods, which generally maximize the order of accuracy, i.e., the order of the leading error term. From the order of the truncation error, one expect that a seven-point sixth order scheme is probably a more accurate approximation than a five-point fourth order scheme, which is, in turn, more accurate than a three-point second order scheme. One does not know, however, how much a higher order scheme is better than a lower order one, and in what sense a higher order scheme is better than a lower order one. Fourier analysis provides a straightforward means of calculating numerical dissipation and numerical dispersion. Although this simplified analysis excludes errors associated with non-uniform meshes and boundaries, it is a very useful tool for scheme evaluation and development. Good performance under the conditions of Fourier analysis, i.e., uniform meshes and periodic boundary conditions is a necessary condition for good performance under more general conditions. The optimization of difference scheme through Fourier analysis was first proposed by Vichnevetsky and De Schutter [1975] and later studied in more detail by Holberg [1987]. High computational requirements for accurate simulations of the propagation of acoustic waves have led to considerable effort to develop optimized high order difference schemes for acoustic applications. Lele [1992] proposed an optimized compact high order finite difference scheme. Tam and Webb [1993] developed optimized dispersion-relation-preserving (DRP) high order difference schemes to minimize the dispersion errors for a given stencil size. The papers by Holberg, Lele, and Tam and Webb spawned a number of optimized schemes (e.g., Kim & Lee, [1996]; Hu et al., [1996a]; Lockard et al., [1994]; Zhuang & Chen, [1998]). In computations of this thesis, a staggered mesh extension of the optimized DRP scheme of Tam and Webb by Djambazov et al. [2000b] is used to solve the acoustic equations (i.e., Eq.(2.87) and (2.88)).

It can be noticed that the numerical schemes in solving partial differential equations may be divided into two distinct groups. In the first group, the spatial and temporal

discretizations are independent, i.e., a discretization is applied to the spatial derivative to produce a system of ordinary differential equations, which is solved numerically using a time-marching method. The second group involves the simultaneous discretization of space and time; there is no intermediate form. The optimized DRP scheme by Tam and Webb drops into the first group.

In order to conveniently describe the optimized staggered-type DRP high order finite difference scheme, DRP scheme of Tam and Webb is introduced in the following section. Subsequently, the optimized staggered-type DRP high order finite difference scheme and some relevant numerical issues (e.g., boundary conditions and determination of time step) are described. Validations of the code are given through considering the wave propagation of a two dimensional acoustic pulse with a background flow.

4.2 DRP scheme

In 1993 Tam and Webb [1993] proposed currently widely-used optimized high order finite difference schemes which are not only meet the usual conditions of consistency, stability, and hence convergence but also support, in the case of small amplitude waves, wave solutions which have (as nearly as possible) the same characteristics as those of the linearized Euler equations.

It is well known in wave propagation theory (e.g., Whitham, [1974]) that the propagation characteristics of the waves governed by a system of partial differential equations are encoded in the dispersion relation in the frequency and wave number space. The dispersion relation is a functional relation between the angular frequency of the waves and the wave numbers of the spatial variables. This relation is usually obtained by taking the space and time Fourier transforms of the governing equations. The dispersion, damping rate, isotropy or anisotropy, group and phase velocities of all the waves supported by the medium governed by the partial differential equations are all determined by the dispersion relation. With this understanding it is clear that what is needed is a finite difference scheme which has the same or almost the same dispersion relation as the original partial differential equations. This class of finite difference schemes are referred to as dispersion-relation-preserving (DRP) schemes by Tam and Webb.

Since the spatial and temporal discretizations are independent in DRP scheme of Tam and Webb, they will be considered separately.

4.2.1 Spatial discretization

Let $f(x, y, z)$ be the instantaneous variables of any of the acoustic field (e.g., p or v_j , see Eq.(2.87) and (2.88)). For the approximation of the first partial derivative $\partial f/\partial x$ at the l th node of a uniform mesh, supposed M values of f to the right and N values of f to the left of the node are used to form the finite difference approximation [Tam & Webb, 1993]:

$$\left(\frac{\partial f}{\partial x}\right)_l \cong \frac{1}{\Delta x} \sum_{j=-N}^M a_j f_{l+j} \quad (4.1)$$

The usual procedure is to expand the right-hand side of expression (4.1) in a Taylor series and determine the coefficients a_j by equating coefficients of the same powers of Δx . Finite difference schemes constructed in this way will be referred to as the standard schemes. For example, letting $M = N = 1$ and expanding the functional terms to second order gives $a_0 = 0$ and $a_1 = -a_{-1} = 1/2$, which corresponds to the standard second order central difference. However, the coefficients a_j were chosen by Tam and Webb in a different way for the DRP scheme. Generally, if $M = N$ is chosen, the coefficients will have $a_0 = 0$ and $a_j = -a_{-j}$ (i.e., the coefficients are antisymmetric). According to Tam and Webb, those coefficients were determined by requiring that the numerical scheme and its corresponding original partial differential equation would have the same (or a good approximation) dispersion relation. This process starts with the Fourier transform of the finite difference approximation and the partial derivative term (right and left sides of expression (4.1), respectively).

Fourier transform is defined only for functions of a continuous variable. The generalized form of expression (4.1), applicable to any set of points at Δx apart, is

$$\frac{\partial f(x)}{\partial x} \cong \frac{1}{\Delta x} \sum_{j=-N}^M a_j f(x + j\Delta x) \quad (4.2)$$

Expression (4.1) is a special case of the above expression (4.2). By setting $x = l\Delta x$ in (4.2), expression (4.1) is recovered. With α being the transform variable the Fourier transform of a function $f(x)$ and its inverse are related by

$$\tilde{f}(\alpha) = \frac{1}{2\pi} \int_{-\infty}^{\infty} f(x) e^{-i\alpha x} dx \quad (4.3)$$

$$f(x) = \int_{-\infty}^{\infty} \tilde{f}(\alpha) e^{i\alpha x} d\alpha \quad (4.4)$$

On applying Fourier transform to the left and right sides of (4.2), it is found

$$i\alpha \tilde{f} \cong \frac{1}{\Delta x} \left[\sum_{j=-N}^M a_j e^{ij\alpha\Delta x} \right] \tilde{f} \quad (4.5)$$

Generally, the variable α represents the wave number of the wave disturbance, and it is related to the temporal frequency of a given wave. By comparing the two sides of expression (4.5), the effective wave number of the Fourier transform of the finite difference scheme (4.2) or (4.1)

$$\bar{\alpha} = \frac{-i}{\Delta x} \sum_{j=-N}^M a_j e^{ij\alpha\Delta x} \quad (4.6)$$

It is clear that $\bar{\alpha}\Delta x$ is a periodic function of $\alpha\Delta x$ with a period of 2π . For example, using the second-order central difference scheme, the above relation becomes $\bar{\alpha}\Delta x = \sin(\alpha\Delta x)$. Clearly, for a given mesh size, Δx , determining the dispersion relation for a numerical scheme amounts to comparing the wave number parameter $\bar{\alpha}\Delta x$ and $\alpha\Delta x$. For the three-point second order central scheme, the approximate wave number matches the exact wave

number only for very small values of $\alpha\Delta x$. Using a very small Δx can ensure the dispersion relation is being preserved. Hence it can be expected that very fine meshes provide superior solution accuracy. However, as the spatial frequency increases (larger α), the mesh size must become even smaller to maintain a good accuracy in the dispersive properties of the numerical scheme.

To ensure the Fourier transform of the finite difference scheme being a good approximation to the partial derivative over the range of wave numbers of interest, for example, waves with wavelengths longer than four Δx or $-\pi/2 \leq \alpha\Delta x \leq \pi/2$, it is required that a_j be chosen to minimize the integrated error, E , over the wavenumber range, where,

$$E = \int_{-\frac{\pi}{2}}^{\frac{\pi}{2}} |\alpha\Delta x - \bar{\alpha}\Delta x|^2 d(\alpha\Delta x) \quad (4.7)$$

On substituting (4.6) into (4.7) E may be written as,

$$E = \int_{-\frac{\pi}{2}}^{\frac{\pi}{2}} \left| i\alpha\Delta x - \sum_{j=-N}^M a_j e^{ij\alpha\Delta x} \right|^2 d(\alpha\Delta x) \quad (4.8)$$

The conditions for E to be a minimum are

$$\frac{\partial E}{\partial a_j} = 0, \quad j = -N \text{ to } M \quad (4.9)$$

With the obtained optimized coefficients from (4.9), the dispersion error of the difference approximation is small for a large range of wave numbers up to $\pi/2$.

Equation (4.9) provides $N + M$ linear algebraic equation by which the coefficients a_j can be determined. If N and M are not equal (i.e., the stencil is asymmetric), $\bar{\alpha}$ is

complex. Tam and Webb [1993] pointed out when such an asymmetric stencil is used over a large region it will generally lead to spatially growing wave solutions. For the case with $N = M$, $\bar{\alpha}$ is real. This will ensure a nondissipative difference scheme. In other words, the finite difference scheme tries to approximate the partial derivative by a Fourier sine series in the wave number space. For this reason, central differencing schemes have become popular for wave propagation application. However, asymmetric stencil may be employed in limited regions (such as at the boundary regions of the computation domain) without leading to accumulated numerical instability.

Now considering the case of $N = M = 3$ (i.e., seven-point stencil), expression (4.2) and (4.8) become

$$\frac{\partial f(x)}{\partial x} \cong \frac{1}{\Delta x} \sum_{j=-3}^3 a_j f(x + j\Delta x), \quad a_{-j} = -a_j \quad (4.10)$$

$$E = \int_{-\frac{\pi}{2}}^{\frac{\pi}{2}} \left| \alpha \Delta x - 2 \sum_{j=1}^3 a_j \sin(j\alpha \Delta x) \right|^2 d(\alpha \Delta x) \quad (4.11)$$

Expression means the finite difference scheme tries to approximate the partial derivative by a sine series in the wavenumber space. There are three coefficients a_1 , a_2 , and a_3 . It is possible to combine the truncated Taylor series method and the Fourier transform optimization method. One requires (4.10) to be accurate to order $O(\Delta x^4)$. This can be done by expanding the right-hand side of (4.10) as a Taylor series and then equating terms of order Δx and Δx^3 . This gives

$$a_2 = \frac{9}{20} - \frac{4}{5}a_1 \quad (4.12)$$

$$a_3 = -\frac{2}{15} + \frac{1}{5}a_1 \quad (4.13)$$

It can be seen that a coefficient, a_1 , is left as a free parameter. This parameter can be determined to minimize the error integral E of (4.11). Substituting (4.12) and (4.13) into (2.11), the value a_1 will be found by solving

$$\frac{\partial E}{\partial a_1} = 0. \quad (4.14)$$

Consequently, all coefficients can be obtained as follows

$$\begin{aligned} a_0 &= 0 \\ a_1 &= -a_{-1} = 0.79926643 \\ a_2 &= -a_{-2} = -0.18941314 \\ a_3 &= -a_{-3} = 0.02651995 \end{aligned} \quad (4.15)$$

Figure 4.1 shows the approximated wave number ($\bar{\alpha}\Delta x$) as a function of the exact wave number ($\alpha\Delta x$) for the optimized fourth-order DRP difference scheme over the interval 0 to π , using the above coefficients. For $\alpha\Delta x$ up to 1.45 the curve is nearly the same as the straight line $\bar{\alpha}\Delta x = \alpha\Delta x$. Thus the finite difference scheme can provide an adequate approximation to the partial derivative for waves with wave lengths longer than 4.5 mesh spacings. For $\alpha\Delta x$ greater than 2.0 the $\bar{\alpha}(\alpha)$ curve deviates completely from the straight line relationship. It clearly indicates that the wave propagation characteristics of the short wave components of the finite difference equations would be very different from those of the partial differential equations.

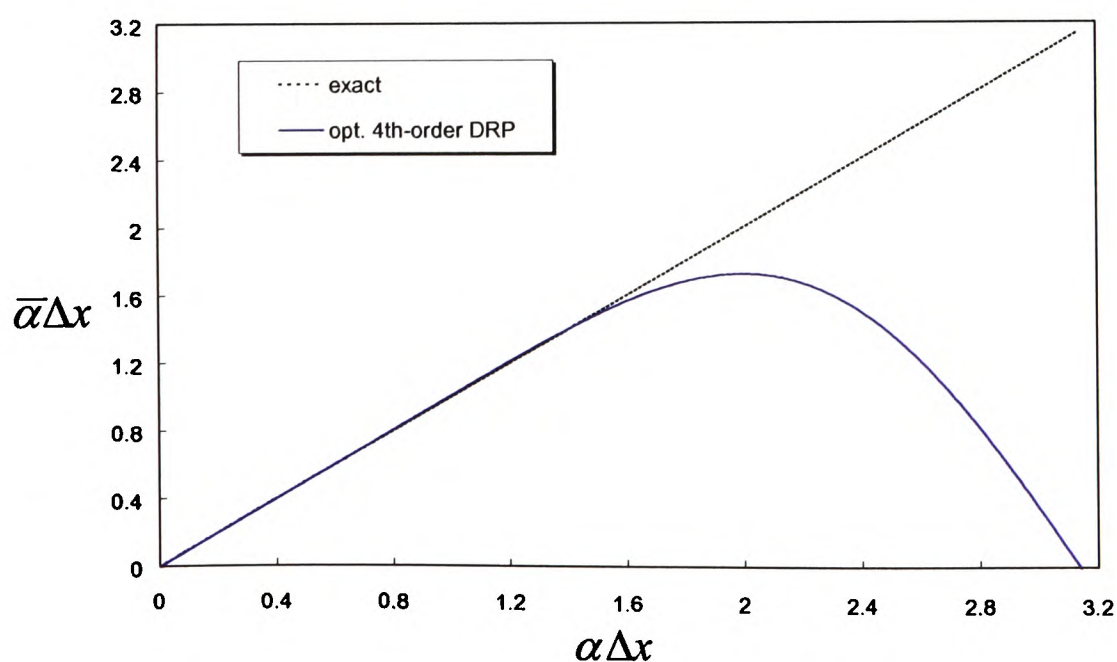


Fig. 4.1. $\bar{\alpha}\Delta x$ versus $\alpha\Delta x$ for the optimized 4th-order DRP difference scheme.

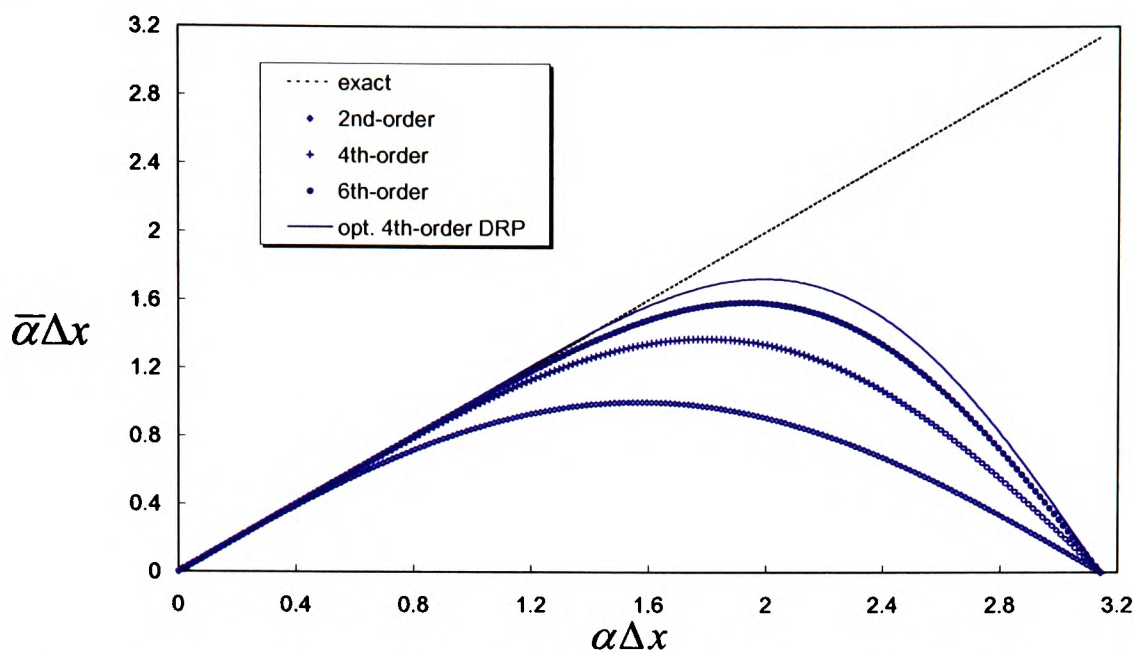


Fig. 4.2. Comparison of the optimized 4th-order DRP scheme with several standard central finite difference schemes

Figure 4.2. shows the comparison of the optimized DRP difference scheme with several standard central finite difference schemes in the terms of the relation of $\bar{\alpha}\Delta x$ versus $\alpha\Delta x$. Ideally, the curve should follow the straight line, $\bar{\alpha}\Delta x = \alpha\Delta x$. It is clear that the higher-order scheme maintains the linear relation for a much larger range of wave numbers. The curve for the standard sixth-order ($N = M = 3$, a seven-point stencil) central finite difference scheme starts to deviate from the straight line at $\alpha\Delta x = 1.0$. Correspondingly, the standard second-order (three-point stencil) and fourth-order (five-point stencil) schemes deviate from the straight line at $\alpha\Delta x = 0.4$ and $\alpha\Delta x = 0.75$, respectively. Compared with the sixth-order scheme, the curve of the optimized fourth-order DRP scheme deviate from the straight line at $\alpha\Delta x = 1.45$. Therefore, the optimized scheme significantly improves the resolution power of the computation at virtually no additional effort and computing time. Thus the use of a high order optimized scheme is necessary in problems involving high frequency (short wave length) waves.

We have discussed the selection and comparison of finite difference schemes by the relation curves of $\bar{\alpha}\Delta x$ versus $\alpha\Delta x$. Another way for selecting a finite difference scheme for the calculation of wave propagation is to compare their group velocity of finite difference schemes. Numerically, the group velocity of a finite difference scheme is determined by $d\bar{\alpha}/d\alpha$. The group velocity should be equal to 1 if the scheme is to

reproduce the same group velocity of the original partial differential equation. If group velocity of a finite difference scheme is considered, Tam [1997] provided the following a set of optimized coefficients through reducing the range of optimization (i.e., the range of the integral in equation (4.7)) for the fourth-order DRP scheme:

$$\begin{aligned}
 a_0 &= 0 \\
 a_1 &= -a_{-1} = 0.7708824 \\
 a_2 &= -a_{-2} = -0.1667059 \\
 a_3 &= -a_{-3} = 0.0208431
 \end{aligned}
 \tag{2.16}$$

Figure 4.3. shows a comparison of the group velocity of the optimized four-order DRP scheme with the sixth-order standard central difference scheme as a function of $\alpha\Delta x$. Clearly, for the optimized DRP scheme, the increase in group velocity (i.e., $d\bar{\alpha}/d\alpha$) near to $\alpha\Delta x = 0.7$ is around 0.3%. The standard sixth-order scheme can resolve waves up to $\alpha\Delta x = 0.6$. There is therefore, an obvious advantage in using the DRP scheme.

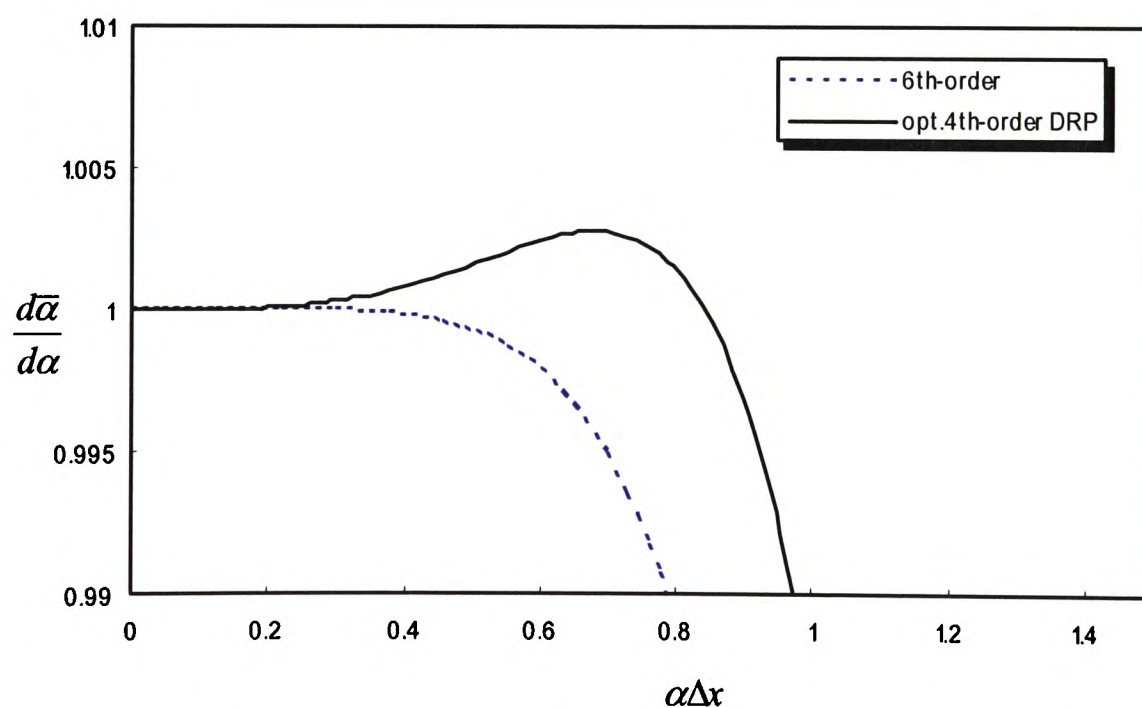


Fig. 4.3. Comparison of group velocity of the DRP scheme with the 6th-order standard central difference scheme

If one wishes to resolve short waves using a fixed mesh size, schemes with large stencil need to be employed. As mentioned previously, large stencil will increase greatly computational costs and difficulties in the treatment of boundary conditions at solid

boundaries. After comprehensively consideration, DRP scheme with seven-point stencil is one of the most widely used schemes for the spatial discretization.

4.2.2 Optimized multi-level time discretization

The acoustic equations (i.e., Eq.(2.87) and (2.88)) provide the time derivatives of the perturbation variables. Suppose $f(x, y, z)$ and df/dt are known at time levels $n, n-1, n-2$ and $n-3$. To advance to the next time, one can use the following 4-level explicit time marching scheme

$$f^{(n+1)} = f^{(n)} + \Delta t \sum_{j=0}^3 b_j \left(\frac{df}{dt} \right)^{(n-j)} \quad (4.17)$$

where superscripts denote the time level on a uniform mesh with time step Δt .

The last term on the right side of (4.17) may be regarded as a weighted average of the time derivatives at the last four mesh points. There are four coefficients, i.e., b_0, b_1, b_2 and b_3 that are to be selected. To ensure the scheme is consistent, three of the four coefficients are chosen so that the term in (4.17) are expanded in a Taylor series with respect to Δt to match to $O(\Delta t^3)$. This leaves one free parameter, b_0 , and relation with the other coefficients are [Tam & Webb, 1993; Tam, 1997]:

$$b_1 = -3b_0 + \frac{53}{12}, \quad b_2 = 3b_0 - \frac{16}{3}, \quad b_3 = -b_0 + \frac{23}{12}, \quad (4.18)$$

The remaining coefficient b_0 is determined by requiring the Laplace transform of the finite difference scheme to be a good approximation to that of the partial derivative. The Laplace transform and its inverse of a function $g(t)$ are related by

$$\tilde{g}(\omega) = \frac{1}{2\pi} \int_0^{\infty} g(t) e^{i\omega t} dt \quad (4.19)$$

$$g(t) = \int_{\Gamma} \tilde{g}(\omega) e^{-i\omega t} d\omega \quad (4.20)$$

The inverse contour Γ is a line in the upper half ω -plane parallel to the real- ω -axis above all poles and singularities. The generalized expression of (4.17) to one with a continuous variable can be written as

$$f(t + \Delta t) = f(t) + \Delta t \sum_{j=0}^3 b_j \frac{\partial(t - j\Delta t)}{\partial t} \quad (4.21)$$

It is easy to obtain (4.17) by setting $t = n\Delta t$. On applying Laplace transform to the left and right sides of (4.21), it is found

$$\tilde{f} e^{-i\omega\Delta t} = \tilde{f} + \Delta t \sum_{j=0}^3 b_j e^{i\omega j\Delta t} \frac{\partial \tilde{f}}{\partial t} \quad (4.22)$$

Thus

$$-i \frac{i(e^{-i\omega\Delta t} - 1)}{\Delta t \sum_{j=0}^3 b_j e^{i\omega j\Delta t}} \tilde{f} = \frac{\partial \tilde{f}}{\partial t} \quad (4.23)$$

However, the Laplace transform of the time derivative of f , i.e., the right side of (4.23) is equal to $-i\omega \tilde{f}$. By comparing the two sides of (4.23), the quantity

$$\bar{\omega} = \frac{i(e^{-i\omega\Delta t} - 1)}{\Delta t \sum_{j=0}^3 b_j e^{i\omega j\Delta t}} \quad (4.24)$$

is the effective angular frequency of the time marching scheme (4.17). The weighted error E_1 incurred by using $\bar{\omega}$ to approximate ω will be defined as

$$E_1 = \int_{-\zeta}^{\zeta} \left\{ \sigma [\operatorname{Re}(\bar{\omega}\Delta t - \omega\Delta t)]^2 + (1 - \sigma) [\operatorname{Im}(\bar{\omega}\Delta t - \omega\Delta t)]^2 \right\} d(\omega\Delta t) \quad (4.25)$$

where $\operatorname{Re}(\)$ and $\operatorname{Im}(\)$ are the real and imaginary part of $(\)$. σ is the weight and ζ is the frequency range we expect $\bar{\omega}$ to be a good approximation of ω . On substituting (4.24) and (4.18) into (4.25), E_1 becomes a function of b_0 . b_0 can be determined by solving the following equation so that E_1 is minimum, i.e.,

$$\frac{dE_1}{db_0} = 0 \quad (4.26)$$

On considering the range of useful frequency and numerical damping rate, Tam and Webb [1993] selected $\sigma = 0.36$ and $\zeta = 0.5$. Then the recommended values of the coefficients b_j ($j = 0, 1, 2, 3$) are

$$\begin{aligned} b_0 &= 2.3025581, & b_1 &= -2.4910076 \\ b_2 &= 1.5743409, & b_3 &= -0.3858914 \end{aligned} \quad (4.27)$$

For a given value of $\bar{\omega}\Delta t$, equation (4.24) yields four roots of $\omega\Delta t$. In order to make the scheme numerically stable, all of the roots must have a negative imaginary part. By choosing a sufficient small Δt , the scheme becomes stable. A detailed discussion of the numerical stability of the DRP scheme is provided by Tam and Webb [1993].

4.2.3 Artificial selected damping

In the process of a numerical solution there are inevitably some short waves which cannot be resolved properly on the used mesh. These short waves will excite dispersive and parasite waves in the discretisation schemes, and contaminate computational results. To obtain a high-quality numerical solution, it is imperative that they be automatically removed from the computation as soon as they are generated. This can be done by introducing artificial selective damping into the finite difference equations. Tam et al. [1993] described

a way to tailor the damping terms specifically for eliminating only the short waves but not effectively affecting the long waves ($\alpha\Delta x < 1.0$). The artificial damping term, as designed by Tam et al. [1993], is added into the right-hand side of the first momentum equation (2.87), has the form (the spatial derivatives are discretized using the seven-point stencil DRP scheme):

$$D_l = -\frac{\nu_{art}}{(\Delta x)^2} \sum_{j=-3}^3 d_j u_{l+j} \quad (4.28)$$

where ν_{art} is the artificial viscosity which may select a value between 0 and 1, u_l is the velocity component in the x -direction at node l of the mesh, and d_j is coefficients. Obviously, the sum implies the neighbouring nodes j along x -direction are involved.

Similarly, taking the Fourier transform of the two side of the momentum equation the damping shows a variation with wavenumber. One may choose appropriately the coefficients d_j so that the damping term does not affect the long waves and efficiently remove the short waves. Tam et al [1993] recommended a set of coefficients for the damping term combining the seven-point optimized DRP scheme

$$\begin{aligned} d_0 &= 0.2873928425, & d_1 &= d_{-1} = -0.2261469518 \\ d_2 &= d_{-2} = 0.1063035788, & d_3 &= d_{-3} = -0.0238530482. \end{aligned} \quad (4.29)$$

4.2.4 Solid wall boundary treatment

In the calculations of aeroacoustic problems various geometrical configurations often occur in the flow field and acoustic field, and wall surfaces are generally curved. In CFD, an often used approach is to map the physical domain into a rectangular computational domain with the curved surface being mapped into a plane boundary. However, this practice is not always possible for complex geometries, especially for three-dimensional cases. Currently, unstructured mesh techniques may be developed, and applied to complex geometry flows. However, mapping or the use of unstructured meshes inevitably introduces inhomogeneities into the acoustic governing equations. Such inhomogeneities could cause

unintended acoustic refraction and scattering [Tam, 1995]. An alternative way is to retain a Cartesian mesh and to develop special treatments for curved wall surfaces. A stepwise treatment of curved surface is the most common and widely used currently, and boundary velocity components perpendicular to the wall are set to zero. The optimized DRP finite difference scheme and many other optimized high-order schemes are implemented on non-staggered meshes. The non-staggered mesh leads to the need of defining ‘ghost points’ into the solid body in order to satisfy both the boundary conditions and the differential equations at the solid wall [Tam & Dong, 1994]. For the pressure variable, Tam and Dong [1994] suggested the use of one layer of non-physical nodes behind the solid wall, and their values are determined from the boundary condition of zero pressure gradient at the wall. At the same time, for the pressure nodes on the wall surface the usual differential equation involving pressure (e.g., Eq.(2.87)) is solve.

Symmetrical differencing stencils as those described above cannot be used near boundaries. Instead, asymmetrical schemes with DRP properties have been derived and implemented in two dimensional calculations (e.g., Tam, [1997]; Tam & Dong, [1994]).

4.3 Staggered DRP-type scheme

It is well-known that there are two discretization schemes to approximate the first-order derivatives, i.e., the non-staggered mesh (collocated mesh) and the staggered mesh. The staggered mesh based methods have been used earlier to overcome *pressure checkerboard effect* and the difficulties with *pressure-velocity coupling* as well as the occurrence of oscillations in the pressure for incompressible flow computation in the development of CFD (e.g., see Patankar, [1980]).

The optimized seven-point stencil fourth-order finite difference DRP scheme described above is one of the most popular numerical schemes used currently in computational aeroacoustics. However, DRP schemes were developed by Tam and Webb [1993] for the non-staggered equally spaced meshes. As pointed out in Section 4.2.4, the treatment of solid wall boundary conditions needs introducing ‘ghost points’ when the DRP scheme on a non-staggered mesh. The ‘ghost points’ outside the computational domain are not of obvious physical meaning although they can be used. Spurious numerical reflecting waves probably are caused which affect computed results. Furthermore, in three

dimensional cases the ‘ghosts points’ become inconvenient to handle when irregular body-surfaces are present. Apart from a map of the surfaces, a record of the type of difference equation to be used with each ghost point is needed, as well as records of the non-symmetric difference schemes for points next to the solid wall boundary. All these will more or less affect the computational efficiency and numerical accuracy of code. The staggered-type finite difference methods may simplify the solid wall boundary treatments and improve further the numerical accuracy.

In the present work of this thesis, a DRP finite difference scheme for a staggered mesh in space and time, extended by Djambazov et al. [2000b] following the idea of Tam and Webb’s DRP scheme, is implemented to solve the acoustic perturbation equations (i.e., Eq.(2.87) and Eq(2.88)) for the acoustic perturbations. In the following Sections, we will describe the fully staggered-type DRP finite difference scheme.

4.3. 1 Arrangement of variables on a fully staggered mesh

In Chapter 3, for the cell-centred finite volume based method all solved variables are stored in the cell centres of the computational mesh. For a non-staggered-type finite difference method all solved variables are defined at nodes of the Cartesian mesh. However, for the spatial discretization of the partial differential equations by a finite difference scheme on a staggered mesh, the solved physical variables are not stored at the same locations on the computational mesh. Generally speaking, the pressure and velocity components are stored at different locations. If variables are only spatially staggered arrangement, the velocity field components are located at the centres of the mesh edges, while other physical variables (e.g., pressure and density) are located the mesh cell’s centres, and time marching and variables storing are at the same time step. If variables are spatially and temporally staggered arrangement, pressure field is computed at $n\Delta t$ and velocity field is computed at $(n \pm 1/2)\Delta t$. We call this type of staggered arrangement as a fully staggered arrangement. Figure 4.4 shows a schematic representation of the arrangement of fully staggered variables on a Cartesian mesh for a two dimensional case.

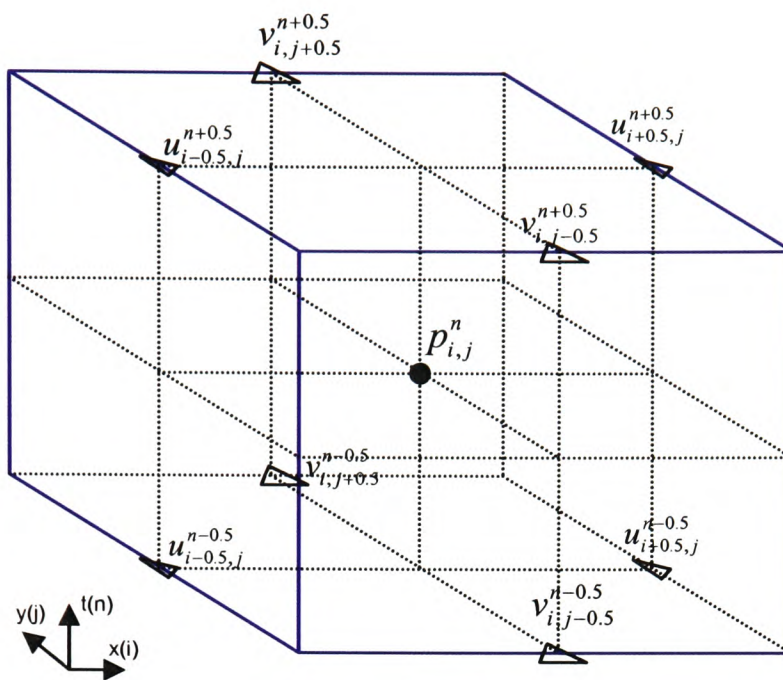


Fig. 4.4. Locations of variables for a fully staggered mesh scheme for a 2-D case

Generally speaking, the pressure and velocity components stored at different locations. If variables are only spatial staggered arrangement, the velocity field components are located at the centres of the mesh edges, while other physical variables (e.g., pressure and density) are located the mesh cell's centres, and time marching and storing variables are at the same time step. If variables are spatial and temporal staggered arrangement, pressure fields are computed at $n\Delta t$ and velocity field is computed at $(n \pm 1/2)\Delta t$. We call this type of staggered arrangement as a fully staggered variables arrangement. Figure 4.4 shows a schematic representation of the arrangement of fully staggered variables on a Cartesian mesh for a two dimensional case.

4.3.2 Staggered spatial discretization

For hyperbolic equations, such as Eq.(2.87) and Eq.(2.88), a staggered form of the leap-frog method may be used, see [Morton & Mayers, 1994]. Unfortunately, the staggered-type leap-frog scheme is only second-order accurate, which is not sufficient for computational aeroacoustics. In the numerical discretization, the velocity components are also stored in the middle of the time steps, as show in the Figure 4.4. To increase the numerical accuracy of the scheme, as in the DRP scheme, larger computational stencil is considered.

Similarly, only uniform Cartesian mesh is considered, i.e., the x-axis be divided into a regular mesh with spacing Δx . The approximation of the first-order spatial derivatives on a staggered mesh has the following form

$$\frac{\partial f}{\partial x} \approx \frac{1}{\Delta x} \sum_{j=-(N-1)}^N a_j f \left[x + \left(j - \frac{1}{2} \right) \Delta x \right] \quad (4.30)$$

where $2N$ determines the length of the stencil due to the staggered mesh. Note that the acoustic perturbation equations (i.e., Eq.(2.87) and Eq.(2.88)) contain the first-order derivative of pressure and the first-order derivatives of velocity components. The above expression is for pressure derivative. Since the locations of pressure and velocity components are different, the range of the above summation needs to make a corresponding change. For example, if the approximation of the first-order derivative of velocity component in x-axis, then j will start at $-N$ and end at $N-1$.

Similarly, the approximation of the first-order derivative takes $N=3$, i.e., the six-point stencil is considered. Similar to developing DRP schemes on a non-staggered mesh, Fourier transform is applied to expression (4.30), and considering $a_{1-j} = -a_j$, the effective wave number of the staggered-type finite difference scheme becomes

$$\bar{\alpha} \Delta x = 2 \sum_{j=1}^3 a_j \sin \left[\left(j - \frac{1}{2} \right) \alpha \Delta x \right] \quad (4.31)$$

To assure that the Fourier transform of the finite difference scheme is a good approximation of that of the partial derivative over a wider range of wavenumbers, one of coefficients a_j is left to be used to minimize the following integral error (or other relations)

$$E = \int_{-\beta\pi}^{\beta\pi} \left[\alpha \Delta x - 2 \sum_{j=1}^3 a_j \sin \left(\left(j - \frac{1}{2} \right) \alpha \Delta x \right) \right]^2 d(\alpha \Delta x) \quad (4.32)$$

A set of coefficients in terms of a_1 , by requiring the scheme, expression (4.30), provides fourth-order accuracy with respect to Δx , are obtained as follows

$$\begin{aligned} a_2 &= \frac{1}{2} \left(\frac{25}{24} - a_1 \right) \\ a_3 &= \frac{1}{10} \left(a_1 - \frac{9}{8} \right) \end{aligned} \quad (4.33)$$

Following Djambazov et al. [2000b], an optimal value can be found for the remaining coefficient a_1 by minimizing the approximation error of the numerical scheme with respect to a sinusoidal wave function. The sinusoidal wave function may be chosen as follows:

$$f(x) = c_0 + c_1 \sin(kx) + c_2 \cos(kx) \quad (4.34)$$

where c_0 , c_1 , c_2 are constants. Requiring the difference scheme to be exact for the expression (4.34), a parametric equation for a_1 can be obtained by using

$$\left(s_1 - \frac{1}{2}s_3 + \frac{1}{10}s_5 \right) a_1 = \theta - \frac{25}{48}s_3 + \frac{9}{80}s_5 \quad (4.35)$$

where $s_1 = \sin \theta$, $s_2 = \sin(3\theta)$, and $s_5 = \sin(5\theta)$. Here θ is a parameter, k is the wave number and $\theta = k(\Delta x/2) = \pi/N_w$. N_w is the number of points per wavelength for this particular frequency.

The range of values that the coefficient a_1 can take is shown in Figure 4.5. With the increase of the number of points per wavelength, the value of a_1 becomes less sensitive and tends to the value corresponding to sixth order of approximation. Figure 4.5 shows that there is no ideal value for the unknown coefficient a_1 . The optimum value of a_1 will depend on the spectrum of the computed acoustic field. Since practical aeroacoustic problems involve often multi-frequency, the point number per wavelength should not be less than 16 points for the dominant frequencies so that a good resolution in the acoustic field can be reached.

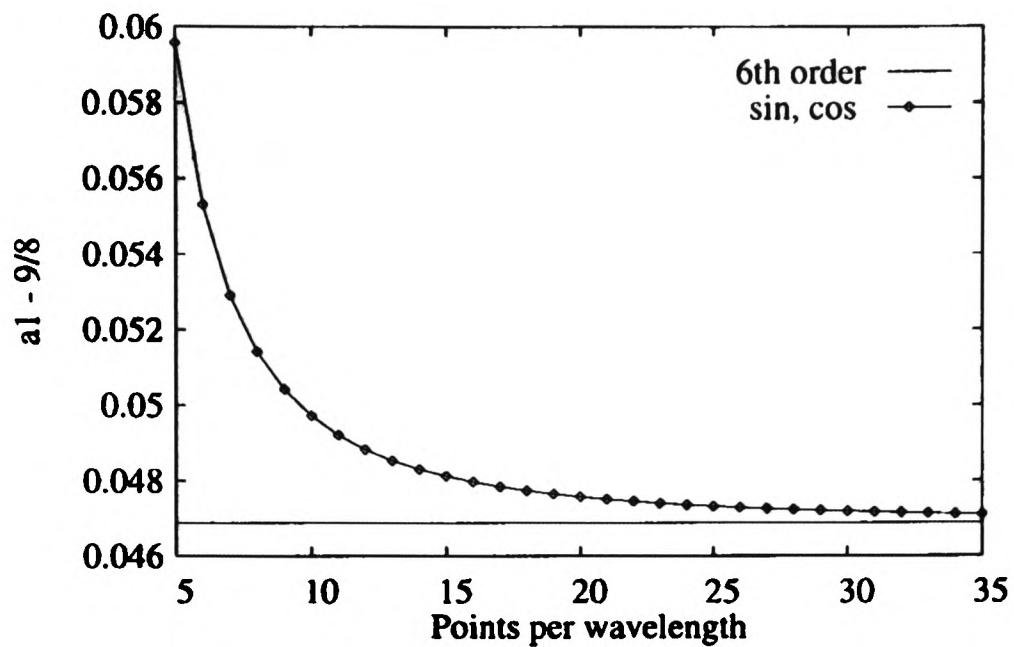


Fig. 4.5. Solution of the parametric equation for the staggered scheme coefficient a_1

If sixteen points per wavelength is chosen, an average value of $(a_1 - 9/8) = 0.048$ can be determined from Figure 4.5. On having obtained the value of a_1 , other five optimized coefficients of the staggered-type DRP scheme are correspondingly determined as follows

$$\begin{aligned}
 a_0 &= -a_1 = -1.173 \\
 a_{-1} &= -a_2 = 0.0656667 \\
 a_{-2} &= -a_3 = -0.0048
 \end{aligned}
 \tag{4.36}$$

A comparison of the non-staggered optimized fourth-order DRP scheme with the staggered-type fourth-order DRP scheme is given in Figure 4.6. The optimized coefficients in (4.15) and (4.36) are used for the plotting. Figure 4.6 illustrates clearly the difference between the non-staggered mesh based scheme and the staggered mesh based scheme. For the non-staggered mesh based scheme, two different physical wave numbers may have the same numerical wave number. This implies that parasite waves can exist in the computation. In contrast the phenomenon does not occur in the staggered mesh based scheme. Hence, a better numerical accuracy and stability can be obtained in the use of a staggered mesh based scheme.

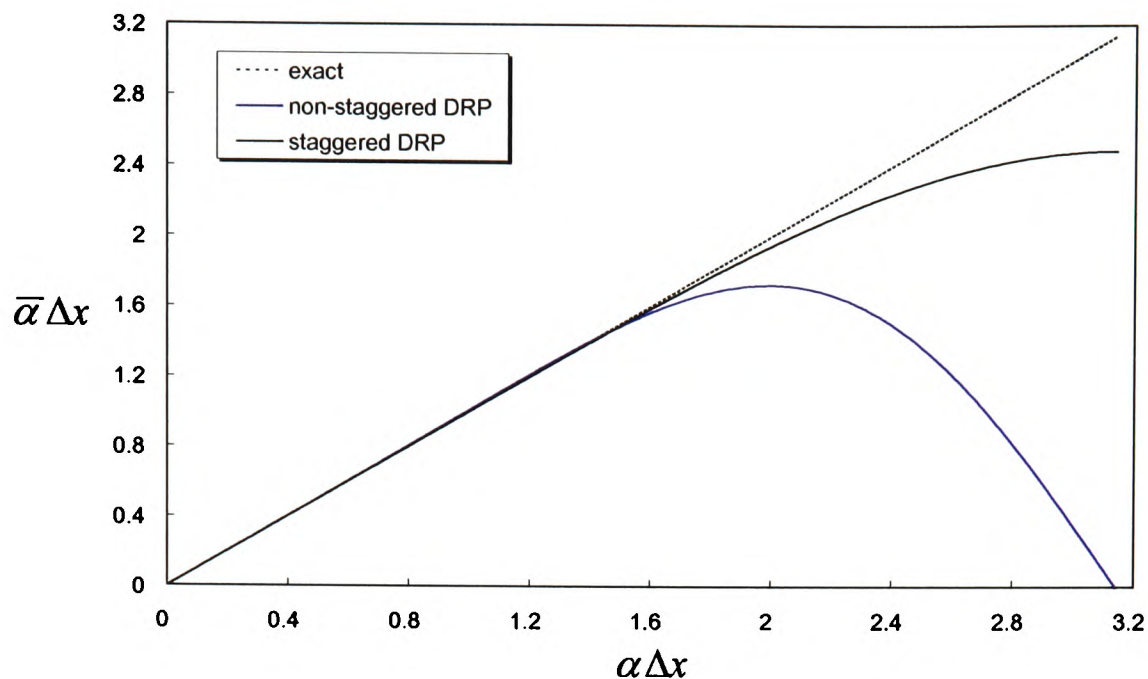


Fig. 4.6. Comparison of the non-staggered optimized 4th-order DRP scheme with the staggered optimized 4th-order DRP scheme

It should be noted that the six-point stencil staggered-type optimized DRP scheme is used only for the discretization of the propagation terms of Eq.(2.86) and Eq.(2.87), i.e., $(\bar{\rho}c^2)\partial v'_j/\partial x_j$ and $(1/\bar{\rho})\partial p'/\partial x_i$ in the present work. The discretization of the convection terms is still done using the non-staggered mesh based DRP scheme. In addition, as discussed in Section 4.2.3, artificial selective damping term may be used to remove the undesirable short waves. It here is not repeated any more.

4.3.3 Time integration of the staggered-type scheme

With the time staggering of the velocity components the propagation terms of Eq.(2.87) and Eq.(2.88), $(\bar{\rho}c^2)\partial v'_j/\partial x_j$ and $(1/\bar{\rho})\partial p'/\partial x_i$, are evaluated at the middle of each time step. The following approximate temporal integration suggested by Djambazov et al. [2000b] is applied to the time marching of numerical calculation.

$$\int_{t-\Delta t/2}^{t+\Delta t/2} f(t)dt = \Delta t \sum_{n=0}^3 b_n f(t-n\Delta t) \quad (4.37)$$

This is also an explicit multi-level time discretization. Similarly, requiring this expression to be exact up to second order provides the following set of the unknown coefficients b_n in terms of b_0 :

$$b_1 = \frac{1}{24} - 3(b_0 - 1), \quad b_2 = 3(b_0 - 1) - \frac{1}{12}, \quad b_3 = \frac{1}{24} - (b_0 - 1) \quad (4.38)$$

Again an optimal way may be performed with respect to an accurate representation of the wave function to obtain the value of b_0 . Because this stencil is not symmetric, the sinusoidal function (4.34) cannot be represented exactly, and a compromise has to be made so that the error is as small as possible. This can be achieved by using a simple least square fitting procedure between the solutions of the two parametric equations obtained separately with the sine and the cosine term of (4.34). The sine and cosine terms are assumed to have equal amplitudes in a real sound signal in minimizing the error of the scheme. The result of this fit is plotted in Figure 4.7.

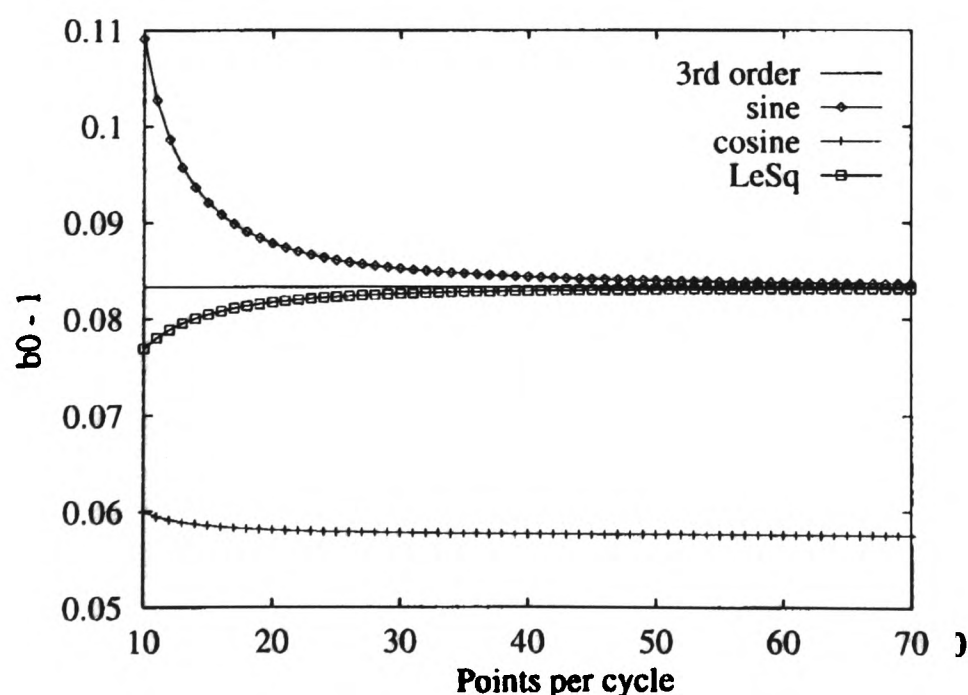


Fig. 4.7. Parametric solutions for the temporal integration coefficient b_0

Because of the requirement of numerical stability for explicit time integration, most applications are likely to have not less than 20 points per cycle, and the third order of approximation, $(b_0 - 1) = 1/12$ may be assumed.

The spatial discretization and temporal integration using the staggered mesh based finite difference scheme implemented in the present work are described. The boundary conditions (solid wall boundary condition and radiation boundary condition) will be discussed in the sections below.

4.3.4 Solid wall boundary conditions

Since the acoustic equations (i.e., Eq.(2.87) and Eq.(2.88)) do not take in account viscous effects, solid walls can be modelled by symmetry planes. That is to say that the velocity component perpendicular to the wall is zero, and that the normal derivatives of pressure and of the other two velocity components are also equal to zero at the solid wall boundary.

Although geometrical configurations of numerical examples considered in the present work are of straight-line wall boundaries, curvature wall surfaces cannot be avoided in practical engineering problems. When solid bodies with curvature wall surfaces exist in computational domain a stepwise manner may be adopted to discretize the curvature wall surfaces. The centres of mesh cells inside the curvature wall are considered as internal cells; they are declared blocked and are not processed. The solid walls are considered to be comprised of cell faces, and the corresponding velocity components at these faces (with the staggered mesh that are always components perpendicular to the faces) are set to zero.

In order to retain the same numerical accuracy at the solid wall boundaries as that at the internal mesh points, the following *mirroring procedure* may be applied to every solid wall boundary face: symmetry of pressure and parallel velocity values and antisymmetry of perpendicular velocity values. In the implementation every cell-centred value of pressure is accessed via a function call rather than directly addressing the storage array. Special integer arrays hold the information about the cell faces that belong to solid wall boundaries, and they are checked every time when a neighbouring pressure value is required.

Successive pressure values along a given coordinate axis are required to compute the spatial derivatives (see (4.30) and (4.1)). Two arrays, each of three elements, have to be defined: one to the left and one to the right of a given centre point or face, respectively. Starting from the centre specified outward, the pressure values are copied into the auxiliary three-element arrays. If a solid wall face is encountered, the advancing direction is reversed. This provides a mirror image of the points in front of the wall for the missing points behind

the wall, which is equivalent to setting zero normal derivatives with both differencing schemes (4.31) and (4.1) at the wall

For the mirroring of the velocity components perpendicular to the wall, a similar procedure has been implemented. The only difference is that the sign of the copied elements is reversed together with the advance direction every time a wall is found.

The above mirroring approach makes the solid boundary treatment of the high-order finite difference schemes as simple as implementing a finite volume method. It is only possible with staggered storage of the pressure and the velocity components.

4.3.5 Radiation boundary conditions

Many interesting acoustic problems are exterior problems. In order to simulate this class of problems it is necessary to impose radiation boundary conditions at the boundaries of the finite acoustic computational domain. Meanwhile, to ensure that the computed solutions are of high quality the boundary conditions must be sufficiently transparent to the outgoing disturbances so that they leave the domain without significant reflections. Since the acoustic perturbation equations support acoustic waves, a set of two dimensional radiation boundary conditions compatible with the DRP based on the asymptotic solution of the linearized Euler equations has been developed by Tam and Webb [1993]. They involve optimised backward finite differences using 7-point stencil close to the outer boundaries of the domain. However, their implementations are relatively tedious in the code programming. Here a less accurate but much simpler set of acoustic radiation boundary conditions proposed by Djambazov [1998b] is used for the present acoustic calculations. Recent advances in the development of accurate and efficient numerical boundary conditions for aeroacoustic problems can be found in some review articles (e.g., Tam, [1998]).

If a regular computational domain (rectangular box) is considered, and the domain is assumed to contain all acoustic sources inside the domain (box), the acoustic waves leaving the box may be considered locally (over each cell) as *plane* waves.

Now considering the following set of perturbation equations (similar to the equations without the right-hand side acoustic source terms):

$$\begin{aligned}\frac{\partial p}{\partial t} + \bar{v}_j \frac{\partial p}{\partial x_j} + c \frac{\partial v_j}{\partial x_j} &= 0 \\ \frac{\partial v_i}{\partial t} + \bar{v}_j \frac{\partial v_i}{\partial x_j} + c \frac{\partial p}{\partial x_i} &= 0\end{aligned}\tag{4.39}$$

Note that the primes for perturbations have been removed in Eq.(4.39). In the presence of a *uniform* mean flow with velocity components (i.e., $\bar{v}_1, \bar{v}_2, \bar{v}_3$), the general solution of these equations for a plane wave normal to the direction $(\cos\theta_1, \cos\theta_2, \cos\theta_3)$ is

$$\begin{aligned}p &= f[(x_1 - \bar{v}_1 t)\cos\theta_1 + (x_2 - \bar{v}_2 t)\cos\theta_2 + (x_3 - \bar{v}_3 t)\cos\theta_3 - ct] \\ &= f[x_j \cos\theta_j - (\bar{v}_j \cos\theta_j + c)t] \\ v_1 &= p \cos\theta_1, \quad v_2 = p \cos\theta_2, \quad v_3 = p \cos\theta_3, \quad \cos^2\theta_1 + \cos^2\theta_2 + \cos^2\theta_3 = 1\end{aligned}\tag{4.40}$$

with f presenting any function of the argument in brackets. This can be verified by substituting (4.40) into Eq.(4.39).

According to Djambazov [1998b], the solution (4.40) may be used to define a boundary radiation formula based on interpolation from inside the domain at the previous time step. Considering a local frame of reference with origin at a given boundary node $(x_j = 0, j = 1, 2, 3)$ at the old time level $(t = 0)$ and a plane wavefront that intersects the x_i axis at the origin at time $t = \Delta t$, the ‘old’ intersection (at $t = 0$) can be found of the same wavefront with the same axis x_i , and it will have coordinates $x_j = 0, j \neq i$ and $x_j \neq 0, j = i$. Since f is any function, it can be assumed that the wavefront that is being traced has an argument of zero. Thus the equation for the internal intersection point becomes

$$x_i = \frac{(\bar{v}_j \cos\theta_j + c)\Delta t}{\cos\theta_i}\tag{4.41}$$

The boundary value at time $t = \Delta t$ can be determined utilizing a simple one dimensional interpolation along the x_i axis from the ‘old’ values at time $t = 0$ with the interpolation point defined by (4.41).

In order to use consistent computational stencil for the spatial derivatives inside the domain and near the outer boundaries, three layers of interpolated nodes are needed. With the present implementation second order interpolation is used

$$f(x) = f_0 + \frac{x}{2\Delta x} \left[f_R - f_L + \frac{x}{\Delta x} (f_L + f_R - 2f_0) \right] \quad (4.42)$$

where $f_L = f(-\Delta x)$, $f_0 = f(0)$, and $f_R = f(\Delta x)$. According to Djambazov [1998b], small false reflections (less than 2% of the amplitude of the plane waves perpendicular to the boundaries) may be observed. For longer time calculations, a full implementation is needed with asymmetrical differencing stencils (e.g., backward differences) at boundaries and only layer of interpolation boundary nodes are taken into account.

It should be pointed out that the direction of the plane waves specified by $\cos\theta_j$ is problem-dependent, and has to be specified by the analyst for each boundary cell. After calculating the cosine values and the resultant interpolation coordinates on the basis of ‘source points’ (origins of spherical waves), complex wave patterns resulting from interference of primary and reflected (by complex configurations) waves can be taken into account. In simplified calculations, the same set of source coordinates may be assigned to all boundary cells. For some cases in which the direction of the plane waves leaving the domain at a given boundary point varies with time in a periodic manner, one may specify an average direction of radiation on an intuitive basis. This is usually accompanied by enlarging the computational domain so that the deviation from the average direction becomes smaller. However, this will lead to the increase in computation cost.

4.4 Validation examples

One- and two-dimensional numerical examples are considered in this section to test the programming code based on the above described acoustic numerical algorithm associated with the treatment of boundary conditions.

A simple example of the wave propagation of a one-dimensional acoustic pulse is first examined with emphasis on the numerical accuracy, including the effect of point number per wavelength and the time step size on computational results. The initial pressure pulse with a peak at the origin, a known acoustic source, generates two acoustic waves, which propagate towards opposite two directions along x-axis. The spatial distribution pressure pulse takes the following function expression:

$$p(x) = \begin{cases} A \left(1 + \cos 2\pi \frac{x}{\lambda} \right), & |x| < \frac{\lambda}{2} \\ 0, & |x| \geq \frac{\lambda}{2} \end{cases} \quad (4.43)$$

where A is the amplitude of the pressure pulse, λ is the wavelength of the pressure pulse. In the present calculation, $A=100(pa)$ and $\lambda=1.0(m)$ are used. The exact solution for this problem is as follows

$$p(x,t) = p(x-ct) + p(x+ct) \quad (4.44)$$

where c is the propagation speed of the pulse, i.e., ambient sound speed. In the present calculation, a symmetry condition is applied at the origin so that only the right-travelling wave is simulated.

From the computational point of view, obtaining a good resolution for the wave propagation and, at the same time, keeping small as possible computational mesh points in the computational domain is very important for reducing the computational time and memory. The effect of the point-number per wavelength on the numerical accuracy of the propagation of the acoustic wave is investigated. Three mesh spacing sizes are tested. They correspond to ten points, twenty points and forty points per wavelength, respectively. In the calculations the time step is taken to be $14.6875\mu s$. Figure 4.8 shows the effect of the point-number per wavelength on numerical accuracy in terms of the maximum absolute difference between the computed and exact solutions at six space locations. For the last location the wave has propagated over thirty wavelengths.

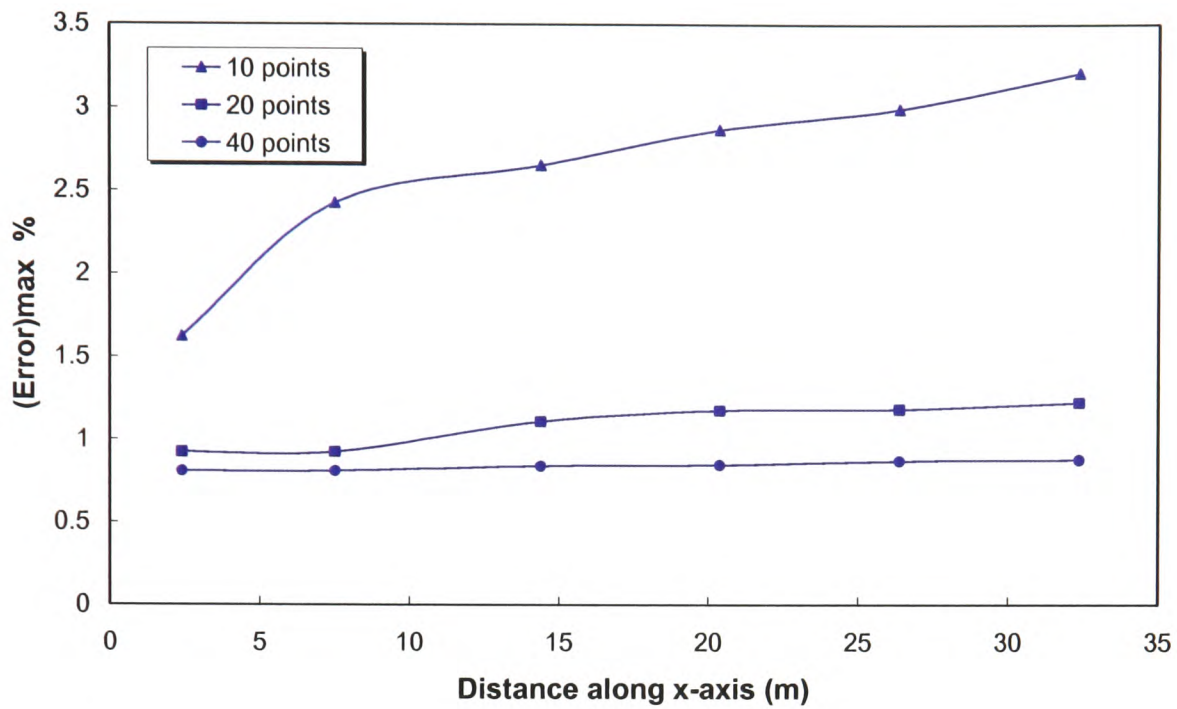


Fig. 4.8. Effect of the point number per wavelength on numerical accuracy

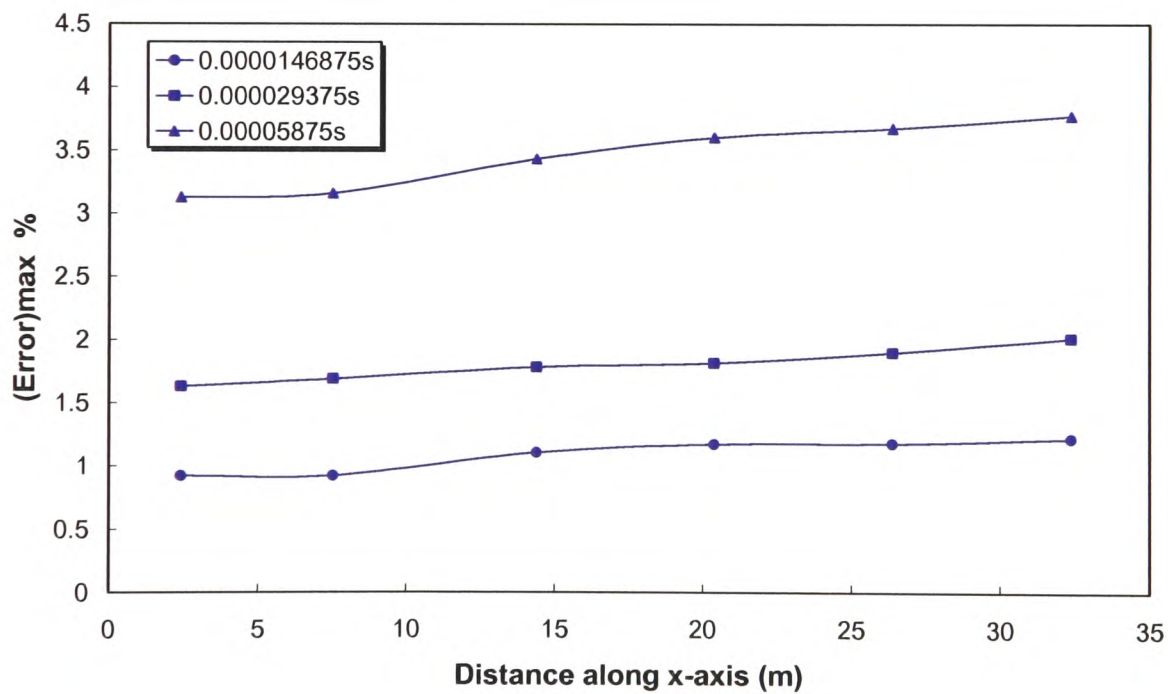


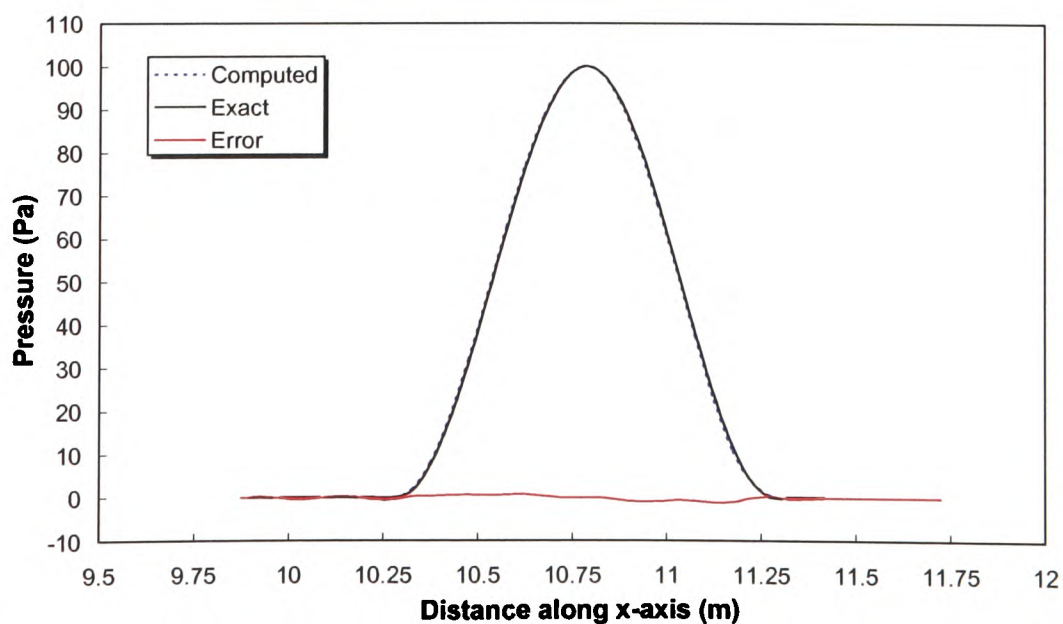
Fig.4.9. Effect of the size of time step on computational results

It can be seen that ten points per wavelength gives rise to relatively large numerical error. In other words, ten points per wavelength in the acoustic calculation can not meet the requirement of resolution for the propagating wave. When the point-number per wavelength is greater than twenty, the maximum errors are less than 1.5 percent within the propagating

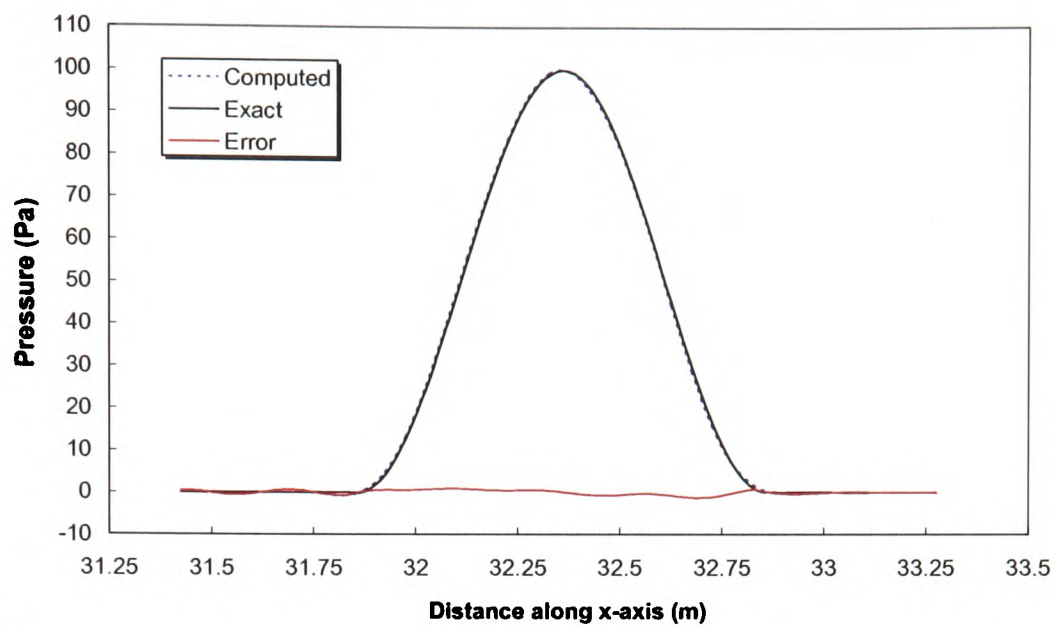
distance of thirty-five wavelengths. Moreover, the increase of the error is not obvious when the point-number per wavelength reaches forty. Multi-frequency often occurs in the calculation of the propagation of waves in practical engineering aeroacoustic problems. Hence, the point-number per wavelength should not less than 20 points for the highest of the resolved frequencies.

Time step needs to meet not only the requirement of resolution for the dominant frequency in the acoustic field but also the requirement of numerical stability. It can easily expect that smaller time step will result in more accurate computational results. However, too small time step will lead unnecessarily to longer computational time when calculation involves a long propagation distance. Effect of time step on the maximum numerical error is presented in Figure 4.9. In the calculations the mesh size is $\Delta x = 0.05m$, i.e., point-number per wavelength equals to twenty. For the three time steps, the Courant numbers are approximately corresponding to 0.1, 0.2, and 0.4, respectively.

Figure 4.10 shows a comparison of computed solution with exact solution at two locations for the wave propagation when $\Delta x = 0.05m$, $\Delta t = 14.6875\mu s$ (corresponding Courant number is 0.4) are used. From Figure 4.10, computed solutions agree well with exact solutions in amplitude and phase. In fact, a series of tests with the wave propagation calculation of this one-dimensional acoustic pulse have been carried out. A good numerical accuracy can be obtained after comprehensively taking into account the point-number per wavelength and time step as well as its courant number. Generally, the Courant number is chosen less than 0.5 for the in calculations in this thesis.



a)



b)

Fig.4.10. Comparison of computed solution with exact solution at two propagating locations

In order to test the radiation boundary conditions described in Section 4.4, the wave propagation of a two-dimensional acoustic pulse with a background mean flow is examined. Similarly, an acoustic pulse is generated by an initial pressure disturbance in a uniform mean flow (from left to right) with velocity of 160m/s. This problem and the size of computational domain is shown schematically in Figure 4.11.

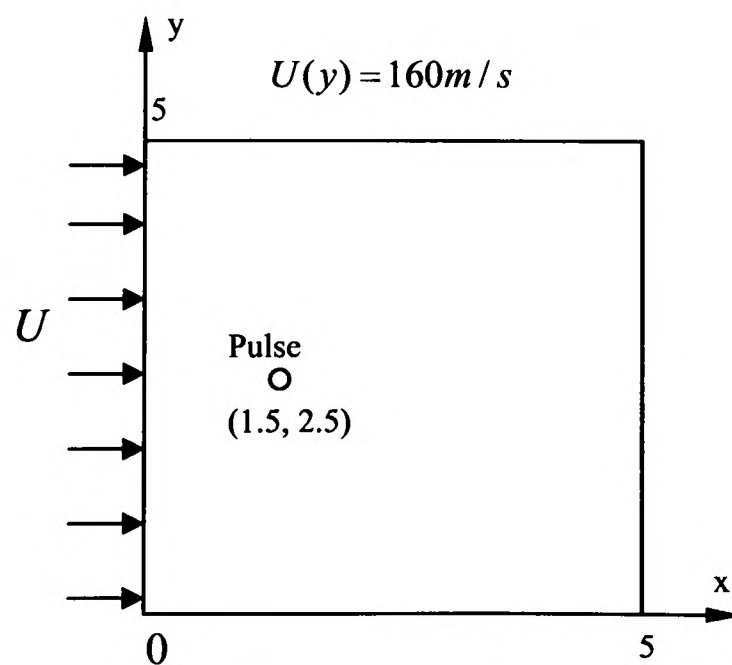


Fig. 4.11. Sketch of computational domain for the 2-D initial pulse propagation problem with a uniform mean flow

The two-dimensional pressure pulse is taken as a Gaussian distribution, which is expressed as following:

$$p(x, y) = A \exp\left\{-\frac{\ln 2}{\alpha^2} [(x - x_0)^2 + (y - y_0)^2]\right\} \quad (4.45)$$

where $A=100(pa)$, α determines the half-width of the Gaussian distribution, and is set to 0.5 in the current calculation. The computational mesh used for this problem has 80 by 80, i.e., $\Delta x = \Delta y = 0.0625m$. This implies that point-number per wavelength is sixteen. Time step is taken to be $\Delta t = 19.608\mu s$. The computed pressure contours at four time steps are shown in Figure 4.12.

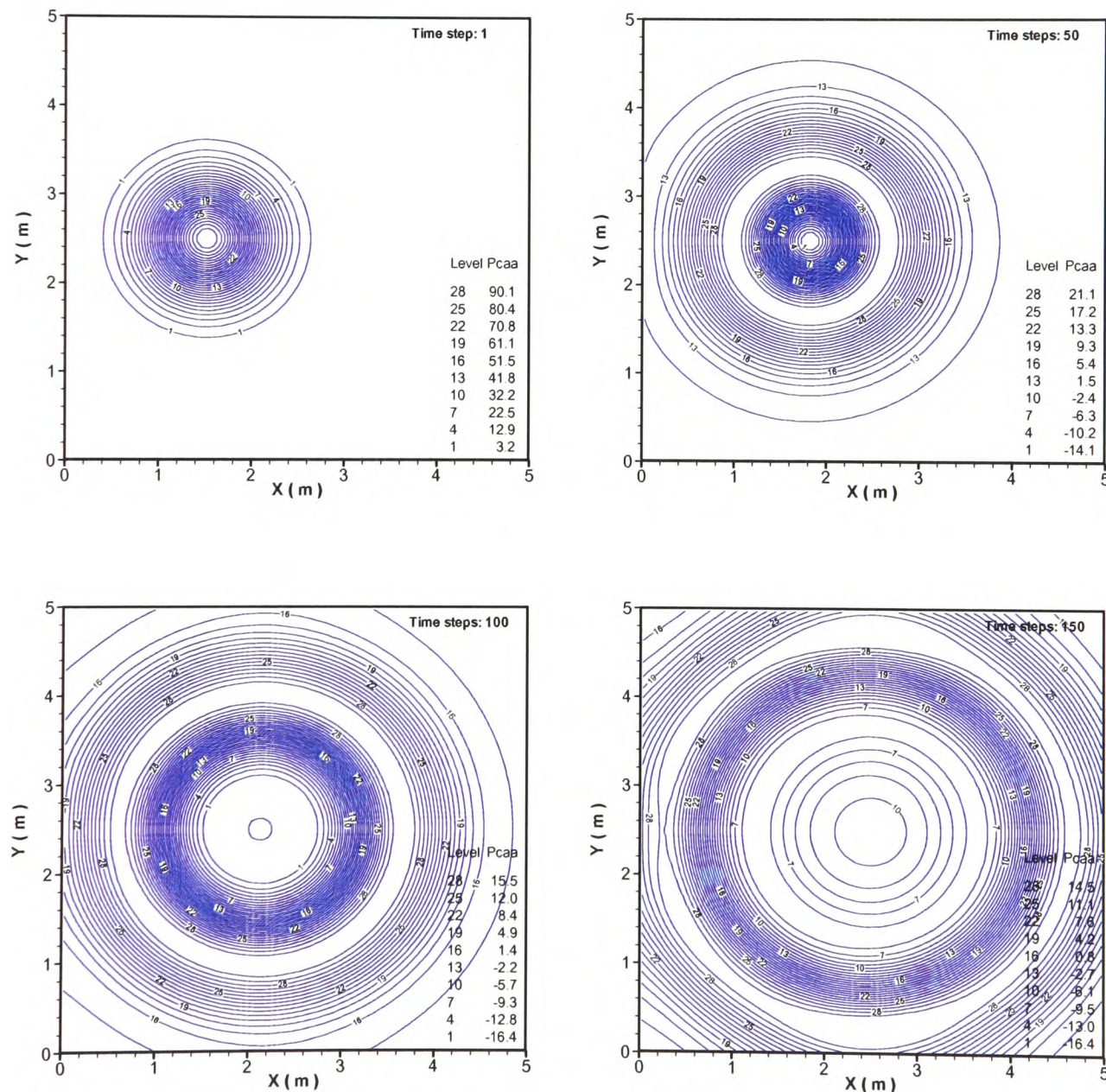


Fig. 4.12. Computed pressure contours of the 2-D wave propagation in a uniform mean flow with at 4 time instants

Clearly, the results show the expected propagation pattern: the radius of the acoustic wave expanded with increasing time while its centre is being entrained downstream with the mean flow. Furthermore, the waves exited from the outflow, top, bottom, and inflow boundaries with very small noticeable reflections (less than 2% of the initial pulse amplitude). Computational results demonstrate that the implementation of the radiation boundary conditions is correct and efficient.

Many practical problems in aeroacoustics that involve noise generation and propagation are actually problems of propagation of waves in a nonuniform mean flow. The above propagation of a two dimensional pulse is simulated in a uniform mean flow. The performance of the radiation boundary conditions is satisfactory with a uniform mean flow. The same problem with a same-direction nonuniform, mean flow is also examined. The mean flow velocity is a simple linear function in y coordinate direction. This is shown schematically in Figure 4.13.

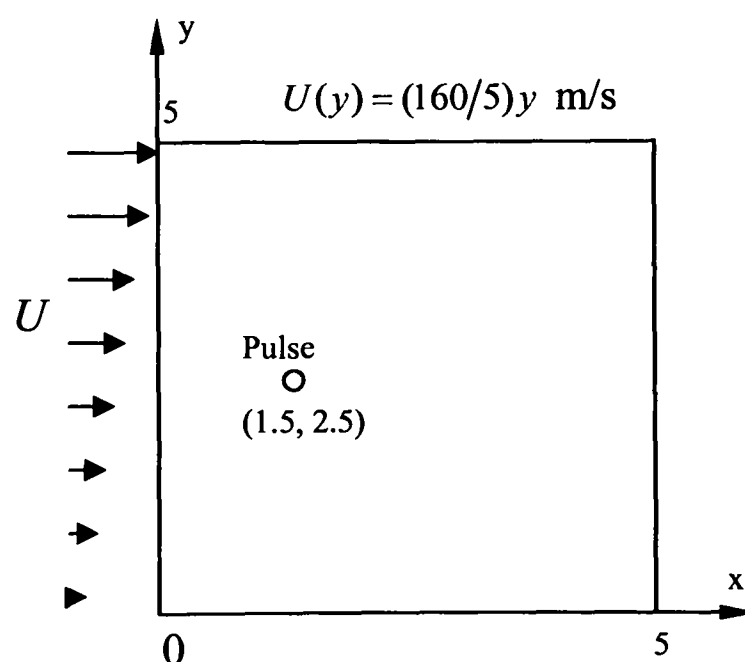


Fig. 4.13. Sketch of computational domain for the initial 2-D pulse propagation in a non-uniform mean flow

Figure 4.14 represents the computed pressure contours at the same four time steps as the above calculation. Comparison with the propagation of the pulse in the uniform mean flow, it can be seen that the propagation pattern is no longer a circular one because the mean flow velocities are different at the upper part and the bottom part. However, the

direction of the nonuniform mean flow is perpendicular to the inflow and outflow boundaries of the computational domain. No noticeable reflections are not seen when the wave propagates throughout the domain boundaries.

The wave propagation of the pulse under a shear mean flow is further investigated for the assessment of the radiation boundary conditions. The mean flow in the upper half part of the computational domain has a positive linear velocity distribution while a negative linear velocity distribution exists in the lower half part of the domain. Figure 4.15 gives a schematic representation for this case. The computed pressure contours at time steps are shown in Figure 4.16.

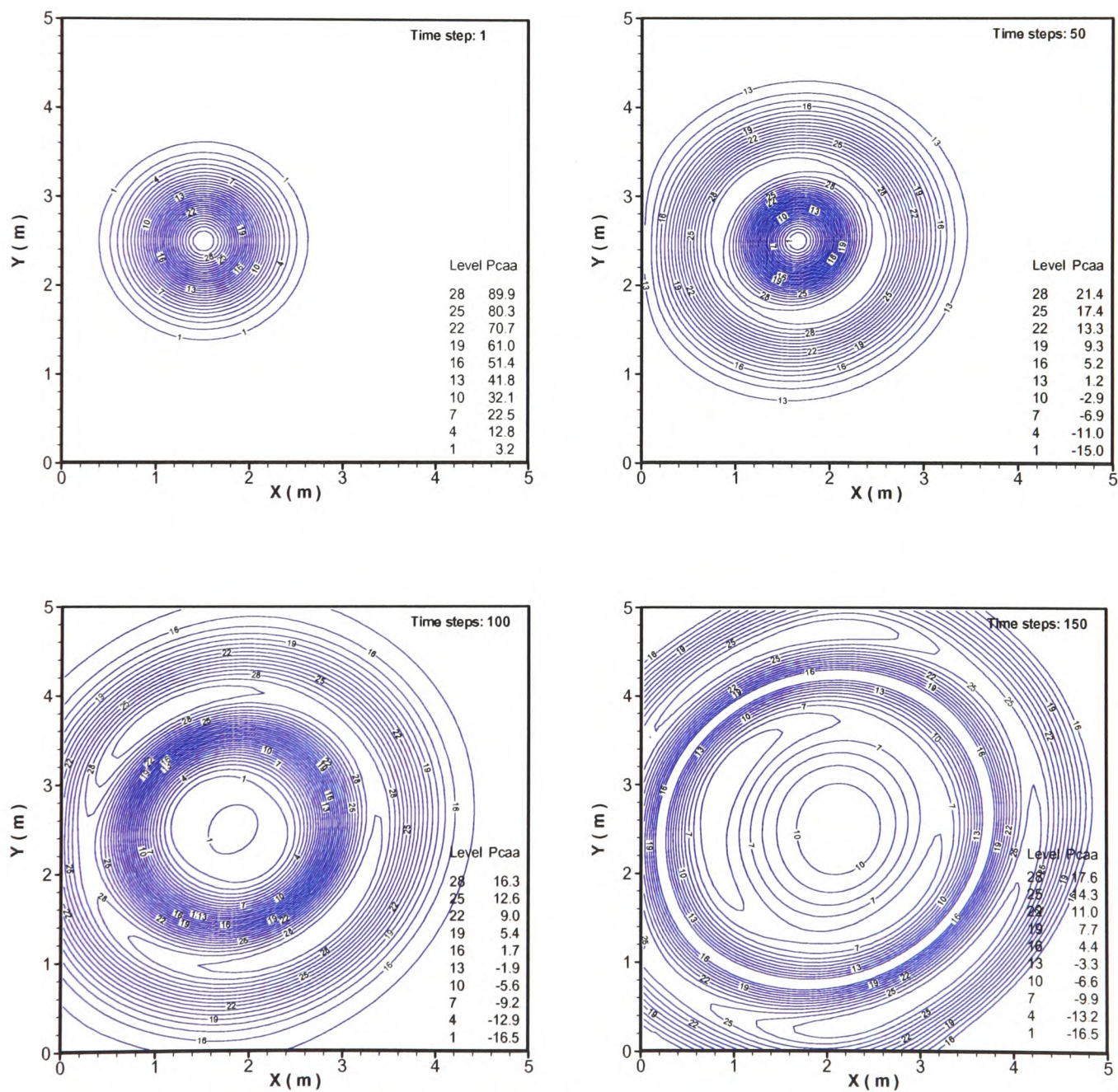


Fig. 4.14. Computed pressure contours of the 2-D wave propagation in a non-uniform mean flow at 4 time instants

As expected, the mean flow stretches the propagation pattern of the pulse in the y direction when it propagates outwards, and it's the shear gradient of mean flow affects also the directivity of the pulse propagation. Although a large change can be seen in the propagation pattern, the pulse can still exit the computational domain without significant reflections. This means that radiation boundary conditions work well in this case. Note that the direction of the shear mean flow is still keep perpendicular to the inflow and outflow boundaries of the computational domain as the above case.

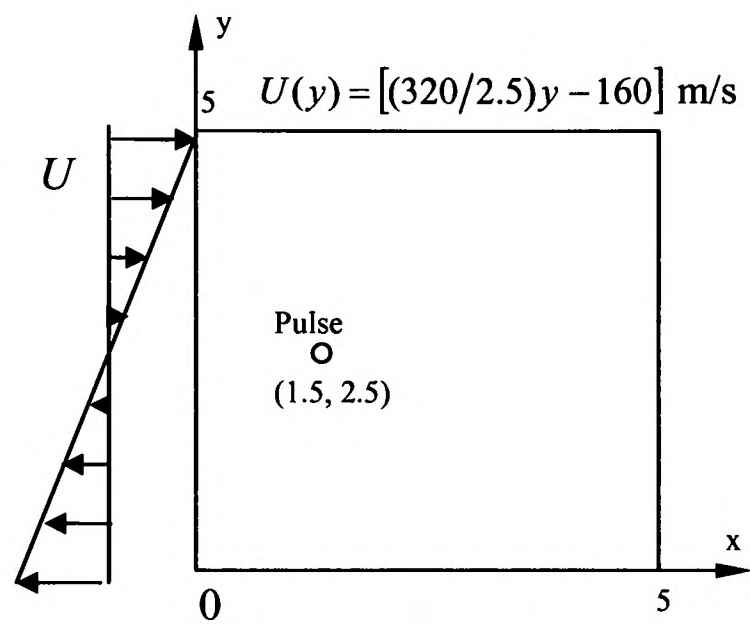
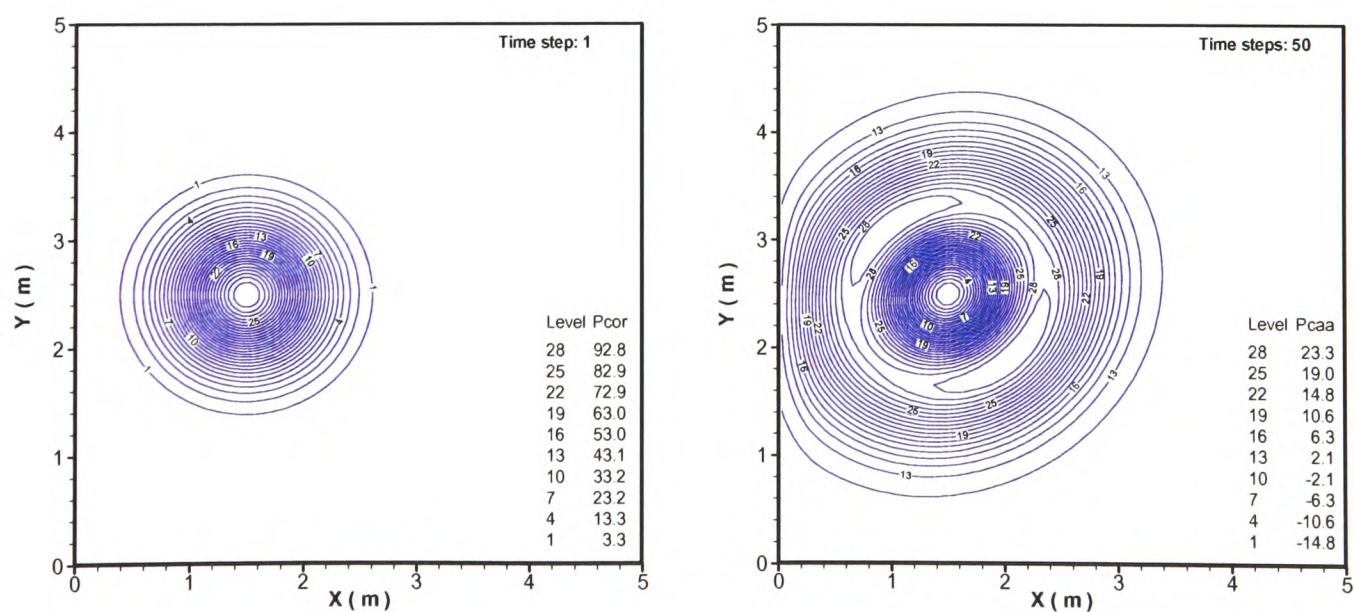


Fig. 4.15. Sketch of computational domain for the initial 2-D pulse propagation in a shear mean flow



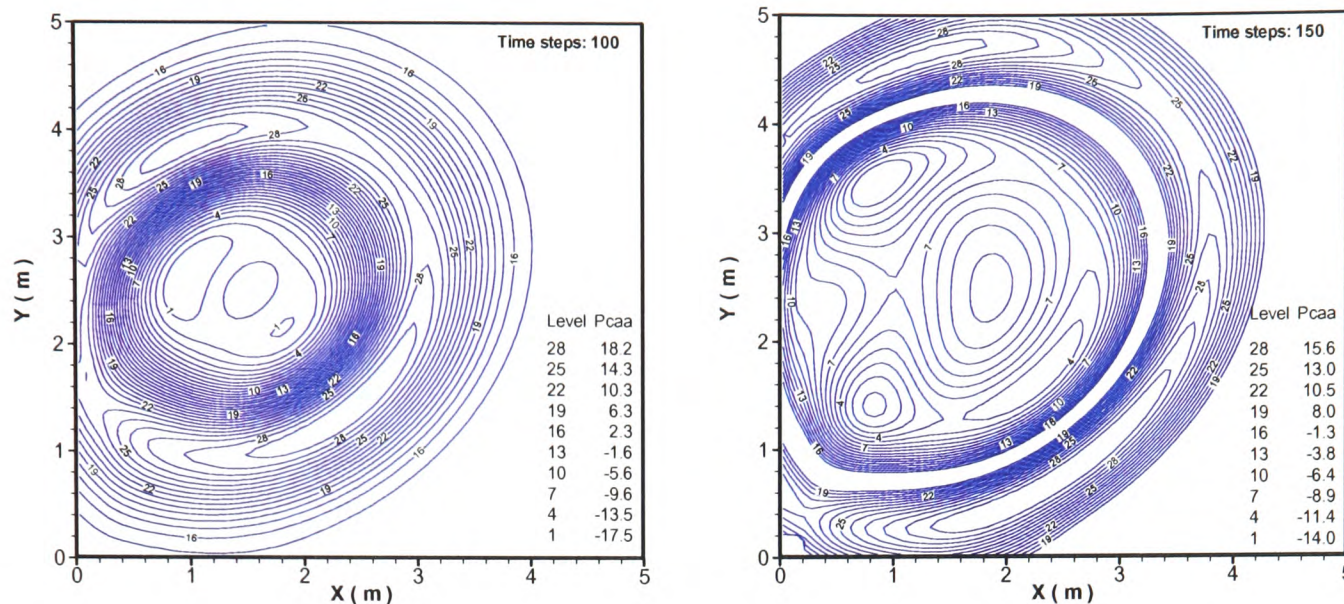


Fig. 4.16. Computed pressure contours of the 2-D wave propagation in a shear mean flow at 4 time instants

In the above cases different mean flows have been considered for testing the radiation boundary conditions. However, the directions of the velocity of the mean flow are all perpendicular to the inflow and outflow domain boundaries. Under this circumstance, it can be seen that the radiation boundary conditions perform well.

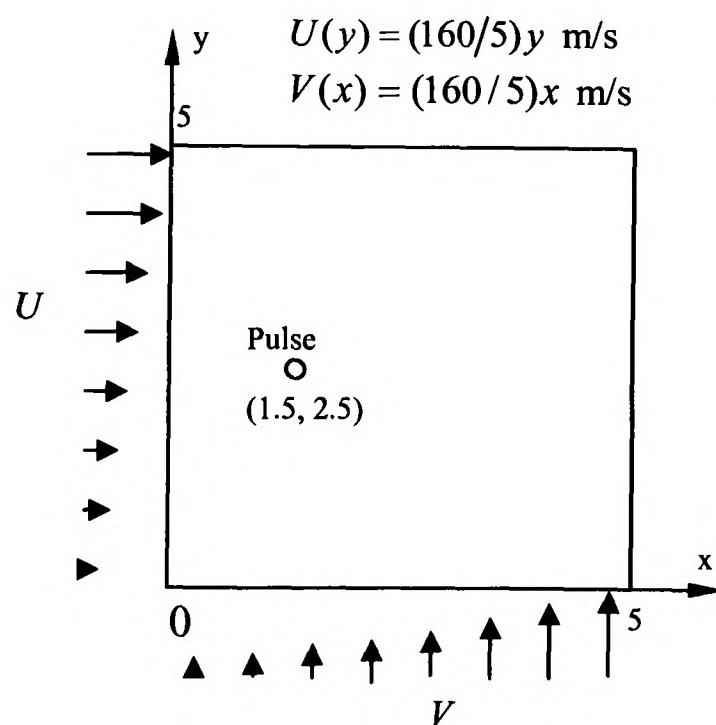


Fig. 4.17. Sketch of computational domain for the initial 2-D pulse propagation in an incidence mean flow

Now a numerical experiment in which the same pulse propagates in the mean flow with an attack of angle to the domain boundaries is further considered to test the radiation

boundary conditions. Likewise, this is shown schematically in Figure 4.17. In both x and y coordinate direction two linear velocity profiles are introduced, respectively. Figure 4.18 shows the computed pressure contours at the same four time steps as the above calculation.

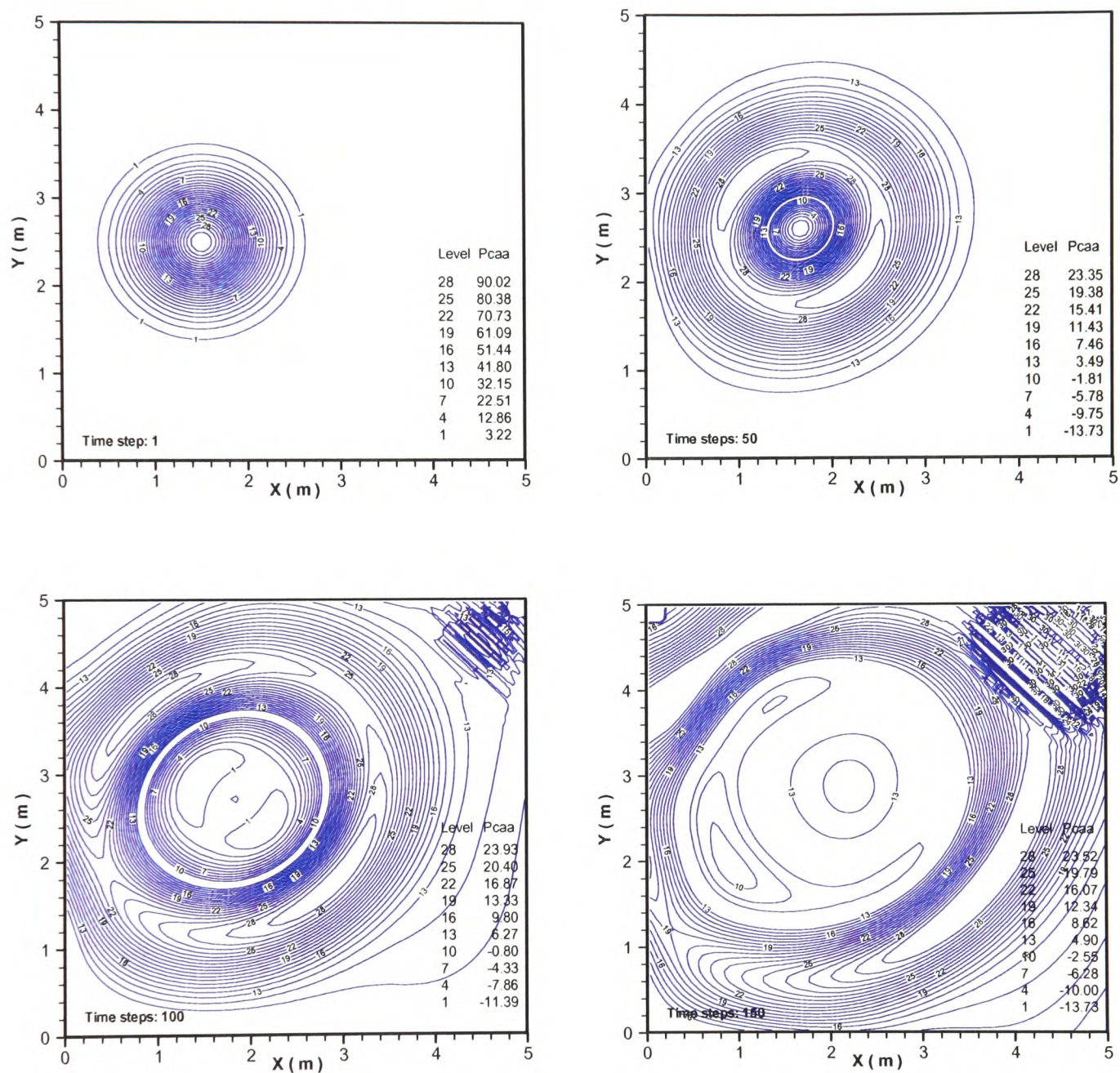


Fig. 4.18. Computed pressure contours of the 2-D wave propagation in an incidence mean flow at 4 time instants

The wave pattern generated by the pulse changes as time moves on. There are numerical reflections appear at the upper right corner. As pointed out previously, the set of acoustic perturbation equations describe acoustic waves, vorticity waves, and entropy waves. The outflow boundary of the computational domain often involves all of the three

types of waves. In the present calculation, only plane acoustic waves are involved whenever there is an implementation of the radiation boundary conditions. When the direction of background flow is normal to the outflow boundary, the influence from both the vorticity waves and the entropy waves is very small for this 2-D case. This is also shown in the first three numerical experiments of this section. In the last numerical experiment, the computational domain is the same as the previous three numerical experiments, and the background flow is with an angle of incidence. As a result, the direction of the background flow is not normal to the outflow boundary any more (especially at the upper corner). Numerical instabilities in this experiment cannot smoothly move out the boundary using the set of radiation boundary conditions. This means that the direction of velocity of the mean flow plays an important role in efficient implementation of the radiation boundary conditions. Hence, it is suggested that the inflow and outflow boundaries should be specified to be perpendicular to the direction of mean flow in order to avoid these numerical instability reflections at acoustic domain boundaries where the radiation boundary conditions are used.

Chapter 5

Coupling Procedure and Model Problem Investigations

The purposes for this chapter are twofold. First, a coupling procedure combining the CFD solver described in Chapter 3 and the acoustic solver described in Chapter 4 will be built. The coupling is achieved through the acoustic source terms extracted from the solved unsteady flow field using the novel acoustic source terms extraction formulation. At the same time, some relevant issues involving the coupling procedure will be discussed. Second, in order to verify and validate the usefulness and feasibility of the proposed extracting formulation for acoustic source terms and the source-extraction based coupling procedure, several acoustic model problems, which involving the propagation, the reflection, the scattering, and the interaction of acoustic pulse(s) with/without a mean background flow are then examined. The computed results through the source-extraction based coupling method are compared with the exact solutions/reference solutions of the corresponding problems.

5.1 The source-extraction based coupling procedure

A coupling procedure combining a cell-centred finite volume CFD solver and a staggered mesh based finite difference acoustic solver is given in this section. For a given acoustic problem, its unsteady flow field in a specified computational domain, in which all or most acoustic sources are contained, is simulated. Obviously, the computational domain is problem-dependent.

The vortex structures (including big- and small-size vortices) in the unsteady flow field are significantly responsible for the sound generation. In order to sufficiently resolve the unsteady flow field for the accurate extraction of the aerodynamically-generated sound sources, a fine mesh is normally used in the simulation of the unsteady flow field. In addition, it is a common practice that the computational mesh being used for the simulation of the unsteady flow field is further squeezed in some large variable gradient regions, especially in regions near to the solid walls, so that computational costs (memory and time) may be reduced.

In the present work, only structured meshes are considered in the unsteady flow calculations although the CFD solver can handle unstructured meshes. In order to avoid excessive refinement of the mesh and to reduce the numerical diffusion of the vortices, second order numerical schemes are generally adopted, for instance, the QUICK scheme.

A key step in the coupling procedure is to extract the acoustics sources. The time steps in the CFD solver and the acoustic solver may be different. Generally speaking, the time step of the CFD simulation can be several times larger than the time step of the explicit acoustic solver. In order to achieve a good overall computational accuracy in the evaluation of the acoustic sources, the extracting calculation of the acoustic source terms is done through the following two steps in the coupling procedure.

First, the pressure, velocity and density fields are calculated and stored at each CFD time step (i.e., the time step used in the solution of the unsteady flow field). The spatial part of the source terms are evaluated temporally from the computed unsteady solutions of the flow near field at each CFD time step. Like the other computed variables, they are also stored at the cell-centres of the computational mesh. Based on the source terms formulation,

Eq.(2.89) (or Eq.(2.90)), the spatial parts of the source terms refer to $c^2(\bar{v}_j \frac{\partial \bar{\rho}}{\partial x_j} + \bar{\rho} \frac{\partial \bar{v}_j}{\partial x_j})$

and $\left[\bar{v}_j \frac{\partial \bar{v}_i}{\partial x_j} + \frac{1}{\bar{\rho}} \frac{\partial \bar{p}}{\partial x_i} - \frac{1}{\bar{\rho}} \frac{\partial}{\partial x_j} \left(\mu \left(\frac{\partial v_i}{\partial x_j} + \frac{\partial \bar{v}_j}{\partial x_i} \right) - \frac{2}{3} \mu \delta_{ij} \frac{\partial \bar{v}_k}{\partial x_k} \right) \right]$, respectively. The complete

acoustic source terms which will be input into the acoustic solver are left to be calculated in a short linking code between the CFD solver and the acoustic solver. In the short link code, new values for the spatial part of the whole acoustic source terms spatial are evaluated by applying a second order integral formula which involves three time levels to the obtained

spatial part of the source terms in the CFD computation. As a demonstration, the acoustic source term involving the continuity equation, i.e., \bar{R}_c in Eq.(2.89), is considered below. Assume the time integration of the acoustic solver is from t to $t + \Delta t_{CAA}$, where Δt_{CAA} stands for the time step used in the acoustic simulation. For the simplicity, \bar{R}_c^s is used to represent the spatial part of the acoustic source term. Thus, the evaluation of the complete acoustic source term \bar{R}_c in the acoustic time integration can be written as follows:

$$\int_t^{t+\Delta t_{CAA}} \bar{R}_c = \int_t^{t+\Delta t_{CAA}} c^2 \left(\frac{\partial \bar{\rho}}{\partial t} + \bar{v}_j \frac{\partial \bar{\rho}}{\partial x_j} + \bar{\rho} \frac{\partial \bar{v}_j}{\partial x} \right) dt = \int_t^{t+\Delta t_{CAA}} c^2 \frac{\partial \bar{\rho}}{\partial t} dt + \int_t^{t+\Delta t_{CAA}} \bar{R}_c^s dt \quad (5.1)$$

Since the source evaluation need to be done through the computed CFD solutions, an approximation to the above integral in terms of the CFD integral limits (i.e., from t to $t + \Delta t_{CFD}$, where Δt_{CFD} denotes the time step used in the CFD simulation.) may be written as, see Figure 5.1,

$$\int_t^{t+\Delta t_{CAA}} c^2 \frac{\partial \bar{\rho}}{\partial t} dt + \int_t^{t+\Delta t_{CAA}} \bar{R}_c^s dt \approx \frac{\Delta t_{CAA}}{\Delta t_{CFD}} \left(\int_t^{t+\Delta t_{CFD}} c^2 \frac{\partial \bar{\rho}}{\partial t} dt + \int_t^{t+\Delta t_{CFD}} \bar{R}_c^s dt \right) \quad (5.2)$$

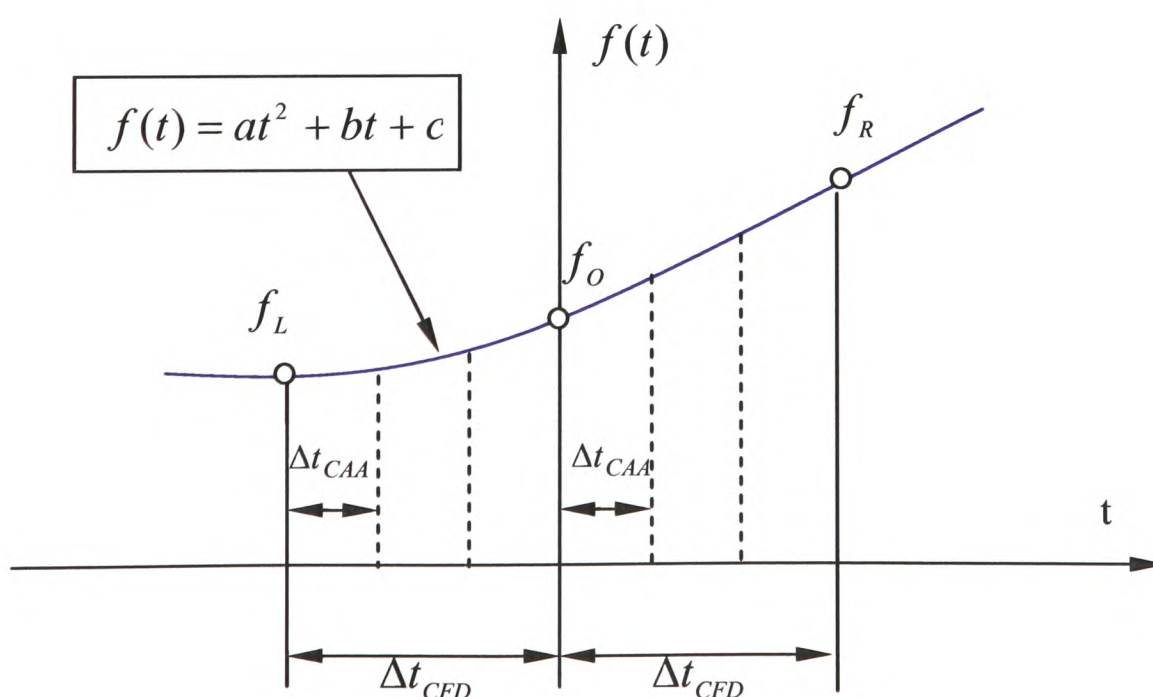


Fig.5.1. Sketch of integral approximation for the evaluation of the source term

For the first integral on the right-hand side of (5.2), it can be calculated directly due to its temporal derivative. The second integral on the right-hand side of (5.2) does not explicitly involve time. In order to achieve a second order accuracy for the time integration, an approximate function of second order in time such as

$$\bar{R}_c^s = f(t) = at^2 + bt + c \quad (5.3)$$

may be used. Let $f_L = f(-\Delta t_{CFD})$, $f_O = f(0)$ and $f_R = f(\Delta t_{CFD})$, see Figure 5.1, the coefficients determined from the corresponding linear equations are

$$a = \frac{(f_L + f_R - 2f_O)}{2\Delta t_{CFD}}, \quad b = \frac{(f_R - f_L)}{2\Delta t_{CFD}}, \quad c = f_O \quad (5.4)$$

Then the second integral on the right-hand side of (5.2) on the integral limits from 0 to Δt_{CFD} is obtained as follows:

$$\int_0^{\Delta t_{CFD}} \bar{R}_c^s dt = \int_0^{\Delta t_{CFD}} f(t) dt = \frac{(-f_L + 5f_R + 8f_O)\Delta t_{CFD}}{12} \quad (5.5)$$

Similarly, one can evaluate the acoustic source terms related to the momentum equations, i.e., $\bar{R}_{m,i}$ in Eq.(2.88). Note that the above extracted acoustic source terms from the computed unsteady field are still stored in the cell-centres of the computational mesh of the CFD simulation at this stage.

Except for the extracted acoustic source terms, it can be seen in the acoustic Eqs.(2.87)~(2.88) that the quantities in front of derivatives on the left-hand side are also from the computed CFD unsteady solutions. In acoustic calculation, the mean flow variables should use the obtained CFD solutions at the nearest CFD cell centre at the nearest available time instant. However, converged steady solutions of the corresponding problem may approximately be used for the mean flow variables. The steady solutions will also be used as initial values to initialize the time dependent simulation of the flow field. As

pointed out previously, the acoustic domain is generally taken larger than the computational domain of the unsteady flow simulation, and CFD mesh cells are typically smaller than the acoustic mesh cells. The schematic representation of a CFD simulation domain and an acoustic computation domain as well as their typical meshes is shown in Figure 5.2.

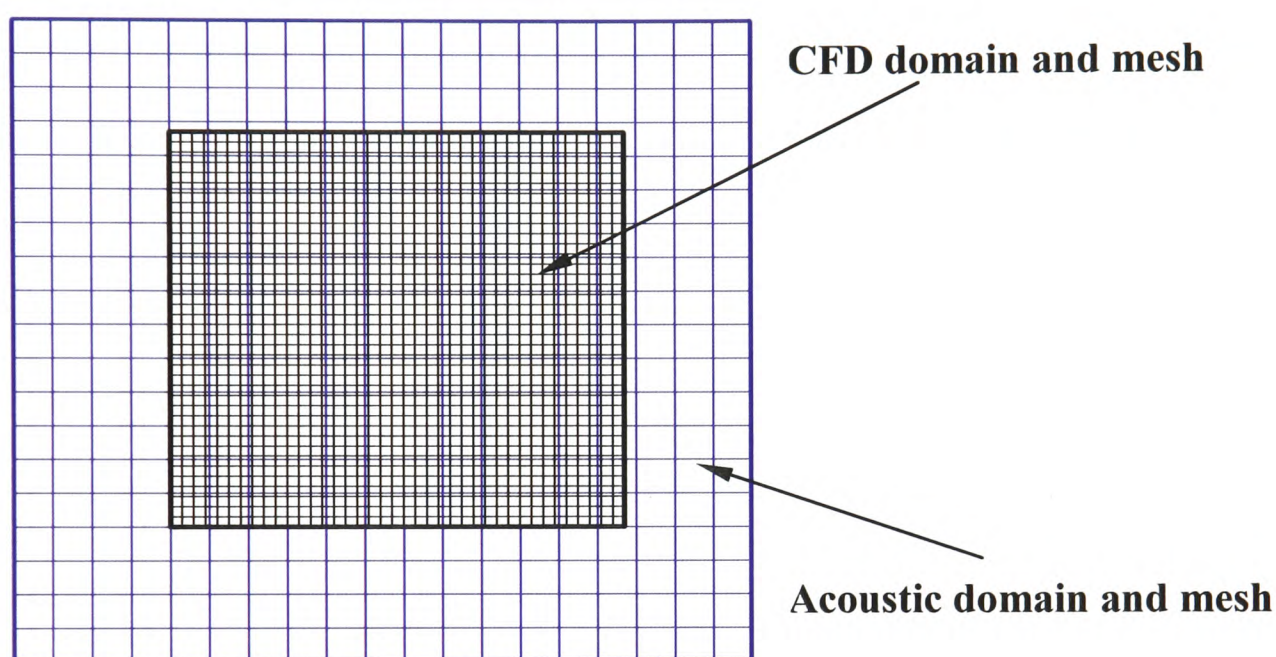


Fig. 5.2. Schematic of a CFD simulation domain and an acoustic computation domain as well as their representative meshes

Within the overlapping region of the CFD simulation domain and the acoustic computation domain, due to different mesh sizes and mesh numbers in both the unsteady flow simulation and the acoustic calculation, the extracted acoustic source terms and the flow field solutions on the CFD computational mesh have to be averaged within each acoustic Cartesian cell before they are fed into the acoustic perturbation equations. In the present work, the mean flow variables (i.e., velocity, pressure, and density) and the extracted source terms are computed on the acoustic mesh via the following weighted volume averaging procedure: at each CFD simulation time step, and for those CFD computational mesh cells contained in each acoustic mesh cell, each flow variable quantity and the extracted source term are multiplied by their own cell volume and are then averaged over the total CFD cell volumes contained within the acoustic cell. Figure 5.3 gives the schematic representation of the map-averaging procedure. In fact, this map-averaging procedure is also suitable for the coupling of an unstructured-based CFD simulation method

and the present acoustic solver. If no CFD cell centre falls inside certain an acoustic mesh cell, the flow variable quantities and the acoustic source terms on the acoustic mesh cell will choose those values on the nearest CFD cell centre to the acoustic cell. A CFD mesh cell “belongs” to a given acoustic cell only when the CFD cell centre is inside the acoustic Cartesian cell. For the acoustic mesh cell outside the CFD simulation domain, the values of the acoustic source terms are all set to zero because of no acoustic sources. The values of the flow variable quantities are taken to be the freestream values.

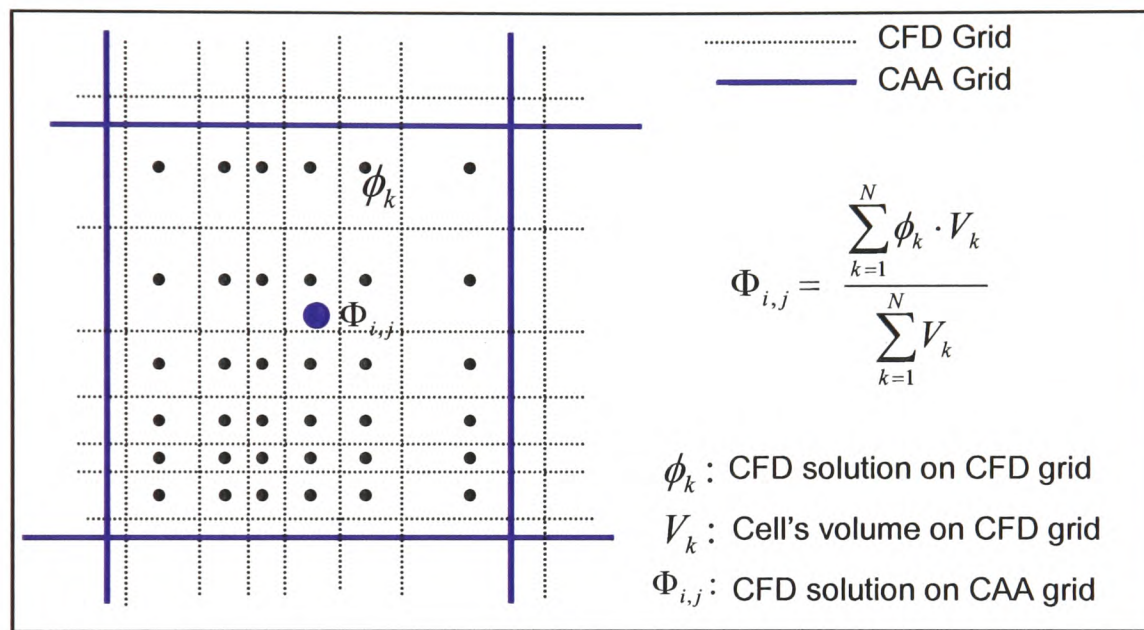


Fig.5.3. Schematic of the mapping of CFD data onto the CAA mesh (k : CFD cell number; i, j : CAA cell number; N : number of CFD cells in each of the CAA cell)

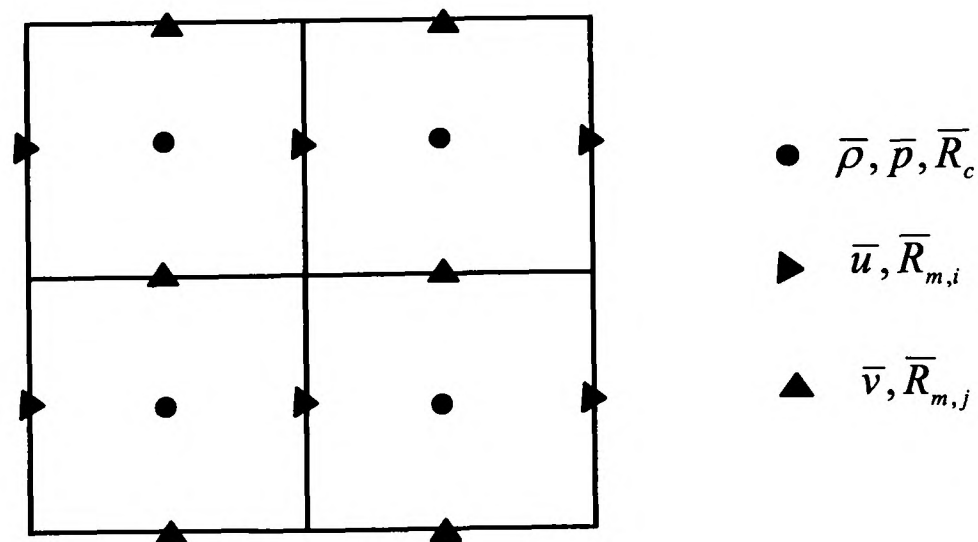


Fig.5.4. Staggered storage locations for the acoustic source terms and the mean flow variables

After the above map-averaging procedure, all the extracted acoustic source terms and the mean flow variables are still stored at the centres of the acoustic mesh cells. Since staggered-type finite difference scheme is used in the acoustic solver, the obtained acoustic source terms and the mean flow variables need to be adjusted to a staggered arrangement on the acoustic mesh.

The velocity components and pressure are arranged on the centres of the different sides of the acoustic Cartesian mesh cells and the centres of the acoustic mesh cells, respectively. This is the same as that in the standard staggered mesh methods. Similarly, the extracted acoustic source terms are also arranged at different locations. The acoustic source term relating to the perturbation continuity equation is stored in the centres of the acoustic mesh cells, while the acoustic source terms involving the perturbation momentum equations are placed on the centres of the different cell faces, respectively. The arrangement locations are represented in Figure 5.4. For the determination of the values on the different sides, a simple two-point averaging procedure based on the central values of the acoustic cells is used.

Based on the CFD solver and the acoustic solver the coupling procedure implemented in the present work may be summarized in the following steps:

- 1) Solve the time-dependent Navier-Stokes equations for the simulation of the unsteady flow field by using the CFD solver;
- 2) Extract the acoustic source terms using Eq.(2.89) or Eq.(2.79) on the CFD computational mesh for the solution of the unsteady flow at each CFD time step (if the CFD time step is larger than the acoustic time step) or at each acoustic time step (if the CFD time step is less than the acoustic time step);
- 3) Map the extracted source terms and the computed flow variables onto the acoustic computational mesh, then arrange them in the staggered way, and input them into the acoustic perturbation Eq.(2.87) and Eq.(2.88);
- 4) Solve the acoustic perturbation equations using the numerical method described in the Chapter 4.

The coupling procedure is also represented in a form of flow chart in Figure 5.5. Note that there is a dotted line loop in the above flow chart. Strictly, a real aeroacoustic problem

always involves the interactions between the unsteady flow field and the resulting acoustic field. The dotted line loop essentially represents a feedback of the acoustic field to the unsteady flow field. Due to numerical stable requirements, the acoustic time step is usually smaller than the CFD simulation time step. Hence, any feedback of the acoustic field on the unsteady flow field has to be averaged over the CFD time step before introduction into the flow simulation. It is generally assumed that such feedback can only have significant influence on the flow field when resonance occurs in the aeroacoustic problem considered. In the present work, the dotted-line feedback loop is not considered.

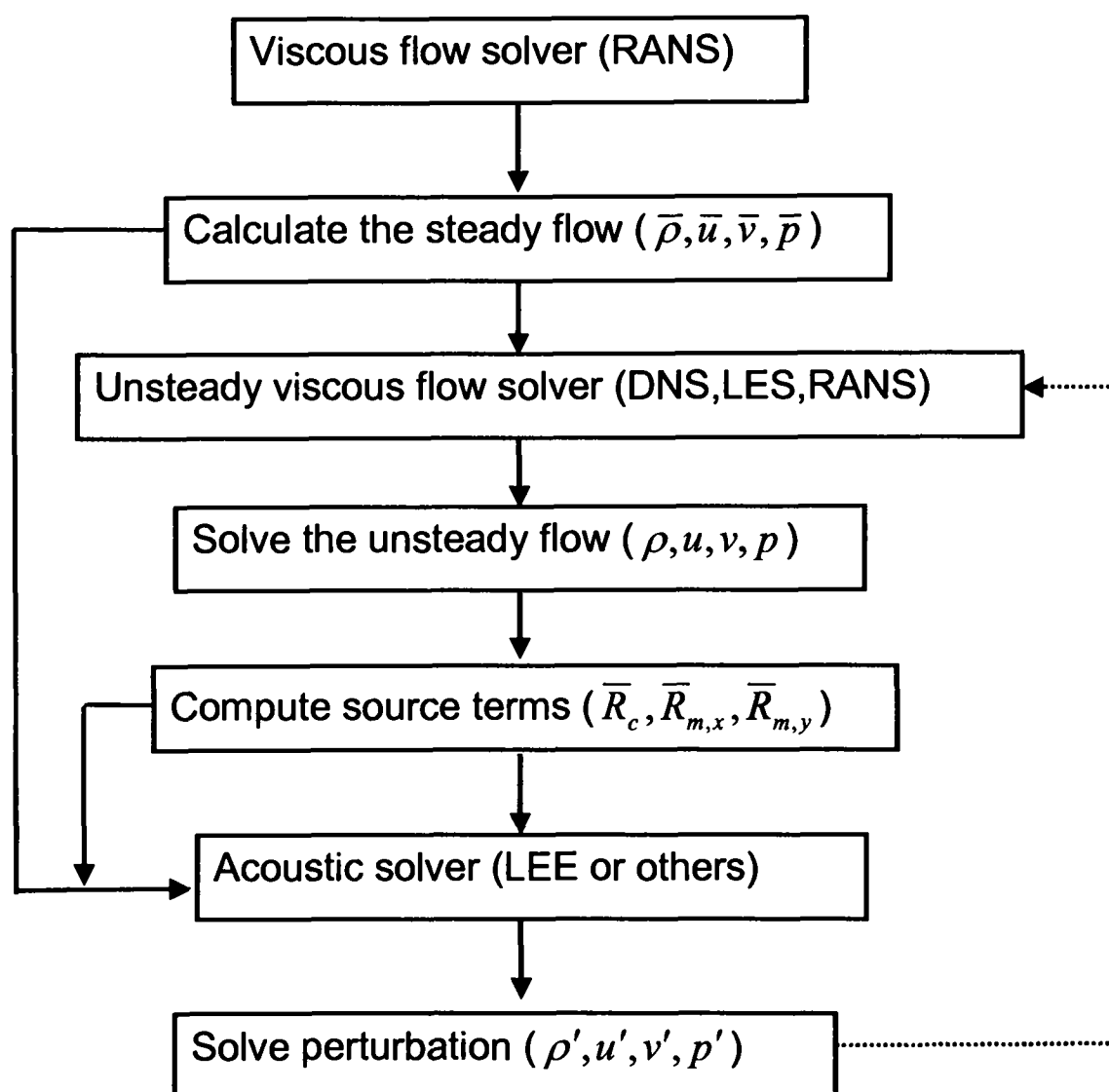


Fig. 5.5. Flow chart for the coupling procedure of a CFD solver and an acoustic solver

The above coupling procedure is general. The concrete process of the transfer and mapping of the data (i.e., the solutions of the unsteady flow field and the extracted source terms) is probably different if different CFD computational methods coupled with different

acoustic solvers. In the present work, the extraction process of the acoustic source terms and the transformation and arrangement of data described above is realized through a linking code which feeds them into the acoustic solver for the acoustic calculations. In the following sections the above coupling procedure is applied to some acoustic model problems.

5.2 Investigations of acoustic model problems

In order to demonstrate the feasibility of the extraction formulation of the acoustic sources and the accuracy of the described coupling procedure, several acoustic model problems are considered. These model problems include wave propagation, reflection, interaction, and scattering, of acoustic pulse with/without background mean flow. These model problems have been widely used in testing the accuracy of aeroacoustic computations.

It should be pointed out that these model problems can be calculated by employing directly an appropriate numerical method (e.g., the DRP scheme) through solving the linearized Euler equations because their sources are actually known a priori. This means that the calculations of these acoustic model problems do not need the coupling procedure. In fact, for the comparison purpose of the computed results from the above coupling procedure, reference solutions of the model problems are obtained by using *only* the acoustic algorithm described in Chapter 4. However, it should be emphasised particularly that the aim of the development of the new source-extraction formulation is not to solve such simple acoustic model problems. For most practical aeroacoustic problems of engineering interest, it is nearly impossible to identify and locate the acoustic sources in advance due to complicated unsteady flow field with complex geometrical configurations. Acoustic model problems provide ideal test cases to assess the feasibility and accuracy of the source-extraction based coupling method. This is very important before the source-extraction formulation is applied to more complex aeroacoustic problems. Therefore, for the following investigations of the model problems, the source terms used in the acoustic code are obtained by means of the source-extraction formulation from the corresponding unsteady flow field of the acoustic pulse(s) instead of directly using the known sources.

As mentioned in the previous section, the computational domain of the unsteady flow simulation is generally small compared to the domain of the acoustic calculation. In general,

different domain sizes may cause some spurious acoustic sources at the boundaries of the CFD domain. In the present work, this issue is temporarily evaded by using the same computational domain sizes in both the unsteady flow field and the acoustic field. In addition, both computational meshes are all Cartesian uniform mesh.

5.2.1 A 1-D pulse problem without mean flow

A one-dimensional acoustic pulse travelling without background mean flow is investigated. This model problem is the same as the first example considered in the Section 4.5. However, the coupling procedure described in the previous section is implemented in the investigation of this model problem.

The spatial distribution pressure pulse takes the same expression as (4.43) in the Chapter 4. The exact solution can be given, see expression (4.44). Similarly, only the right propagating part is solved. Mesh spacing $\Delta x_{CFD} = 0.025m$ is used in the CFD computation. The corresponding mesh size used in the acoustic calculation is $\Delta x_{CAA} = 0.05m$. This implies that there is 20 mesh points per wavelength (i.e., $\lambda = 1m$), which meets the requirement of the resolution of the pressure pulse propagation (see Fig. 4.8). Computational domain size for both CFD and acoustic calculations is taken to be $12m$. The time steps in both CFD and acoustic calculations are the same in the present investigation, i.e., $\Delta t_{CFD} = \Delta t_{CAA} = 58.75\mu s$. Because a cell-central finite volume CFD code is used, the face values of a cell for the extracting calculation of the source terms are obtained by the means of an interpolation formula. For this case, we experiment with both a first-order interpolation (a geometric weighted average of adjacent two cell-centre values) and a second-order interpolation (a three-point formula involving three cell-centre's values) in the calculations. Figure 5.6 shows the computed pressure distributions at six time instants, corresponding to the 40th, 140th, 240th, 340th, 440th, and 540th time steps. In this calculation, the first-order interpolation was used. From Figure 5.6, it can be seen that the CFD solution decays gradually with the propagation of the pressure pulse. This may serve as an illustration why a conventional CFD numerical scheme can not be used for the calculation of acoustic problems. The source-extraction based coupling approach described above corrects this error, and the corrected pressure pulse agrees well with the exact

solution. The error in the figure represents the maximum difference between exact solution and the computed correction solution. The maximum error is about 3.5 percentage of the pulse peak value after the pulse's peak propagates about 11 wavelengths.

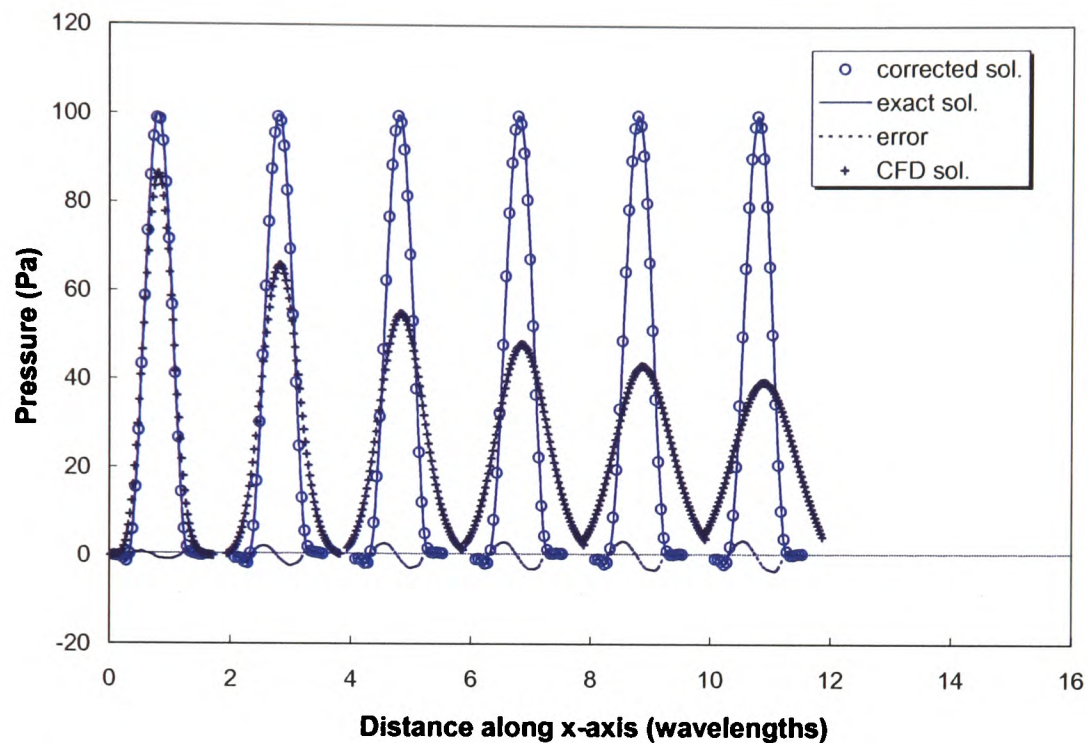


Fig. 5.6. Pressure distribution along x-axis at 40th, 140th, 240th, 340th, 440th, 540th acoustic time steps with the first-order interpolation

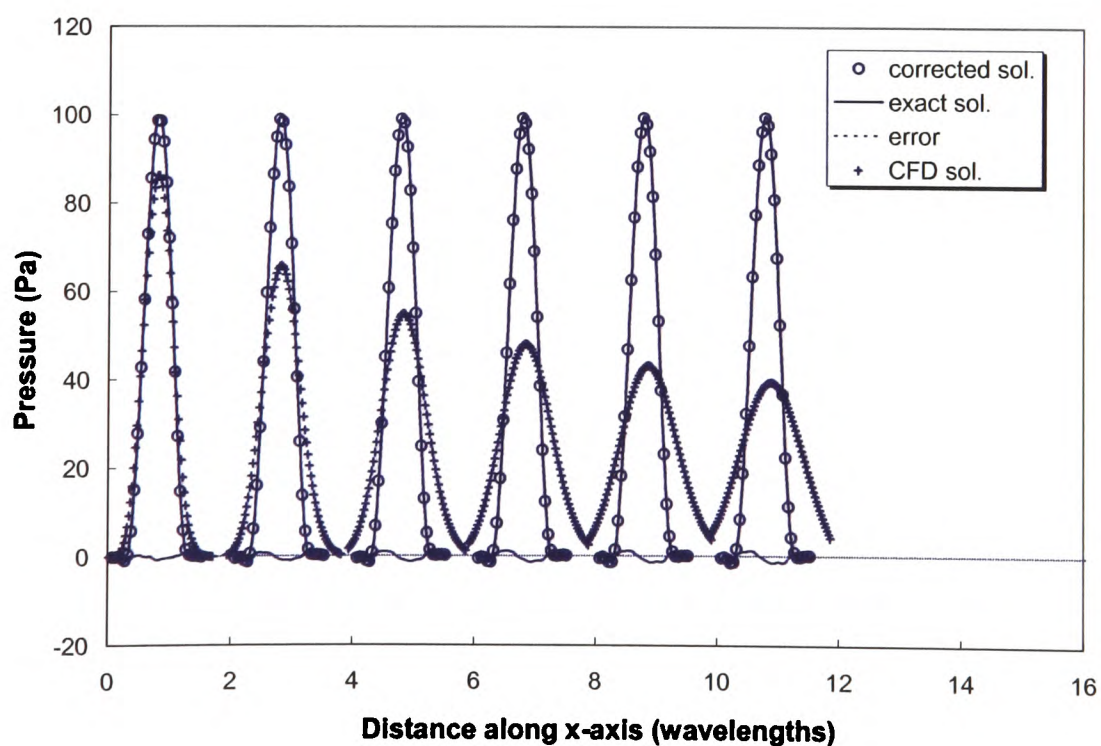


Fig. 5.7. Pressure distribution along x-axis at 40th, 140th, 240th, 340th, 440th and 540th acoustic time steps with the second-order interpolation

Figure 5.7 gives the computed pressure distributions using the second-order interpolation formula at the same time instants as those in Figure 5.6. Clearly, the maximum error decreases, and the corrected solutions are improved further. The maximum error is about 1.4 percentage of the pulse peak value after the pulse's peak propagates about 11 wavelengths. Hence, the second order interpolation formulation is used in the following investigations of model problems.

The coupling computational results show the extraction formulation of acoustic source terms provide accurate acoustic source information of the one-dimensional pulse for the acoustic wave propagation, and the implementation of the coupling procedure is feasible.

5.2.2 A 2-D pulse problem with/without mean flow

The generation and propagation of a two-dimensional acoustic pulse is examined in this section. The prescribed coupling procedure is carried out for this model problem instead of using only the acoustic calculation as presented in Chapter 4. Similarly, an acoustic pulse is generated by an initial pressure disturbance by using setting $u = v = 0.0$ in a static or a uniform mean flow (from left to right) with Mach number of 0.5.

For the case without mean flow, the expression for the spatial distribution of the pressure pulse is a two-dimensional extension of the pulse used in the above one-dimensional case. This two-dimensional pressure pulse may be written as:

$$p(r) = \begin{cases} A \left(1 + \cos 2\pi \frac{r}{\lambda} \right), & |r| < \frac{\lambda}{2} \\ 0, & |r| \geq \frac{\lambda}{2} \end{cases} \quad (5.6)$$

where $A = 100(Pa)$, $\lambda = 1.0(m)$, and $r = \sqrt{(x - x_0)^2 + (y - y_0)^2}$ (m). The initial position of the pulse is at $x_0 = 0.0$ and $y_0 = 0.0$. Only a quarter of the computational domain is used due to the symmetrical situation. Grid sizes $\Delta x = \Delta y = 0.0625m$ are used in both CFD simulation and the acoustic calculations. This implies that the number of points per wavelength is equal to 16. The time steps used in the unsteady flow and the acoustic

propagation calculations are different. A time step, $\Delta t_{CFD} = 3\Delta t_{CAA} = 19.608\mu s$, which meets the requirement of numerical stability for the acoustic calculation, is used. Computational domain is specified to be the same dimensions, Computational mesh with 108×108 cells is chosen for this case. Figure 5.8 gives the pressure distribution along $y = 0.03125m$ at several different acoustic time steps. Again one can see the CFD solutions decay quickly as propagation time increase. Following the source extraction formulation along with the coupling procedure, the decaying CFD solution is complemented by the acoustic solution to form the corrected results, which show quite a good agreement with the corresponding reference solutions. This means that the information of the acoustic source of the pulse is extracted accurately by the source extraction formulation.

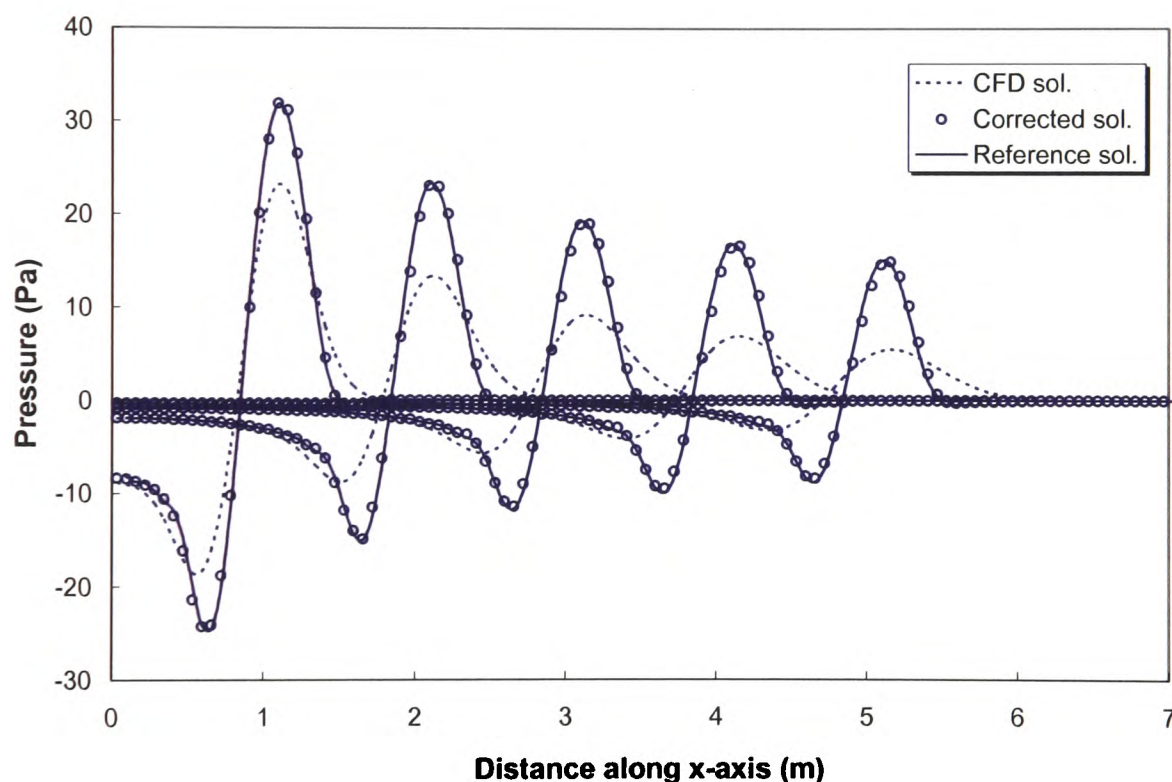


Fig. 5.8. Pressure distribution along $y = 0.03125m$ at 50th, 100th, 150th, 200th and 250th acoustic time steps for the acoustic pulse without mean flow

For the same model problem in which a uniform mean flow exist, a Gaussian distribution is considered (see expression (4.45)). The initial location is placed at $x_0 = 5.5m$ and $y_0 = 7.5m$, and a full domain is set up. The grid spacings and time steps are as the same as the above calculation. The whole computational domain contains 240×240 cells. Figure 5.9 gives computational pressure distribution from the CFD solver, the corrected pressure solution, and reference solution along $y = 7.46875m$ at four different acoustic time

steps. Note that the corrected solution refers to a summation of the CFD solution and the acoustic perturbation solution. It can be seen that the corrected results from the coupling procedure agree well with the reference solutions.

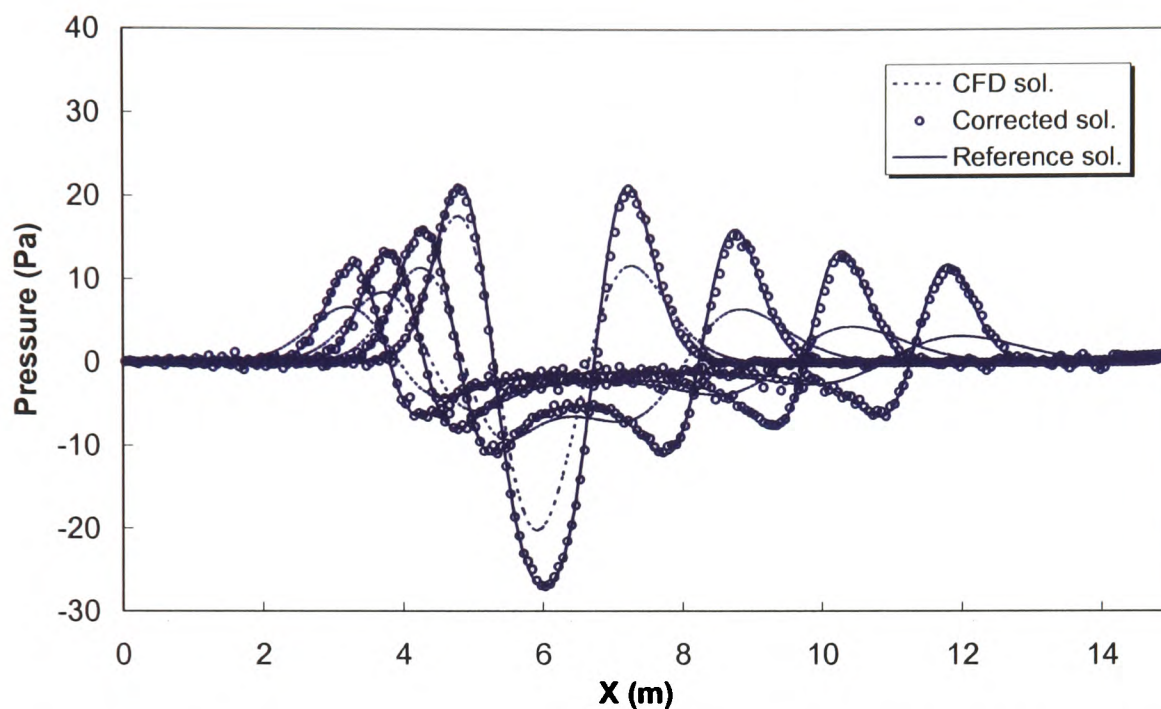


Fig. 5.9. Pressure distribution along $y = 7.46875\text{m}$ at 75th, 150th, 225th and 300th acoustic time steps for the acoustic pulse with a mean flow

The computed corrected pressure contours at four time instants for the acoustic propagation of the pulse are shown in Figure 5.10. Like the results from only the acoustic calculation presented in Chapter 4, the results obtained through the extracted acoustic source terms and the coupling procedure display also the expected propagation pattern: the radius of the acoustic wave expands with increasing time while its centre is being convected downstream with the mean flow. Hence, the good matched wave form and the accurate amplitude as well as the propagation speed of the pulse after such a coupling procedure demonstrates a good performance of the extraction formulation of source terms. However, small fluctuations in the low-value pressure region are also clearly seen in Figure 5.9 and Figure 5.10. This can be explained by the fact that the values of the extracted source term from the unsteady flow solution also exhibit fluctuations in the presence of the background flow. In other words, the extracted source is not smooth like the original source. In fact, this is also expected because some numerical errors can not be avoided to be introduced in such an extracted and coupled procedure. However, compared with the case with no mean flow, it can also be seen that, with a mean background flow, the numerical oscillation of the

numerical are more apparent. This indicates also the convection terms play an important role in the extraction of the acoustic source terms and the calculation of wave propagation.

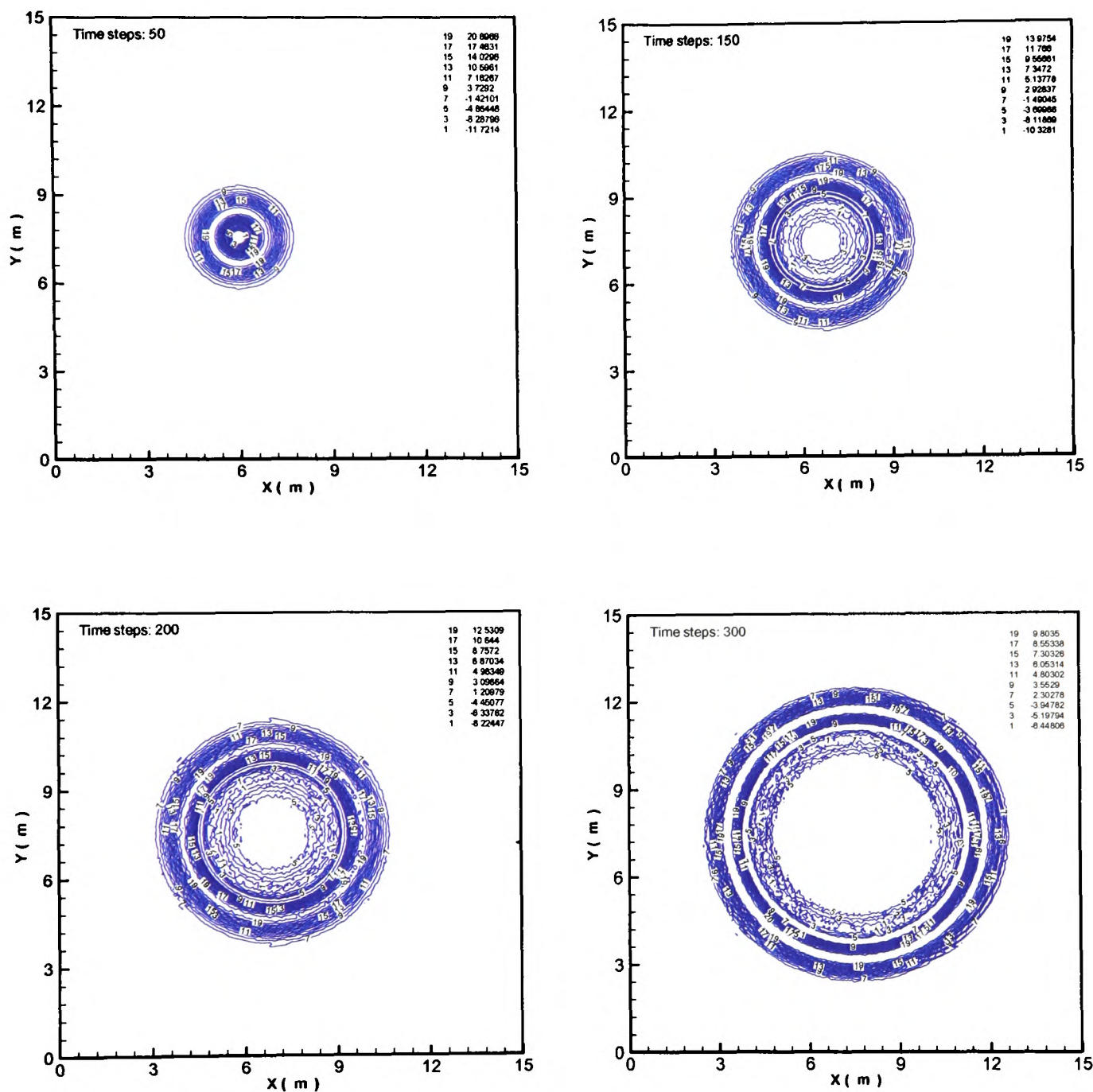


Fig. 5.10. Instantaneous computed corrected pressure contours at 4 acoustic time instants for the acoustic pulse with mean flow

5.2.3 Interaction of two 2-D pulses in a static medium

In practical aeroacoustic problems, it can be often seen that the waves from acoustic sources at different locations interact each other when they propagate outwards. The source

extraction formulation is tested for a model problem involving multi-sources. This model problem consists of two simultaneous acoustic pulses, with the same spatial pressure distribution as expression (4.45), located at two different initial positions. These two pulses are generated in a static medium (i.e., there is no background mean flow). One initial pulse is generated at $x_0 = 3.125m$ and $y_0 = 0.0m$ and the other generated simultaneously at $x_0 = 7.125m$ and $y_0 = 0.0m$. The mesh spacing and time step size used are $\Delta x = \Delta y = 0.0625m$ and $\Delta t_{CFD} = 3\Delta t_{CAA} = 19.608\mu s$ in this computation. The computational domain encompasses only the upper half-plane with 164×68 cells. Dispicited in Figure 5.11 are the computed pressure distributions from CFD solver, the acoustic calculation and the corrected solution from the coupling procedure along $y = 0.03125m$ at three acoustic time steps. The corrected pressure is compared with a reference solution obtained by using only the acoustic solver. A disparity between the reference solution and the corrected solution can be seen at domain boundaries at the 150th acoustic time step. It can also be noticed in the pressure contours below. This means that the extraction of the acoustic source terms at the boundaries produce certain numerical errors when both wave systems are exiting outside the domain. The primary cause may be due to the imperfect non-reflecting boundary conditions in the CFD solver. Figure 5.12 gives the corrected pressure contours at four acoustic time instants for the propagation and the interaction of the two acoustic sources. It can be observed that two pulses intersected as they propagate outward. The interaction of the waves is crisply reproduced using the source-extraction based coupling procedure. If the case is repeated on a bigger domain, at the same time instant (i.e., the 150th time step) the apparent errors are not be found.

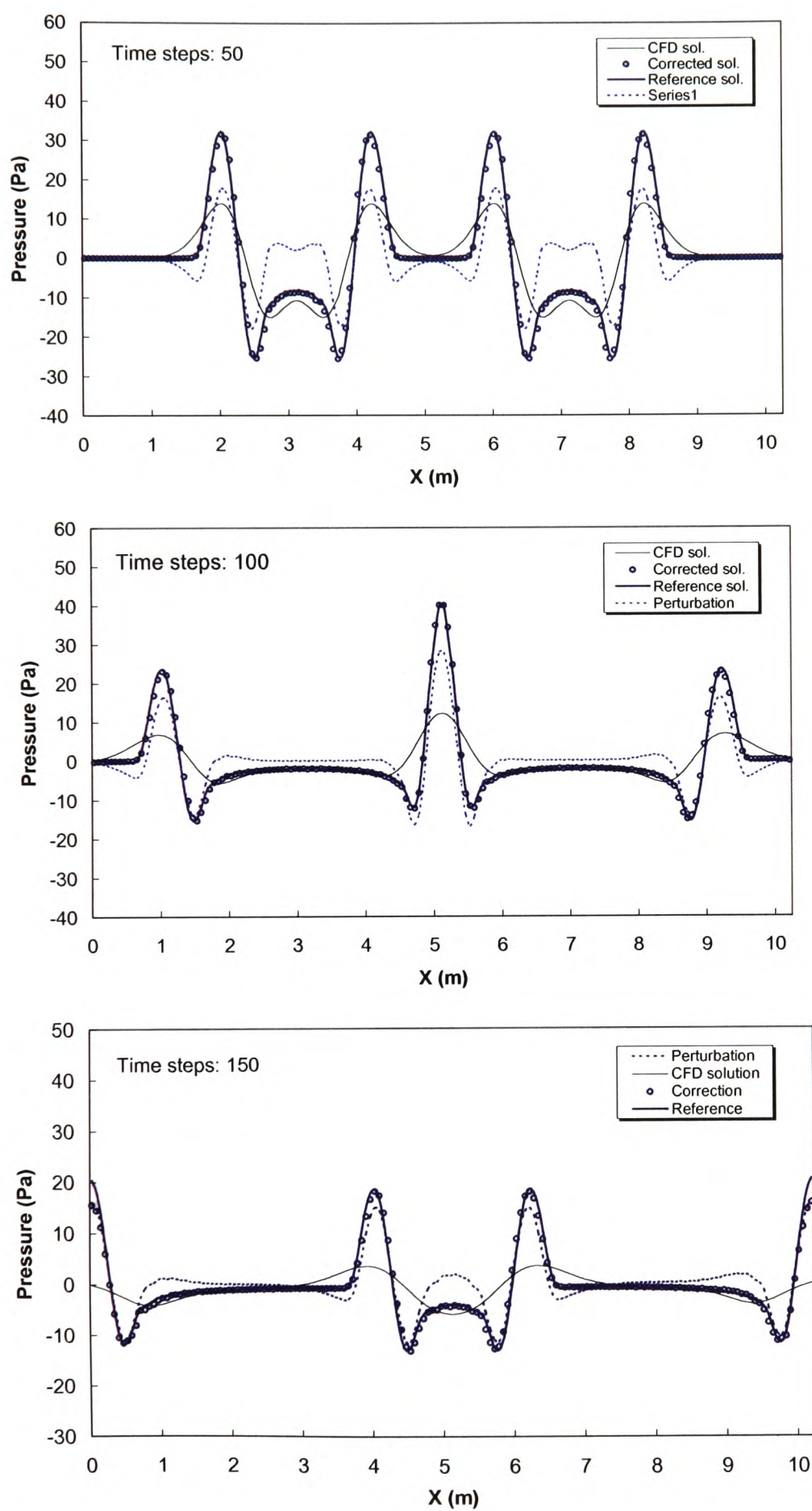


Fig. 5.11. Pressure distribution along $y = 0.03125\text{m}$ at 50th, 100th, and 150th acoustic time steps for two simultaneous pulses without mean flow

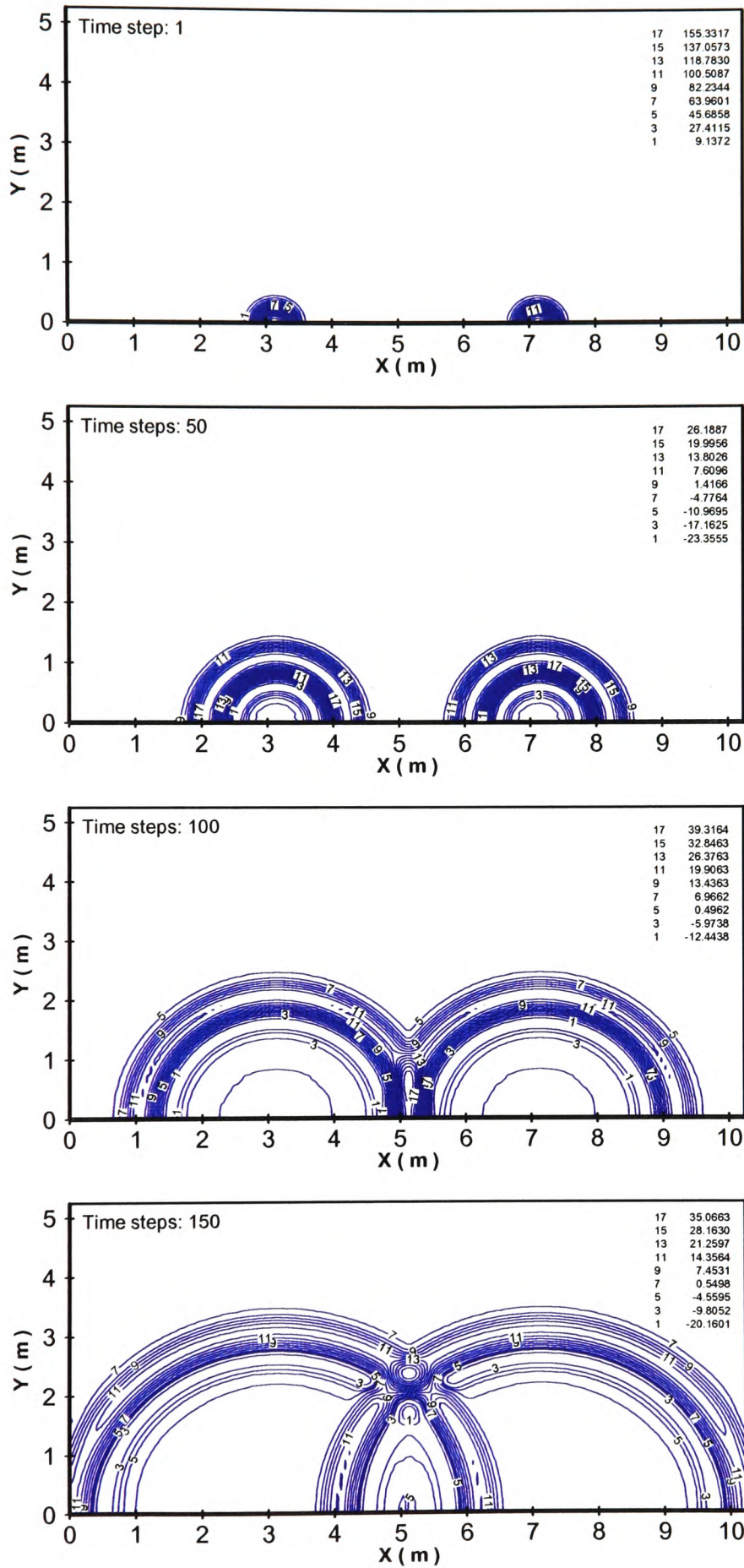


Fig. 5.12. Instantaneous corrected pressure contours at four acoustic time steps for two simultaneous pulses without mean flow

5.2.4 Reflection of a 2-D pulse from an infinite plate

The reflection of sound waves from the surfaces of bodies emerged in the flow field is common situation whenever the aerodynamic sound generates. In this section a model problem involving the reflection of a two-dimensional acoustic pulse is examined. The same acoustic pulse with a Gaussian distribution (see (4.45)) is used in this reflection computation. Obviously, this case may also test the source extracting formulation and the coupling procedure in the presence of solid wall.

In the present calculation, the infinite flat plate is added as the lower boundary of the domain. The initial pulse is placed at $x_0 = 3.9375m$ and $y_0 = 1.50m$. The mean flow is of Mach number of 0.5. The mesh spacings and time step sizes in both the CFD simulation and the acoustic calculation are the same with the prior cases. The time step, $\Delta t_{CFD} = 5\Delta t_{CAA} = 19.608\mu s$, are used in the CFD simulation and the acoustic calculation. The computational domain contains 240 x 144 cells. Figure 5.13 shows the CFD, reference and corrected pressure distribution along $y = 0.03125m$ at four acoustic time steps. The corrected pressure has a good agreement with the reference solution.

A comparison of the CFD solution with the perturbation is given in Figure 5.14. Again, small oscillation of the acoustic solution can be seen clearly. Figure 5.15 represents computed pressure along $x = 5.0m$ at four acoustic time steps. The corrected pressure contours of the reflection of the pulse by the flat plate are shown in Figure 5.16. These plots show that the acoustic pulse reaches the flat plate and is reflected off the wall creating a double pulse pattern. This indicates the interference pattern of the incident and the reflected waves is captured well by the coupling procedure via the extracted source terms.

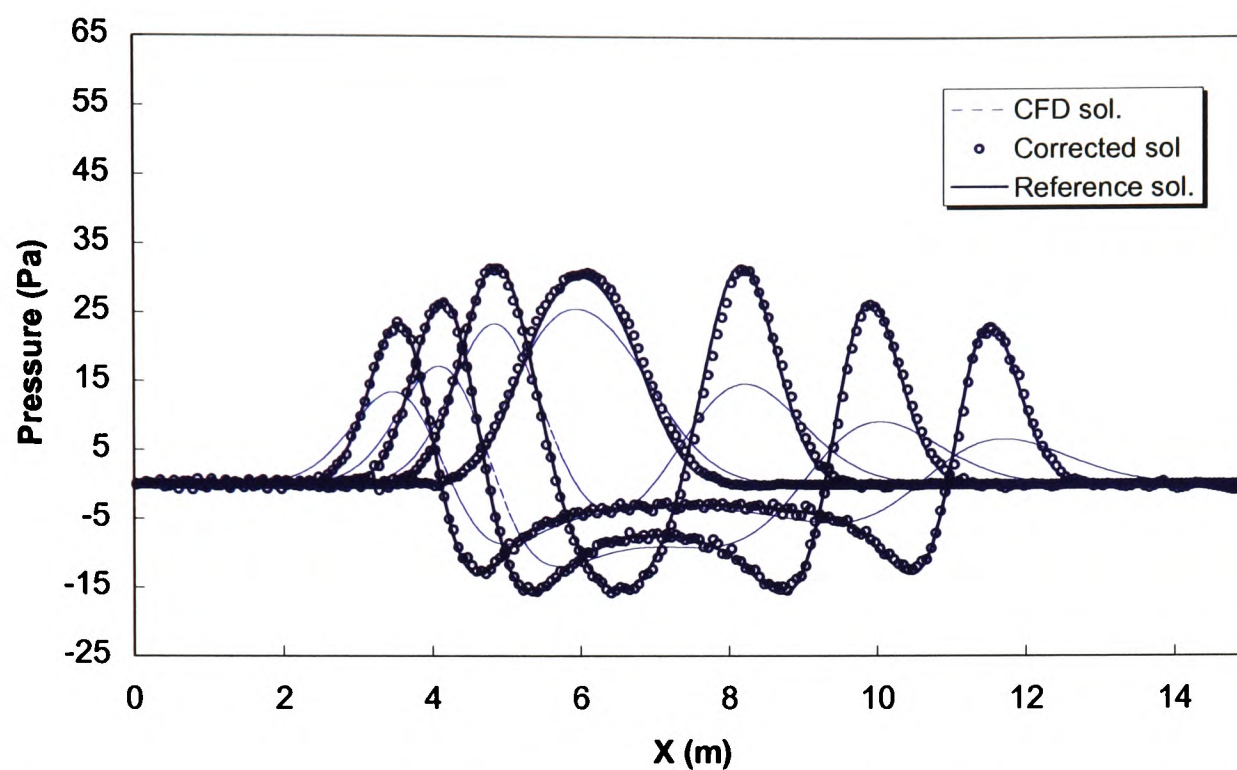


Fig. 5.13. Pressure distribution along $y = 0.03125\text{m}$ at 75th, 150th, 225th, 300th acoustic time steps for the reflection of the acoustic pulse by the infinite flat plate

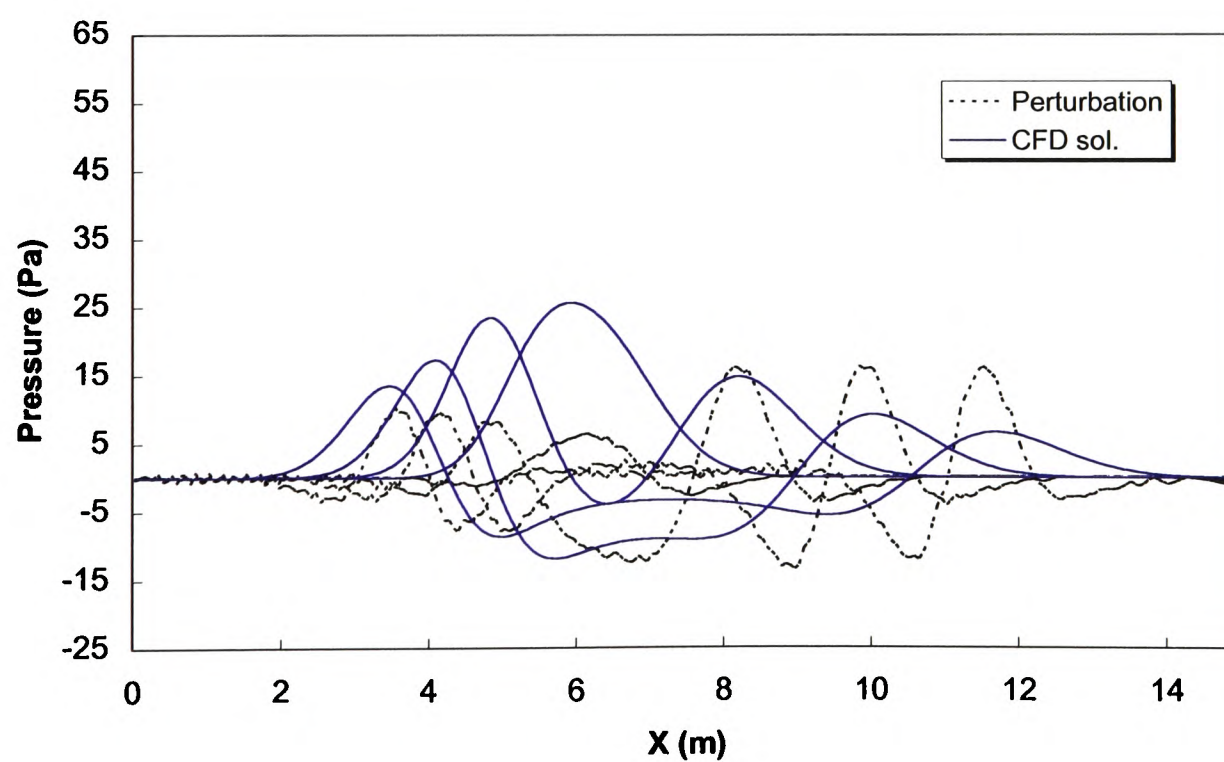


Fig. 5.14. Comparison of the CFD pressure and the acoustic perturbation pressure along

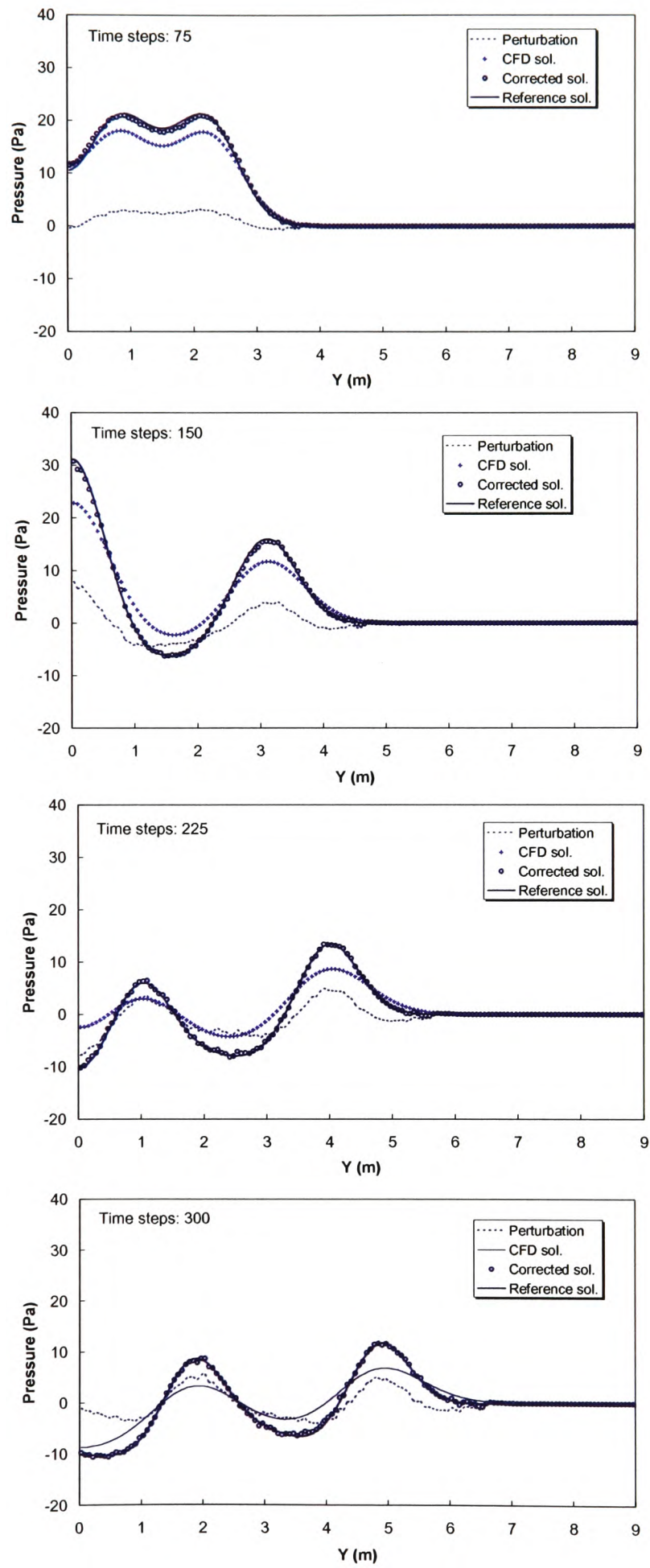


Fig. 5.15. Pressure distribution along $x = 0.5\text{m}$ at 4 acoustic time steps for the reflection of the acoustic pulse by the infinite flat plate

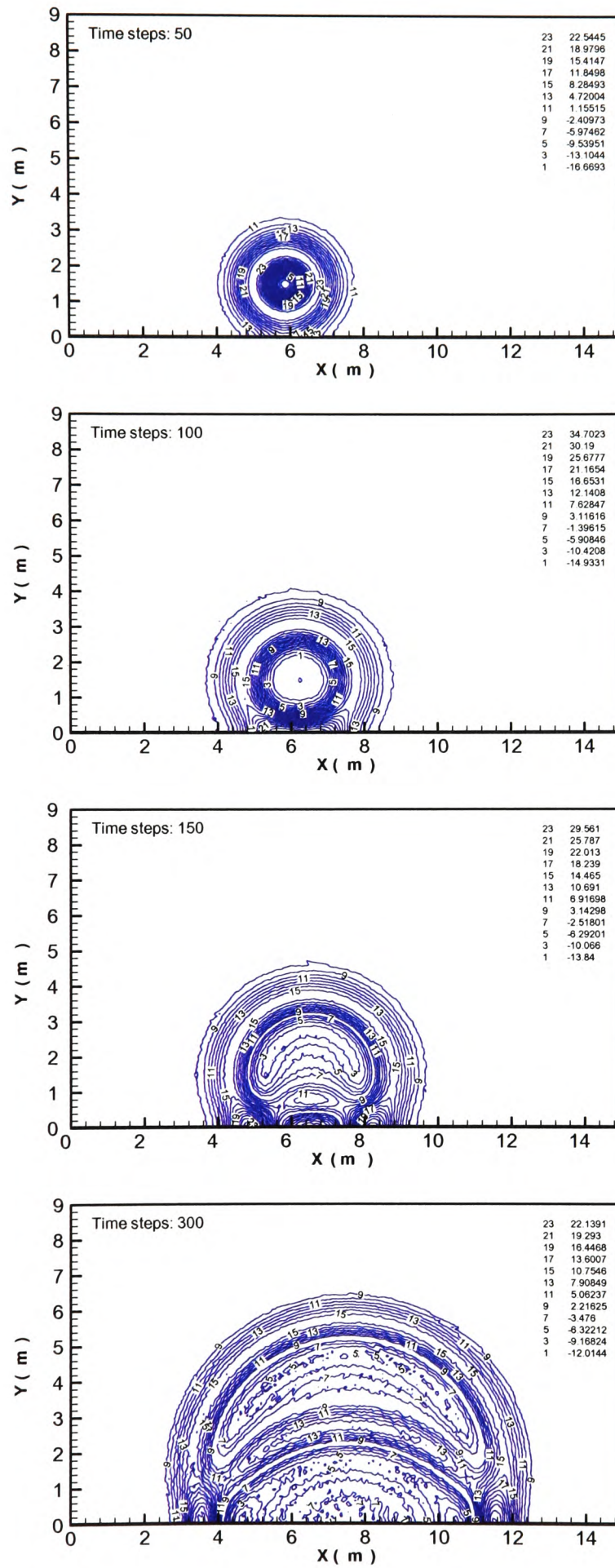


Fig. 5.16. Instantaneous corrected pressure contours at four acoustic time steps for the reflection of the acoustic pulse by the infinite flat plate

5.2.5 Scattering of a 2-D pulse by a square object

The sound waves scattering by objects is common phenomena in aeroacoustics. In order to further test the source extraction formulation and the coupling procedure, the scattering of an acoustic pulse by a two-dimensional square object within no mean flow is exemplified. The choice of the square configuration avoids the computational error due to a circular solid boundary being represented by a stepwise fashion (e.g., scattering by a circular cylinder). In this case, the pressure pulse with a Gaussian distribution used in the above section is considered (see expression (4.45)). The pressure pulse is generated at $x_0 = 7.5m$ and $y_0 = 7.5m$. A square object with a side-length of 1.5m is placed at the right-hand side of the introduced pulse with a distance of 1.5m. The centre of the square object is located at $x_0 = 9.75m$ and $y_0 = 7.5m$. In this calculation, mesh size, $\Delta x = \Delta y = 0.05m$, is used in the CFD simulation and the acoustic calculation. The computational domain contains 320 x 320 cells. The time steps used are $\Delta t_{CFD} = 4\Delta t_{CAA} = 0.00018s$. The mirroring procedure described in the section of boundary treatment in Chapter 4 is applied to every solid boundary face of the square.

Figure 5.17 and Figure 5.18 show pressure distribution for the CFD simulation, four acoustic time steps, and comparison with the corresponding reference solution. Similarly, those pressure distributions along $x = 8.225m$ and $x = 10.525m$ at the same acoustic time steps are given in Figure 5.19 and Figure 5.20. The two positions are at front of the square and behind the square object. The comparison of the corrected solutions from the coupling procedure with the reference solutions achieves a good agreement. Figure 5.21 presents the corrected pressure contours at four acoustic time steps. The scattering pattern behind and in front of the square object can be seen clearly. In addition, a comparison of time history of the corrected pressure and the reference solution at three selected observation points (point A: $x = 9.725m$, $y = 8.975m$; point B: $x = 10.975m$, $y = 8.975m$; point C: $x = 10.975m$, $y = 7.525m$) is given in Figure 5.22. Once again, a good agreement between both results is shown.

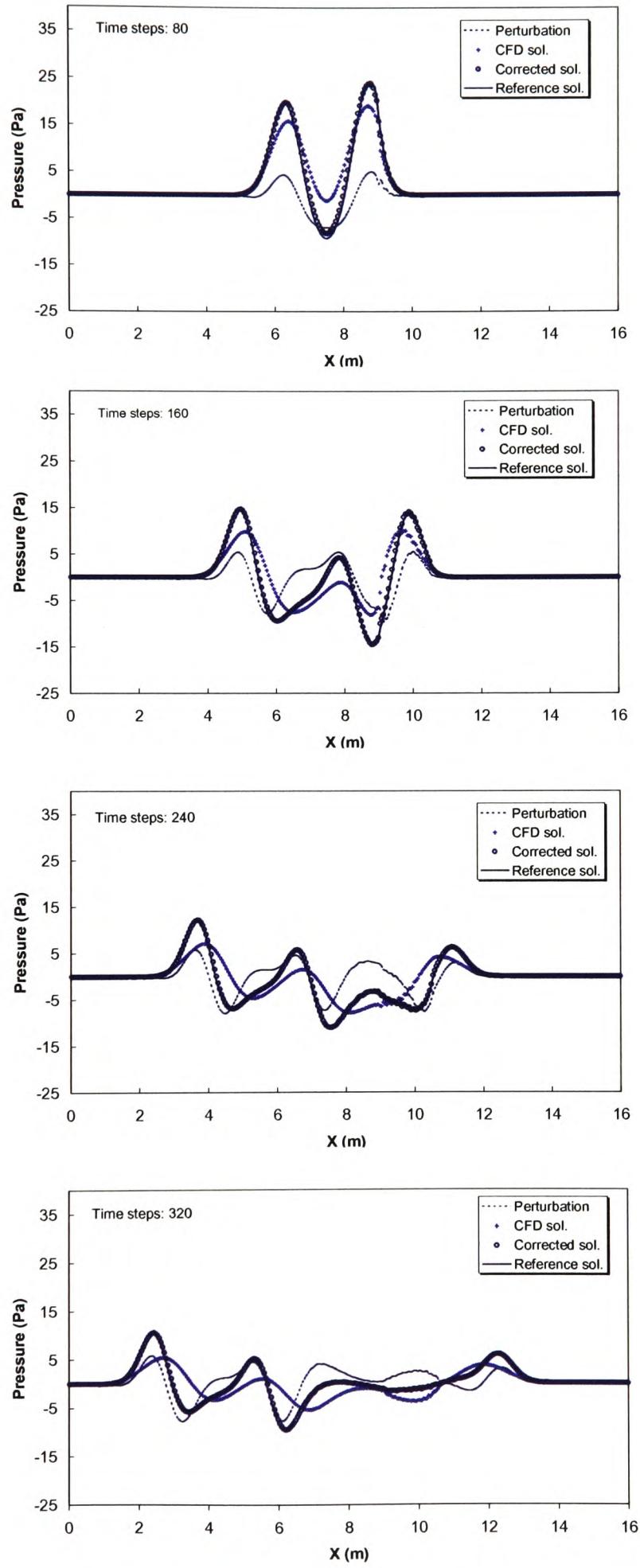


Fig.5.17. Pressure distribution along $y = 8.275\text{m}$ at four acoustic time steps for the pulse scattering by the square object

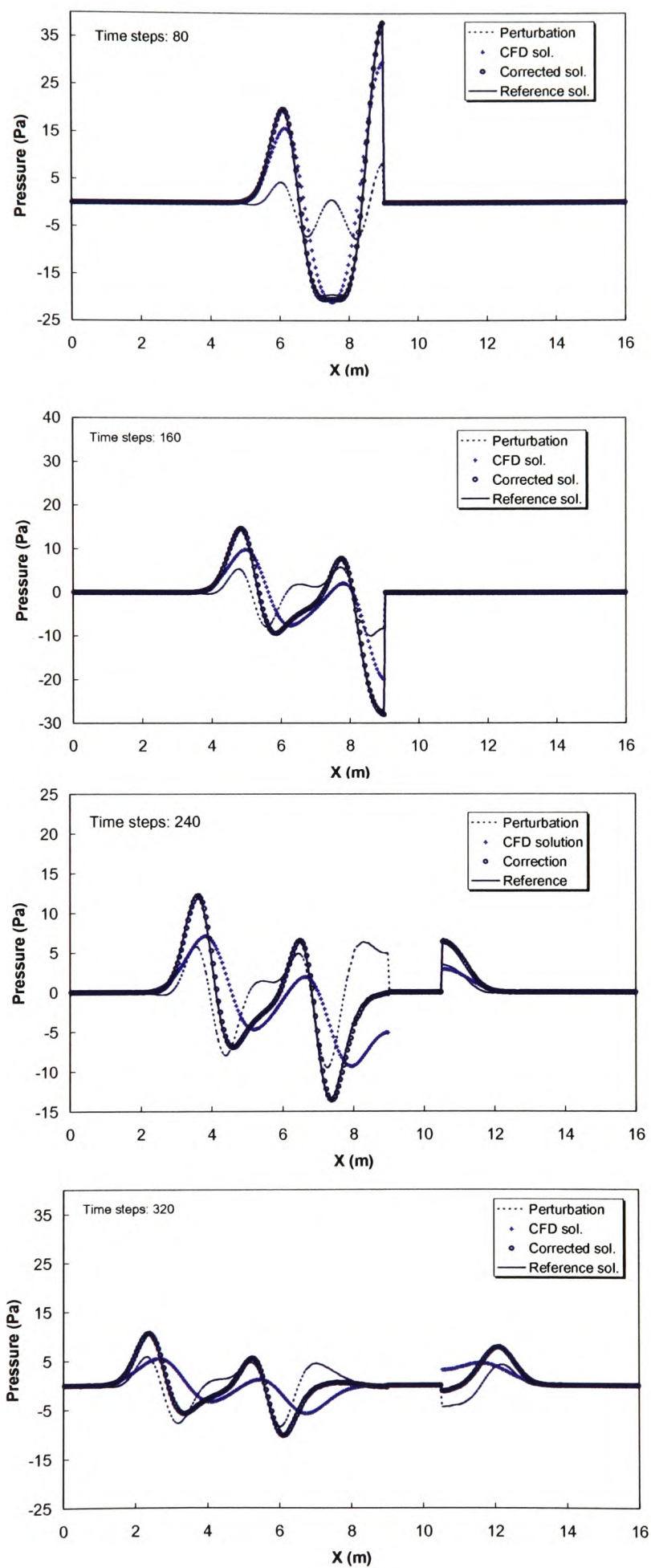


Fig. 5.18. Pressure distribution along $y = 7.525\text{m}$ at four acoustic time steps for the pulse scattering by the square object

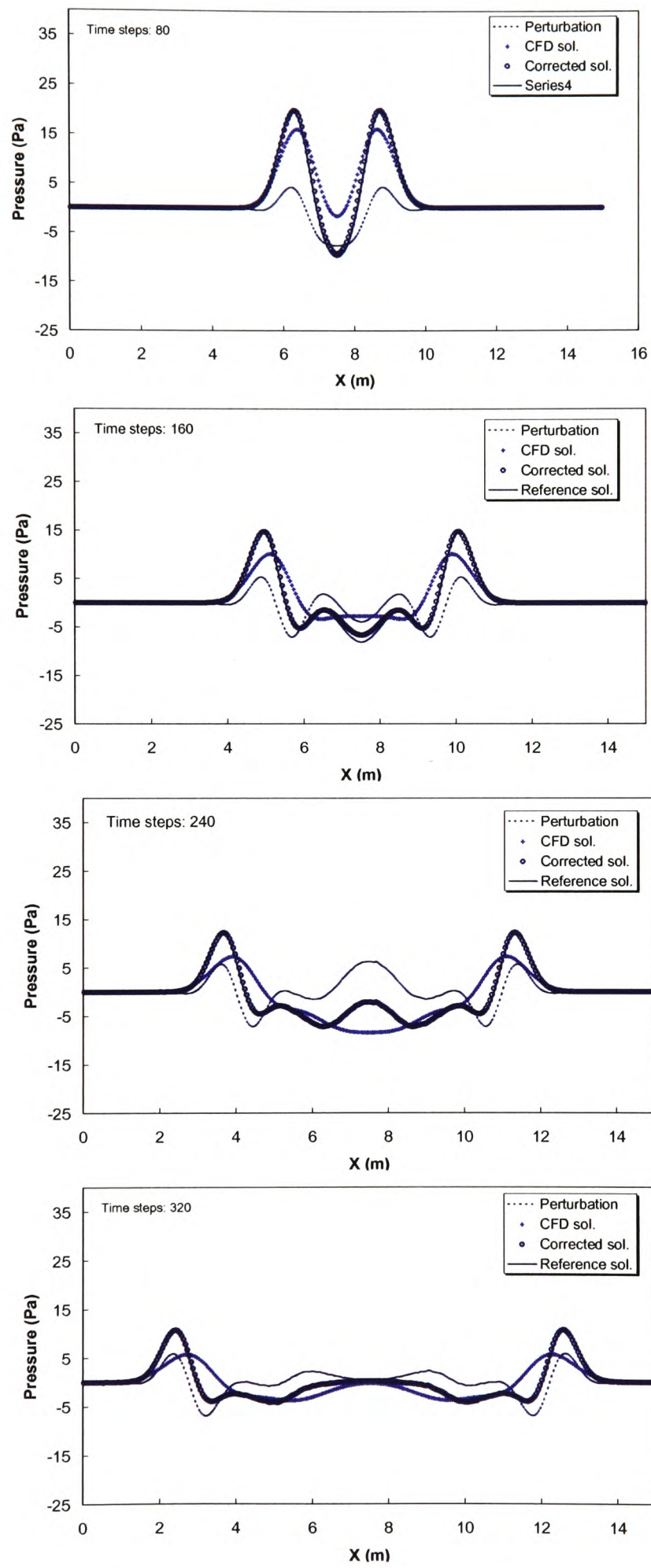


Fig. 5.19. Pressure distribution along $x = 8.225$ m at four acoustic time steps for the pulse scattering by the square object

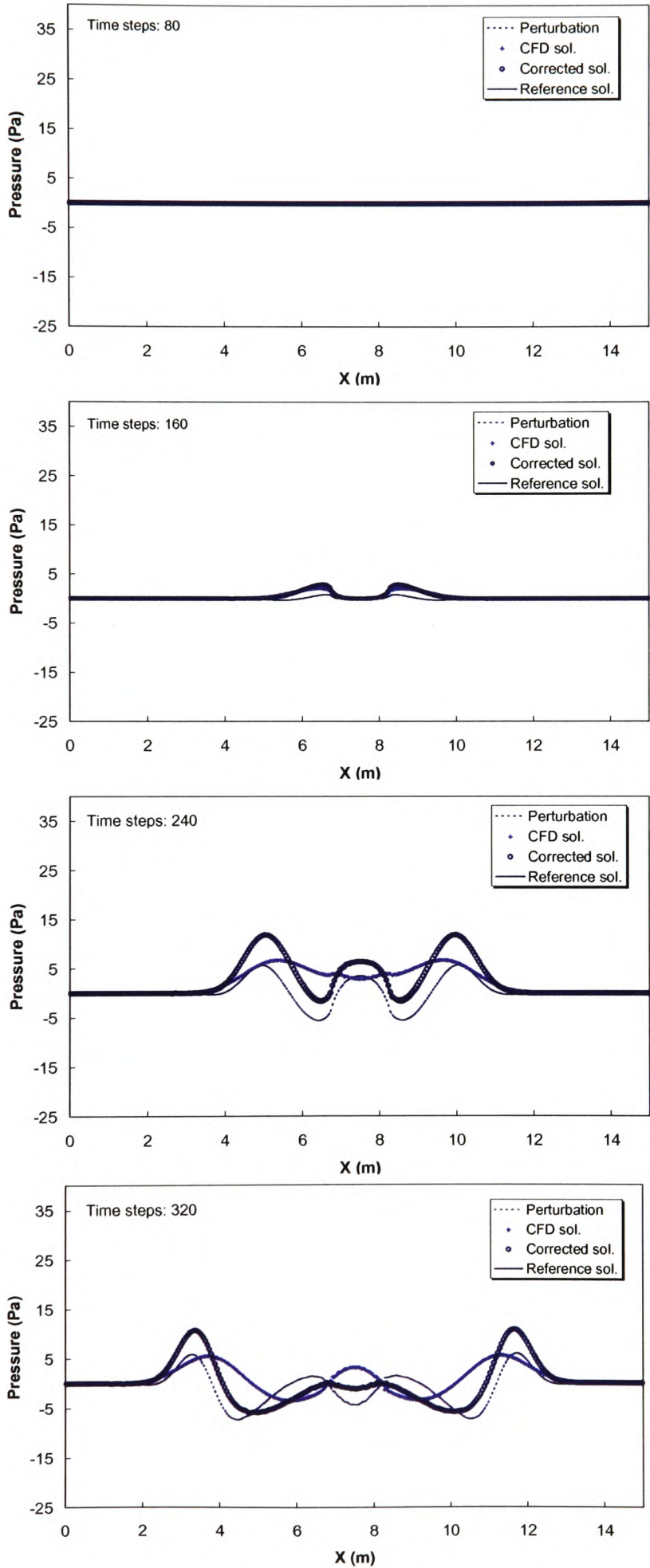


Fig. 5.20. Pressure distribution along $x = 10.525$ m at four acoustic time steps for the pulse scattering by the square object

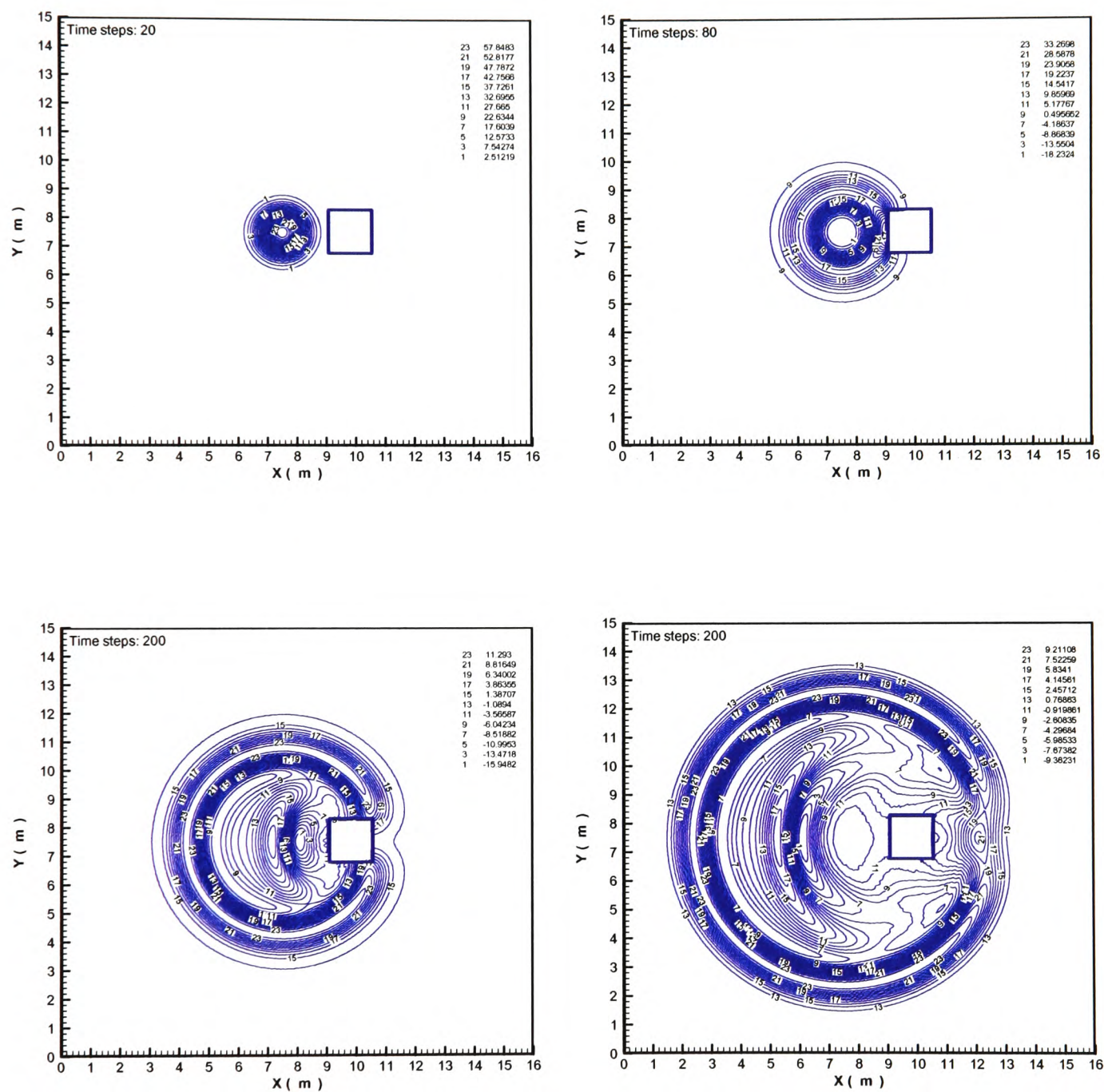


Fig. 5.21. Instantaneous corrected pressure contours at four acoustic time steps for the pulse square object

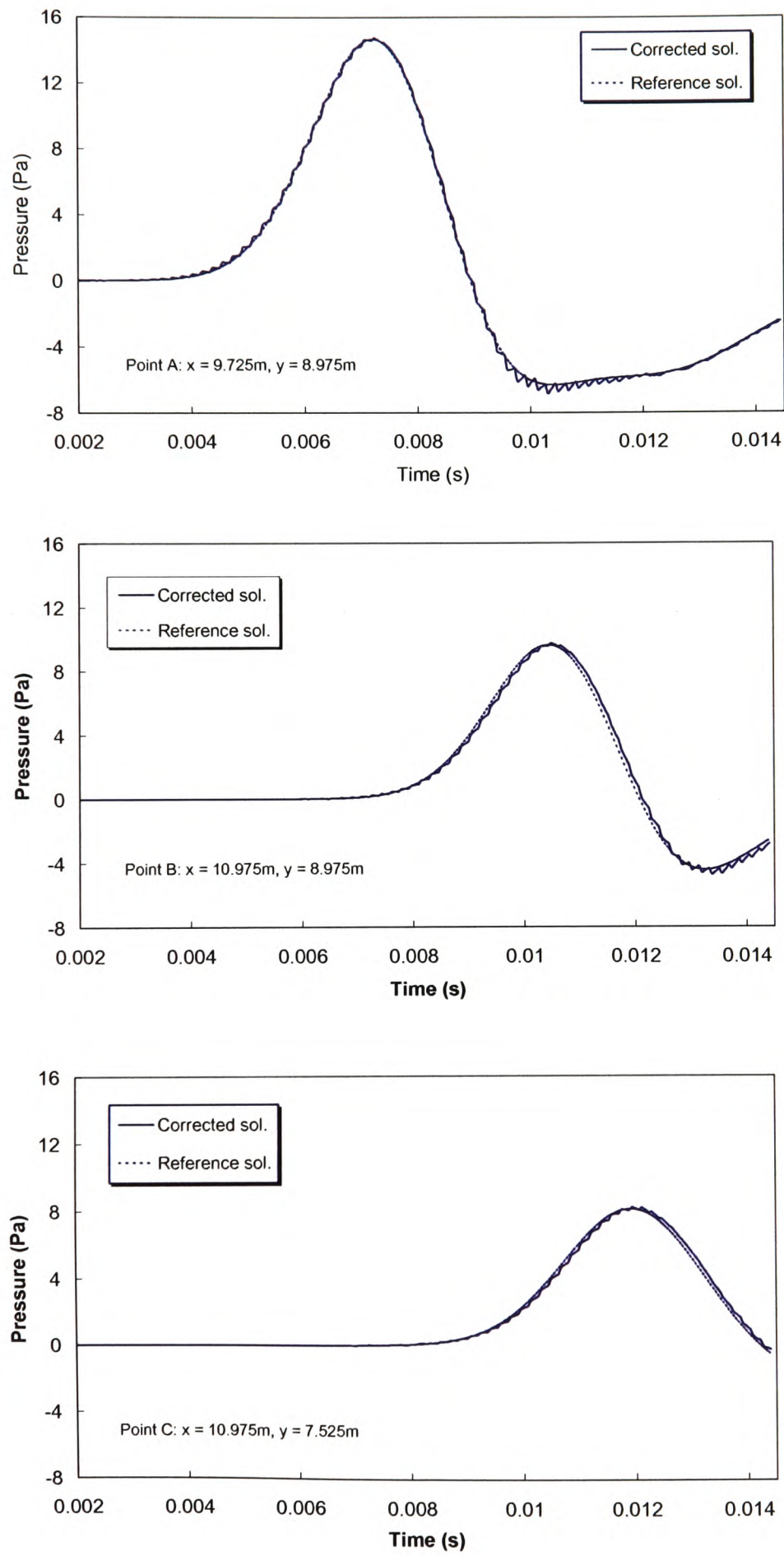


Fig. 5. 22. Time history of the corrected pressure and the reference solution at three points for the pulse scattering by the square object

Chapter 6

Preliminary Application Investigations

In the Chapter 5 investigations of some typical acoustic model problems have revealed the feasibility and usefulness of the proposed acoustic source extraction formulation, and have been used in conjunction with the described coupling procedure. Good numerical accuracy has been demonstrated through comparisons with analytical and reference solutions. However, as pointed out in the chapter, the acoustic sources in those model problems are relatively simple, and the types and locations of the sources (pulses) are all known *a priori*. In addition, the unsteady flow field does not involve complex flows. As a matter of fact, in practical engineering aeroacoustic problems the acoustic sources are very complicated (especially when turbulent flow is involved). The types (including their intensities) of the acoustic sources are generally *unknown* before simulation and calculation, and the sources inside the unsteady flow are likely to move (i.e., the locations of the sources are not known). Such situations are easily observed in jet noise, wake noise and other similar types of noise problems. In Chapter 2 it has been specifically emphasised that one of the main advantages of the source-extraction formulation is to automatically extract *various* types of aerodynamically generated sound sources contained in the unsteady flow. Hence, in order to further test the potential of the source-extraction formulation, several cases of aerodynamic sound generation and the wave propagation with somewhat engineering background will be considered below. These cases include the simulation of the acoustic field generated from a series of vortices impinging on a thin flat plate, the sound generation from a subsonic flow past a flat plate with a small angle of attack, and the flow-induced noise due to an unsteady laminar flow past a two-dimensional car-door cavity. Finally, as an attempt, the Large Eddy Simulation technique is coupled with the acoustic solver in conjunction with the source-

extraction formulation to simulate the generation and near field radiation of aeroacoustic sound from an unsteady turbulent flow over a two-dimensional open cavity.

6.1 Acoustic field of vortices impinging on a thin flat plate

Sound generation from vortices and the interaction between the vortices and the bodies in unsteady flows occurs often in many noise problems of practical interest, for example, blade-vortex interaction, edge tones, and jet noise. The motion of vortices is considered to be directly related to the source of sound generation by vertical flows and vortex-induced flows. As a simplified case, aerodynamic sound generation and its radiation from a vortex series impinging on a thin flat plate with a flow of Mach number of 0.5 is simulated.

In this case, the length of the flat plate is 1m. The thickness of the flat plate is 0.0001m. This implies that the flat plate is a thin flat plate. The thin flat plate is placed inside a background flow, and parallel to the direction of the background flow. A box surrounding the flat plate is used as computational domain. The sides of the box are located at dimensional positions of $x = -3.4\text{m}$, $x = 4.0\text{m}$, $y = -3.4\text{m}$ and $y = 3.4001\text{m}$. The bottom of the flat plate is aligned with the line of $y = 0.0\text{m}$, and the leading edge is located at $x = 0.0\text{m}$. The background mean flow is from the left side to the right side in the computational domain. In order to create the vortices impinging on the thin flat plate, a disturbance function of vertical velocity is specified within the background flow. Introducing the vertical disturbance velocity is implemented via setting up a *patch* in the CFD code. This disturbance velocity can be regarded as time dependent source of momentum in the flow. The disturbed vertical velocity is specified as: $v(t) = -0.1M_{\infty}a_{\infty}\sin(t/100 \times 2\pi)$, where M_{∞} is Mach number of the free stream flow, a_{∞} the speed of sound. The patch of the vertical disturbance velocity, the thin flat plate, the computational domain and the numerical boundary conditions used in the CFD simulation is shown schematically in Figure 6.1.

In order to accurately resolve the structure of the flow field and extract the resulting acoustic sources, a relatively fine mesh is used in the calculation of the unsteady flow. The CFD simulation mesh uses 185 x 341 Cartesian cells in the whole domain. In the region above the flat plate and the region below the flat plate contain 185 x 170 cells, respectively.

The computational mesh in the two regions has the mesh spacing 0.04m and 0.02m in x and y-direction, respectively. One row of the cell of the mesh is allotted to represent the thickness of the flat plate. This means that the mesh spacing in y-direction is 0.0001m. However, the mesh spacing in x-direction for the row of cell is still 0.04m.

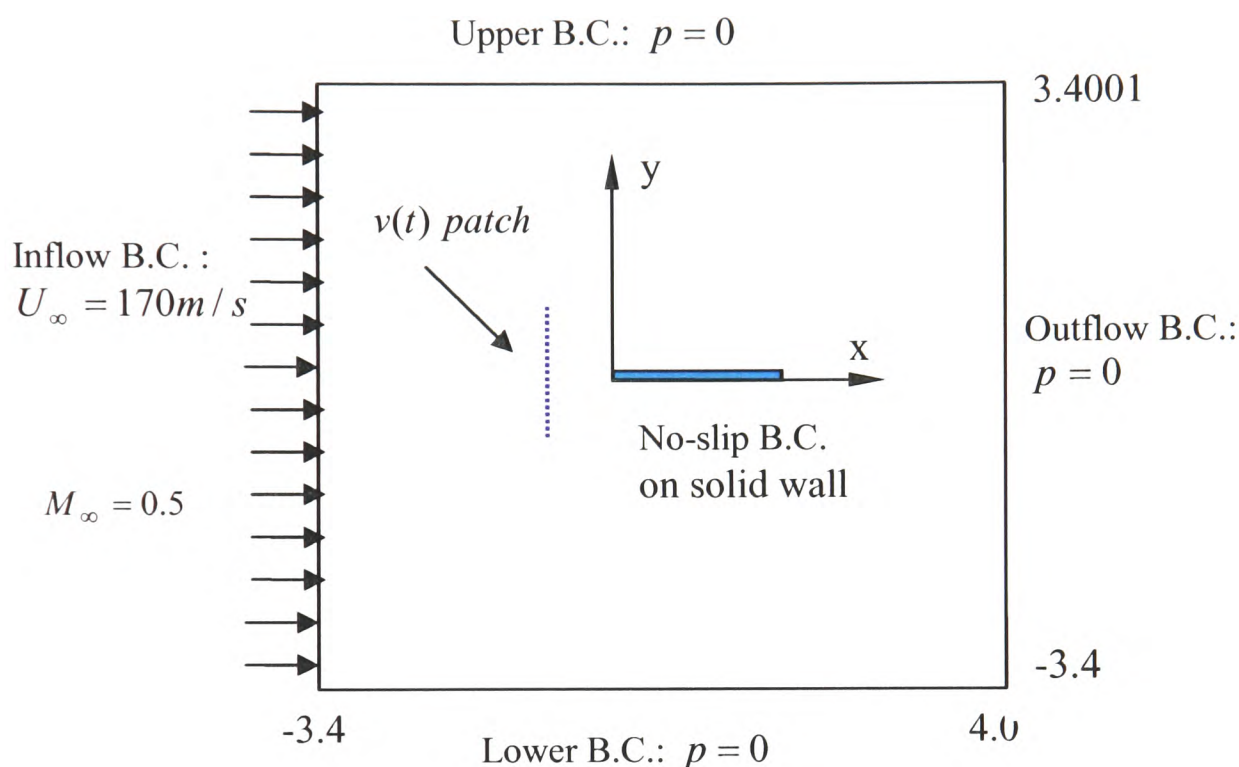


Fig. 6.1. Sketch of vortices impinging on a thin flat plate and CFD boundary conditions

In the acoustic calculation, the thickness of the flat plate is not taken into account because the acoustic solver can be used only for uniform Cartesian mesh. The non-thickness flat plate, the computational domain and the numerical boundary conditions used in the acoustic solver is shown schematically in Figure 6.2. The mesh for the acoustic calculation contains 185 x 170 uniform cells, i.e., $\Delta x_{CAA} = \Delta y_{CAA} = 0.04m$.

It should be noted that the Reynolds number based on the flat plate length is about 1.1×10^7 . Strictly speaking, the unsteady flow field due to the introduced sinusoidal velocity disturbance is of turbulence nature. However, in the present unsteady flow simulation, no turbulence model is employed.

The time step used in the CFD simulation is taken to be $0.625\mu s$. A time step of $0.25\mu s$ for the acoustic calculation, which is determined following numerical stability limit,

is used for the time integration. In the present investigation, the CFD simulation runs 120 time steps. At the 60th time step the introduced disturbance of the vertical velocity is switched off. The acoustic simulation runs 300 acoustic time steps.

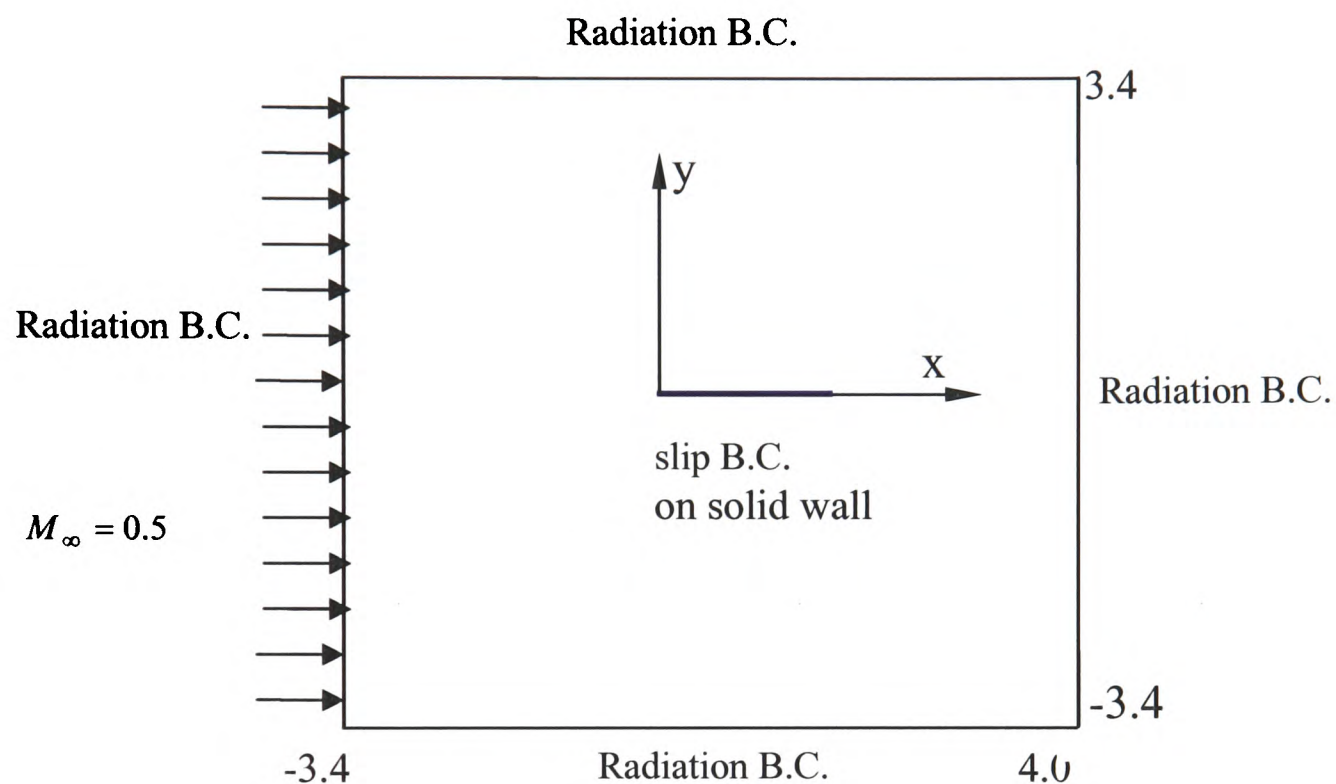


Fig. 6.2. Computational domain and boundary conditions for the acoustic calculation

The computed velocity perturbation vectors (i.e., the mean velocity has been subtracted before plotting) in the unsteady flow field at four CFD time steps are shown in Figure 6.3. These vector plotting depict the perturbation and the structure of the unsteady flow field caused by the generated vortices and the interaction between the vortices and the thin flat plate. Except for the introduced vortices, some vortices from the interaction clearly occur at the upper surface and low surface of the flat plate. These vortices are brought toward downstream by the background flow. The small perturbation vortex shed from the trailing edge of the flat plate is also seen. These vortices will make contribution to the generation of aerodynamic sound.

The structure of the three sound source terms obtained from the source-extraction formulation (i.e., Eq.(2.90)) on the acoustic mesh at two acoustic time steps is displayed in

Figure 6.4, Figure 6.5 and Figure 6.6. It can be seen clearly that the sound sources are attributed mainly to the introduced vortices and the resulting interaction vortices.

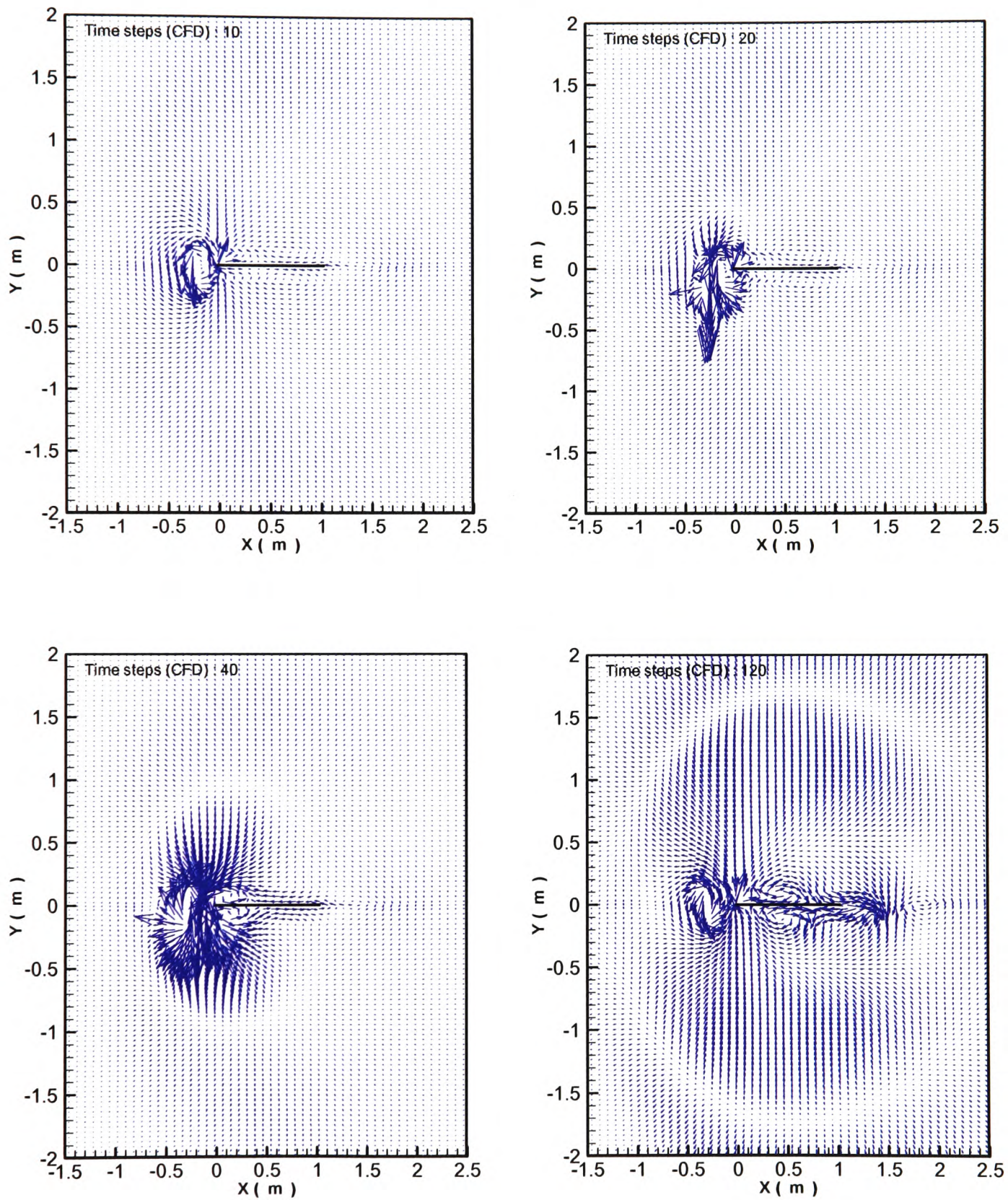


Fig. 6.3. Perturbation velocity vectors in the unsteady flow field at 4 different CFD time step

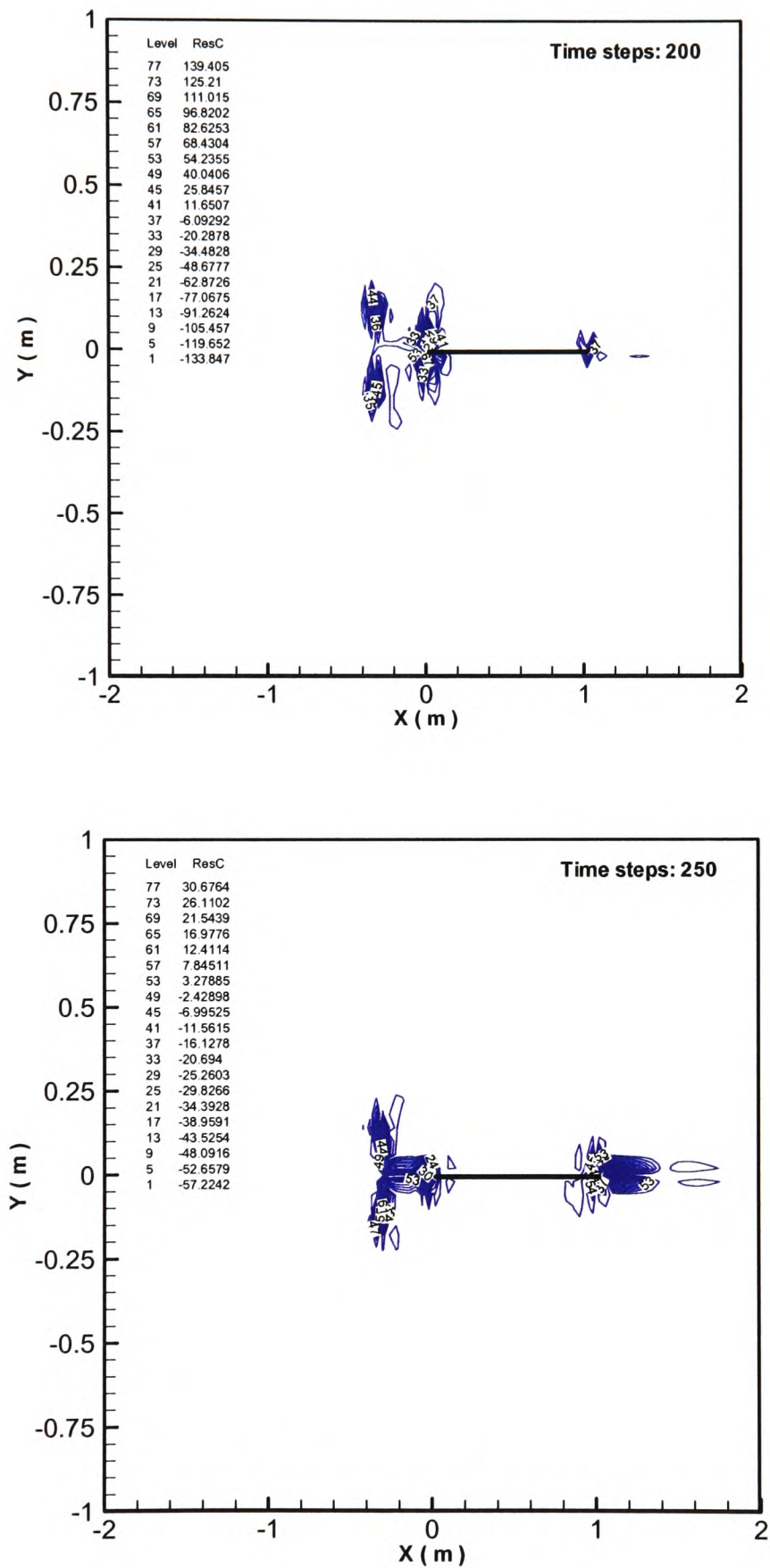


Fig. 6.4. Contours of the acoustic source term, \bar{R}_c , in Eq.(2.90) at the 200th and the 250th acoustic time step

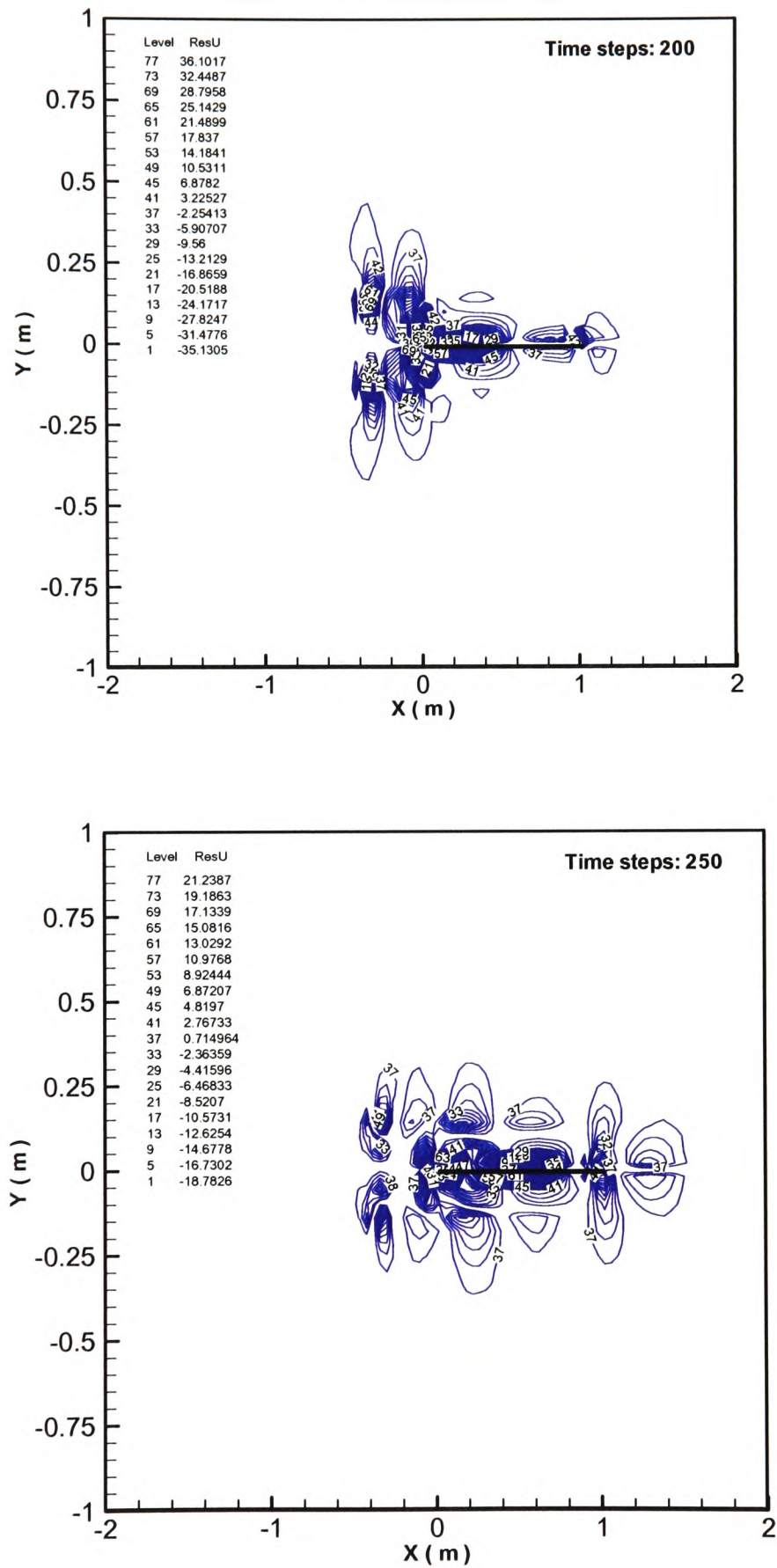


Fig. 6.5. Contours of the acoustic source term, $\bar{R}_{m,x}$, in Eq.(2.90) at the 200th and the 250th acoustic time step

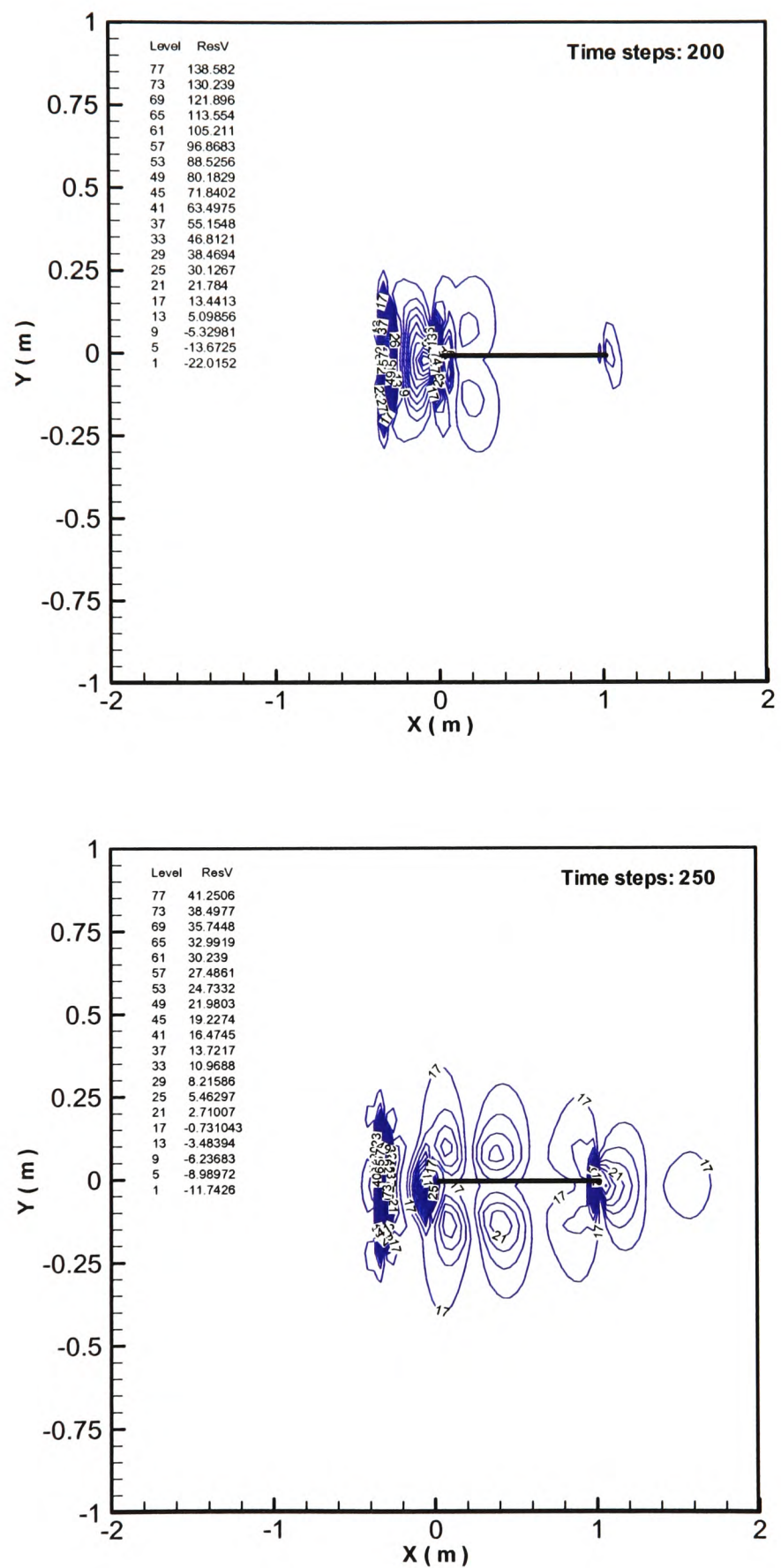


Fig. 6.6. Contours of the acoustic source term, $\bar{R}_{m,y}$, in Eq.(2.90) at the 200th and the 250th acoustic time step

The acoustic perturbation pressure as a function of time at different locations above and below the flat plate is plotted in Figure 6.7. In this graph, the numbers refer to the number of the cells monitored above and below along the central mesh cell column. These curves of perturbation pressure time history agree well with our expectation.

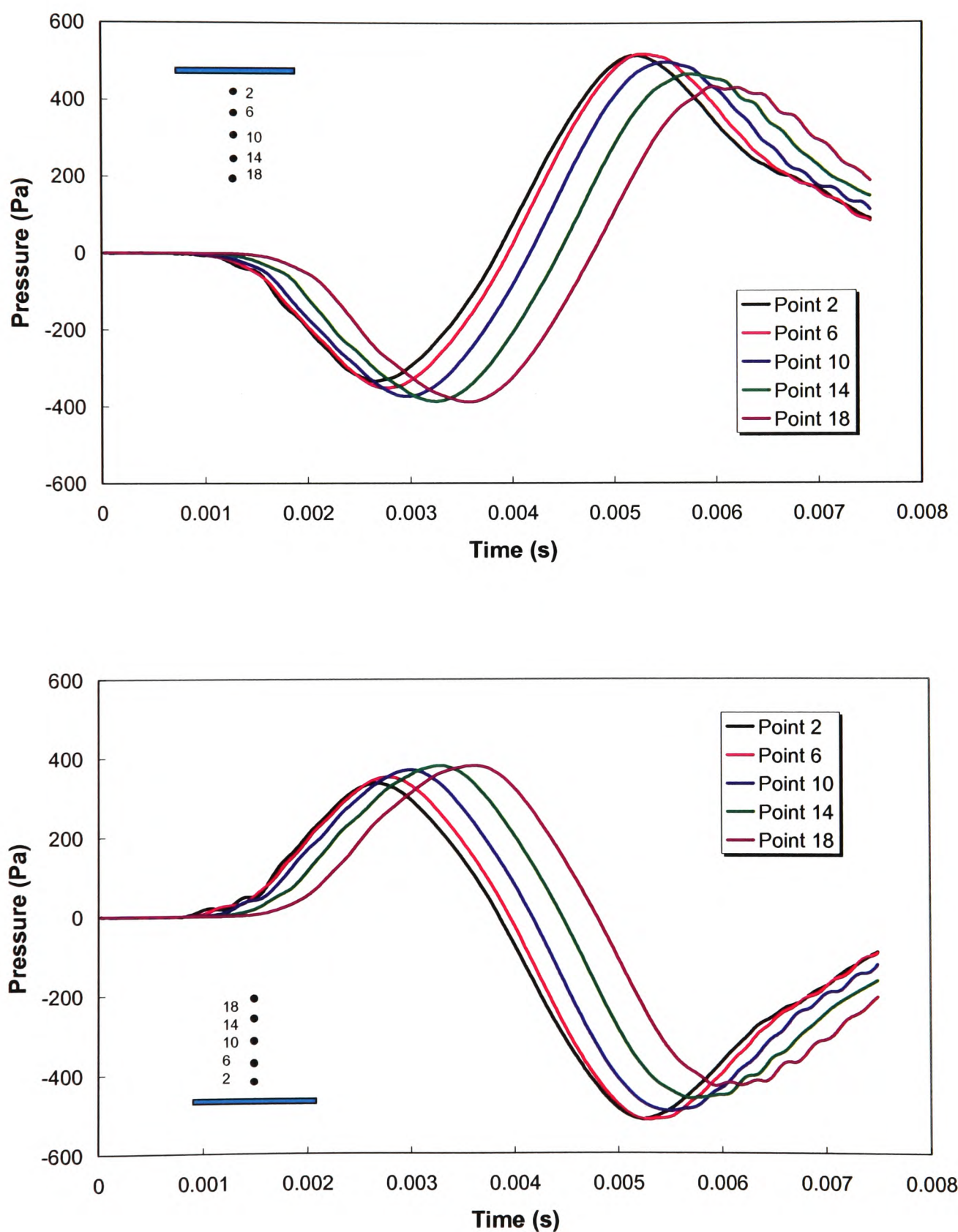


Fig. 6.7. Perturbation pressure in the specified cells above and below the flat plate

Instantaneous corrected pressure contours at four acoustic time steps are shown in Figure 6.8. Correspondingly, the instantaneous perturbation pressure contours at the same acoustic time steps are given in Figure 6.9.

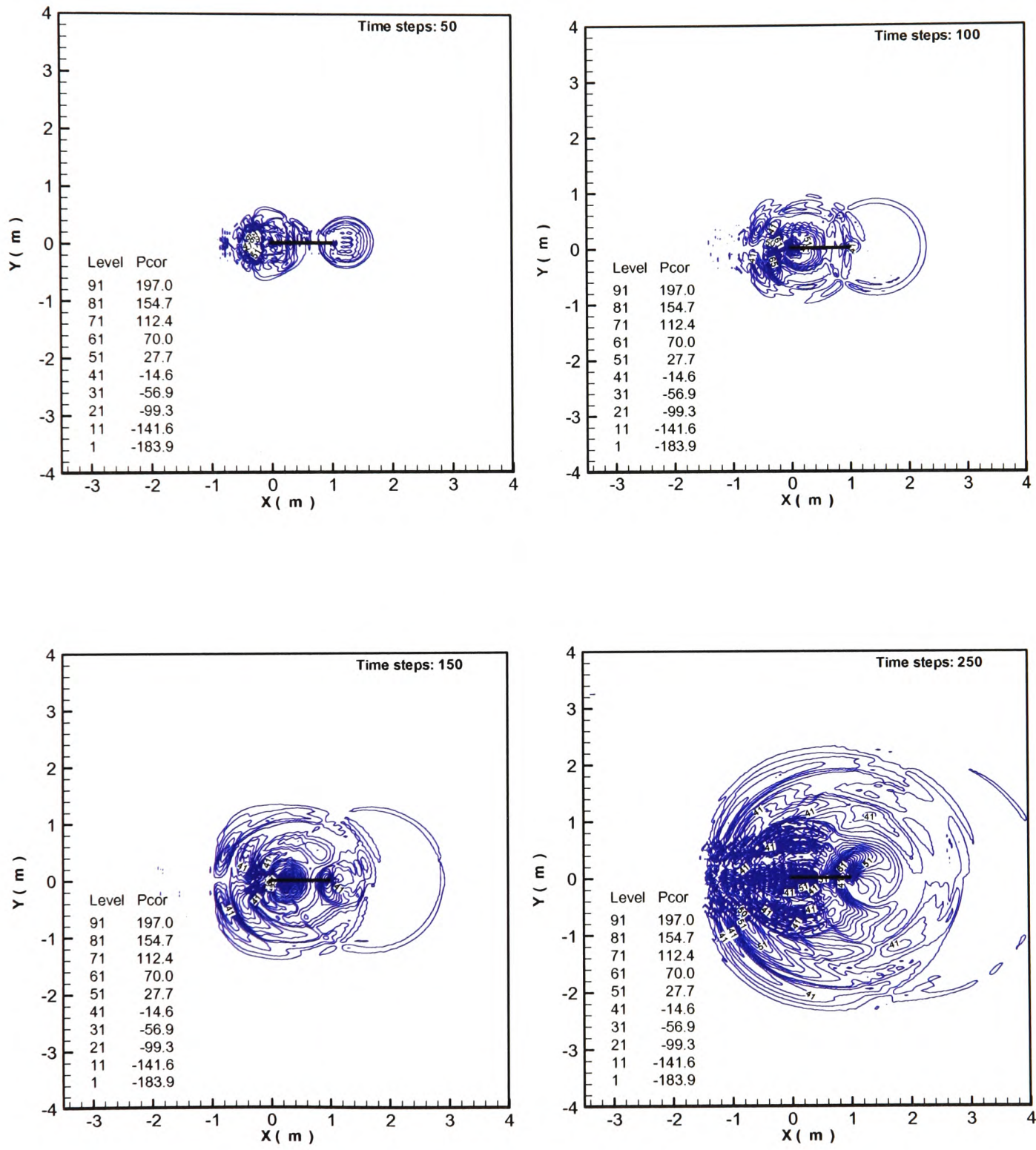


Fig. 6.8. Instantaneous corrected pressure contours at 4 acoustic time step for the vortices impinging on the thin flat plate

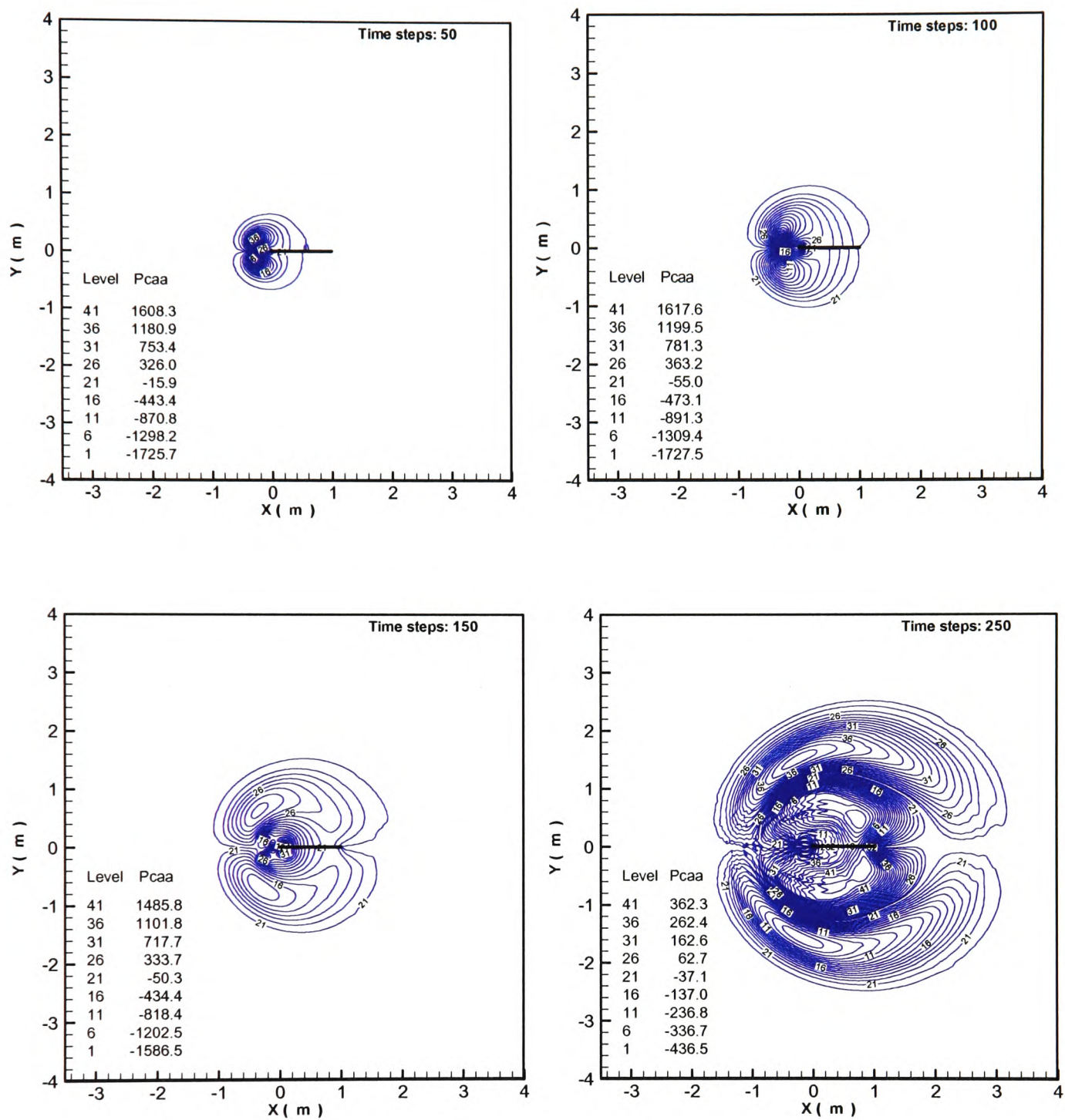


Fig. 6.9. Instantaneous acoustic perturbation pressure contours at 4 acoustic time steps for the vortices impinging on the thin flat plate

The difference between the corrected pressure and the perturbation pressure is displayed clearly. The process of the sound generation and the resulting propagation may be seen. The acoustic waves generate from the vortex patch and the flow interaction around the flat plate, and propagate outwards with the development of the flow. Note that the acoustic wave generated at the trailing edge of the plate will interact with the acoustic waves from the vortex patch and the leading edge. However, its intensity is relatively weak. There is no analytical validation for this example, but the results obtained are physically reasonable.

6.2 Sound generation due to a subsonic flow past a thin flat plate

Generally, an unsteady flow may probably be initialized when a freestream passes a thin flat plate with an angle of attack. Aerodynamic sound generation and its radiation due to a subsonic flow past a thin flat plate with a small angle of attack are simulated in this section. In this case, geometrical parameters of the flat plate are as same as in the above case. Compared to the above case, the vertical velocity disturbance patch is removed and the freestream flow pasts over the flat plate with a small incidence. The Mach number of the freestream flow is taken to be 0.5. The angle of attack is 4 degrees. The computational domain is set to: $-3.4m \leq x \leq 4.4m$ and $-4.0m \leq y \leq 4.0001m$. In the calculation of the unsteady flow, 195 x 401 Cartesian cells are used, whereas the calculation of the acoustic field contains 195 x 200 cells. This means the computational mesh in the above and the below regions in CFD simulation is two times finer in the direction perpendicular to the plate than the corresponding mesh for the acoustic calculation. The time step used in the CFD simulation is taken to be 12.5ms. The acoustic time step is 0.25 μ s. In the present calculation, the CFD simulation runs for 60 CFD time steps. The acoustic calculation runs for 300 acoustic time steps.

Similarly, the computed perturbation velocity vectors in the unsteady flow field at four CFD time steps are presented in Figure 6.10. Compared with Figure 6.3, it can be seen that the perturbation velocity vectors are different from that in the case of the vortices impinging on the flat plate. Some small vortices along the above and under the surface of the flat plate are not found. For the case in the previous section, the background flow is parallel with the flat plate, and the plate is very thin. It can be infer that the freestream flow itself does not basically contain any vortices. Therefore, those vortices around the flat plate come mainly from the interaction between the introduced velocity disturbance and the plate. Due to the free stream with an angle of attack in this case, relatively strong disturbance will occur in the leading edge and trailing edge of the plate. This is demonstrated clearly in Figure 6.11. A large scale acoustic wave radiates toward the far field. At the same time, another wave is generated at the trailing edge. This wave interacts with the large scale

wave, and propagates to the upstream and downstream. Clearly, the generation of the sound from an incident flow past initially a thin flat plate is different from the case in section 6.1.

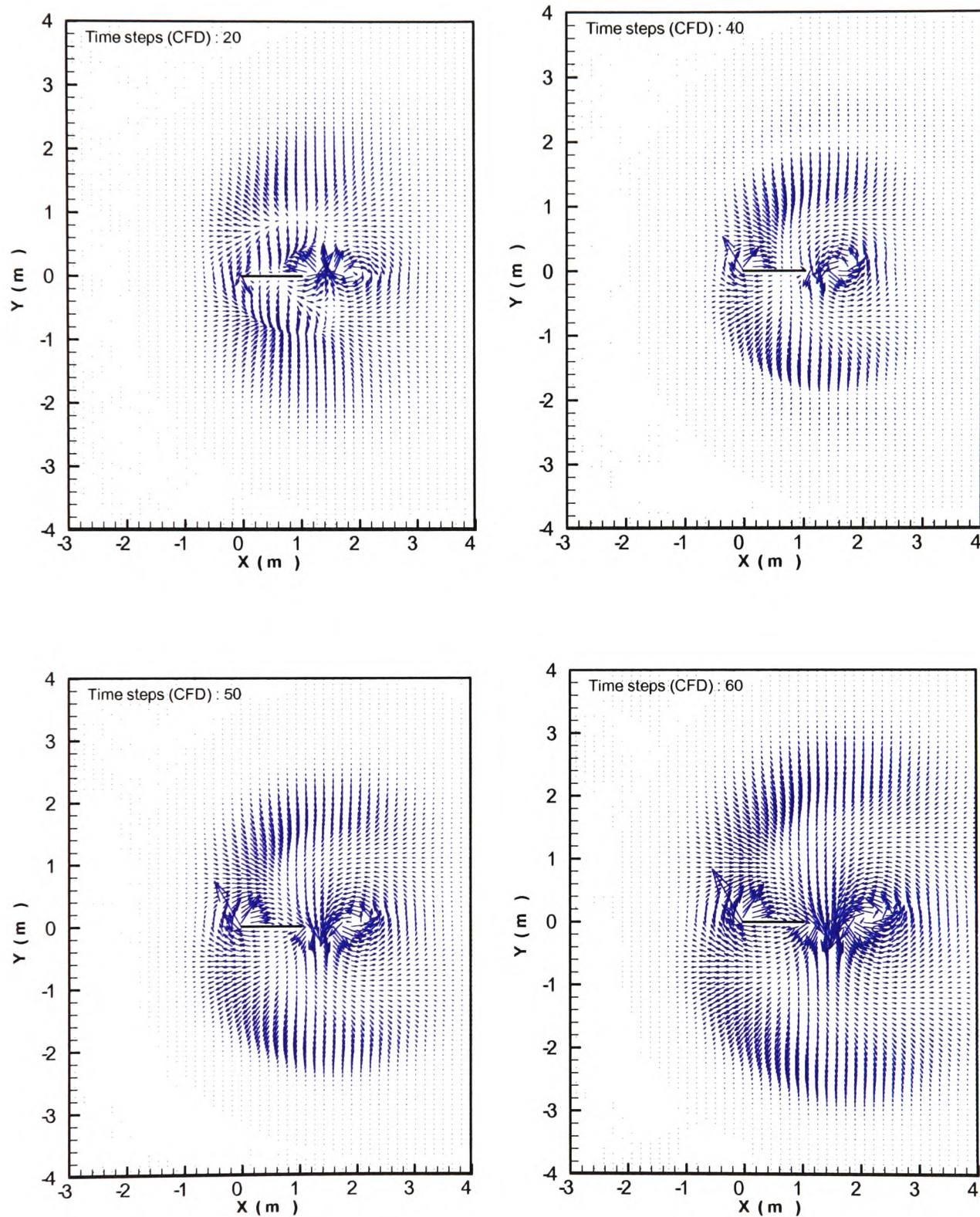


Fig. 6.10. Perturbation velocity vectors in the unsteady flow field at 4 different CFD time steps

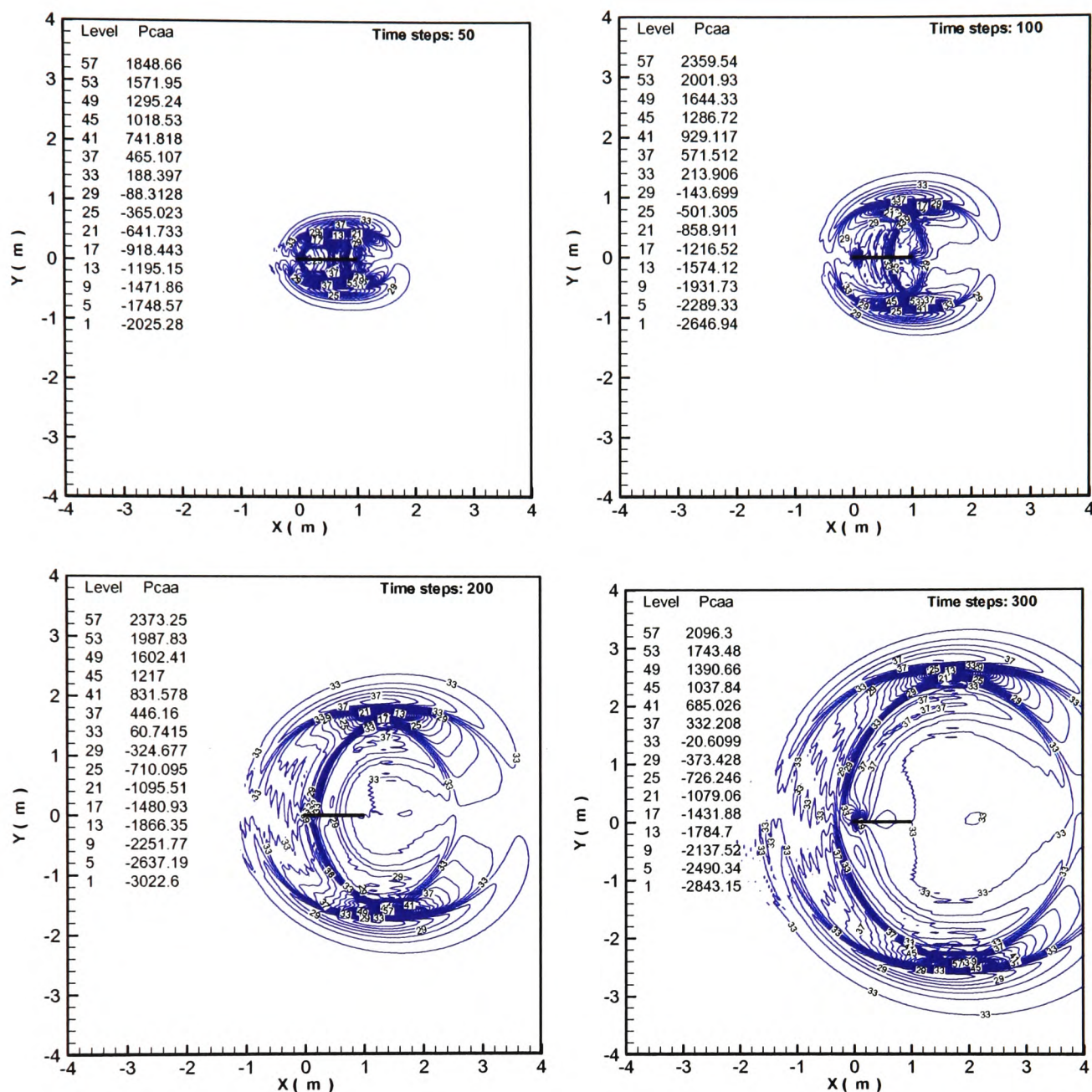


Fig. 6.11. Instantaneous acoustic perturbation pressure contours at 4 acoustic time steps

These results and some results of model problems, together with a detailed derivation of the acoustic source extracting formulation described in the Chapter 2, are presented in two submitted journal papers [Wang et al., 2003a; 2003b].

6.3 Flow-induced cavity noise

The investigation of the above two cases has reveals preliminarily the potential of the new acoustic source terms formulation in extracting aerodynamically-generated sound sources from the unsteady flow.

As we all know, the flow past various cavities has been extensively investigated numerically and experimentally due to a wide variety of physical phenomena subject to this type of flow and their engineering application. The flow induced cavity noise has attracted considerable attention because it has been identified as a common noise source in many transport systems. It is also a major source of automobile aerodynamic noise due to flow over door seals or gaps. The reduction of such flow-induced noise can offer a commercial advantage in the automobile industry by creating a more comfortable and environmental friendly vehicle. The mechanism of sound generation of a cavity flow comes from a self-sustained oscillation process involving shear layer instability, the growth of vortices in the shear layer, and the impinging of the vortices on the trailing edge of the cavity. However, the calculation of such flow-induced cavity noise is currently a challenging problem due to its flow complexity and enormous disparities in the length and time scales involved in the unsteady viscous flow simulation and the aeroacoustic calculation. In this section such a more realistic aeroacoustic problem, i.e., the flow-induced cavity noise in self-sustained oscillations in a low speed flow, is investigated. The objective is to reveal further the application potential of the source-extraction formulation, and simulate the unsteady flow field and the flow-induced acoustic field.

In the present calculation, a low speed flow over an automobile door cavity configuration is considered. The geometry of the cavity and the dimensions of the computational domain are depicted in Figure 6.12.

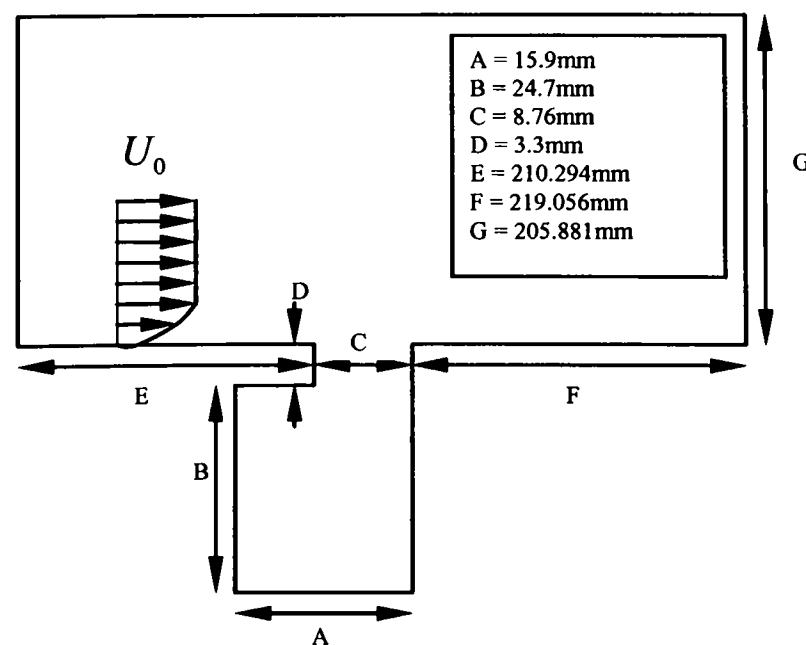


Fig.6.12. Schematic of the car door cavity and the computational domain sizes

The velocity of the streamflow is taken to be $U_0 = 50.9 \text{ m/s}$, which is equivalent to Mach number of 0.147. Hence, the flow may be assumed to be incompressible. The Reynolds number based on the cavity base length is about 53,266. However, the corresponding Reynolds number based on the displacement thickness is about 1625. This is certainly within the range of laminar instability of the free shear layer (i.e., $Re_{\delta^*} = 600 \sim 3000$). The simulation of the unsteady flow is done by assuming a laminar flow instead of turbulent one. The non-uniform computational mesh around the cavity for the CFD simulation is shown in Figure 6.13.

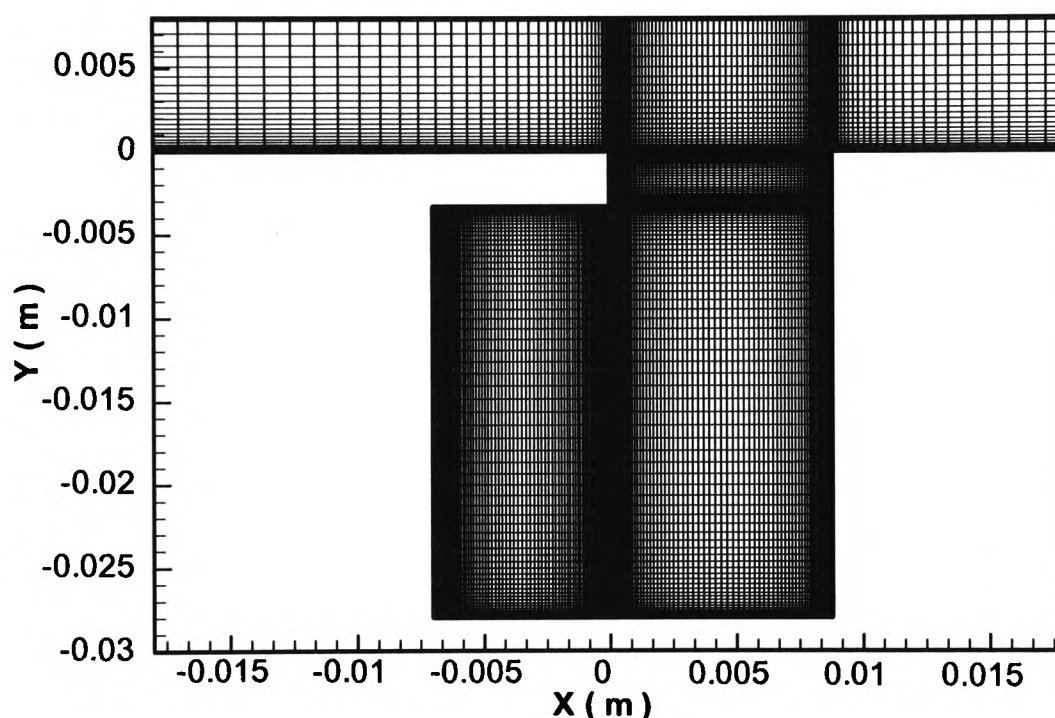


Fig. 6.13. Computational grid around the cavity mouth and the cavity

In this problem, the behaviour of the shear layer and viscous effects are important. To accurately resolve the viscous shear layer along the cavity mouth and the viscous effects near walls, the mesh is refined significantly in these regions. In contrast the mesh is stretched towards the region far away from the cavity mouth. In the present CFD simulation, a total of 35,900 mesh cells are used. There are 90 cells in the streamwise direction for the upstream region. In the cavity mouth, 80 cells are used along the mouth part, 40 cells across the mouth opening. Under the cavity-lip and inside the cavity, 170 by 170 cells are used. For the downstream region, 90 cells in the flow direction are distributed

to resolve the convection of the vorticity waves. Over the cavity 80 cells are used in the y -direction from the wall to the top boundary. For the mesh, the minimum mesh spacing is about $7.48 \times 10^{-6} \text{ m}$. After preliminary computation, this mesh is found to be able to resolve main flow structures within and around the cavity.

In the present simulation, we have not imposed a boundary layer profile at the inflow boundary; instead, a naturally developed boundary layer is obtained from a specified uniform freestream inflow boundary condition. No-slip boundary conditions are imposed on all solid walls. For the specified upstream distance in the computational domain, the boundary layer develops to a thickness of 10% cavity base length close to the trailing edge of the cavity lip. Figure 6.14 shows the computed boundary layer velocity profile.

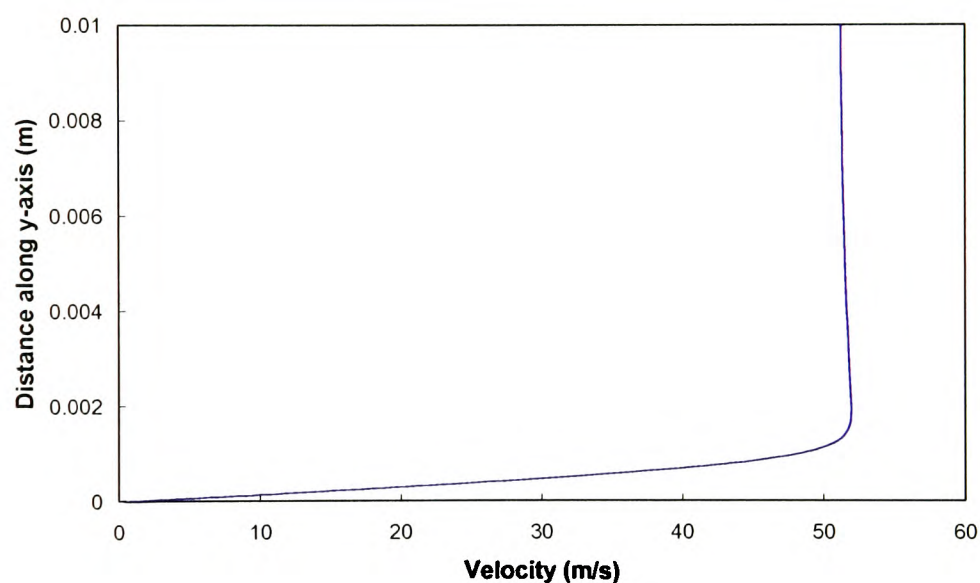


Fig. 6.14. The computed boundary layer velocity profile in the vicinity of the trailing edge of the cavity lip

For the unsteady flow simulation, a steady solution is first obtained, and restarted then with the steady solution as the initial field in the transient computation. The time step for the CFD simulation is $0.12 \mu\text{s}$. The oscillation of the unsteady flow develops quickly. After about 10,700 CFD time steps, the oscillation enters a stable state, and is able to repeat itself as a self-sustained oscillation. A few selected points are used to monitor the unsteady oscillation. Figure 6.15 displays the time history of the pressure and normal component of the velocity at the corner right before the rear cavity edge. Figure 6.16 shows the time history of the pressures at the upper corner of the trailing edge of the lip, the centre of the left vertical wall inside the cavity, and a certain point away from the cavity in downstream.

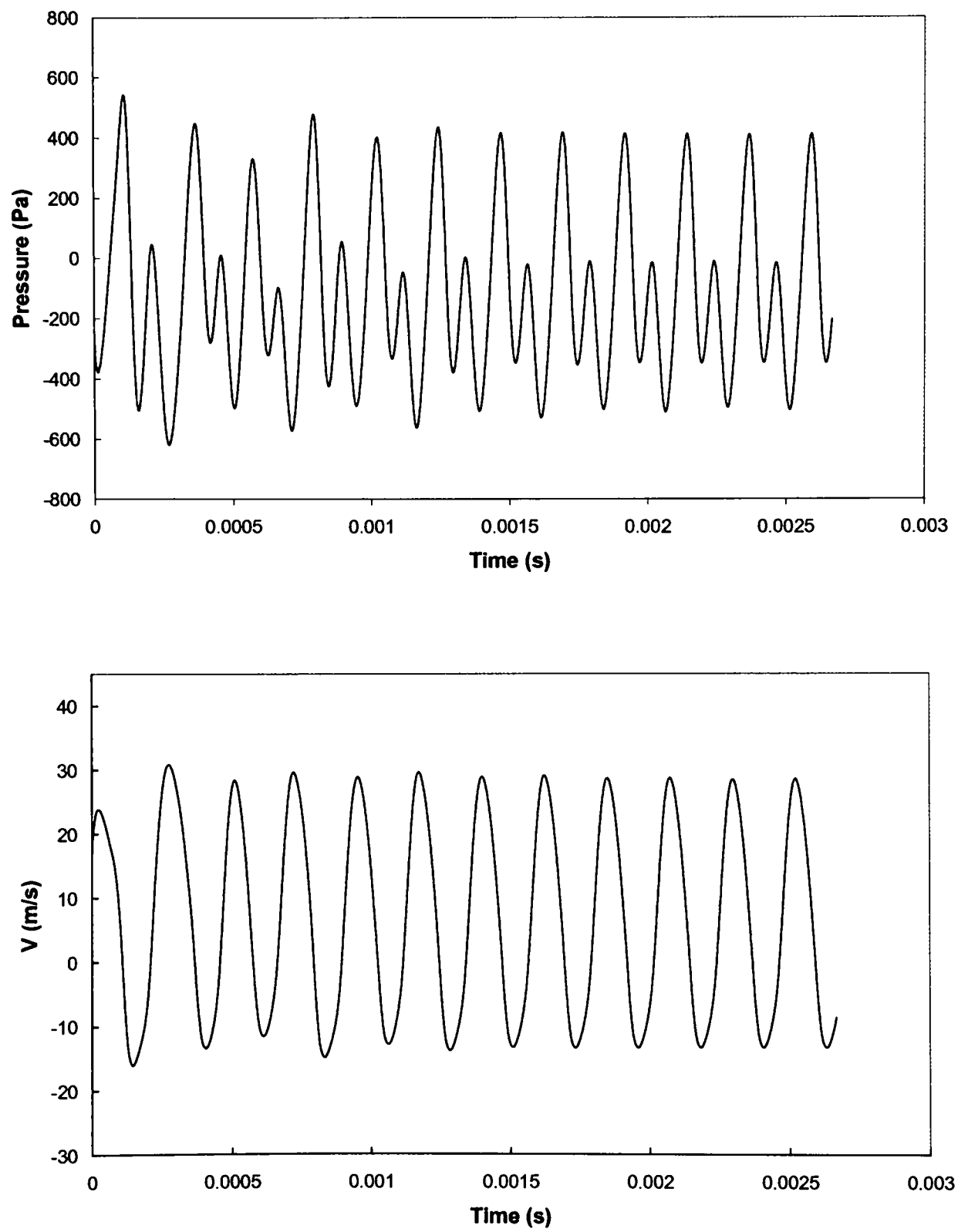
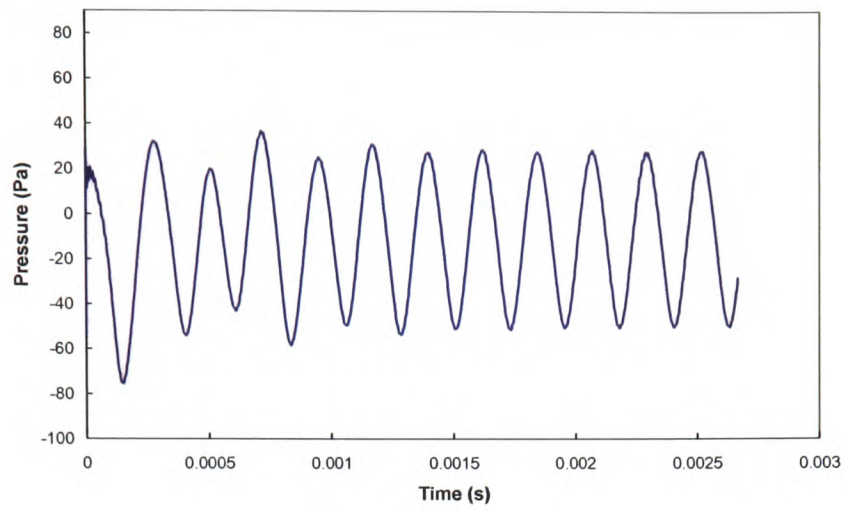
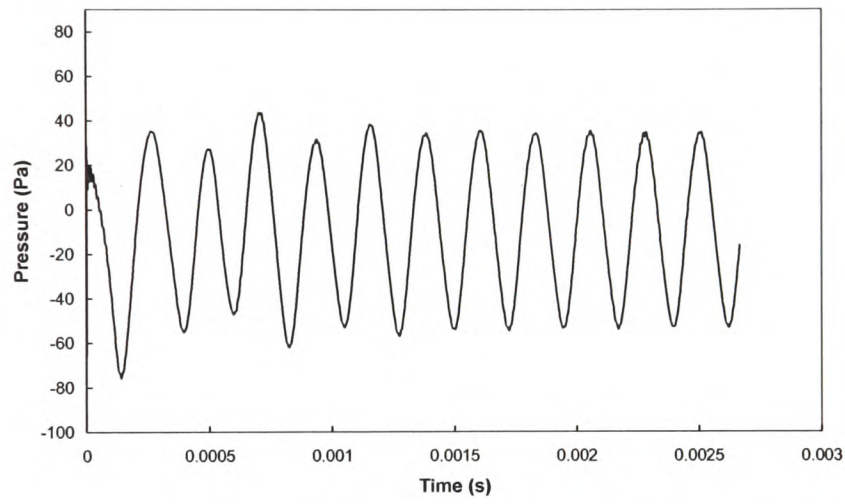


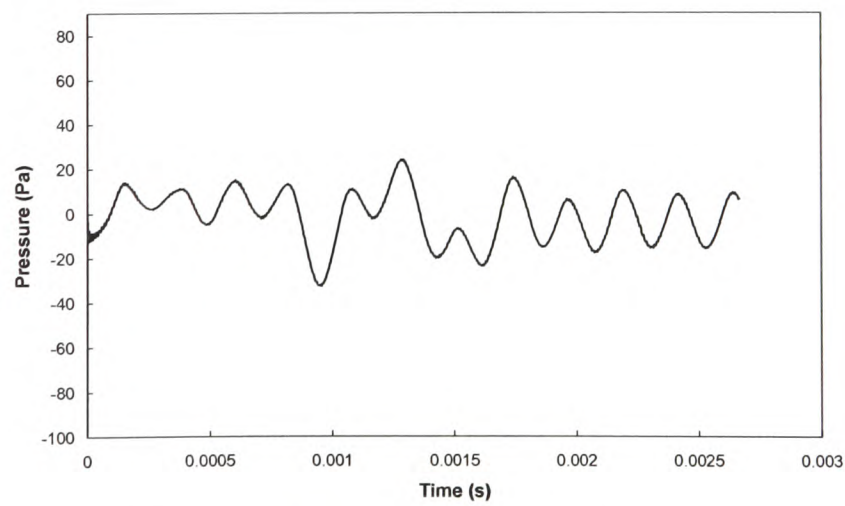
Fig. 6.15. Time history of pressure and normal component of velocity at the corner right before the rear cavity edge



a) at the upper corner of the trailing edge of the lip



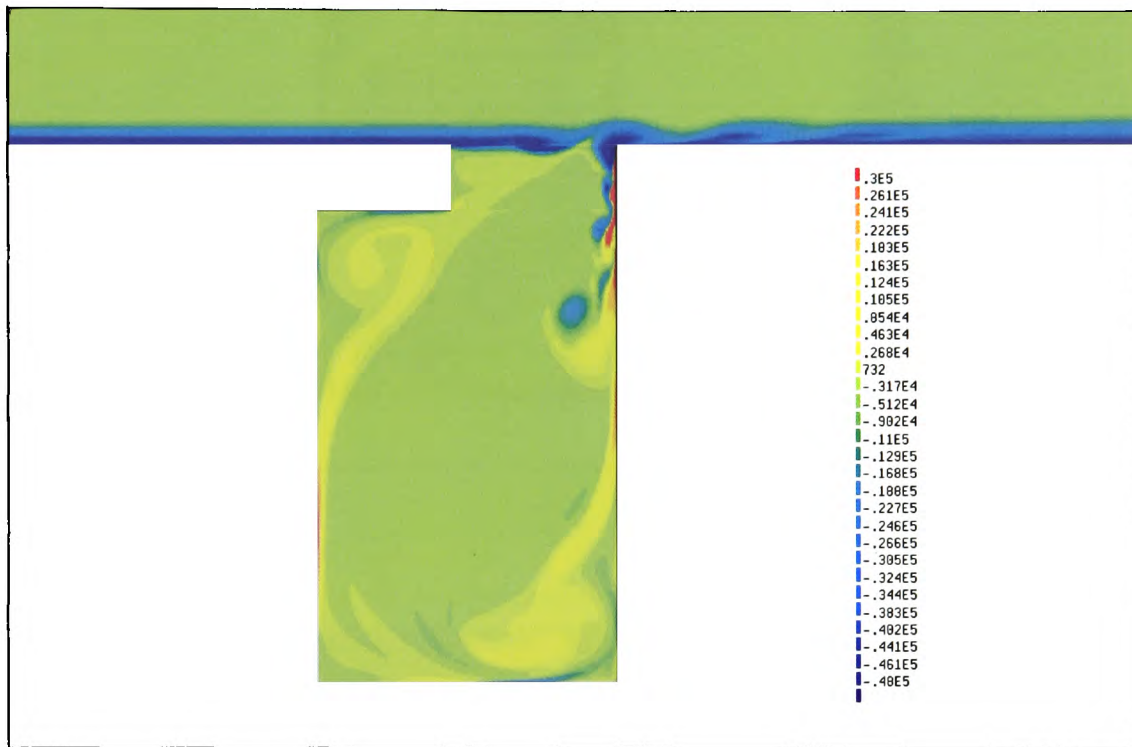
b) at the centre of the left vertical wall inside the cavity



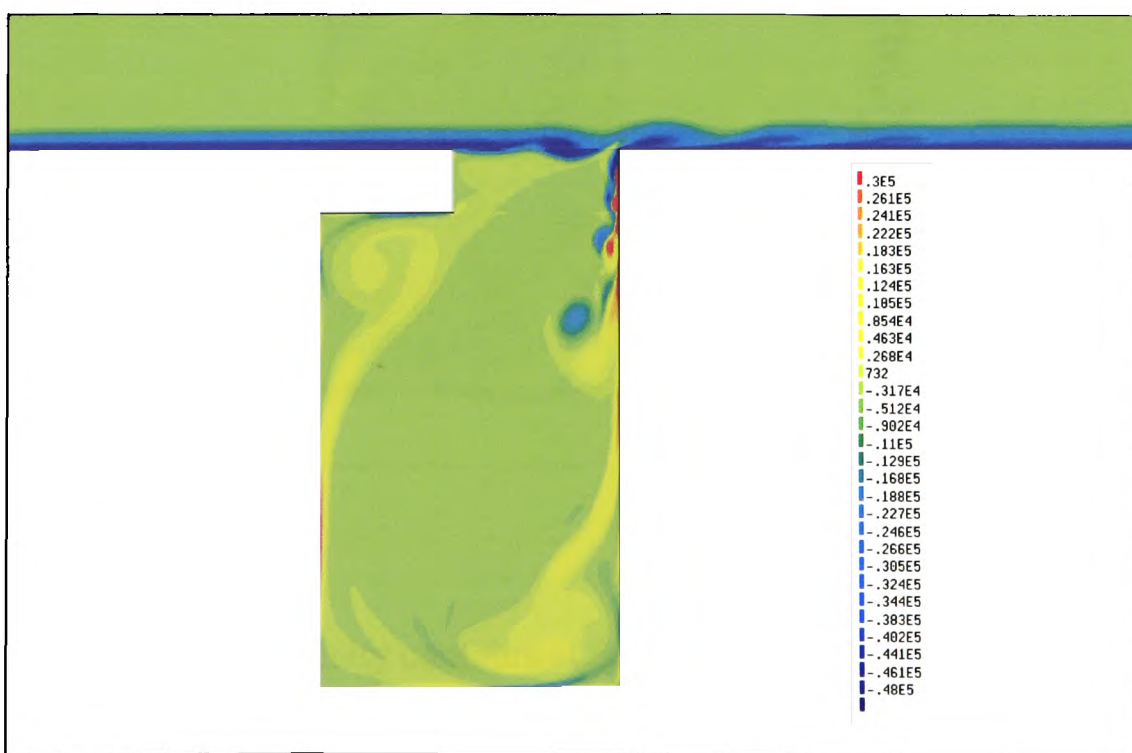
c) at certain a point away from the cavity in downstream

Fig. 6.16. Time history of pressure at 3 selected points

The self-sustained and periodical oscillating characteristics of the flow in the vicinity of the cavity can also be found by examining the instantaneous vorticity and pressure contours. Figure 6.17 shows the instantaneous vorticity contours at four time instants (corresponding to approximate one oscillation period).

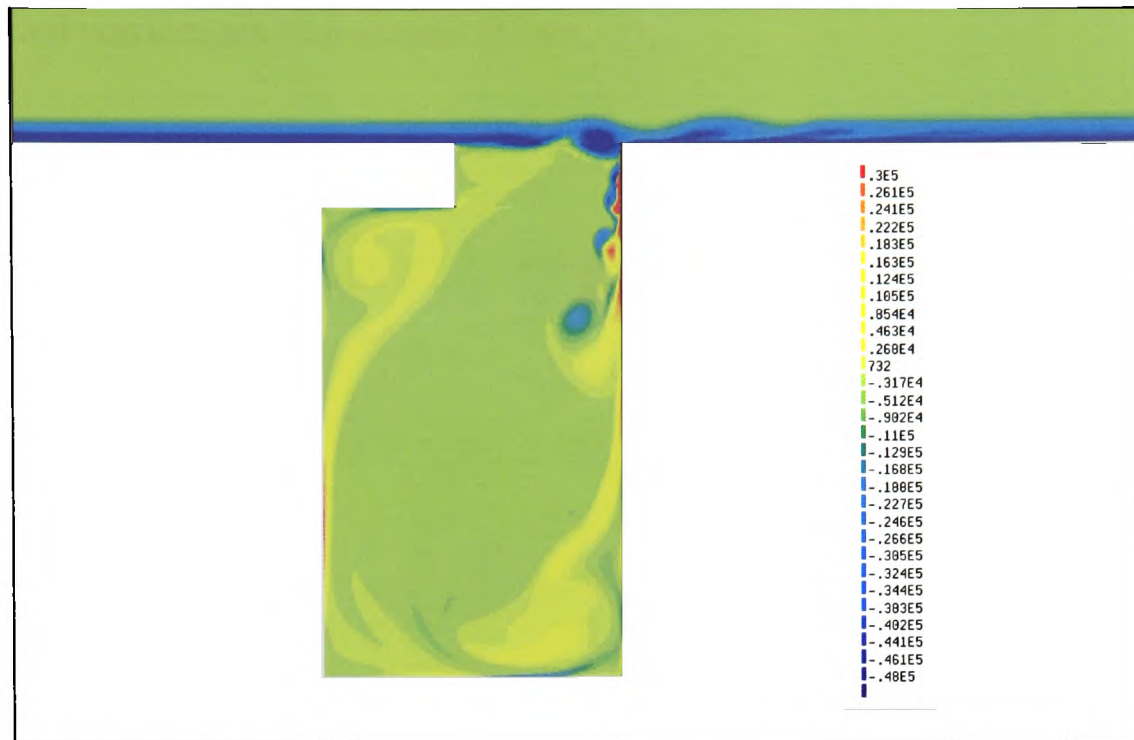


a) $t = 0.00245s$

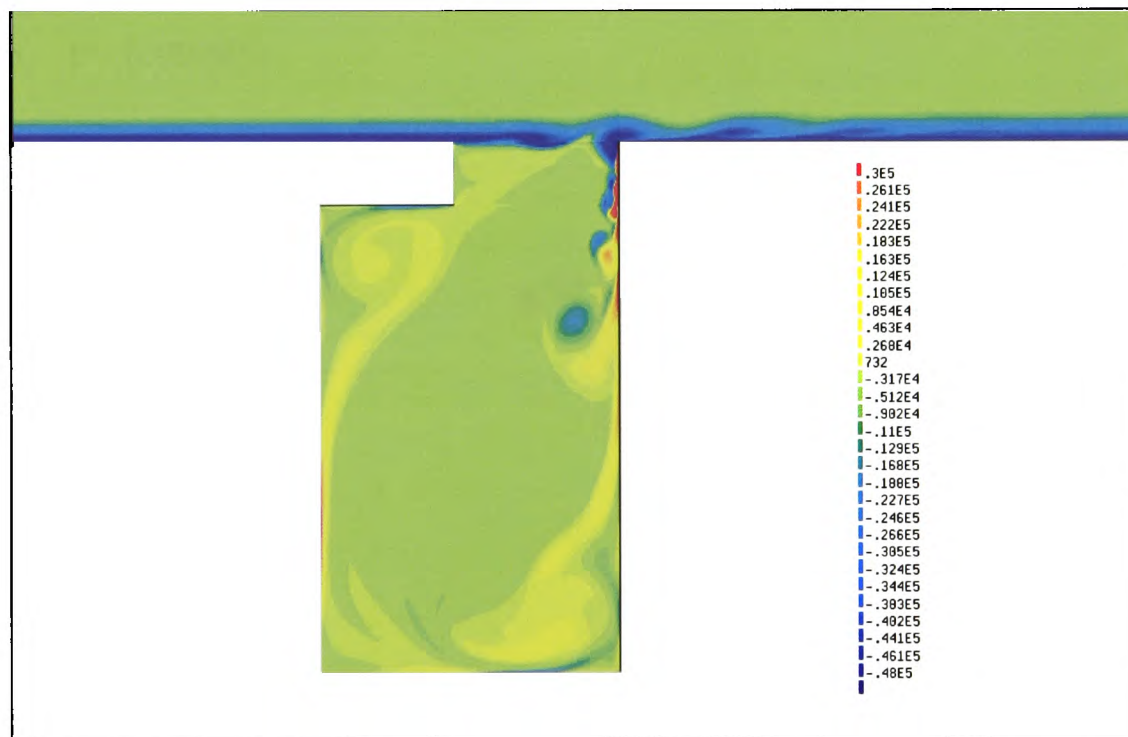


b) $t = 0.00251s$

Fig. 6.17. Instantaneous vorticity contours at 4 time instants



c) $t = 0.00260s$

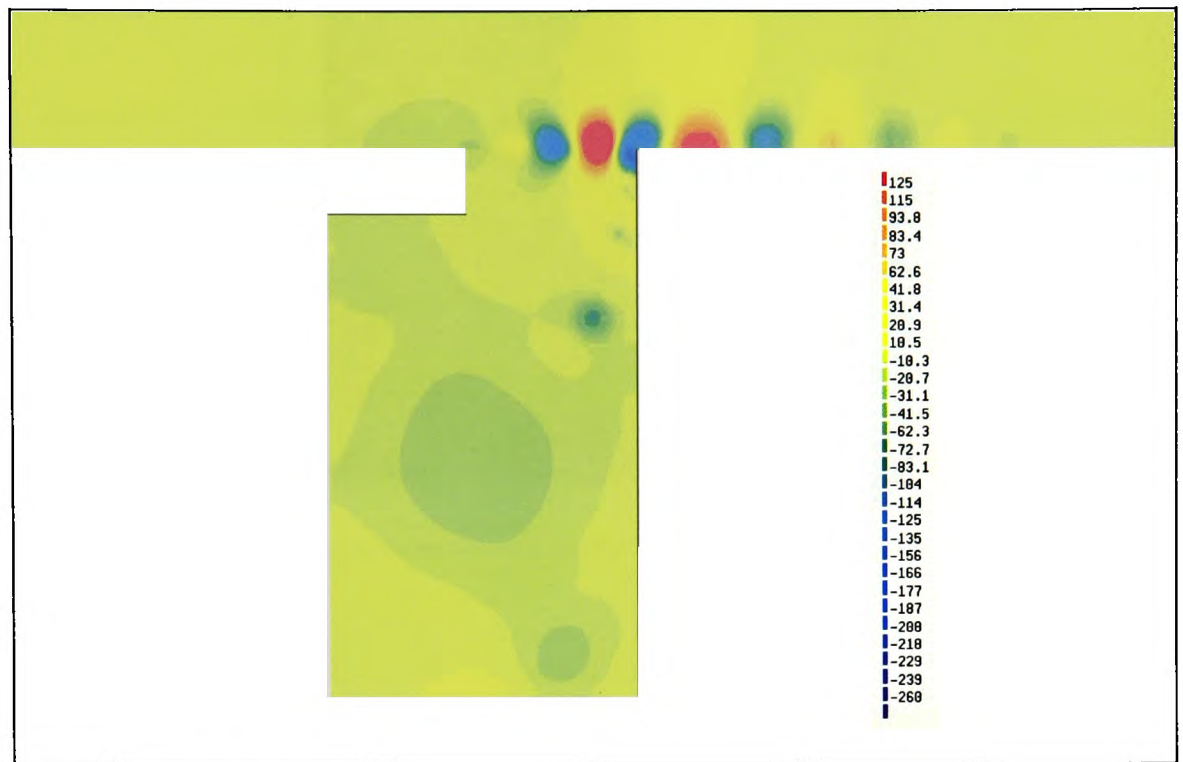


d) $t = 0.00267s$

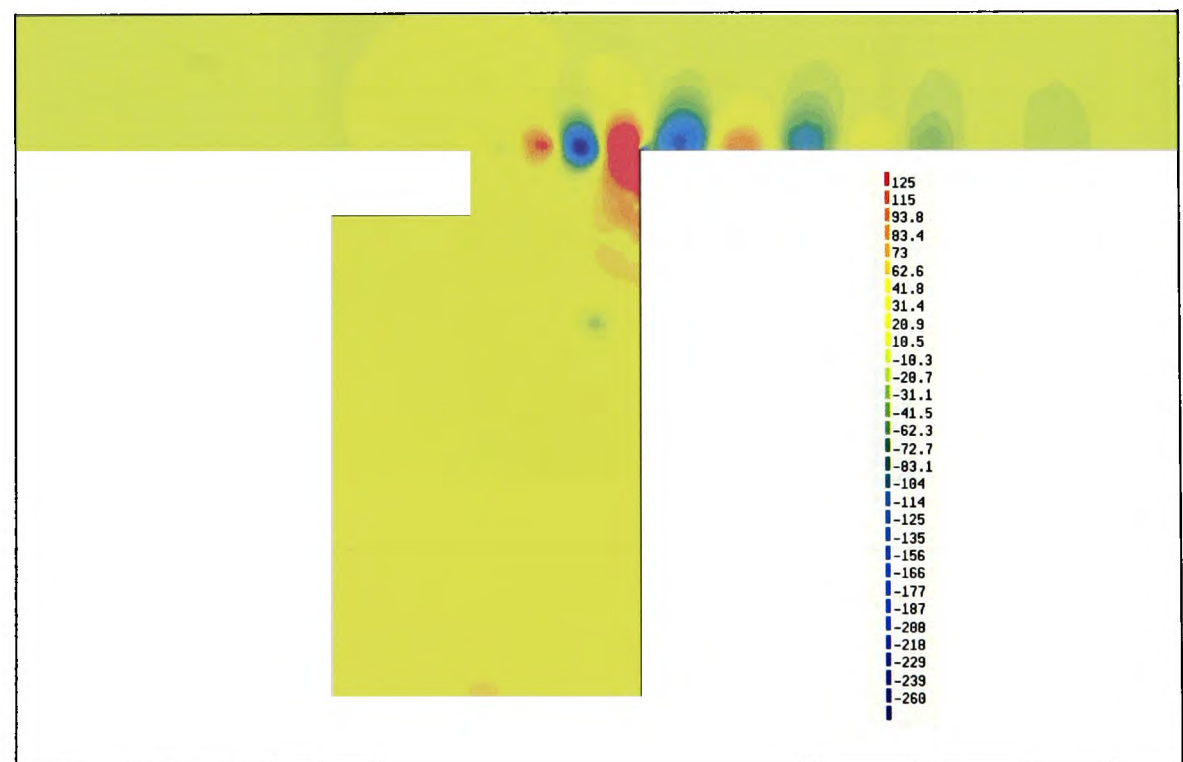
Fig. 6.17. Instantaneous vorticity contours at four time instants (cont.)

One can see vortices are shed periodically at the trailing edge of the cavity. They are convected downstream by the boundary layer flow. Upon impinging the rear corner part of the cavity, the shed vortices partly enter the cavity, and continually develop along the

trailing edge of the cavity. Figure 6.18 gives corresponding pressure contours, from which the convected vortices are also clearly shown.

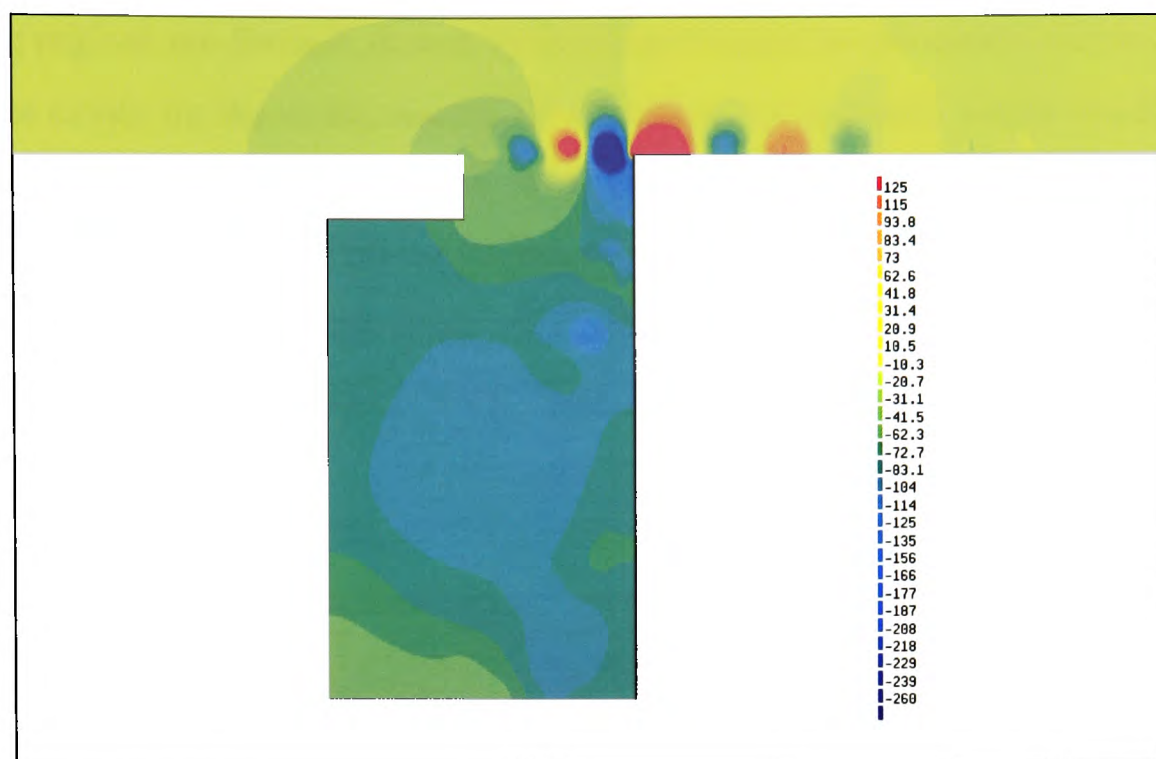


a) $t = 0.00245s$

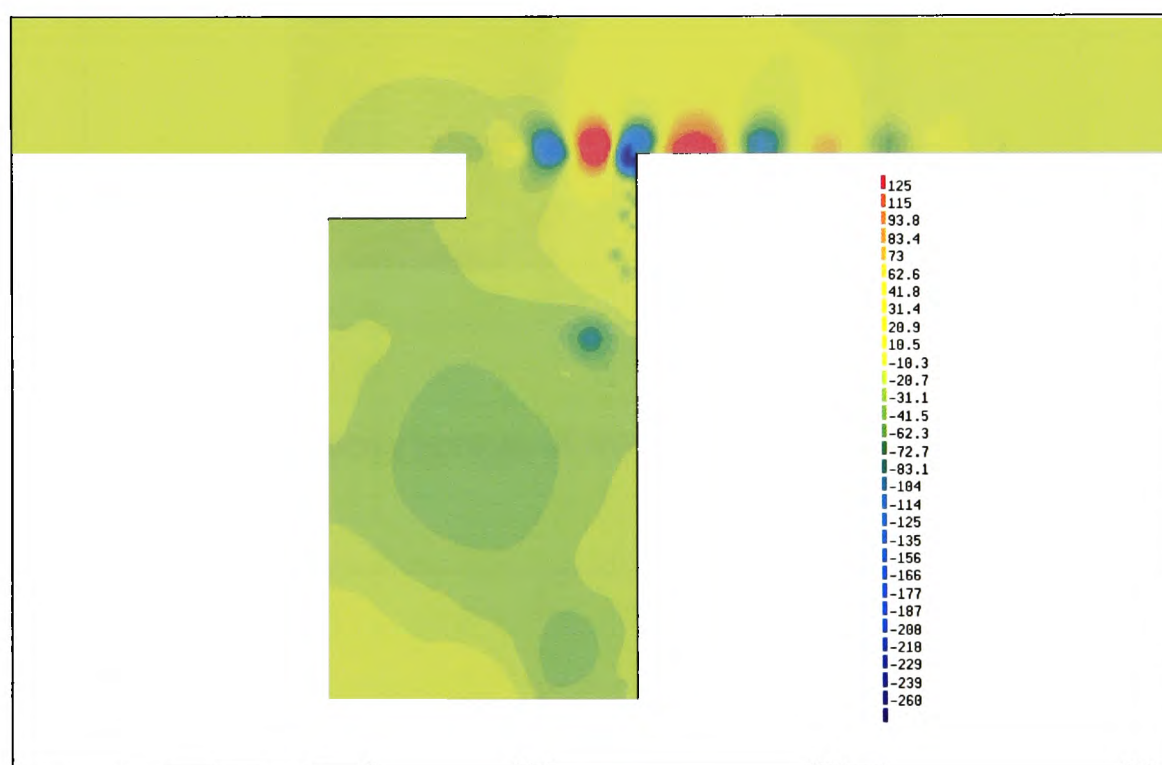


b) $t = 0.00251s$

Fig. 6.18. Instantaneous pressure contours at 4 time instants



c) $t = 0.00260s$



d) $t = 0.00267s$

Fig. 6.18. Instantaneous pressure contours at four time instants (cont.)

Other vortical structures developed inside the cavity can be seen in the velocity vectors as shown in Figure 6.19. Within the middle part of the cavity there is a large re-circulating flow, with smaller re-circulating regions in upper portion. In the corners, secondary re-

circulating regions are formed, driven by the larger region in the centre. Behind the trailing edge of the cavity lip the re-circulating flow leads to the unsteady vortex shedding and the shear layer instability. Actually, the flow inside the cavity experiences a process of compression and expansion with the rolling-up of the shed vortex from the lip of the cavity, and impinging the downstream cavity edge. The mean pressure coefficient on the floor of the cavity is given in Figure 6.20. The mean pressure coefficient is defined as $C_p = \bar{p}/(0.5\rho U_0^2)$.

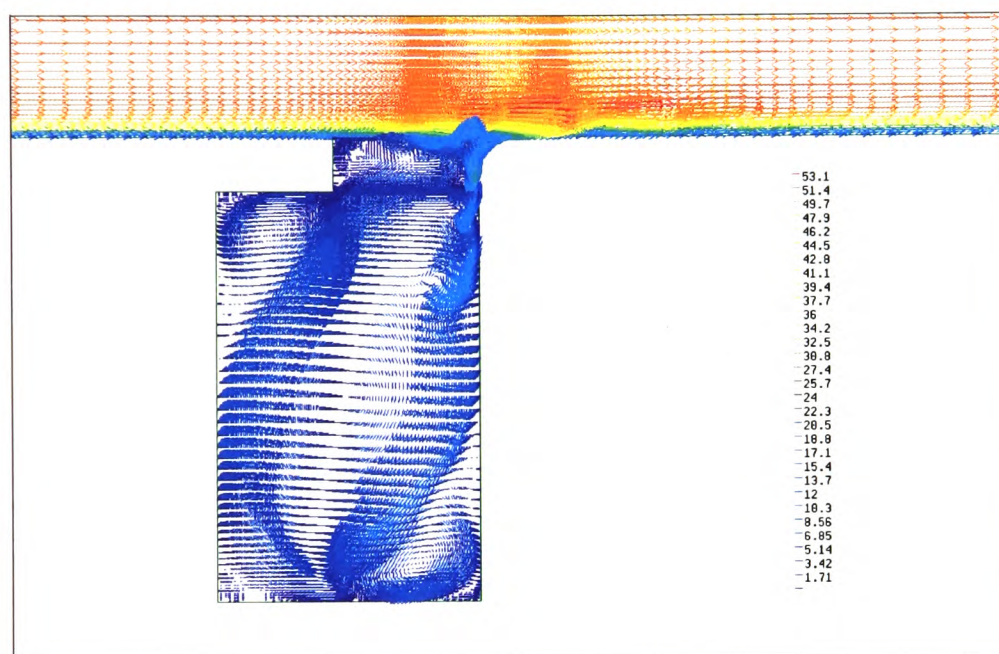


Fig. 6.19. Instantaneous velocity vectors of the unsteady flow field at 0.00242s

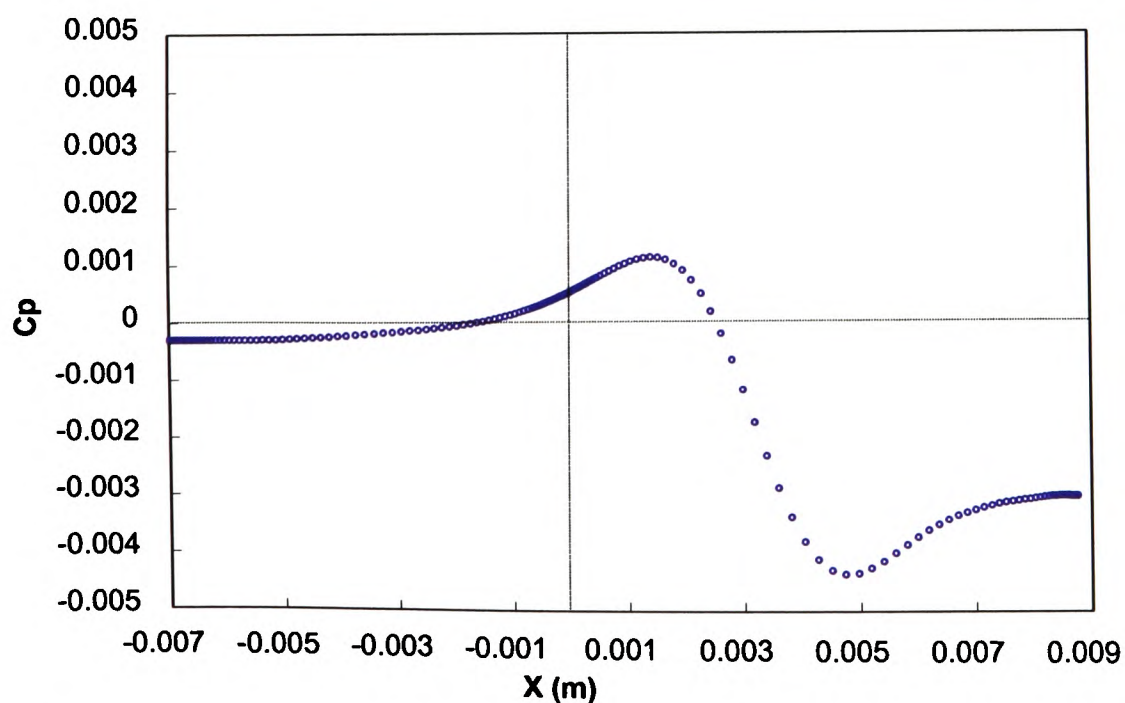


Fig. 6.20. Mean pressure coefficients on the floor of the cavity

Since there is no reference solution available to this problem, the frequency components of the self-sustained oscillation cavity flow are computed, and the frequency components are compared with the resonant frequency determined approximately from the known-well resonance frequency formula which was developed through combining theory with experimental studies for the Helmholtz resonators.

In order to determine the frequency components of the cavity flow, the discrete Fourier transform, producing power spectrum (a measurement of power at various frequencies), of the time history of pressure or normal velocity component at 5 selected points is done by sampling 16384-point Fast Fourier Transform (FFT). The selected 5 points are shown in Figure 6.21. They are: point 1) the upper corner of the trailing edge of the cavity lip; point 2) the centre of the left vertical wall; point 3) the centre of the cavity floor; point 4) the centre of the right vertical wall inside the cavity; and point 5) the corner right before the rear cavity edge.

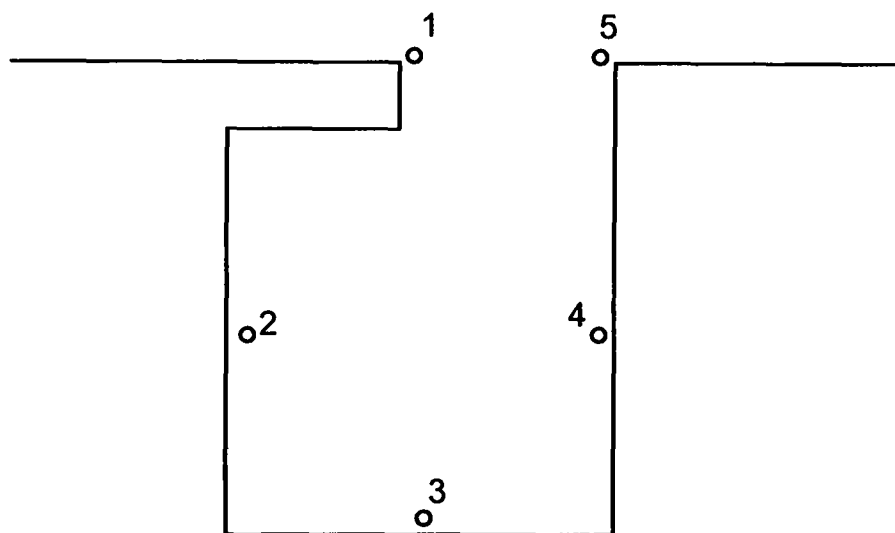


Fig. 6.21. Sketch of the cavity configuration and the selected points for FFT

The power spectrums for the pressure fluctuation history at point 1, point 2, point 3 and point 4 are represented in Figure 6.22. Similarly, the power spectrums for the pressure and the normal velocity component at point 5 are shown in Figure 6.23(a) and Figure 6.23(b), respectively.

It can be seen clearly in Figure 6.22, there exist two spectral peaks with an obvious dominant frequency for the unsteady car-door cavity flow. The frequencies corresponding to the two peaks can be determined to be about 1900Hz and 3375Hz, respectively.

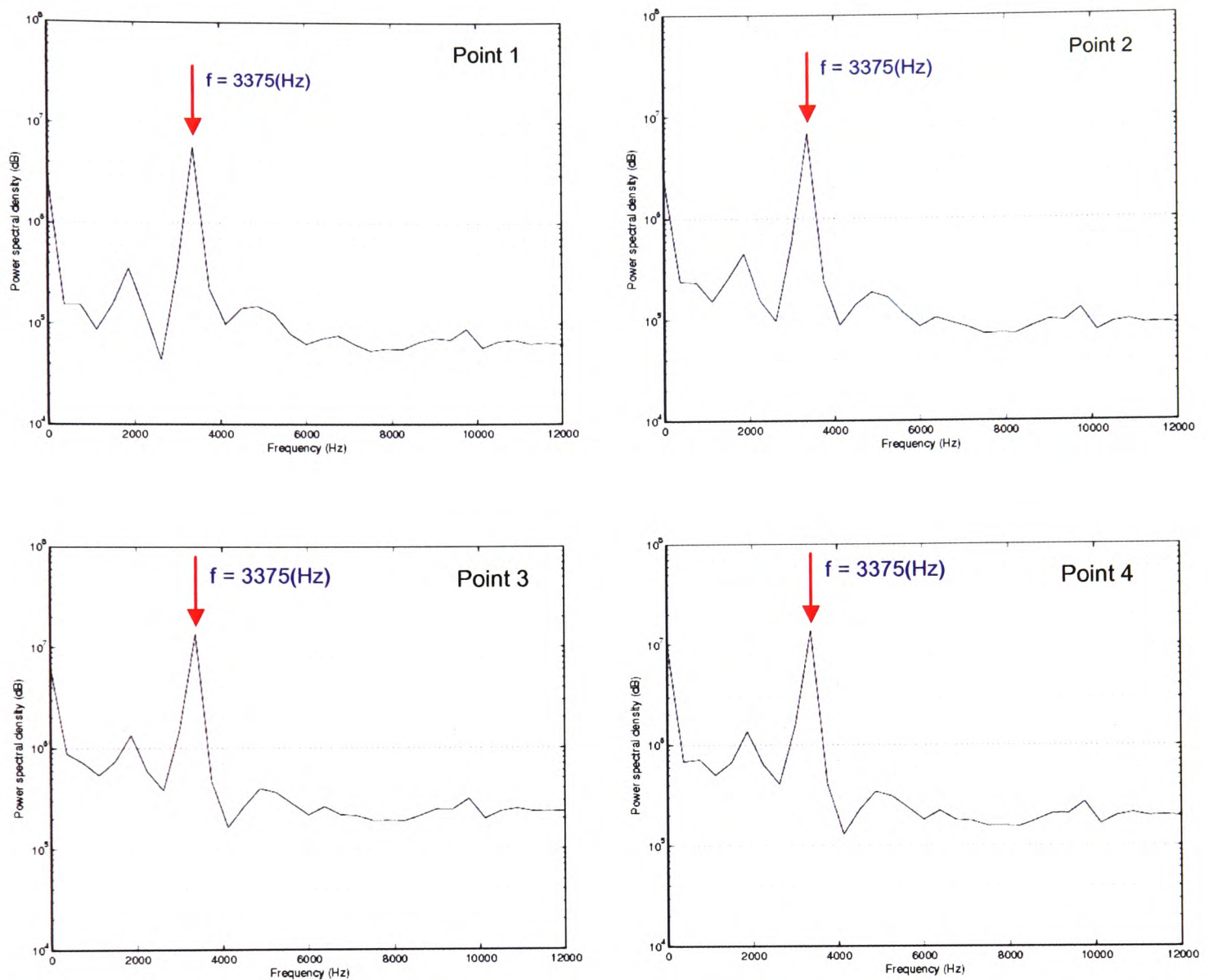


Fig. 6.22. Power spectrums of the time of the pressure at 4 selected points

However, it can also be noticed that the power spectrum at the corner right before the rear cavity edge (i.e., point 5) are somewhat different compared to others. The spectrum at point 5 shows a multiple peaks spectra, especially for the pressure signal. Henderson [2000] argued that multiple discrete frequencies often occur for cavity flows at the cavity mouth. This is mainly attributed to the shear layer periodically impinges the rear corner part of the cavity, which causes unsteady mass exchange into and out of the cavity, and is demonstrated in the time history of the pressure signal (see Figure 6.15). The number of peaks in the spectrum analysis depends on the flow speed and the boundary layer thickness. These discrete frequencies may be associated with fluid-dynamic oscillations and transverse cavity waves as well as other unknown origins. The present computational result has a boundary layer thickness, at the location close to the trailing edge of the cavity lip, of 10%

of the length of the cavity base. The frequency corresponding to the maximum spectrum value is the same as the dominant frequency values at the other 4 points.

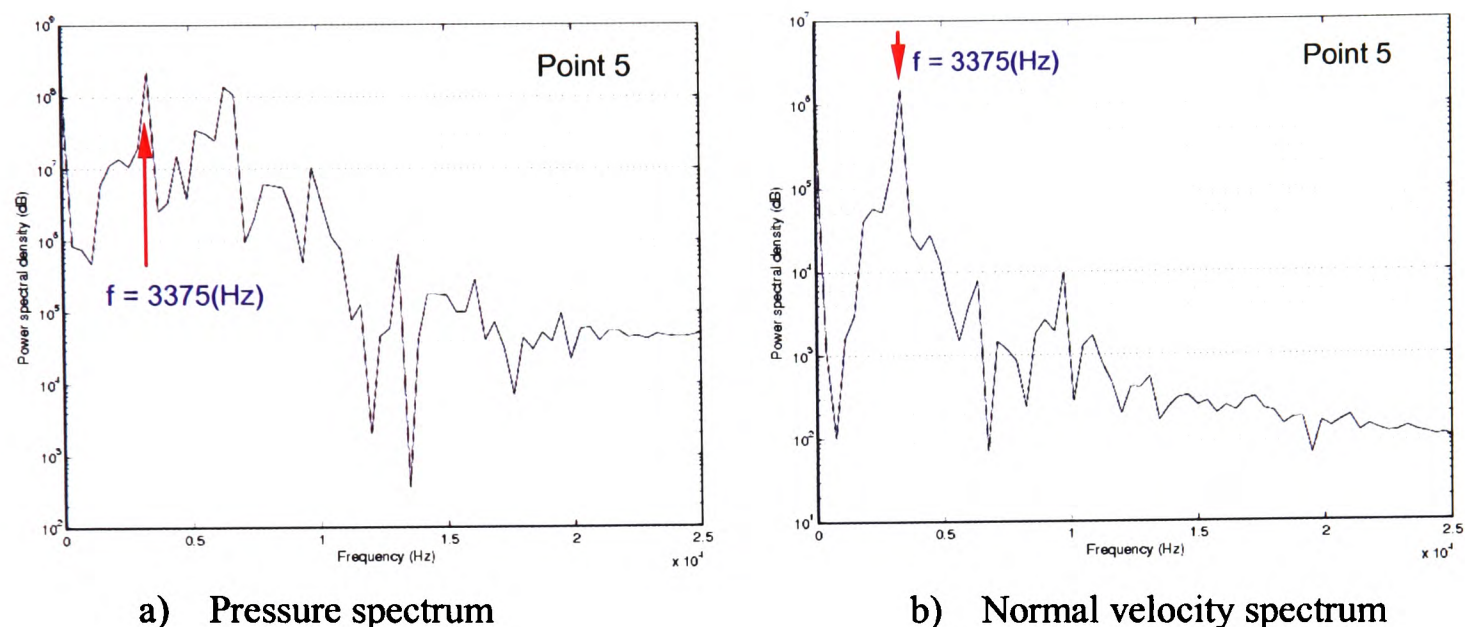


Fig 6.23. Power spectrums of the pressure and normal velocity signal at point 5

As mentioned in the description of the problem specified in Category 6 of the third CAA Workshop on Benchmark Problems [see NASA/CP-2000-209790]. As mentioned in the description of the problem of Category 6, there are two edgetone frequencies occur between 0Hz and 2000Hz and frequencies associated with longitudinal cavity modes occur between 2000Hz and 4000Hz. The computed frequencies above are basically consistent with the description of the frequencies.

The validity of the results of the dominant frequency is also checked against the Helmholtz resonator, which is an air container with an open hole (or neck or port). A volume of air in and near the open hole vibrates because of the 'springiness' of the air inside. Since the apparatus has a shape topologically close to the car-cavity considered in the present computation, a comparison of the computed dominant frequency value with the value obtained from the approximate formula for the Helmholtz –resonator. The resonant frequency for a typical Helmholtz-resonator may be approximately calculated by the formula, $f = (c/2\pi)\sqrt{A/(l_{eff}V)}$, where $l_{eff} = l + l_{cor}$ denotes the effective length of the air in the neck, l is the geometric neck length (i.e., the length, D , in Figure 6.12), l_{cor} is the end correction on the neck length, A is cross sectional area of the neck, V represents the

volume of the inside cavity (i.e., the part under the neck). For the determination of the effective length, some previous studies have given some empirical ways. One popular way of calculating the effective length is given by $l_{eff} = l + l_{cor} = l + \eta r$, where r is the radius of the neck, and η is an empirical coefficient which significantly depends on geometrical configuration and sizes. Although the formula is for an idea situation and completely neglects the shear layer, it gives only an approximate indication of the frequency of oscillation of the cavity. One coefficient, $\eta = 1.45$, for cylindrical cavity with centered, circular orifice is mentioned by Kinsler et al. [1982]. An approximate value based on the formula of the dominant resonant frequency formula with $\eta = 1.45$ is 2635 (Hz). It must be pointed out that this is not a strict comparison due to the coefficient unavailable currently for the car door cavity considered. However, even so, this crude comparison shows that the dominant frequency value obtained through the unsteady computation is a physically acceptable approximation.

The above computational results from CFD simulation demonstrate the features of the unsteady flowfield: highly unsteady vortex shedding, free shear layer instability and strongly pressure oscillation. The interaction between the vortices and the adjacent solid walls result in aerodynamic sound generation. The most significant acoustic sources come from the shear layer being impinging periodically on the trailing edge of the cavity. Because of the different length scale required to capture sound wave information, a regular Cartesian mesh is used in the acoustic calculation. The computational mesh for the acoustic calculation is shown in Figure 6.24. The computational domain is taken to be the same for both the unsteady flow and the acoustic calculation. However, the cavity geometric sizes are changed slightly for the convenient use of the acoustic solver. For the acoustic mesh, the region over the cavity has 245 x 125 mesh cells. In the mouth of the cavity, the mesh cell number is 5 x 2. The region inside the cavity contains 9 x 15 mesh cells. Mesh sizes in x- and y-direction are 0.00175245m and 0.00164705m, respectively.

The extraction of the aerodynamically generated sources and the coupling calculations follow the described procedure in Chapter 4. The boundary conditions used in the acoustic calculation are: the radiation boundary conditions for the all domain boundaries and slip-flow solid wall condition for the cavity walls.

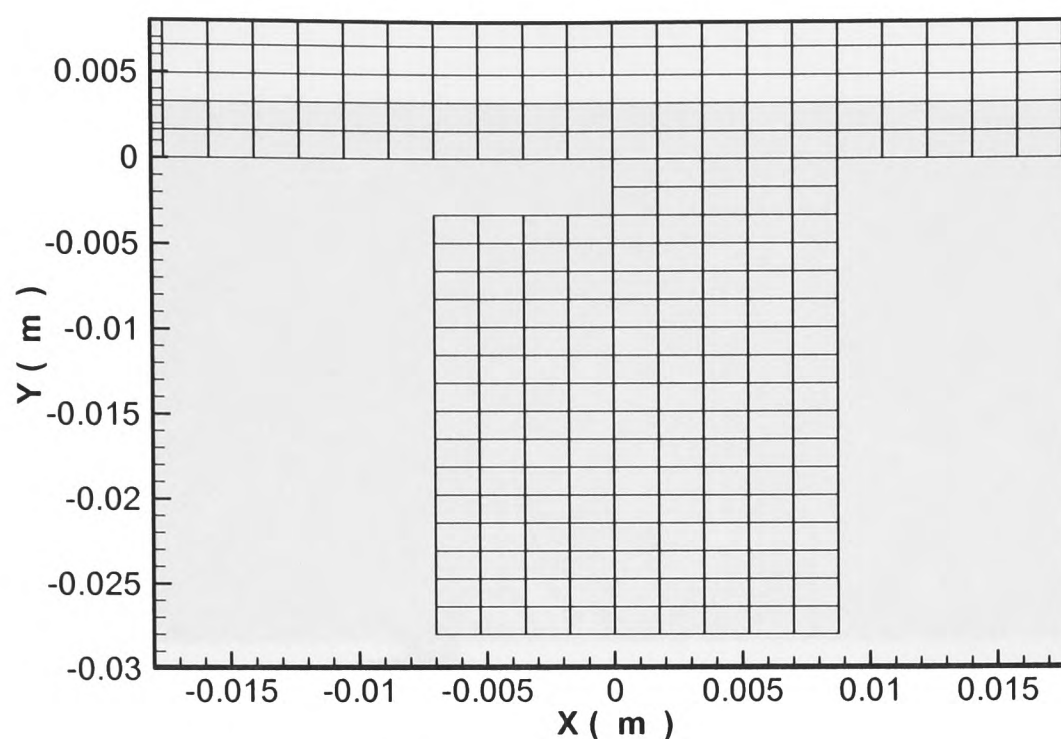
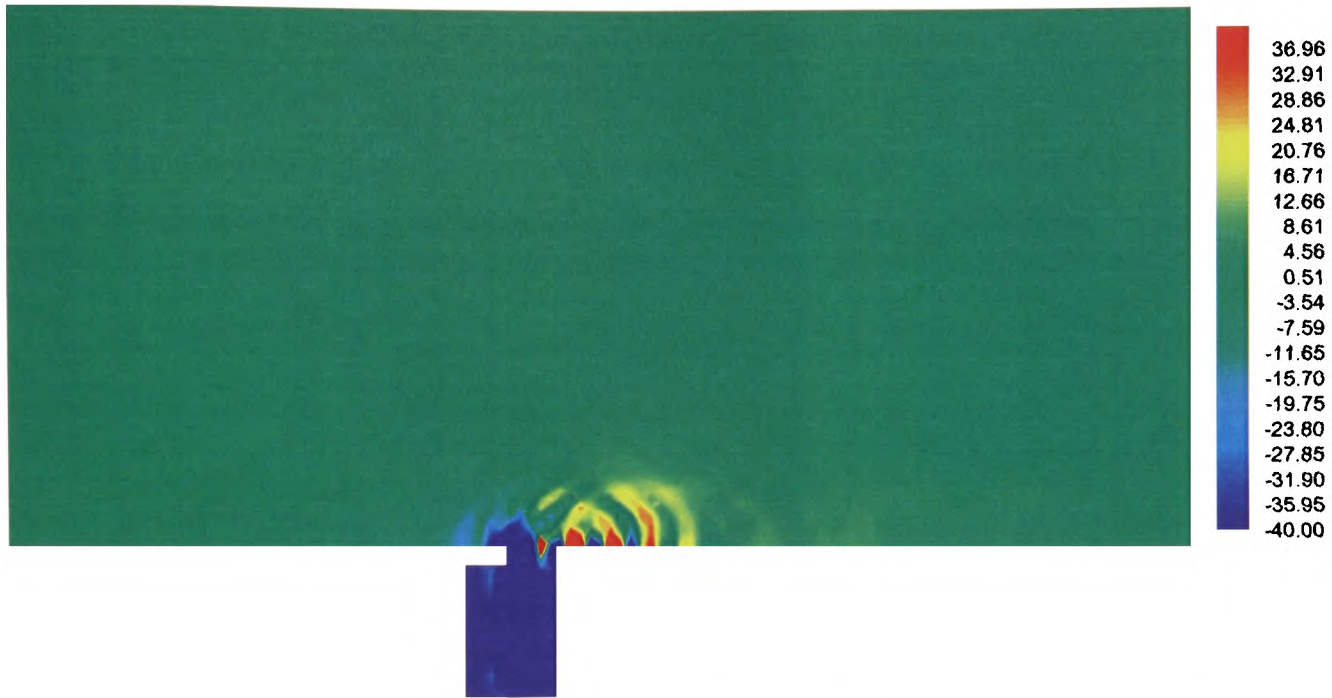
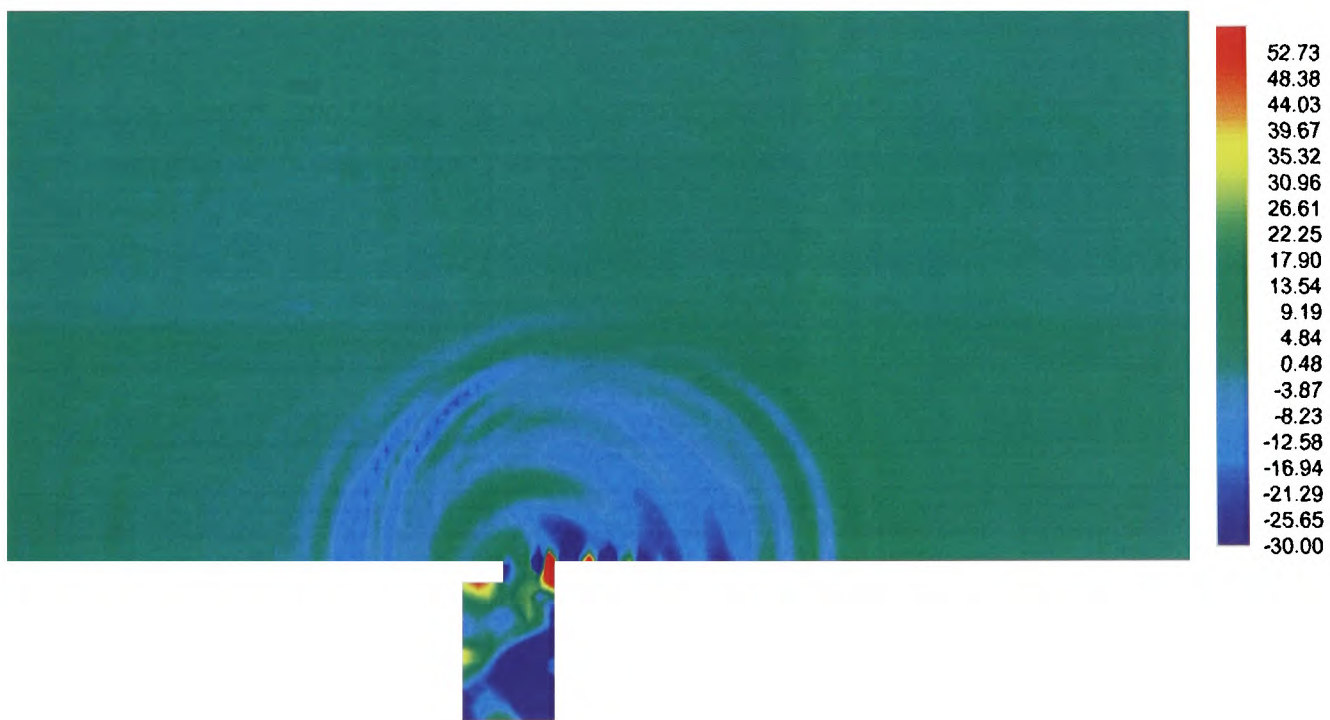


Fig. 6.24. Computational mesh for acoustic calculation

In the present acoustic calculation, the acoustic time step is $1.5\mu\text{s}$. To save computational time and computational memory, the CFD simulation are output at an interval of every CFD time steps which is equivalent to 25 output data for each period of the unsteady flow. In the present calculation, the acoustic running is marched for only about 3 periods. Figure 6.25 shows the computed perturbation pressure in the near-field at four time instants. The picture illustrates the acoustic wave radiation from the flow-induced cavity noise. It can be seen that the highest intensity of the radiated sound noise lies in between $0\sim 45$ degree measuring anticlockwise from the x-axis. Note that the acoustic radiation pattern as shown here is somewhat different from some results reported in literature (e.g., Ashcroft et al., [2000a]). However, the current results seem to be physically reasonable. It should be mentioned that some obvious reflections are still found in the calculation. In author's opinion, this is mainly because some spurious acoustic sources (numerical errors and numerical reflections) are triggered at the truncated boundaries due to the smaller CFD simulation domain. This is also a major reason that the acoustic calculation can not be carried out for longer time. The study on accurately extracting the acoustic sources at CFD simulation boundaries embedded in the acoustic computational domain and more advanced non-reflecting boundary conditions is required for a long time calculation.



$t = 0.000036\text{s}$ (24 acoustic time steps)



$t = 0.000126\text{s}$ (84 acoustic time steps)

Fig. 6.25. Instantaneous acoustic perturbation pressure contours at 4 time instants

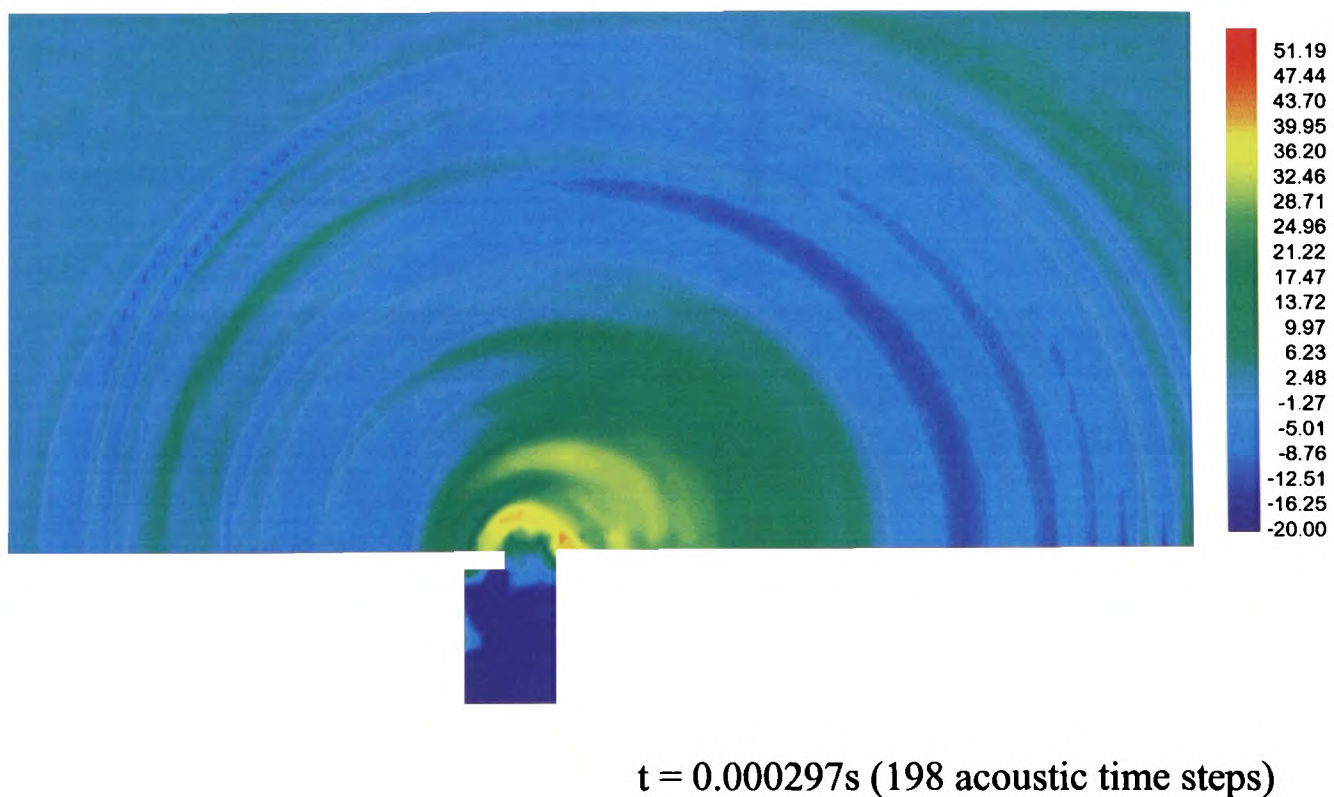
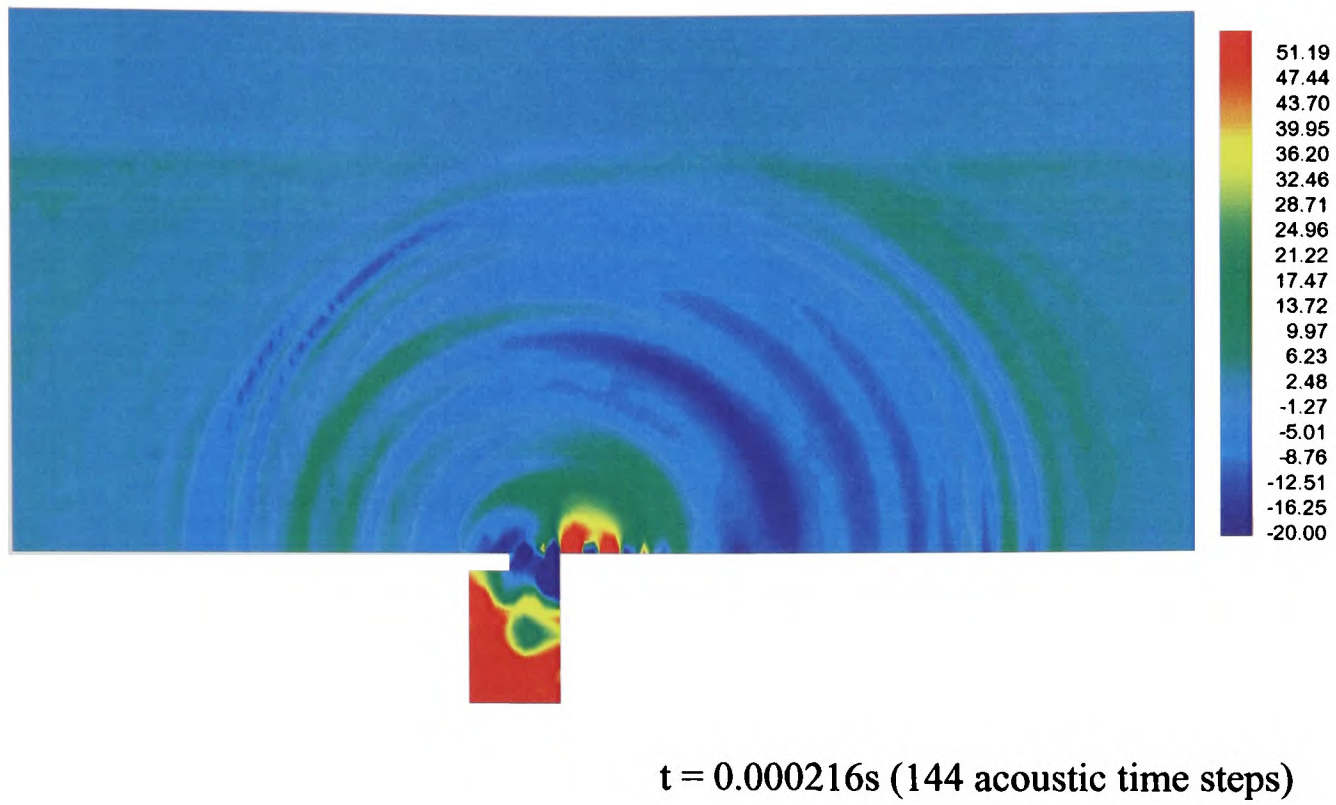


Fig. 6.25. Instantaneous acoustic perturbation pressure contours at four time instants (cont.)

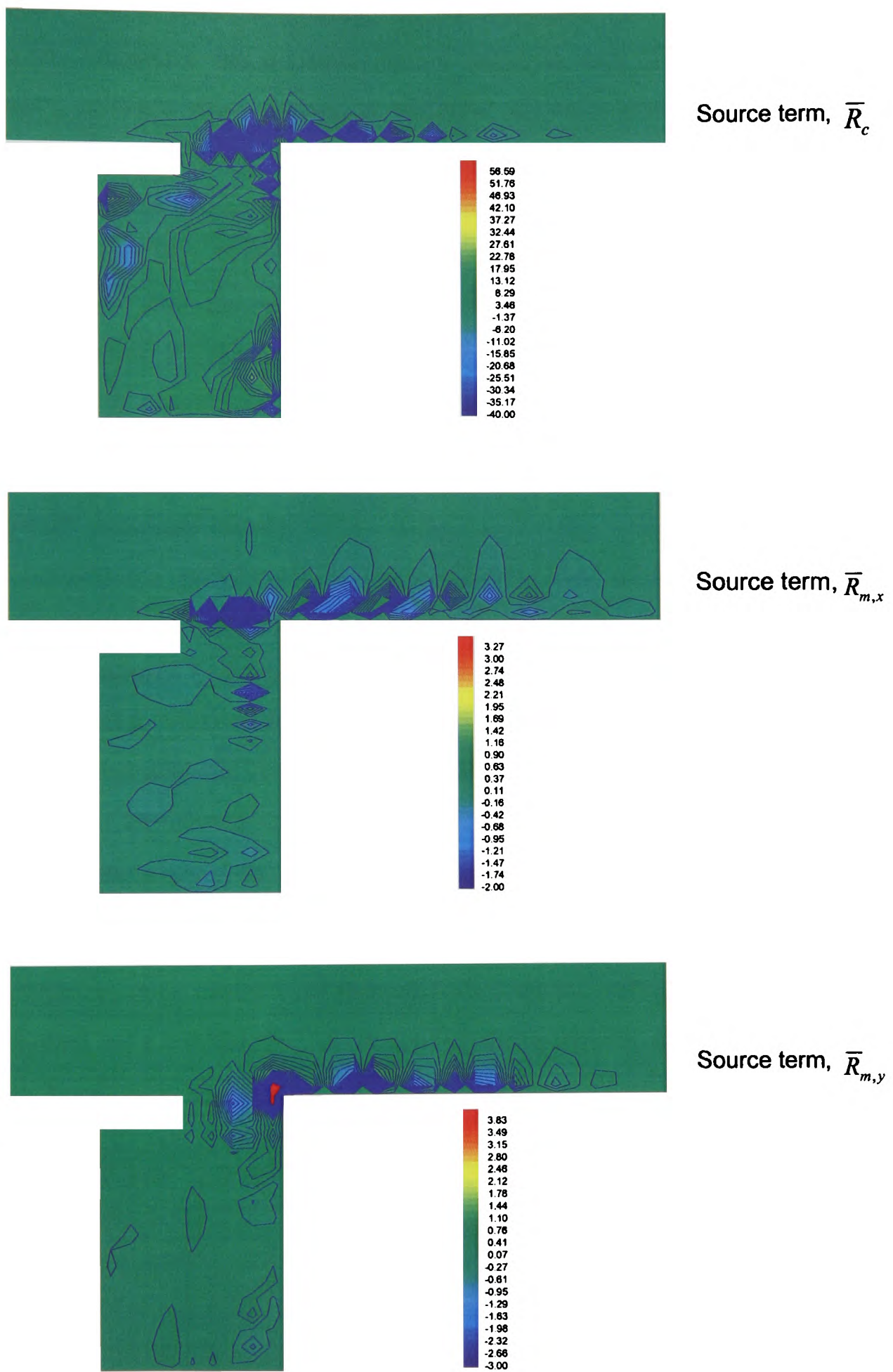


Fig. 6.26. Instantaneous contours of the acoustic source term in Eq.(2.90) at the 240th acoustic time step

In order to give some insights into the mechanism of the flow-induced cavity noise, observing the structures the acoustic source terms is one of ways. The contours of instantaneous acoustic source terms at different acoustic time steps, as given in the formulation (2.90), are plotted. These contours pictures are basically the same in the structure. Figure 6.26 shows the contours of instantaneous acoustic source terms at the 240th acoustic time step. It should be noted that the instantaneous contours displayed in Figure 6.26 are not from the minimum value to the maximum value in the acoustic source results. For the term \bar{R}_c , the instantaneous contours is between -40.00 and 56.59. For the terms, $\bar{R}_{m,x}$ and $\bar{R}_{m,y}$, the instantaneous contours are shown from -2.00 to 3.27 and from -3.00 to 3.83, respectively. In this picture, the acoustic sources generated by the unsteady cavity flow are visualized clearly.

As pointed out in Chapter 4, the feedback effect of the acoustic field on the aerodynamic flow field is not considered in the present study. These results were presented at the 9th International Congress of Sound and Vibration [Wang et al., 2002a], and have polished to submit to a journal for publication [Wang et al., 2003c].

In the present acoustic calculations, the extracted acoustic source terms are evaluated by Eq.(2.90). For an incompressible case, the flow density is viewed as keeping constant. \bar{R}_c is approximately equal to $c^2 \bar{\rho} \partial \bar{v}_j / \partial x_j$ if Eq.(2.89) is used to evaluate the acoustic source term. A comparison of the use of \bar{R}_c in Eq.(2.89) with the use of \bar{R}_c in Eq.(2.90) is given for this car door cavity case through valuating the values of the source term at 3 selected points at $t = 0.00252s$. A sketch of the positions of the 3 points and their coordinates is shown in Figure 6.27.

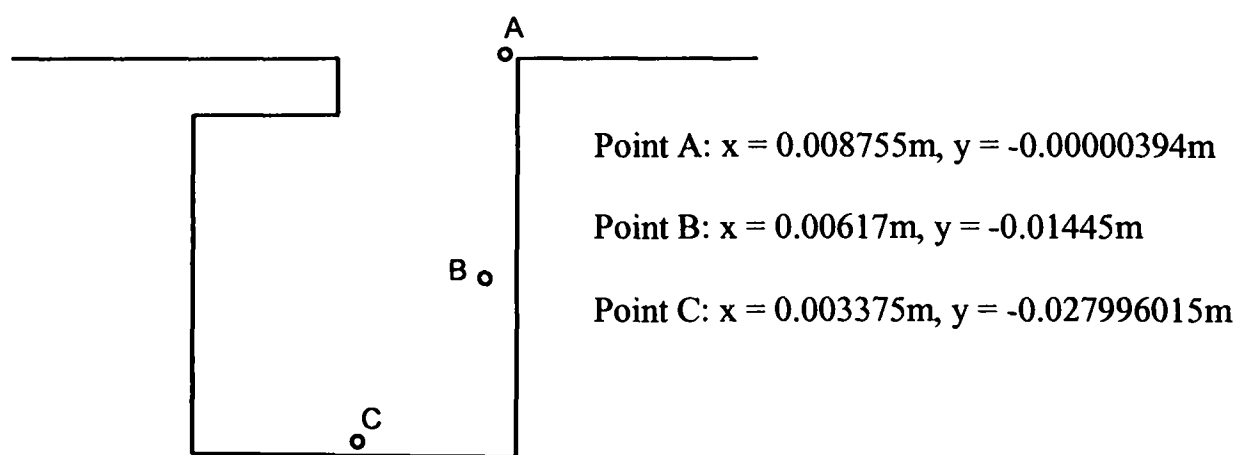


Fig.6.27. Sketch of the 3 selected points and their coordinates

The values of the acoustic source terms for \bar{R}_c in Eq.(2.89) and \bar{R}_c in Eq.(2.90) and their relative percent error are presented in Table 6.1. Those values are calculated approximately using first-order difference schemes. As seen in Table 6.1, the error of using \bar{R}_c in Eq.(2.90) instead of \bar{R}_c in Eq.(2.89) to evaluate the acoustic source term is very small for this incompressible car door cavity flow.

Table 6.1. \bar{R}_c in Eq.(2.89) and \bar{R}_c in Eq.(2.90) and their relative percent error

$$\left(\bar{R}_c^{(2.89)} = \bar{\rho}c^2 \frac{\partial \bar{v}_j}{\partial x_j}, \bar{R}_c^{(2.90)} = \left(\frac{\partial \bar{p}}{\partial t} + \bar{v}_j \frac{\partial \bar{p}}{\partial x_j} + \bar{\rho}c^2 \frac{\partial \bar{v}_j}{\partial x_j} \right) \right)$$

Point \ Term	$\bar{R}_c^{(2.89)} (\times 10^5)$	$\bar{R}_c^{(2.90)} (\times 10^5)$	$\left \frac{\bar{R}_c^{(2.89)} - \bar{R}_c^{(2.90)}}{\bar{R}_c^{(2.89)}} \right \times 100\%$
A	-1398528.8	-1398933.549	0.02%
B	561.30	570.165	1.57%
C	270.34	279.153	3.26%

6.4 An open cavity flow-induced noise using LES for the unsteady flow

In the all above cases, the RANS-based numerical method is coupled with the acoustic numerical method through the acoustic-source extracting formulation. Note that those cases don't take account of turbulence. As mentioned previously, aeroacoustic computation will become more challenging when the unsteady flow field involves turbulent flows. As an attempt, the generation of sound and near field radiation of the resulting aerodynamic sound from a turbulent flow over an open cavity is considered in this section.

It should be pointed out that the three-dimensional features of open cavity flows have been received some attention. The spanwise aspect ration may have some effects upon the vortical structure inside cavity. The streamwise vortices in the shear layer, side walls effects on the shear layer and in cavity, or certain instabilities arising from the curvature of recirculation flow may give rise to three-dimensionalities of cavity flows. However, in the present simulations, the three-dimensional geometry effects are not taken into account

though unit mesh spacing is given in the spanwise direction. This implies that the flow structures of the cavity flow are the same inside each section in the spanwise direction. The shear layer and vortex structure inside cavity have without stretching.

The unsteady flow field characteristics for a freestream flow over a cavity are significantly dependent on the length-to-depth (L/D) of the cavity, the freestream condition, and the upstream boundary layer, etc. Cavity flows can be categorized into at least three types in terms of the length-to-depth ratio, i.e., open type, closed type and transitional type [Stallings_1]. For L/D ratio is greater than 10, the flow is termed as a “closed” cavity flow. For L/D ratio is less than 8, the flow is termed an “open” cavity flow. A cavity with L/D ratio between about 8 and 11 is considered to be transitional, where either type of flow may occur.

In the present calculation, the cavity is with a length-to-depth ration (L/D) of 2 ($L = 0.03\text{m}$ and $D = 0.015\text{m}$). The freestream Mach number is of 0.5. The Reynolds number based on the cavity base length (L) is about 2.0×10^5 . Hence, the turbulent flow over the cavity is a kind of open cavity flow. At low speed and subsonic flow, open cavity flow is said to oscillate in certain “shear layer mode”, in which the shear layer spans the mouth of the cavity and stagnates at the rear edge [Suhs, 1993]. Figure 6.28 gives the schematic of the unsteady flow field, the geometry of the cavity and the computational domain sizes.

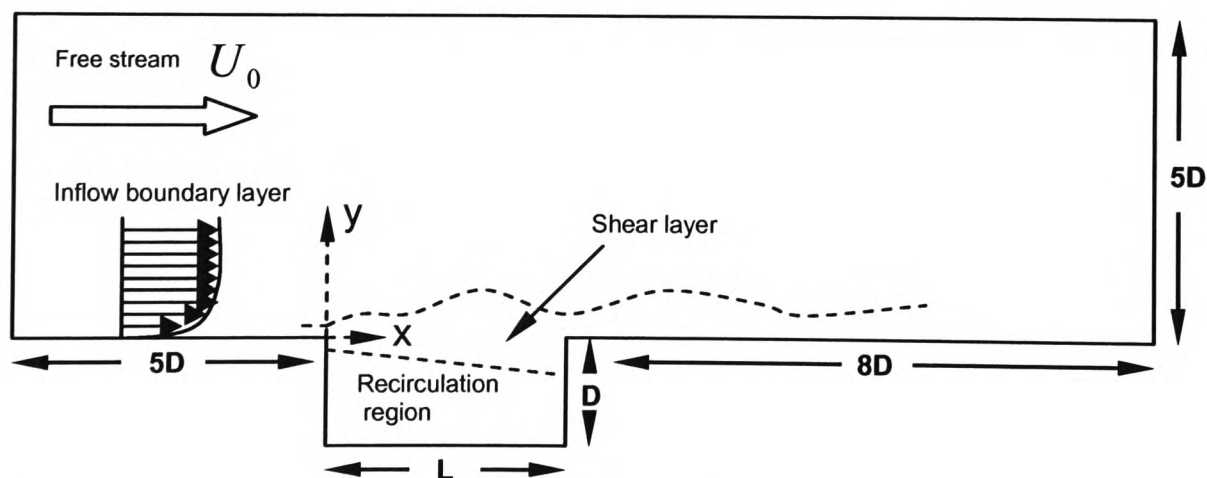


Fig. 6.28. Schematic of the 2-D open cavity flowfield and the computational domain sizes

The non-uniform computational mesh for the unsteady flow is shown in Figure 6.29. The mesh consists of 150×75 cells above the cavity and 30×25 cells within the cavity. This mesh arrangement employed 50 cells upstream, 70 cells downstream of the forward and after edge, respectively. The whole computational mesh consists of two blocks. One

block is the part of $y \geq D$ in the domain (cf. Figure 6.28). The other block is the rest part of the domain (including the cavity). In both mesh blocks, the mesh spacing in x-and y-direction is increased linearly outwards so that the mesh is refined in near wall regions and within the cavity. The minimum mesh spacings in the streamwise and normal direction are 0.001m and 0.0006m, respectively.

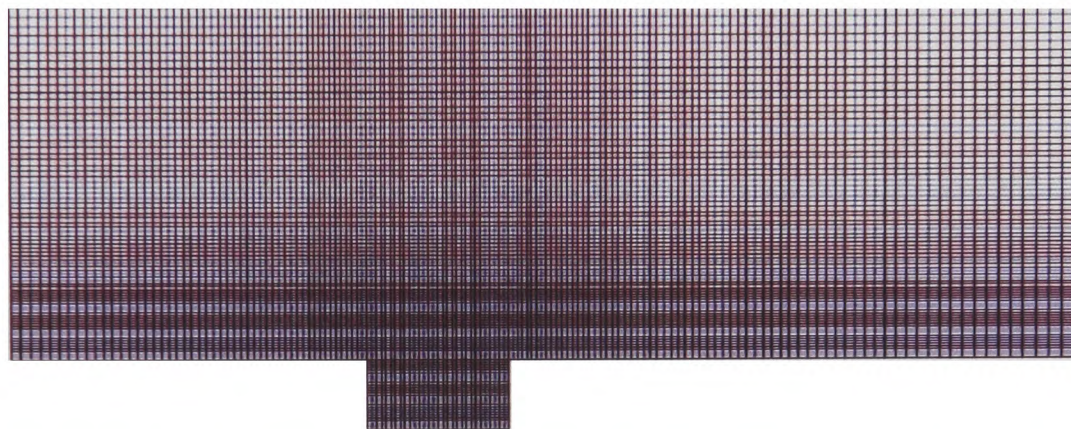


Fig. 6.29. Computational mesh for the CFD simulation of the open cavity flow

The RANS-based CFD simulation method prescribed in Chapter 3 is attempted to compute the unsteady cavity flow field. The standard $k - \varepsilon$ two-equation turbulence model (then only turbulence model in the CFD code) is selected. The central difference scheme is used associated with the standard boundary treatments. A small time step of $0.42\mu\text{s}$ is used. On the inflow boundary, we don't impose a turbulent boundary solution. Instead, a naturally developed boundary layer is introduced by specifying a uniform freestream velocity. A turbulent intensity level I , defined as $I = \sqrt{(2/3)k_\infty}/U_\infty$, is set to 2% in the freestream to prescribe the magnitude of the turbulent kinetic energy. Corresponding values of the freestream dissipation, ε_∞ , are then determined by requiring that eddy viscosity is equal to the freestream molecular viscosity. At the solid walls, the no-slip and adiabatic wall conditions are applied with vanishing normal pressure gradient. The turbulent variables k and ε are equal to zero. In the other outer boundaries (including the outflow boundary), zero pressure condition are used.

Figure 6.30 shows the time history of pressure at three monitoring points, whose positions are near the corner of the upstream edge, the middle on the cavity floor, and the

corner of the downstream edge, respectively. It can be seen that the cavity flow is initially unsteady. However, the transient feature of the unsteady flow is damped quickly as running time marches forward.

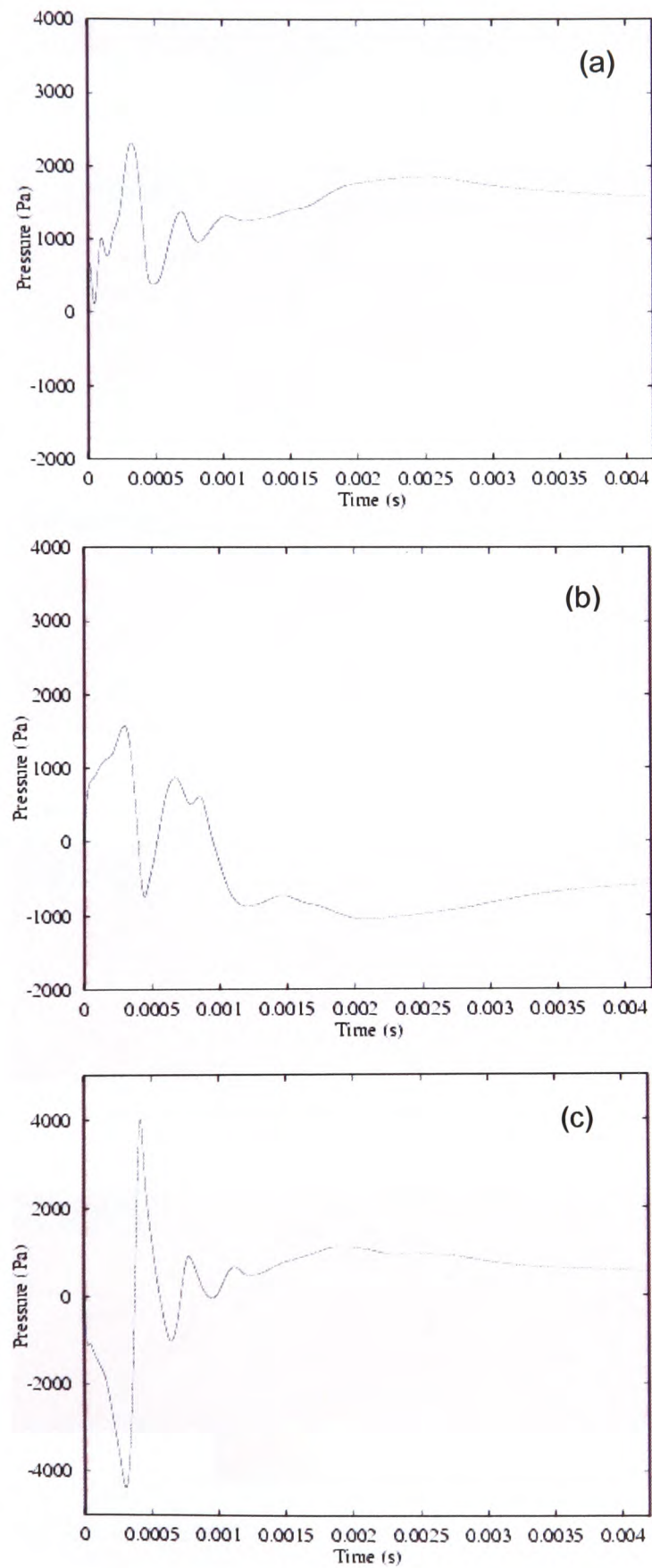


Fig.6.30. Time history of pressure from $k-\varepsilon$ modelling, a) near the corner of the leading edge; b) near the middle on the floor; c) near the corner of the trailing edge

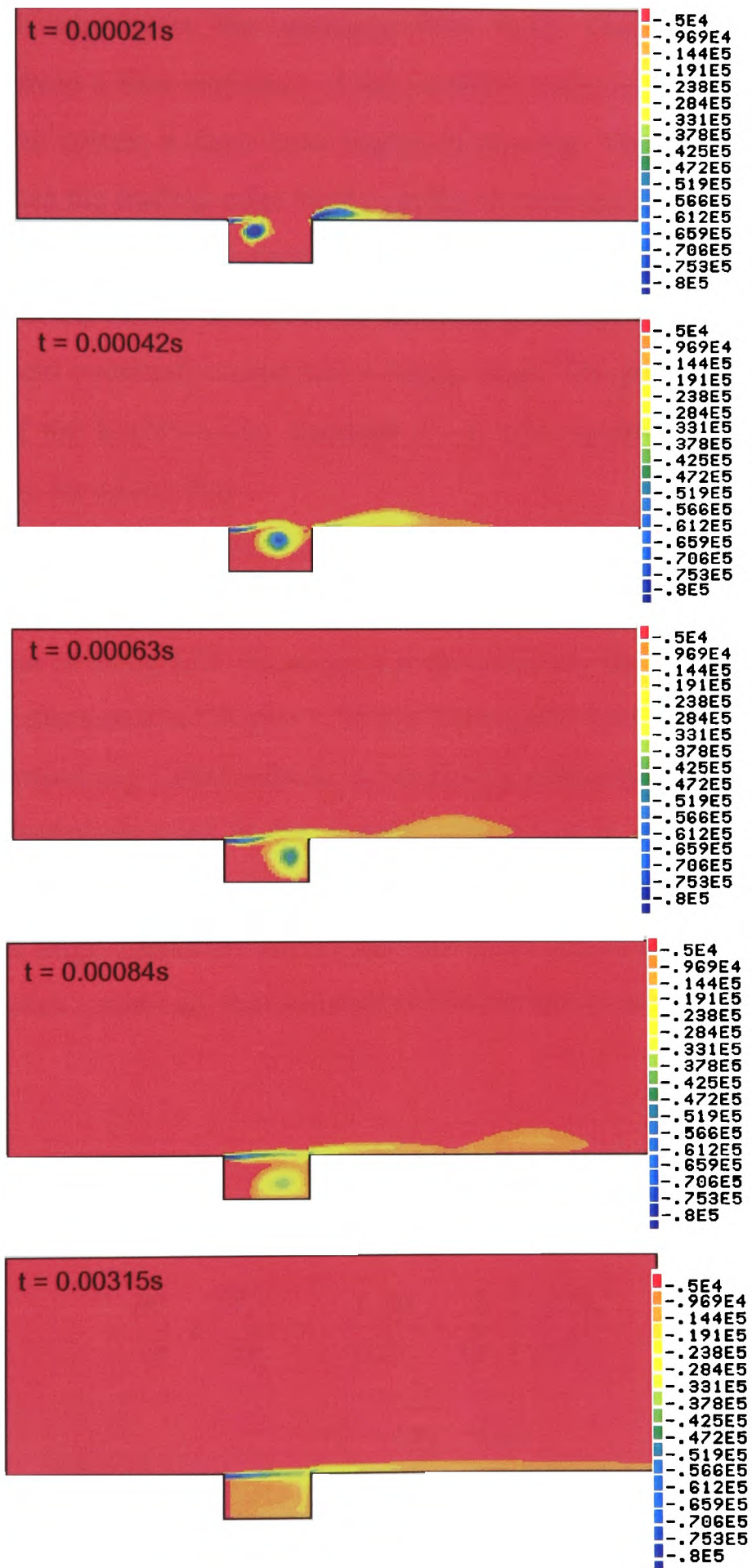


Fig. 6.31. Instantaneous vorticity contours from $k-\varepsilon$ modelling at 5 different CFD time instants

This indicates that $k - \varepsilon$ two-equation turbulence model gives rise to excessive dissipation which suppresses the unsteady flow field. The phenomenon can also be observed clearly from a time sequence of the vorticity contours of the in Figure 6.31. With the shedding of the vortex, a shear layer begins to develop. The vortex is convected by the flow until it reaches the trailing edge of the cavity. Within the cavity, a recirculation region forms, and the region gradually enlarges to fill the whole cavity. However, the shear layer along the mouth of the cavity is seen to be smeared gradually with the increase of running time. The flow field eventually turns into a steady state. The present simulation may serve as an example of the RANS-based standard $k - \varepsilon$ two-equation turbulence model is not generally adequate for cavity flow.

Although $k - \omega$ two-equation turbulence model is reported to successfully simulate supersonic cavity flow [Zhang et al., 1995] and low speed cavity flow [Ashcroft et al., 2000a], an attempt of using LES technique for the unsteady flow computation of the cavity flow is made. As discussed in Chapter 1, in the foreseeable future, LES technique becoming one of the most promising CFD methods in simulating unsteady flows. A simple description about the LES technique used in the present simulation is given below. More detailed introduction about LES can be found in many references and textbooks.

In LES, the large eddies are solved and the small scales are modelled. After filtering of the Navier-Stokes equations, the incompressible continuity and momentum equations can be written as:

$$\frac{\partial \bar{v}_i}{\partial x_i} = 0 \quad (6.1)$$

$$\frac{\partial \bar{v}_i}{\partial t} + \frac{\partial \bar{v}_i \bar{v}_j}{\partial x_j} = -\frac{1}{\rho} \frac{\partial \bar{p}}{\partial x_i} + \frac{\partial}{\partial x_j} \left(\frac{\mu}{\rho} \frac{\partial \bar{v}_i}{\partial x_j} - \tau_{ij}^s \right) \quad (6.2)$$

$$\tau_{ij}^s = \overline{v_i v_j} - \bar{v}_i \bar{v}_j \quad (6.3)$$

where τ_{ij}^s are the subgrid scale (SGS) Reynolds stresses. They are the contribution of the small scales, the unresolved stress, and are unknown. Hence, it must be modelled. In the present simulation, the most commonly used Smagorinsky's SGS model [Smagorinsky,

1963] is adopted. It is an eddy viscosity model. The subgrid scales are of the order of the filter width, Δ . According to Smagorinsky, using the eddy viscosity assumption and mixing length theory, the anisotropic part of τ_{ij}^s is modelled as

$$\tau_{ij}^s - \frac{1}{3}\tau_{kk}^s = -2\nu_{sgs}\bar{S}_{ij}, \quad \nu_{sgs} = (C_s D\Delta)^2 |\bar{S}|, \quad |\bar{S}| = \sqrt{2\bar{S}_{ij}\bar{S}_{ij}} \quad (6.4)$$

where $\bar{S}_{ij} = 0.5(\partial\bar{v}_i/\partial x_j + \partial\bar{v}_j/\partial x_i)$ is the filtered strain rate and ν_{sgs} is the Smagorinsky eddy viscosity. Close to the solid wall, the Van Driest damping function [Van Driest, 1956], $D = 1 - [\exp(y^+/25)]$, is utilized. The Smagorinsky constant, C_s , is taken to be 0.08 in the present computation. The filter width is computed using the definition $\Delta^3 = \Delta x\Delta y\Delta z$, i.e., Δ is taken as the cubic root of the volume of the finite volume cell. Note that the mesh spacing in the spanwise direction is, Δz , equal to the spanwise unit length of the cavity. The above LES technique is implemented within finite volume method based CFD computational framework prescribed in Chapter 3. The same computational mesh shown in Figure 6.29 is used in the present LES computation. The central scheme is used in order to avoid numerical smearing of the fluctuations. The time step for the explicit time marching is $0.4\mu s$. Time history of pressure from this LES computation at three points, which correspond to points in the $k - \varepsilon$ turbulence model based computation, is given in Figure 6.32. Compared to the results in Figure 6.30, LES computation demonstrates self-sustained oscillatory cavity flow. The LES simulation reveals many details of the unsteady flow field. The interaction between the shear layer above the cavity mouth and the external stream results in the periodic addition/removal of mass, near the cavity trailing edge. This behaviour of the shear layer of the shear layer can be clearly seen in the vorticity contours. Figure 6.33 shows the contours of instantaneous vorticity at four different time instants. Each snapshot of instantaneous vorticity corresponds to approximately one-fourth of the period of the cavity flow oscillation. It is clear that vortices shed periodically at the leading edge of the cavity. A large-scale vortical structure grows as they are convected by the flow, while the rest of the unsteady mass flux passes to the downstream. The rolled-up vortex within the cavity interacts with the next vortex shed from the leading edge of the cavity. As

a representative, instantaneous pressure contours and velocity vectors at the time instant of 0,0042s are shown in Figure 6.34.

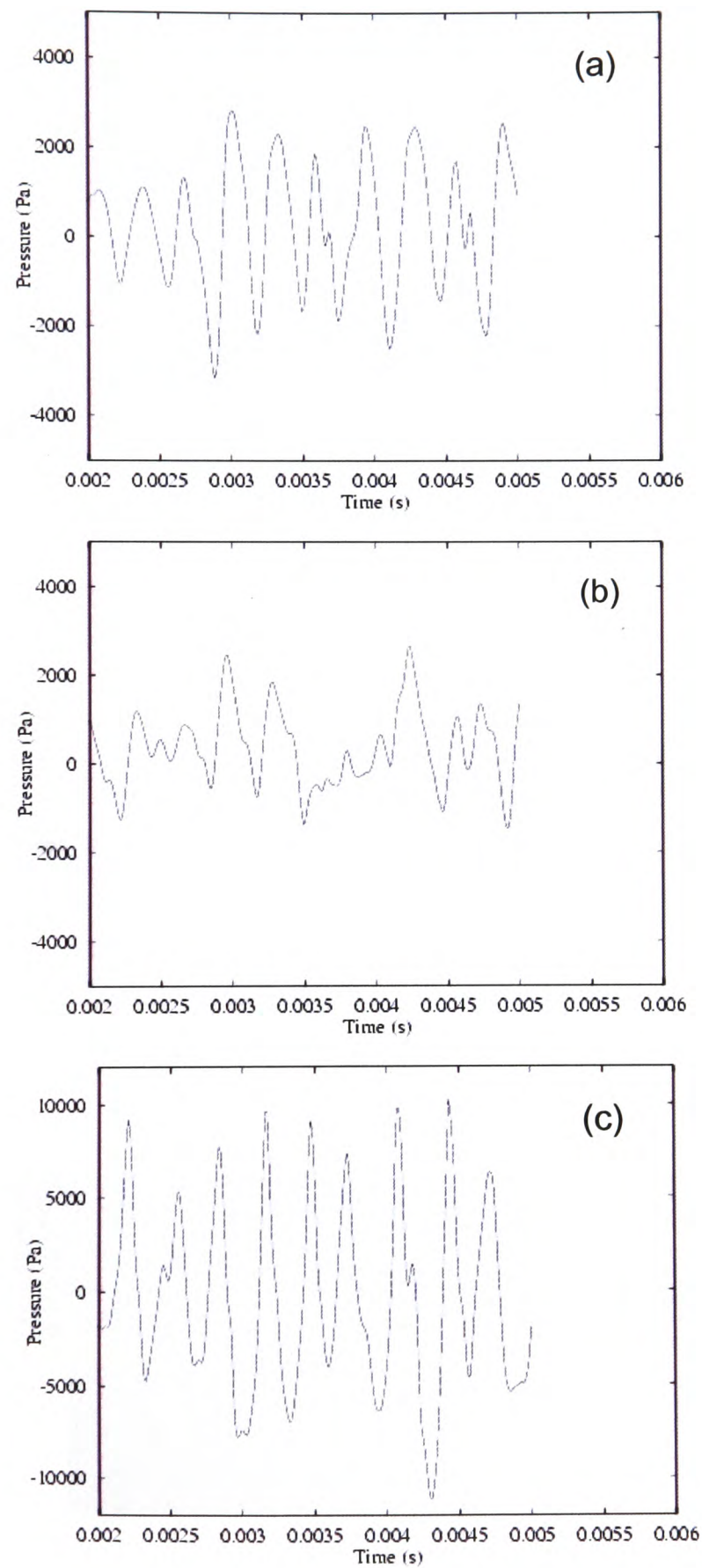


Fig.6.32. Time history of pressure from LES, a) near the corner of the leading edge; b) near the middle on the floor; c) near the corner of the trailing edge

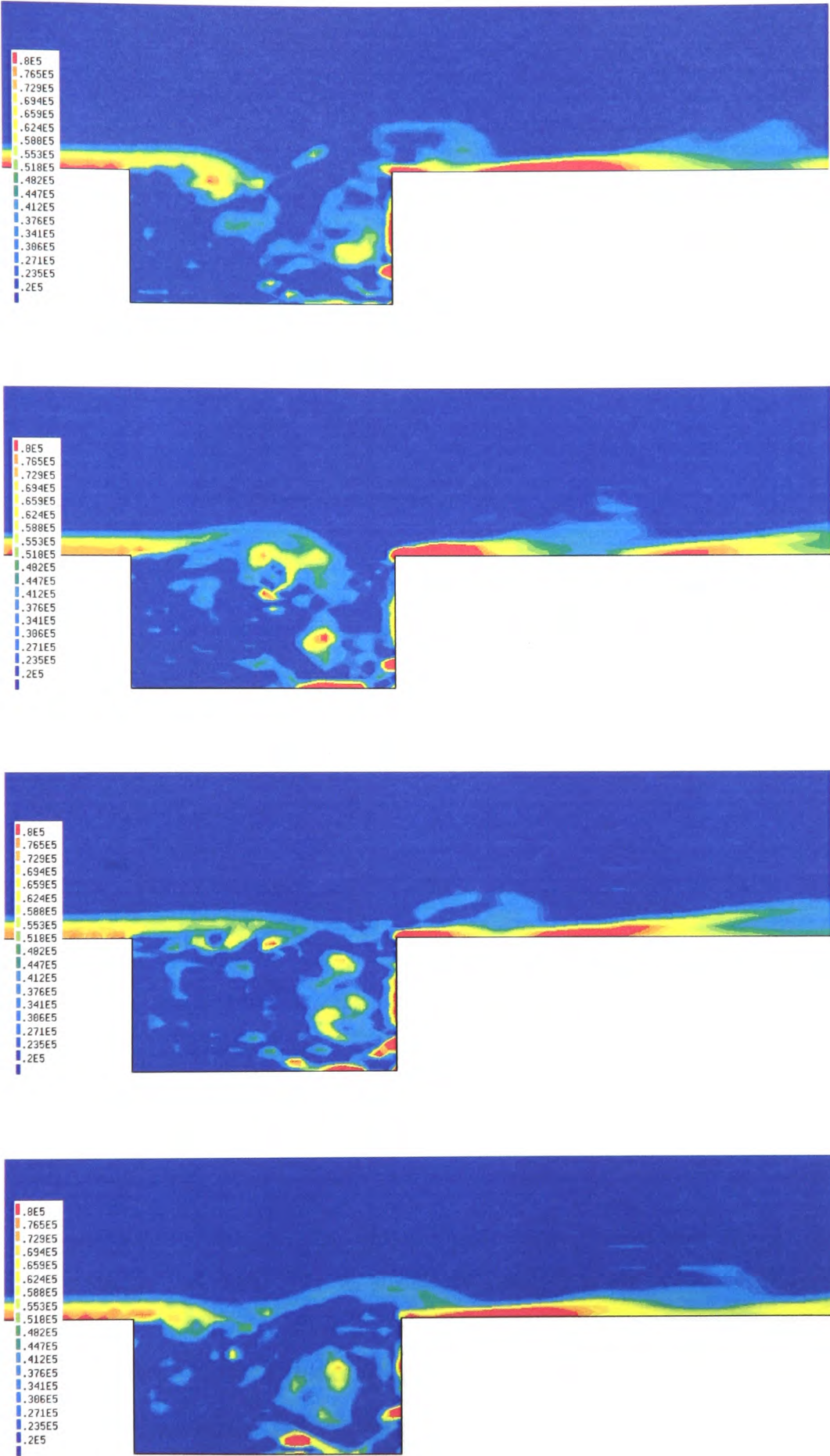
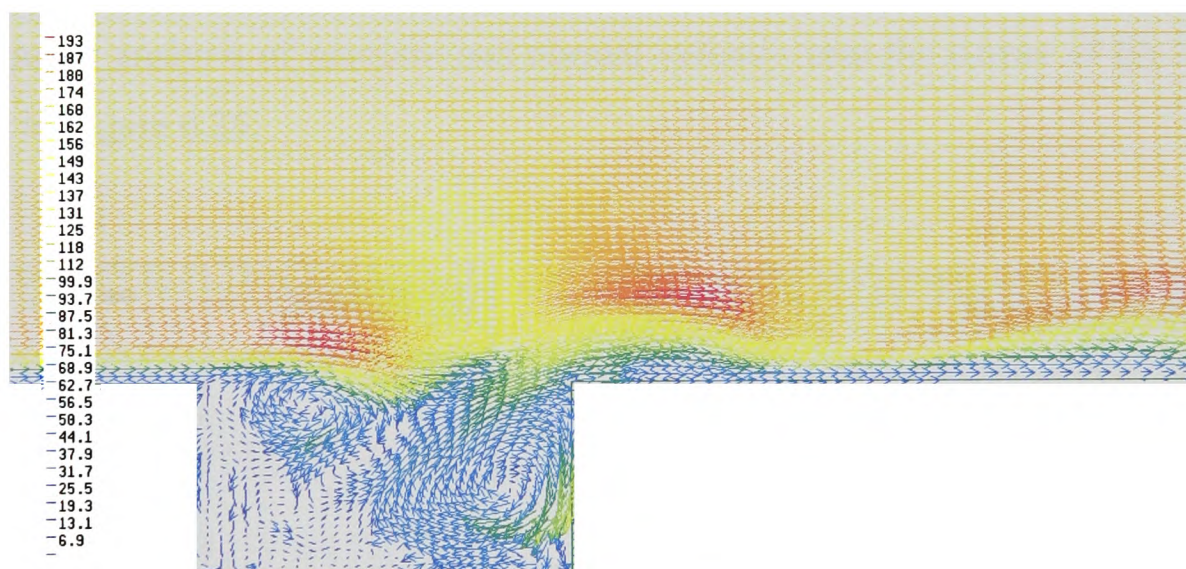


Fig. 6.33. Instantaneous vorticity contours from LES for the cavity flowfield at 5 different CFD time instants



a)



b)

Fig. 6.34. Instantaneous pressure contours and velocity vectors from LES for the cavity flowfield at time instant of 0.0042s. a) pressure contours; b) velocity vectors

A semi-empirical formula developed by Rossiter [1964], and modified by Heller and Bliss [1975] for compressible flows was used to predict the resonant cavity modes. The Rossiter formula is built through simplifying the complex phenomenon of open cavity flows: the free shear layer is viewed as two-dimensional, and the recirculating flow is neglected. Rossiter formula has provided insight into the principal frequencies of discrete tones. The modified Rossiter formula by Heller and Bliss is expressed as follows:

$$f_m = \frac{U_0}{L} \frac{1}{k_c} \frac{m - \alpha}{\sqrt{1 + \frac{\gamma - 1}{2} M_0^2}} \quad (6.5)$$

where γ is the ratio of specific heats, f_m and m are resonant frequency and mode of the oscillation, M_0 and U_0 are the freestream Mach number and velocity, and k_c is the ratio of the convective velocity of the vertical structures in the shear layer to the freestream velocity. Here, α is the phase delay between the interaction of the pressure wave with the leading edge and the subsequent formation of a new shear layer structure. Heller and Bliss determined from their experiments that $\alpha = 0.25$ and $k_c = 0.57$. According to Heller and Bliss, the difference between the Rossiter formula and experiments should be within $\pm 10\%$. A Fourier analysis of pressure and normal velocity near the corner of the trailing edge is given in Figure 6.35.

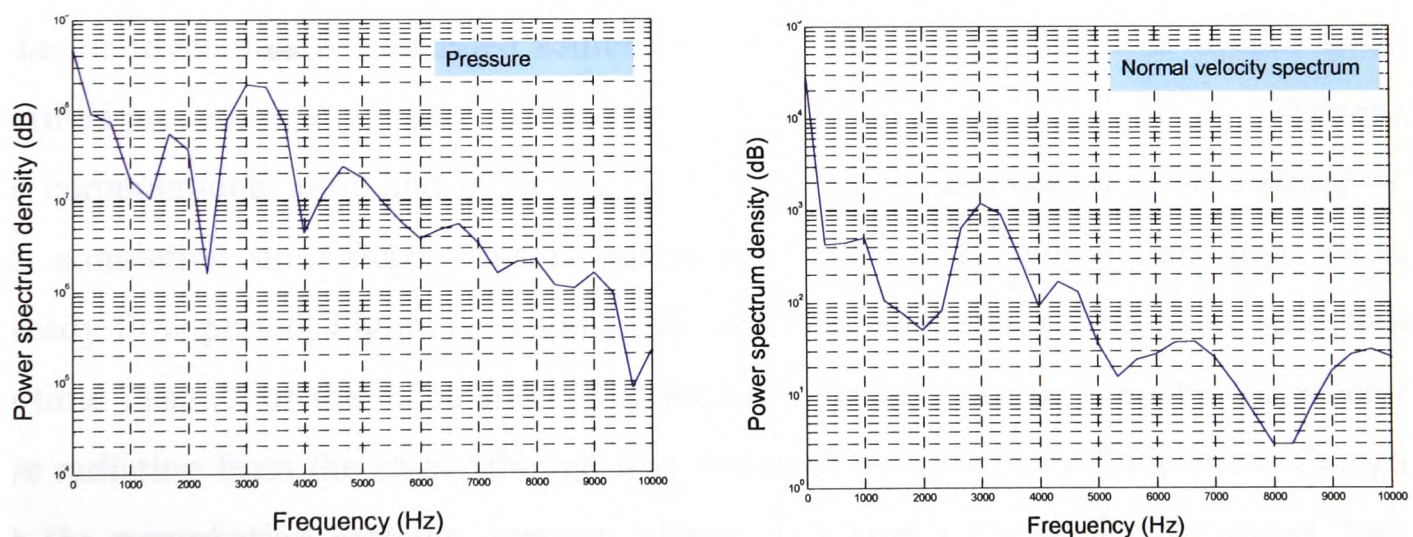


Fig. 6.35. Power spectrums of the pressure and normal velocity near the corner of the trailing edge

It can be identified that the dominant frequency (i.e., the first mode) is obvious. However, harmonics of the fundamental modes become less distinct. Table 6.1 compares the spectral frequencies of the present computation and the Rossiter formula. Only the first two modes

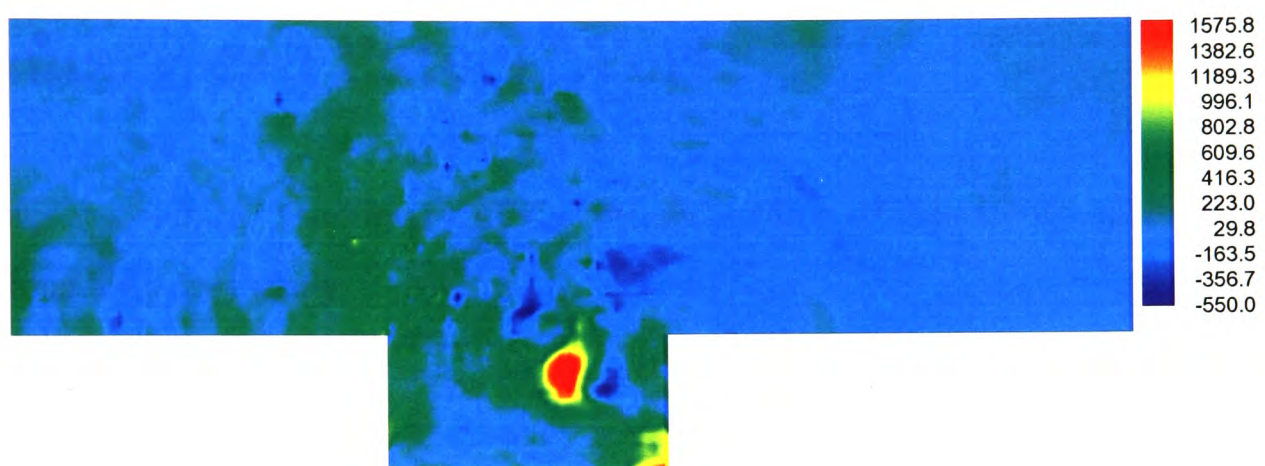
are shown. The computational values are within the acceptable error range that Heller and Bliss estimated.

Table 6.2. Comparison of computational spectral frequencies with the predicted from the modified Rossiter formula (6.5)

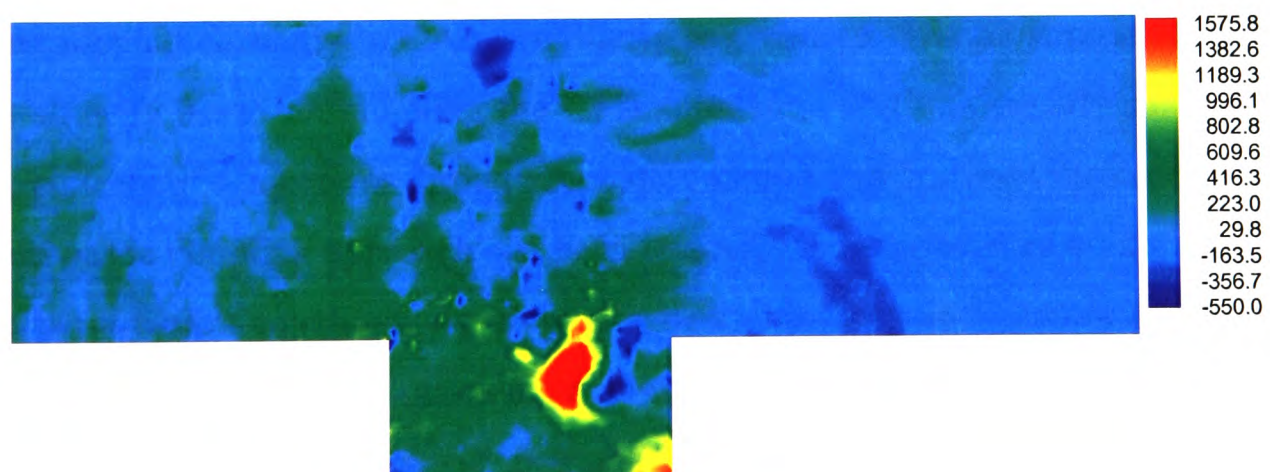
Mode	Present (Hz)	Rossiter(Hz)	Error(%)
1st	3350	3246	3.2
2nd	6750	7570	10.8

The dimensions of the domain for the acoustic calculation are set to the same as the domain in the unsteady flow calculation. The domain sizes are approximately 0.8λ upstream and above the cavity, and 1.3λ downstream, where λ is the acoustic wavelength at the fundamental tonal frequency. From the perspective of the acoustics, such a domain is within the acoustic near-field. A regular Cartesian mesh is used in the acoustic field calculation. The acoustic mesh contains 30×25 and 225×125 cells in the streamwise and vertical direction for the cavity and the region over the cavity, respectively. The extraction of the aerodynamically generated sources and the coupling procedure is similar with the described procedure in Chapter 4. The acoustic time step is taken to be $4.8\mu\text{s}$. Likewise, to save computational time and memory, the CFD solutions are output at an interval of 30 CFD simulation time steps. This is equivalent to about 25 output data files for each unsteady flow period. Figure 6.36 shows the perturbation pressure field in the near field at two time instants of the calculation. The picture reveals, more or less, the main acoustic wave radiating from the cavity though it is obscured by turbulence fluctuation. Compared with the perturbation pressure contours shown in Figure 6.25 for the low-speed laminar flow over the car door cavity, the radiation pattern of the acoustic wave is not apparent but physically reasonable. Note that this is only acoustic results in the near field. In the near field, as mentioned previously, it might be difficult to distinguish both the turbulent fluctuations and acoustic perturbations. In the coupling calculation, some spurious “acoustic sources” are extracted due to the resolved turbulence component. Although the flow condition is compressible (Mach number 0.5), the unsteady flow simulation above is from an incompressible calculation since the LES code used is under development. In addition,

the computational mesh used in the LES calculation is probably slightly coarse. The above preliminary calculation is only an attempt. More research and computational effort on the coupling of a LES technique and the acoustic solver is required. We have to leave this for the future work. These preliminary results obtained by coupling the LES and the acoustic solver were reported at ISMA 2002 International Conference on Noise and Vibration [Wang et al., 2002b].



$t = 0.000072\text{s}$



$t = 0.000108\text{s}$

Fig. 6.36. Instantaneous perturbation pressure contours in the near acoustic field at 2 acoustic time instants

Chapter 7

Summary and Future Work

This chapter contains a summary of the research work of this thesis, along with some suggestions for future study.

7.1 Summary

Various aspects of the direct calculation of aerodynamic sound generation and acoustic wave propagation/radiation using Computational Aeroacoustics (CAA) have been considered. Some state-of-the-art developments, main challenges, and major solution strategies adopted currently in CAA are briefly overviewed. The most promising coupling solution strategy based on coupling the CFD simulation and numerically solving a set of acoustic perturbation equations through acoustic source terms has been discussed. A source-extraction based coupling approach has been studied. The emphasis is on deriving a set of acoustic perturbation equations, developing a new extracting formulation for the acoustic source terms, and designing an efficient coupling procedure.

Some representative acoustic perturbation equations and treatment ways of the acoustic source terms are briefly introduced before describing our source-extraction based coupling method. In the present coupling method, the unsteady aerodynamic calculation and the calculation of the resulting acoustic wave propagation are separated artificially. The technique of variable decomposition is well known, and has been used to study a number of multi-scale flow problems in fluid mechanics. In this thesis, we have applied this technique in terms of two-scale decomposition to the time-dependent compressible Navier-Stokes

equations. Two-scale variable decomposition essentially means splitting a flow variable into a base component (unsteady flow quantity) and a perturbation component (acoustic quantity). A set of acoustic perturbation equations has been derived by rearranging each term in the expanded flow motion equations through certain particular consideration and neglecting some small-magnitude terms. The set of acoustic perturbation equations are further simplified into a set isentropic perturbation equations which are used in the present computations. Accompanying the derivation of the acoustic perturbation equations, a new extracting formulation for the acoustic source terms generated aerodynamically in the unsteady flow field is proposed. The acoustic source terms, which are required in solving the derived acoustic perturbation equations, are extracted numerically from the time-dependent solutions of the unsteady flow field. Compared with *some* existing treatment ways of acoustic source terms in the coupling CFD simulation and the solution of acoustic perturbation equations, this new extracting formulation has two distinct features: no Mach number limit, which can be applied to both incompressible and compressible flows, and no requirement of taking into account the acoustic source characteristics (e.g., dipole and quadrupole or others), which may automatically extract various types of aerodynamic sound sources.

The Reynolds-Averaged-Navier-Stokes equations (RANS) based cell-central finite volume method is mainly used in the simulation of the unsteady flow for the numerical cases considered. As an attempt, a large eddy simulation (LES) technique is also employed for the unsteady flow calculations in the investigation of the flow-induced noise from the subsonic flow over an open cavity.

A powerful and efficient high-order dispersion-relation-preserving (DRP) finite difference scheme with fully staggered-mesh type variable arrangements is investigated in the solution of the acoustic perturbation equations. A set of optimized discretization coefficients for the spatial derivatives and temporal integration in the staggered DRP-type scheme is provided by requiring the schemes to be exact up to certain accuracy order, respectively. Compared with the original DRP scheme, the staggered DPR-type scheme with the optimized coefficients reveals further improvement in the numerical performance. A set of radiation boundary conditions is examined for various background flows.

A suitable and efficient coupling procedure, in conjunction with the source-extraction formulation, is designed between the cell-centred finite volume based CFD solver and the

fully staggered finite difference based acoustic solver. The treatment ways used in the coupling procedure may be directly combined with other CFD codes (or after some small corresponding changes are made). This means that widely available CFD codes can be employed as the first step of the coupling procedure.

The feasibility and suitability of the new source-extraction formulation through the coupling procedure for a range of acoustic model problems have been investigated preliminarily. The computational results from the coupling procedure have been compared with the exact/reference solutions. It is shown that the accuracy of the coupling procedure is very encouraging when reasonable computational mesh sizes and time steps are used in the CFD solver and the acoustic solver.

We have applied the new source-extraction based coupling method to several application cases where the sound is truly flow-generated. These application calculations have demonstrated preliminarily the capability and potential of the new source extraction formulation for more realistic aeroacoustic problems. The computational results have shown the source-extraction based coupling method is able to deal with aerodynamically generated sound. Finally, an attempt of the coupling a LES technique and the acoustic solver also provide some invaluable experience for the further study of the use of LES in the coupling method.

The objectives set up at the beginning of the present research work have basically been achieved. The research in this thesis has provided a novel aerodynamic sound source terms extraction under the framework of coupling strategy for CAA, and has built a good basis for further developing and applying the source-extraction based coupling method to aeroacoustic problems of engineering interest.

7.2 Suggestions for future work

As pointed out in the thesis, one of the important features of the source extracting formulation is that it does not need take into account the types of the acoustic sources and automatically extract various types of acoustic sources. However, the new sound source extraction formulation may lead to a ‘difficulty’ in interpreting the acoustic source terms physically or mathematically in the concept of dipole or quadrupole. In the future work, it is very desirable, if possible, to attempt to give a more physical interpretation for the terms in

the source extracting formulation. Although the suitability and numerical accuracy of the new general formulation for extracting the acoustic sources in the unsteady flows have been preliminarily validated through some model problems, further validation against analytical or DNS solutions in more complex aerodynamic sound model problems is required. In addition, a comparison of the extracted numerically source terms using the extracting formulation with some other source formulations mentioned in the Chapter 2 (including the acoustic source term given in acoustic analogy theory) for a selected model problem or a benchmark problem is also desirable.

The investigation of the application of the source-extraction based coupling approach to some aeroacoustic problems with physical significance and engineering background is also important in the future. Since Large Eddy Simulation (LES) is the most promising numerical technique for the high Reynolds number unsteady flows in the foreseeable future, the coupling of a LES technique with an acoustic solver, in conjunction with the source formulation, is a trend and development direction for computational aeroacoustics (CAA). However, it does not mean RANS-based CFD methods are out-of-date. The RANS simulations with suitable turbulence models methods will continue to play an important role in coupling computation of CAA. One can find that the results of the open cavity flow are not perfect compared to the results of car-door cavity flow. The reasons for that are complicated. They involve different numerical methods (one is RANS based, the other LES), different Mach numbers (one is incompressible, the other compressible), and different flow states (one is laminar, the other turbulent). Further careful computation through coupling a LES technique with the source formulation for the flow-induced noise from the open cavity flow (especially when turbulence is considered), and further comparison of the obtained computational results with experimental results (if available) is strongly suggested.

As stated in the thesis, the computational domain of the simulation of the steady flowfield is generally a small subdomain inside the computational domain of the acoustic field. Different domains may give rise to some particular numerical problems in the coupling procedure. One of them is spurious acoustic source (non-physical reflection, numerical errors, etc.) caused at the boundaries of the CFD domain in the acoustic calculation due to simple truncation of extracting of the acoustic sources. This problem was also addressed by Crighton [1993]. In the present study, the same computational domains

are temporarily used. The development of a technique (method) to damp the spurious sound source is crucial to the practical application of the coupling method.

Since uniform Cartesian mesh is required in the present acoustic solver, it inevitably results in the difficulties in handle non-Cartesian domains and complex curved geometrical configurations. Although stepwise boundary treatment may be approximately used when inclined or curved boundaries occur in the flowfield, the steps at the boundaries will introduce some spurious sound sources and errors into the acoustic solution. In addition, the treatment of the boundary conditions at stepwise walls also requires special attention. One possible attempt to handle this problem is cast all perturbation equations, boundary conditions, and numerical scheme in generalized curvilinear coordinates. In the author's opinion, the development of accurate interpolation ways to handle the curved boundaries is probably more practical.

In the present acoustic solver, a less accurate but much simpler set of acoustic radiation boundary conditions is implemented. More accurate non-reflection boundary conditions are desirable for solution of the acoustic perturbation equations. Many acoustic boundary conditions have been developed. A set boundary conditions based on the perfect match layer (PML) concept [Hu et al., 1996; Hu, 1996] is a good choice for updating the present radiation conditions. One great advantage of the PML method is that if the mean flow is uniform the boundary of the computational domain can be placed very close to the acoustic sources. This allows the use of a small computational domain, and significantly reduces the computation cost.

Low-storage Runge-Kutta methods are currently preferable because of their reduced memory requirements. The integration in time may be attempted to perform the fourth order low dissipation and low dispersion Runge-Kutta scheme proposed by Hu et al. [1996]. This is not, however, essential to the present acoustic solver.

Bibliography

- Al-Qadi, I.M.A., and Scott, J.N. (1998) "A Numerical Investigation of the Influence of Jet Lip Geometry on Mixing", *AIAA Paper-98-2265*
- Ashcroft, G., Takeda, K., and Zhang, X. (2000a) "Computational Modelling of the Aeroacoustics of a Door Cavity Flow Oscillation", in *Proceedings of the 7th International Congress on Sound and Vibration*, Garmisch-Partenkirchen, Germany, July 4-7, pp.1331-1338
- Ashcroft, G., Takeda, K., and Zhang, X. (2000b) "Computations of Self-Induced Oscillatory Flow in an Automobile Door Cavity", Third Computational Aeroacoustics (CAA) Workshop on Benchmark Problems, *NASA CP-2000-209790*, pp.335-361
- Avital, E.J., Sandham, N.D., Luo, K.H. (1999a), "Calculation of Basic Sound radiation of Axisymmetric Jets by Direct Numerical Simulation", *AIAA Journal*, Vol. 97, No.2, pp.161-172
- Avital, E.J., and Lou, K.H. (1999b) "Large Eddy Simulations of Cold and Hot Mixing Layers", *Direct and Large Eddy Simulations III*, ed. Voke P.R., Sandham, N.D. and Kleiser, L., Dordrecht, Kluwer, Academic
- Avital, E.J. (2001) "Direct and Large Eddy Simulations of Compressible Open Cavity Flows", *Direct and Large Eddy Simulation IV*, ed. Geurts, B.J., Friedrich R., and Metais, O., Kluwer Academic Publishers, pp.213-220
- Bailly, C., Lafon, P., Candel, S. (1996) "Subsonic and Supersonic Jet Noise from a Statistical acoustic model and a Compressible Turbulence Closure", *Journal of Sound and Vibration*, Vol. 194, No. 2, pp.219-242
- Bailly, C., Candel, S., and Lafon, P. (1997) "Prediction of Supersonic Jet Noise from a Statistic Source Models", *AIAA Journal*, Vol. 35, No. 11, pp.1688-1696
- Bailly, C., Daniel, J. (1999) "A Stochastic Approach to Compute Subsonic Noise Sing Linearized Euler's Equations", *AIAA Paper 99-1872*
- Bailly, C. Bogey, C. and Juve D. (2002) "Computation of the Flow Noise Using Source Terms in Linearized Euler's Equations", *AIAA Journal*, Vol. 40, No. 2, 2002, pp.235-243
- Baldwin, B.S., and Lomax, H. (1978) "Thin Layer Approximation and Algebraic Model for Separated Turbulent Flows" *AIAA Paper 78-257*
- Baysal, O., Yen, G.W. and Fouladi, K. (1992), "Navier-Stokes Computations of Cavity Aeroacoustics with Suppression Devices", *AIAA/DGLR Paper 92-02-161*
- Bechara, W., Lafon, P., Bailly, C., and Candel, S. (1995) "Application of a k-e Model to the Prediction of Noise for Simple and Coaxial Free Jets", *Journal of Acoustic Society of America*, Vol. 97, No. 6, pp.3518-3531

- Billson, M., Eriksson, L.E., and Davidson, L. (2002) "Acoustic Source terms for the Linear Euler Equations on Conservative Form", *AIAA Paper-2002-2582*
- Bodony, D., and Lele, S.K. (2002), "Spatial Scale Decomposition of Shear Layer Turbulence and the Sound Sources Associated with the Missing Scales in a Large-Eddy Simulation", *AIAA Paper 2002-2454*
- Bogey, C., Bailly, C., and Juve, D. (2000a), "Noise Investigation of a High Subsonic, Moderate Reynolds Number Jet Using a Compressible LES", *AIAA Paper 2000-2009*
- Bogey, C., Bailly, C., and Juve, D (2002), "Computation of flow Noise Using Source Terms in Linearized Euler's Equations", *AIAA Journal*, Vol. 40, No.2, pp.235-243, 2002
- Bogey, C. and Bailly, C. (2002), "Direct Computation of the Sound Radiated by a High-Reynolds Number Subsonic Round Jet", *CEAS Workshop From CFD to CAA*, Athens, Greece, Nov. 2002
- Bogey, C. and Bailly, C. (2003), "LES of a High Reynolds, High Subsonic Jet: Effects of the Subgrid Modellings on Flow and Noise" *AIAA Paper 2003-3557*
- Böhmer, K., and Stetter, H.J. (1984) (Ed.) "Defect Correction Methods: Theory and Applications", Springer-Verlag
- Brentner, K.S. and Farassat, F. (1998) "Analytical Comparisons of the Acoustic Analogy and Kirchhoff Formulation for Moving Surfaces", *AIAA Journal*, Vol. 36, pp.1379-1387
- Brentner, K.S., Cox, J.S., Rumsey, C.L., and Tounis, B.S. (1997) "Computation of Sound Generated by Flow over A Circular Cylinder: An Acoustic Analogy Approach", Second Computational Aeroacoustics (CAA) Workshop on Benchmark Problems, NASA CP-3352
- Chapman, D.R. (1979) "Computational Aerodynamics Development and Outlook", *AIAA Journal*, Vol. 17, pp.1293
- Chu, B.T., and Kovasznay, L.G.S. (1958) "Non-linear Interactions in a Viscous Heat-Conducting Compressible Gas", *Journal of Fluid Mechanics*, Vol. 3, No. 5, pp.494-514
- Choi, D., Barber, T.J., Chiappotta, L.M., and Nishimura, M. (1999) "Large eddy Simulation of High Reynolds Number Jet Flows", *AIAA Paper-99-0230*
- Cohen, G., and Joly, P. (1990), "Fourth Order Schemes for the Heterogeneous Acoustics Equation", *Computational Methods in Applied Mechanics and Engineering*, Vol. 80, pp.397-407
- Colonus, T, Lele, S.K., and Moin, P. (1993) "Boundary Conditions for Direct Computation of Aerodynamic Sound Generation", *AIAA Journal*, Vol. 31, No. 9, pp.1574-1582
- Colonus, T, Lele, S.K., and Moin, P. (1997) "Sound Generation in a Mixing Layer", *Journal of Fluid Mechanics*, Vol. 330, pp. 375-409
- Colonus, T., Basu, A.J., and Rowley, C.W. (1999) "Numerical Investigation of the Flow Past a Cavity", *AIAA Paper 99-1921*
- Constantinescu, G.S., and Lele, S.K. (2001) "Large Eddy Simulation of a Near Sonic Turbulent Jet and Its Radiated Noise", *AIAA Paper 2001-0376*
- Cottet, G. H. and Koumoutsakos, P. (2000) "Vortex Method: Theory and Practice", Cambridge University Press

- Crighton, D.G. (1993) "Computational Aeroacoustics for Low Mach Number Flows", in *Computational Aeroacoustics*, Eds. Hardin, J.C. and Hussaini, Springer-Verlag
- Croft, N., Pericleous, K., and Cross, M. (1995) "PHYSICA: A Multiphysics Environment for Complex Flow Processes", *Numerical Methods in Laminar and Turbulent Flow*, edited C. Taylor and P. Durbetaki, Vol. 9, Pt. 2, Pineridge, Swansea, Wales, U.K., pp.1269-1280, also see <http://physica.gre.ac.uk>
- Davis, A. (1991) "Low Dispersion Finite Difference Methods for Acoustic Waves in a Pipe", *Journal of the Acoustical Society of America*, Vol. 90, pp.2775-2781
- Difrancesantonio, P. (1997) "A New Boundary Integral Formulation for the Prediction of Sound Radiation", *Journal of Sound and Vibration*, Vol. 202, pp.491-509
- Disselhorst, J.H.M., and Van Wijngaarden, L. (1980) "Flow in the Exit of Open Pipes during Acoustic Resonance", *Journal of Fluid Mechanics*, Vol. 99, pp.293-319
- Djambazov, G., Lai, C.H., and Pericleous, K. (1998a), "Efficient Computation of Aerodynamic Noise", *Contemporary Mathematics*, Vol. 218, pp.500-506
- Djambazov, G. (1998b) "Numerical Techniques for Computational Aeroacoustics", Ph.D. thesis, University of Greenwich
- Djambazov, G., Lai, C.H., and Pericleous, K. (2000a) "On the Coupling of Navier-Stokes and Linearized Euler Equations for Aeroacoustic Simulation", *Computing and Visualization in Science*, Vol. 9, pp.9-12
- Djambazov, G., Lai, C.H., and Pericleous, K. (2000b), "Staggered-Mesh Computation for Aerodynamic Sound", *AIAA Journal*, Vol. 38, No.1, pp.16-21
- Ekaterinaris, J.A. (1997) "Upwind Scheme for Acoustic Disturbances Generated by Low-Speed Flows", *AIAA Journal*, Vol.35, No.9, pp.1448-1455]
- Eldredge, J.D., Colonius, T., and Leonard, A. (2002) "A Vortex Particle Method for Two-Dimensional Compressible Flow" *Journal of Computational Physics*, Vol. 179, No.,2, pp.371--399.
- Ewert, R, Meinke M., and Schröder, W.S. (2000) "Aeroacoustic Source Terms for the Linearized Euler Equations", *AIAA Paper-2000-2046*
- Ewert, R, Meinke M., and Schröder, W.S. (2001) "Comparison of Source Term Formulations for a Hybrid CFD/CAA Method", *AIAA Paper-2001-2200*
- Ewert, R, Meinke M., and Schröder, W.S. (2002) "Computational of Trailing Edge Noise via LES and Acoustic Perturbation Equations", *AIAA Paper-2002-2467*
- Ewert, R, Meinke M., and Schröder, W.S. (2003) "Acoustic Perturbation Equations Based on Flow Decomposition via Source Filtering", *Journal of Computational Physics*, Vol. 188, pp.365-398
- Farassa, F. and Myers, M.K. (1988) "Extension of Kirchhoff's Formula to Radiation From Moving Surfaces", *Journal of Sound and Vibration*, Vol. 123, pp.451-461
- Farassa, F. and Myers, M.K. (1995) "The Kirchhoff's formula for a Supersonically Moving Surfaces", *Proceedings .of the first Joint CEAS/AIAA Aeroacoustic Conference*, Vol. 1, pp.455-461

- Freund, J.B., Lele, S.K. and Moin, P. (1997) "Results of a Compressible Round Shear Layer Direct Simulation", *AIAA Paper-97-0760*
- Freund, J.B., Lele, S.K. and Moin, P. (1998) "Direct Simulation of a Mach 1.92 Jet and Its Sound Field", *AIAA Paper-98-2291*
- Freund, J.B., Lele, S.K. and Moin, P. (2000) "Direct Numerical Simulation of a Mach 1.92 Turbulent Jet and its Sound Field", *AIAA Journal*, Vol. 38, No.38, pp.2023-2031
- Ffowcs, J.E., and Hawkings, D.L. (1969) "Sound Generated by Turbulence and Surfaces in Arbitrary Motion", *Philosophical Transactions of the Royal Society of London*
- Gloerfelt, X. Bailly, C and Juve, D. (2001) "Computation of the Noise Radiated by a Subsonic Cavity Using Direct Simulation and Acoustic Analogy", *AIAA Paper 2001-2226*
- Gloerfelt, X. Bailly, C and Juve, D. (2002) "Aerodynamic Noise Induced by Laminar and Turbulent Boundary Layers over Rectangular Cavities", *AIAA paper-2002-2476*
- Golanski, F., Prax, C., and Valiere, J.C. (2003) "An Aeroacoustic Hybrid Approach for Non-isothermal Flows at Low Mach Number" submitted to *International Journal of Numerical Methods in Fluids*
- Goldstein, M.E. (1976) "Aeroacoustics", McGraw-Hill Book Company, Inc., New York
- Granger, R. (1985), "Fluid Mechanics", Holt, Rinehart and Winston, New York
- Goodrich, J.W. (1997) "High accuracy Finite Difference Algorithms for Computational Aeroacoustics", *AIAA Paper-97-1584*
- Grogger, H., Lummer, M. and Lauke, T., (2001) "Simulating the Interaction of a Three-Dimensional Vortex with Airfoils Using CAA", *AIAA Paper 2001-2137*
- Hardin, J. C. (1993) "Regarding Numerical Considerations for Computational Aeroacoustics", *Computational Aeroacoustics*, Eds. J.C. Hardin, M. Y. Hussaini. New York, Springer-Verlag, pp.216-229
- Hardin, J.C. and Pope, D.S. (1994) "An Acoustic/Viscous Splitting Technique for Computational Aeroacoustics", *Theoretical and Computational Fluid Dynamics*, Vol. 6, pp.323-340
- Hardin, J.C. and Pope, D.S. (1995) "Sound Generation by Flow over a Two-Dimensional Cavity", *AIAA Journal*, Vol. 33, No.3, pp.407-412
- Hayase, T, Humphrey, J.A.C., and Grief, R. (1992) "A Consistently Formulated QUICK Scheme for Fast and Stable Convergence Using Finite Volume Iterative Calculation Procedure", *Journal of Computational Physics*, Vol. 98, pp.108-118
- Heller, H.H., and Bliss, D.B. (1975) "Physical Mechanism of Flow-Induced Pressure Fluctuation in Cavities and Concepts for their Suppression", *AIAA Paper-75-491*
- Henderson, B. (2000) "Automobile Noise Involving Feedback Sound Generation by Low Speed Cavity Flows", in proceedings of the 3rd Computational Aeroacoustics Workshop on Benchmark Problems, *NASA/CP-2000-209790*
- Hessenius, K.A. (1993) "Welcome Address", *Computational Aeroacoustics*, Eds. J.C. Hardin, M. Y. Hussaini. New York, Springer-Verlag, pp.xi-xiii

- Holberg, O. (1987) "Computational Aspects of the Choice of Operator and Sampling Interval for Numerical Differentiation in Large-Scale Simulation of Wave Phenomena", *Geophysical Prospecting*, Vol. 35, pp.629-655
- Howe, M.S. (1975) "Contribution to the Theory of Aerodynamic Sound, with Application to Excess Jet Noise and the Theory of the Flute", *Journal of Fluid Mechanics*, Vol. 71, pp.625-673
- Howe, M.S. (1984) "On the Absorption of Sound by Turbulence and Other Hydrodynamic Flows", *I.M.A. Journal of Applied Mathematics*, Vol. 32, pp.187-203
- Howe, M.S. (1996), "Emendation of the Brown and Michael Equation with Application to Sound Generation by Vortex Motion near a Half-Plane", *Journal of Fluid Mechanics*, Vol. 329, 1996, pp.89-101
- Hu, F.Q., Hussaini, M.Y., and Manthey, J.L. (1996) "Low-Dissipation and Low-Dispersion Runge-Kutta Schemes for Computational Acoustics", *Journal of Computational Physics*, Vol. 124, pp.177-191
- Hu, F.Q. (1996) "On Perfect Matched Layer as an absorbing Boundary Condition", *AIAA Paper-96-1664*
- Inoue, O., Hatakeyama, N., Hosoya, H., and Shoji, H. (2001) "Direct Numerical Simulation of Aerolian Tones", *AIAA Paper 2001-2132*
- Jones, W.P., and Launder, B.E. (1973) "The Calculation of Low-Reynolds Number Phenomena with a Two-Equation Model of Turbulence", *International Journal of Heat and Mass Transfer*, Vol. 16, pp.1119-1130
- Katoh, C. (1992) "Numerical Prediction of Aerodynamic Sound by Using the Large Eddy Simulation, in Proceedings of the 70th Convention of JSME, Vol. C
- Kim, C., Roe, P.L., and Thomas, J.P. (1997) "Accurate Schemes for Advection and Aeroacoustics", *AIAA Paper-97-2091*
- Kim, J.W., and Lee, D.J. (1996) "Optimized Compact Finite Difference Schemes with Maximum Resolution", *AIAA Journal*, Vol. 34, pp.887-893
- Kinsler, L., Frey, A., Coppens, A., and Sanders, J. (1982) "Fundamental of Acoustics", John Wiley & Sons, New York
- Kirchhoff, G.R. (1883) "Toward a Theory of Light Rays", *Annals of Physical Chemistry*, Vol. 18, pp.663-695
- Lee, D.J., and Koo, S.O. (1995) "Numerical Study of sound Generation Due to a Spinning Vortex Pair", *AIAA Journal*, Vol. 33, No. 1, pp.20-27
- Lele, S.K. (1992) "Compact Finite Difference Schemes with Spectral-like Resolution", *Journal of Computational Physics*, Vol. 103, pp.16-42
- Lele, S.K. (1997) "Computational Aeroacoustics: A Review", *AIAA Paper 97-0018*
- Leonard, B.P. (1979) "A Stable and Accurate Convective Modelling Procedure Based on Quadratic Upstream Interpolation", *Computer Methods in Applied Mechanics and Engineering*, Vol. 19, pp.59-98
- Lighthill, M.J. (1952) "On Sound Generated Aerodynamically. Part I Generally Theory", *Proceedings of the Royal Society*, Vol. 211A, pp.564-587

- Lighthill, M.J. (1954) "On Sound Generated Aerodynamically. Part II Turbulence as a Source of Sound", *Proceedings of the Royal Society*, Vol. 222, A, pp.1-32
- Lighthill, M.J. (1993) "The Final Panel Discussion", *Computational Aeroacoustics*, Eds. J.C. Hardin, M. Y. Hussaini. New York, Springer-Verlag, pp.499-513
- Lighthill, M.J. (1962) "Sound Generated Aeroacoustically", *Phil. Trans. Royal Soc. London*, A267, pp.147-182
- Lilley, G. (1974) "On the Noise from Jets," *AGARD CP-131*, pp.13.1-13.10
- Lockard, D.P., Brentner, K.S., and Atkins, H.L. (1994) "High Accuracy Algorithm for Computational Aeroacoustics", *AIAA Journal*, Vol. 33, pp.246-251
- Loh, C.Y., and Wang, X.Y. (2000) "Computation of Feedback Aeroacoustic System by the CE/SE method", *NASA/TM-2000-210479*
- Lui, C., and Lele, S.K. (2002) "A Numerical Study of Shock-Associated Noise", *AIAA Paper 2002-2530*
- Lupoglazoff, N., Biancherin, A., Vuillot, F., and Rahier, G. (2002) "Comprehensive 3D Unsteady Simulations of Subsonic and Supersonic Hot Jet Flow-Field", *AIAA Paper 2002-2599*
- Lyrantzis, A., and Mankbadi, R.R. (1988) "On the Prediction of the Far-Field Noise using Kirchhoff Method", *AIAA Journal*, Vol. 34, pp.413-416
- Mankbadi, R.R., Hayder, M.E., and Povinelli, L.A. (1994) "Structure of Supersonic Jet Flow and Its Radiated Sound", *AIAA Journal*, Vol. 32, No.5, pp.897-906
- Manoha, E., Elias, G., Troff, B., and Sagaut, P. (1999) "Towards the Use of Boundary Element Method in Computational Aeroacoustics", *AIAA Paper 99-1980*
- Meneveau, C. and Katz, J. (2000) "Scale-Invariance and Turbulence Models for Large-Eddy Simulation", *Annual Review of Fluid Mechanics*, Vol. 32, pp.1-32
- Mitchell, B.E., Lele, S.K., and Moin, P. (1995) "Direct Computation of the Sound from a Compressible Co-rotating Vortex Pair", *Journal of Fluid Mechanics*, Vol. 285, pp.181-202
- Mitchell, B.E., Lele, S.K., and Moin, P. (1996) "Direct Computation of Mach wave Radiation in an Axisymmetric Jet", *AIAA Paper 96-1729*
- Miyake, Y., Tsujimoto, K., Miyamoto, Y., and Ryo, T. (2001) "A DNS of Acoustic Field emitted from a Near-Wall Turbulent Flow", *AIAA Paper-2001-2134*
- Morfey, C.L. (2000) "Fundamental Problems in Aeroacoustics", *Proceedings of the 7th International Congress on Sound and Vibration*, July 4th-7th, Garmisch-Partenkirchen, Germany, pp.59-74
- Morris, P.J., Long, L.N., Bangalore, A. and Wang, Q.Z. (1997) "A Parallel Three-Dimensional Computational Aeroacoustics Method Using Nonlinear Disturbance Equations," *Journal of Computational Physics*, Vol. 133, pp.56-74
- Morton, K., and Mayers, D. (1994) "Numerical Solution of Partial Differential Equations", Cambridge University Press, Cambridge, U.K., pp.114~118

- Ogawa, S., and Kamioka, T. (1999) "Review of Aerodynamic Noise Prediction Using CFD", *AIAA Paper 1999-1126*
- Patankar, S.V., and Spalding, D.B. (1972) "A Calculation Procedure for Heat, Mass and Momentum Transfer in Three-dimensional Parabolic Flows", *International Journal of Heat and Mass Transfer*, Vol. 15, pp.1787-1806
- Patankar, S.V. (1980) "Numerical Heat Transfer and Fluid Flow", Hemisphere Publishing Corporation, New York
- Peters, M.C.A., and Hirschberg, A. (1993) "Acoustically Induced Periodic Vortex Shedding at Sharp Edged Open Channel End: Simple Vortex Models", *Journal of Sound and Vibration*, Vol. 161, pp.281-299
- Pierce, A. (1981) "Acoustic: An Introduction to Its Physical Principles and Applications", McGraw-Hill
- Phillips, O.M. (1960) "On the Generation of Sound by Supersonic Turbulent Shear Layers", *Journal of Fluid Mechanics*, Vol. 9, pp.1-28
- Pilon, A.R. and Lirintzis, A. (1998) "Development of an Improved Kirchhoff Method for Jet Aeroacoustics", *AIAA Journal*, Vol. 36, pp.783-790
- Piomelli, U., Streett, C.L., and Sarkar, S. (1997) "On the Computation of Sound by Large-Eddy Simulations", *Journal of Engineering Mathematics*, Vol. 32, pp.217-236
- Pothou, K.P., Voutsinas, S.G., Huberson, S.G. and Kino, O.M. (1996) "Application of 3-D Particle Method to the Prediction of Aerodynamic Sound", In *Vortex Flow and Related Numerical Methods II*, Vol 1 of European Series in Applied and Industrial Mathematics
- Powell, A. (1964) "Theory of Vortex Sound", *Journal of the Acoustic Society of America*, Vol. 36, pp.177-195
- Raithby, G. D. (1976) "A Critical Evaluation of Upstream Differencing Applied to Problems Involving Fluid Flow", *Computer Methods in Applied Methanics and Engineering*, Vol. 9, pp.75-103
- Rayleigh, J. W. S. (1877) "Theory of Sound", 2 Vols. New York, Macmillan
- Rhie, C., and Chow, W. (1983) "A Numerical Study of the Turbulent Flow Past an Isolated Airfoil with Trailing Edge Separation", *AIAA Journal*, Vol. 21, No.11, pp.1525-1532
- Ribner, H.S. (1981) "Perspectives on Jet Noise" *AIAA Paper 81-0428*
- Rossiter, J.E. (1964) "Wind Tunnel Experiments on the Flow over Rectangular Cavities at Subsonic and Transonic Speeds", *Royal Aircraft Establishment, TR No. 64307*
- Rubinstein, R. and Zhou, Y. (1999) "Characterization of Sound Radiation by Unresolved Scales of Motion in Computational Aeroacoustics", *NASA/CR-1999-209688*
- Seror, C., Sagaut, P., and Juve, D. (1999) "Subgrid Scale Contribution to Noise Production in Decaying Isotropic Turbulence", *AIAA Paper 99-1979*
- Shen, W.Z. and Sørensen, J.N. (1999a) "Comment on the Aeroacoustic Formulation of Hardin and Pope", *AIAA Journal*, Vol. 37, No. 1, pp.141-143

- Shen, W.Z. and Sørensen, J.N. (1999b) "Aeroacoustic Formulation of Low Speed Flows", *Theoretical and Computational Fluid Dynamics*, Vol. 13, No. 4, pp.271-289
- Shen, W.Z. and Sørensen, J.N. (2001) "Aeroacoustic Modelling of Turbulent Airfoil Flows", *AIAA Journal*, Vol. 39, No. 6, pp.1057-1064
- Shieh, C.M. and Morris, P.J. (1999) "Parallel Numerical Simulation of Subsonic Cavity Noises", *AIAA Paper 99-1891*
- Shieh, C.M. and Morris, P.J. (2000) "Parallel Computational Aeroacoustic Simulation of Turbulent Subsonic Cavity Flow", *AIAA Paper 2000-1914*
- Shih, S.H., Hamed, A., and Yeuan, J.J. (1994) "Unsteady Supersonic Cavity Flow Simulations Using Coupled k-e and Navier-Stokes Equations", *AIAA Journal*, Vol. 32, No.10, pp.815-913
- Sinha, N., and Arunajatesan, S. (2000) "High Fidelity Simulation of Weapons Bay Aeroacoustics and Active Flow Control", *AIAA Paper-2000-1968*
- Smagorinsky, J. (1963) "General Circulation Experiments with the Primitive Equations", *Monthly Weather Review*, Vol. 91, pp.40-65
- Spalart, P.R., and Allmaras, S.R. (1992) "A One-equation Turbulence Model for Aerodynamic Flows", *AIAA Paper 92-0439*
- Spalding, D. B. (1972) "A Novel Finite Difference Formulation for Differential Expressions Involving Both First and Second Derivatives", *International Journal for Numerical Methods in Engineering*, Vol. 4, pp.551-559
- Stallings, R.L., and Wilcox, F.J. (1987) "Experimental Cavity Pressure Distributions at Supersonic Speeds", *NASA TP-2683*
- Suhs, N.E. (1993) "Unsteady Flow Computations for a Three-dimensional Cavity with and without an Acoustic Suppression Device", *AIAA Paper 93-3402*
- Tam, C.K.W., and Burton, D.E. (1984) "Sound Generated by Instability Waves of Supersonic Flows, Part 2: Axisymmetric Jets", *Journal of Fluid Mechanics*, Vol. 138, pp.273-295
- Tam, C.K.W., and Morris, P.J. (1985) "Tone Excited Jets, Part V: A Theoretical Model and Comparison with Experiment", *Journal of Sound and Vibration*, Vol. 102, No.1, pp.119-151
- Tam, C.K.W., and Webb, J.C. (1993) "Dispersion-Relation-Preserving Finite Difference Schemes for Computational Acoustics", *Journal of Computational Physics*, Vol. 107, pp.262-281
- Tam, C.K.W., Webb, J.C., and Dong, Z. (1993) "A Study of the Short Wave Components in Computational Aeroacoustics", *Journal of Computational Acoustics*, Vol. 1, pp.1-30
- Tam, C.K.W. (1997) "Numerical Methods in Computational Aeroacoustics", in *Computational Aeroacoustics: Methods and Applications*, Short Course, AIAA, Atlanta, USA, pp.1-78
- Tam, C.K.W., and Dong, Z. (1993) "A Study of the Short Wave Components in Computational Acoustics", *Journal of Computational Acoustics*, Vol. 1, No.1, pp.1-30

- Tam, C.K.W., and Dong, Z. (1994) "Wall Boundary Conditions for High-Order Finite Difference Schemes in Computational Aeroacoustics", *Theoretical and Computational Fluid Dynamics*, Vol. 8, No.6, pp.303-322
- Tam, C.K.W. (1995) "Computational Aeroacoustics: Issues and Methods", *AIAA Journal*, Vol. 33, No.10, pp.1788-1796
- Tam, C.K.W. (1998) "Advances in Numerical Boundary Conditions for Computational Aeroacoustics", *Journal of Computational Acoustics*, Vol. 6, No.4, pp.377-402
- Thomas, J.W. (1995) "Numerical Partial Differential Equations", Springer-Verlag, New York, 1995
- Tsujimoto, K., Hayashi, A., and Miyake, Y. (1998) "Identification of Noise Source in Low Mach Number Flow by DNS", *AIAA Paper-98-2366*
- Uzun, A., Blaisdell, G.A., and Lyrantzis, A.S. (2002) "Recent Progress Towards a large Eddy Simulation Code for Jet Aeroacoustics", *AIAA Paper 2002-2598*
- Van Driest, E.R. (1956) "On Turbulent Flow near a Wall", *Journal of Aeronautical Sciences*, Vol. 23, pp.1007-1015
- Vichnevetsky, R., and De Schutter, F. (1975) "A Frequency Analysis of Finite Difference and Finite Element Methods for Initial Value Problems", in *Advances in Computer Methods for Partial Differential Equations*, Vichnevetsky, R., (ed.), AICA/IMACS, Rutgers University, New Brunswick, New York, pp.46-52
- Vichnevetsky, R. (1987) "Wave Propagation and Reflection in Irregular Grids for Hyperbolic Equations", *Applied Numerical Mathematics*, Vol.3, pp.133-166
- Viswanathan, K. and Sankar, L.N. (1995) "Toward the Direct Calculation of Noise: Fluid/Acoustic Coupled Simulation," *AIAA Journal*, Vol.33, No. 12, pp 2271-2279
- Wang, Z.K., Djambazov, G., Lai, C.H., and Pericleous, K. (2002a), "Numerical Simulation of Flow-induced Cavity Noise Using A Source-Extraction Based Coupling Algorithm", in *Proceedings of the 9 International Congress on Sound and Vibration, Aeroacoustics II*, pp.1-9, July 8th-11th, Orlando, USA
- Wang, Z.K., Tilford, T., Djambazov, G., Lai, C.H., and Pericleous, K. (2002b), "Aeroacoustic Computation of an Open Cavity Flow Using a Coupled LES/LEE Approach", in *Proceedings of International Conference on Noise and Vibration Engineering*, Vol. I, pp. 231-242, Sept. 16th -18th, Leuven, Belgium
- Wang, Z.K., Djambazov, G., Lai, C.H., and Pericleous, K. (2003a) "A Novel Aerodynamic Sound Source Terms Extraction Formulation for Hybrid methods in Computational Aeroacoustics", submitted to *International Journal of Aeroacoustics*
- Wang, Z.K., Djambazov, G., Lai, C.H., and Pericleous, K. (2003b), "Numerical Investigation of a Source Extraction Technique Based on an Acoustic Correction Method", submitted to *Computers & Mathematics with Applications*
- Wang, Z.K., Djambazov, G., Lai, C.H., and Pericleous, K. (2003c), "Numerical Simulation of Flow-Induced Cavity Noise in Self-Sustained Oscillations", submitted to *Computing and Visualization in Science*

- Whitham, G.B. (1974) "Linear and Nonlinear Waves", Wiley and Sons, New York
- Wilcox, D.C. (1988) "Reassessment of the Scale-Determining Equation for Advanced Turbulence Models", *AIAA Journal*, Vol. 26, No. 6, pp.1299-1310
- Zhao, W., Frankel, S.H., and Mongeau, L. (2000a) "Large Eddy Simulation of Sound Radiation from a Subsonic Turbulent Jet", *AIAA Paper 2000-2078*
- Zhao, W., Frankel, S.H., and Mongeau, L. (2000b) "Effects of Spatial Filtering on Sound Radiation from a Subsonic Axisymmetric Jet", *AIAA Journal*, Vol. 38, No.11, pp.2082-2089
- Zhang, X., Rona, A., and Lilley, G.M. (1995) "Far -Field Noise Radiation from an Unsteady Supersonic Cavity Flow", *CEAS/AIAA-95-040*
- Zingg, D.W., Lomax, H., and Jurgen, H. (1996) "High Accuracy Finite Difference Schemes for Linear Wave Propagation", *SIAM Journal of Scientific Computing*, Vol. 17, No. 2, pp.328-346
- Zhuang, M., and Chen, R.F. (1998) "Optimized Upwind Dispersion-Relation-Preserving Finite Difference Scheme for Computational Aeroacoustics", *AIAA Journal*, Vol. 36, No. 11, pp.2146-2148